

WORKSHOP ON NUCLEAR DYNAMICS III

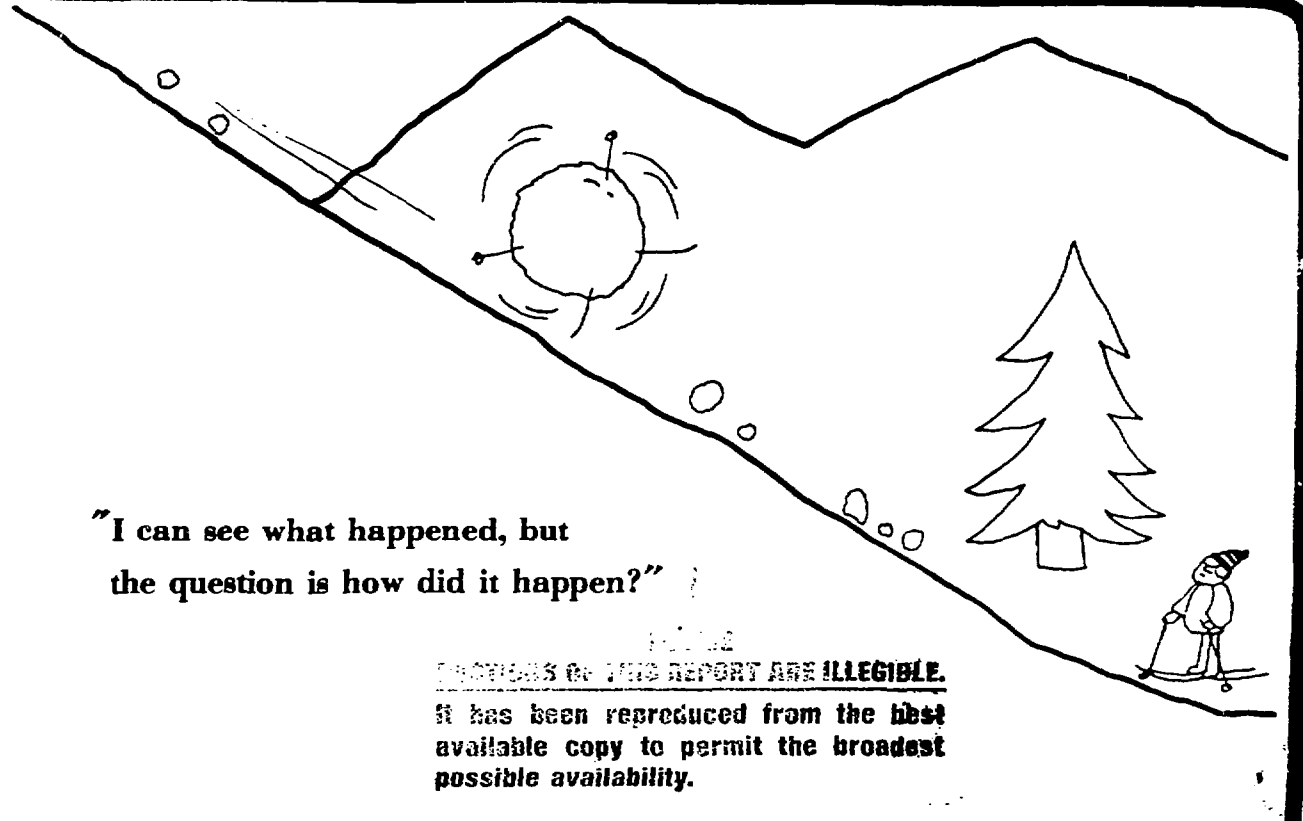
5-9 March 1984

Copper Mountain, Colorado

APRIL 1984

CONF-8403101--

DE84 013540



"I can see what happened, but
the question is how did it happen?"

PORTIONS OF THIS REPORT ARE ILLEGIBLE.

It has been reproduced from the best
available copy to permit the broadest
possible availability.

Organizers: V. E. Viola, Jr., F. Plasil, J. R. Nix,
W. D. Myers, J. R. Huizenga, J. J. Griffin,
and C. K. Gelbke

PREFACE

The 1984 Workshop on Nuclear Dynamics can best be characterized in a few phrases - excellent presentations of forefront research results, active scientific interchange among the participants, and great weather - for skiers as well as those content with just soaking up the beauty of the Colorado Rockies. Despite a crowded schedule, the intensity of participation maintained a very high level throughout the week. As a consequence, the workshop provided a very productive environment for examining the complex features of nucleus-nucleus collisions.

Among the many important contributions to the workshop, only a few are noted in these introductory remarks. With respect to nuclear fission, the self-consistent application of the finite-range liquid-drop model to heavy-ion induced fission data now appears to provide a satisfactory description of these processes, removing many previous ambiguities. The sessions on damped collisions were distinguished by increasingly sophisticated efforts, in terms of theoretical developments as well as the quality of the available data base. As indicated in Jørgen Randrup's cover cartoon, considerable attention was given to the important problem of deriving primary fragment distributions from the observed experimental data. Particular emphasis was given to discussions of data obtained from the new generation of heavy-ion accelerators. These talks highlighted the need for greater theoretical attention to this regime of nucleus-nucleus collisions. Finally, the recent results from the plastic ball and streamer chamber experiments are now yielding impressive results which promise to have a major impact on our understanding of the nuclear equation of state.

The meeting proved highly successful due to the efforts of many individuals. First of all, my secretary at IU, Betty Grubb, did a superb job of handling the workshop details, ranging from our first announcement to completion of these proceedings. My daughter, Gina, also proved very helpful in assisting with many workshop arrangements. Also, the staff at Copper Mountain deserves commendation for its friendly, efficient service - including everyone from the lodging and food service personnel to the lift operators. The lodging and conference facilities helped contribute to a healthy conference environment.

Finally, I wish to acknowledge the strong support of the workshop organizing committee: Konrad Gelbke, Jim Griffin, John Huizenga, Bill Myers, Ray Nix and Franz Plasil. Bill Myers, who will be retiring from the committee this year, deserves special commendation for his efforts over the years as one of the initial organizers of the workshop. Preparation of these proceedings was partially supported through Indiana University and the U. S. Department of Energy, contract no. DE-AC01-81ER-40007.

Vic Viola, Editor

PROGRAM AND CONTENTS

Page

Monday, March 5, 1984

Morning Session (V. E. Viola, Jr., presiding)

F. Plasil, "Recent Results in Heavy-Ion-Induced Fission"	1
K. Lesko, "Mass Dependence of the Fusion of Ni + Sn"	5
H. Weidenmuller, "Transients in Fission and their Implications for Light-Particle Emission" (oral presentation only)	
J. Kunz, "Nuclear Inertia for Fission in a Generalized Cranking Model"	9
Contributed paper: J. Mateja, "A Study of $^{11}\text{B} + ^{12}\text{C}$ and $^{10}\text{B} + ^{13}\text{C}$ Fusion Cross Sections"	13

Evening Session (W. D. Myers, presiding)

J. R. Huizenga, "Measurement of Nuclear Potentials from Fusion Excitation Functions"	16
M. J. Rhodes-Brown, "A Self-Consistent Approach to Low-Energy Heavy- Ion Reactions"	20
K. McVoy, "The Nearside/Farside Decomposition of Heavy-Ion Elastic Scattering Amplitudes"	23
P. Müller, "Nuclear Mass Formula with a Neutron Skin Degree of Freedom and Finite-Range Model for the Surface Energy"	28
Y. Boneh, "Particles + Core Reduction of the Fission Equations in the Time-Dependent Mean-Field Approximation"	32
M. Dworzecka, "Macroscopic Implications of Diverse Transfer Mechanisms in Heavy-Ion Collisions"	37
Contributed paper: S. Ayik, "Damping of Collective Motion in Extended TDHF"	42

Tuesday, March 6, 1984

Morning Session (A. C. Mignerey, presiding)

F. Beck, "Dissipation and Fluctuations in Nucleus-Nucleus Collisions"	46
H. Feldmeier, "Exchange of Particles, Momentum and Entropy" . . .	50
H. Breuer, "Nucleon and Energy Exchange in Low-Energy Heavy-Ion Reactions"	58
J. J. Griffin, "Exact Quantal Schrödinger Model of Dinuclear Flow: Importance of Kinetic Pressure for Flux Rates"	62

Evening Session (D. Cline, presiding)

R. Vandenbosch, "How is Excitation Energy Divided in Partially Damped Collisions?"	67
H. Freiesleben, "Sharing of Excitation Energy in the Kr + Pb Reaction"	72
Contributed paper: A. C. Mignerey, "Quasielastic Structure in the Reaction $^{58}\text{Fe} + ^{56}\text{Fe}$ at 14.6 MeV/Nucleon"	76
J. Randrup, "Relaxation Times for Angular Momentum in Damped Nuclear Reactions"	80
W. Trautmann, "A Polarization Study of Incomplete Fusion Dynamics"	84
Contributed papers: F. Lefebres, "What Can We Learn from Spin Depolarization Measurements in Damped Nuclear Reactions?"	88
S. T. Thornton, "Observation of a Critical Angular Momentum for Deep Inelastic Processes with Light Heavy Ions"	97

Wednesday, March 7, 1984

Morning Session (R. L. Robinson, presiding)

T. C. Awes, "Projectile Fragmentation in ^{58}Ni -Induced Reactions at 15.3 MeV/u"	101
U. Winkler, "Three Nuclei Fragmentation in Light-Ion Reactions at 11 MeV/u Bombarding Energy"	105
F. Lefebres, "First Results of 35 MeV/u Kr + Au Experiment at GANIL"	109

	Page
H. Oeschler, "Linear Momentum Transfer Studies at Energies Around 100 MeV/u"	116
Evening Session (J. R. Huizenga, presiding)	
M. B. Tsang, "Enhanced Emission of Non-Compound Light Particles in the Reaction Plane"	120
K. Kwiatkowski, "Linear Momentum Transfer in Intermediate-Energy Projectile-Nucleus Collisions"	126
Y. Chan, "Velocity Distribution of Fusion-Like Products for Medium Mass Heavy-Ion Systems"	131
M. Moehring, "Simple Estimates for Fermi-Jets"	136
G. Wozniak, "Complex Fragment Emission from Compound Nuclei" (oral presentation only)	
<u>Thursday, March 8, 1984</u>	
Morning Session (S. Thornton, presiding)	
W. G. Lynch, "Formation and Decay of a Localized Region of High Excitation in Heavy-Ion Reactions".	140
G. D. Westfall, "Entropy Production in High Energy Nuclear Collisions"	145
N. T. Porile, "Droplet Model of Nuclear Fragmentation at High Energies - Application to Fragment Charge Distribution"	149
L. P. Csernai, "Stopping Power of Heavy Nuclei"	153
P. Danielewicz, "Transport Properties of Excited Nuclear Matter"	156
Evening Session (M. Levine, presiding)	
E. Remler, "Robust Observables in Nuclear Dynamics"	161
U. Mosel, "Mean-Field Approach to Pion Production in Intermediate-Energy Heavy-Ion Collisions"	165
K. L. Wolf, "Pion Production in High Energy Heavy-Ion Collisions"	169
J. Aichelin, "New Evidence for Hot Spots from Subthreshold Pions"	174

Contributed papers: B. Schürmann, "The Anisotropy Ratio for Particle-Inclusive Production in High Energy Nucleus-Nucleus Collisions: A Sensitive Probe for Pion Production Mechanisms"	178
W. Zwermann, "Aspects of Particle-Inclusive Production in Nucleus-Nucleus Collisions at 2.1-GeV Nucleon"	182

Friday, March 9, 1984

Morning Session (R. Nix, presiding)

B. Ludewigt, "Collective Flow Effects Observed with the Plastic Ball"	186
C. M. Ko, "Effect of Final State Interactions on Subthreshold K^- Production in Heavy-Ion Collisions".	191
H. Stoecker, "Microscopic Calculations of Nuclear Matter Collective Flow in Nb (400 MeV/N) : Nb"	195
C. Y. Wong, "Baryon Distribution in Relativistic Heavy-Ion Collisions"	203
Contributed Papers: C. Y. Wong, "Initial Energy Density of Quark-Gluon Plasma in Relativistic Heavy-Ion Collisions"	207
L. Csernai, "Statistically Generated Events and the Fluid-Dynamical Expectation in High Energy Nucleon Collisions"	211
G. Bozzolo, "Thermal Properties of Light Nuclei with Realistic Effective Hamiltonians"	215
J. Boguta, "High Energy Nuclear Structures"	219
List of Participants	223

RECENT RESULTS IN HEAVY-ION-INDUCED FISSION*

F. Plasil, T. C. Awes, B. Cheynis,^a D. Drain,^a R. L. Ferguson, F. E. Obenshain, A. J. Sierk,^b S. G. Steadman,^c and G. R. Young
Oak Ridge National Laboratory, Oak Ridge, Tennessee 37831

A. Gavron, J. Boissevain, H. C. Britt, K. Eskola,^d P. Eskola,^d M. M. Fowler, Z. Fraenkel,^e H. Ohm, and J. van der Plicht^f
Los Alamos National Laboratory, Los Alamos, New Mexico 87545

S. Wald

Lawrence Berkeley Laboratory, Berkeley, California 94720

In this report we summarize our results on three aspects of heavy-ion-induced fission studies: angular-momentum-dependent fission barriers;¹ fission cross sections at relatively high energies;² and angular distributions.^{2,3}

A systematic investigation of angular-momentum-dependent fission barriers has been completed. Fission excitation functions were measured for the compound nuclei ^{153}Tb , ^{158}Er , ^{181}Re , ^{186}Os , and $^{204,206,208,210}\text{Po}$. In the case of ^{153}Tb and ^{181}Re , evaporation residue cross sections were also measured. With the exception of some of the Po systems, two to five different reactions were used to produce the same compound nucleus with projectiles ranging from ^9Be to ^{64}Ni . Angular momentum effects were thus isolated, and the studies were carried out over a large range of both excitation energy and angular momentum. As an example, measured fission excitation functions are shown in Fig. 1 for the compound nucleus ^{158}Er formed in reactions with ^{16}O , ^{24}Mg , ^{32}S , and ^{64}Ni projectiles. In this case, it is estimated that the average angular momentum leading to fission ranged from 40-60 \hbar

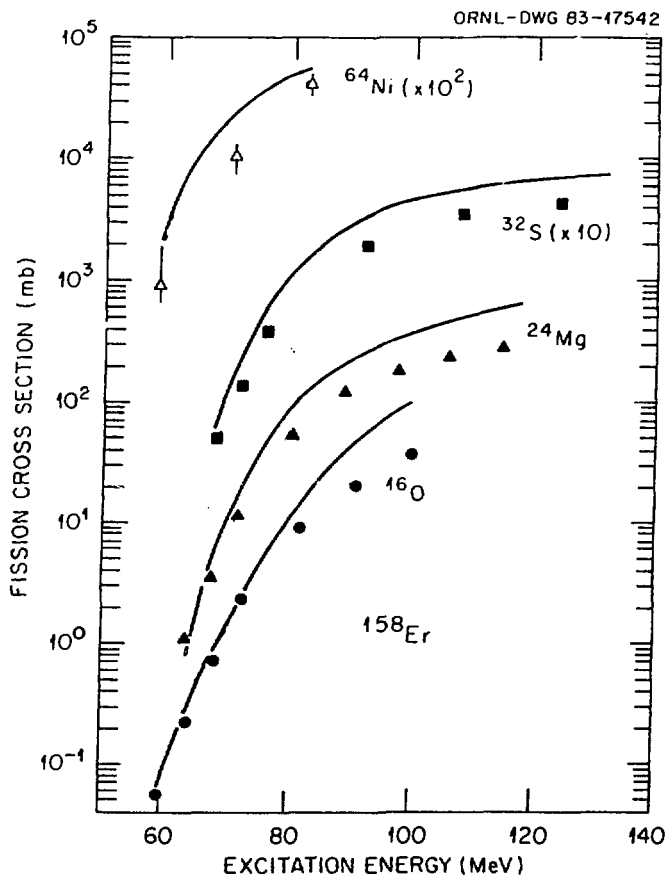


Fig. 1. Measured (points) and calculated (curves) fission excitation functions for the compound nucleus ^{158}Er formed in reactions with various projectiles.

for ^{16}O -induced reactions to 60-80 μ for ^{64}Ni -induced reactions and that the excitation energy ranged from 60 to 120 MeV. The excitation functions were analyzed by means of statistical model calculations using fission barriers from the recently developed rotating finite-range model⁴ (RFRM). It was found that the measured excitation functions are adequately described without any adjustment of the RFRM fission barriers (see Fig. 1). The RFRM takes into account the finite range of the nuclear force as well as surface diffuseness effects. An example of calculated angular-momentum-dependent fission barriers is shown in Fig. 2, both for the RFRM and for the rotating liquid drop model (RLDM). In contrast to earlier studies in which RLDM barriers had to be arbitrarily scaled, the ratio of the level density parameter for fission to that for particle emission was the only variable parameter used in the fitting procedure, and its value was kept constant for any given compound nucleus. It was concluded that the new RFRM fission barriers are valid in the mass region from 150 to 210 amu and that the RFRM model should replace the widely used RLDM.

The fission cross section measurements described above have been extended to higher energies. We have studied ^{12}C reactions with ^{174}Yb , ^{198}Pt , and ^{238}U at energies from 95 to 291 MeV; ^{16}O reactions with ^{142}Nd , ^{170}Er , ^{192}Os , and ^{238}U at energies from 140 to 315 MeV; ^{32}S reactions with ^{126}Te , ^{144}Nd , and ^{238}U at energies from 350 to 700 MeV; and ^{58}Ni reactions with ^{96}Zr , ^{116}Cd , and ^{238}U at 352 and 875 MeV. Velocities and positions of coincident fission fragments were measured, allowing the determination of the extent of fission following incomplete momentum transfer. Such contributions were found to be substantial only in reactions on ^{238}U targets. In our fission cross section analysis, we have included only events with complete and nearly complete momentum transfer. Results from ^{12}C and ^{16}O bombardments are shown in Fig. 3, together with calculated fusion cross sections using a combination of the statistical model and the Bass model.⁵ The calculated results agree with experiment in cases involving ^{238}U targets, but serious discrepancies are evident in the case of the ^{158}Er and ^{186}Os systems. We conclude that in the lighter systems, either the Bass model does not apply at these high energies or strong nonequilibrium charged-particle emission (e.g., from incomplete fusion) results in enhanced cross sections for evaporation residues at the expense of the fission process. Attempts to describe our results with the "extra-push" model have been only moderately successful.

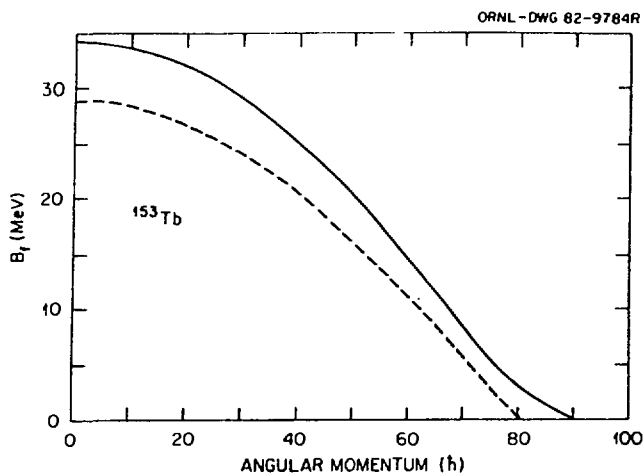


Fig. 2. Calculated fission barrier of ^{153}Tb as a function of angular momentum. The solid curve is from the rotating liquid drop model, and the dashed curve from the RFRM.

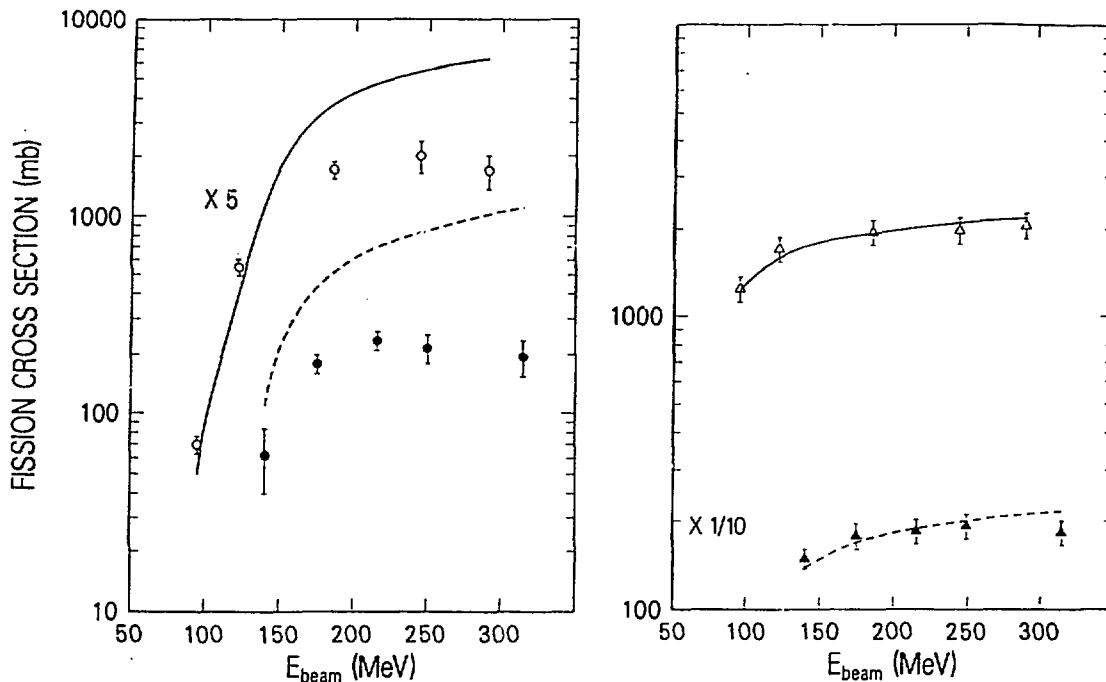


Fig. 3. Measured and calculated fission excitation functions for the reactions $^{16}\text{O} + ^{142}\text{Nd}$ (closed circles), $^{12}\text{C} + ^{174}\text{Yb}$ (open circles), $^{16}\text{O} + ^{238}\text{U}$ (closed triangles), and $^{12}\text{C} + ^{238}\text{U}$ (open triangles). The curves represent calculations using the Bass model, together with a statistical model computer code.

Fission fragment angular distributions were measured for the above ^{12}C - and ^{16}O -induced reactions. The results were analyzed in terms of saddle-point moments of inertia obtained from the RFRM. It was found that in cases in which the fission barrier is higher than the temperature at the saddle point for a significant fraction of the partial waves contributing to fission, the measured angular distributions are consistent with those expected on the basis of the RFRM. This observation was also found to hold in the case of a large number of previously published angular distributions. In cases where the nuclear temperature exceeds the fission barrier, it is not possible to predict the extent of agreement between theory and experiment. For partial waves beyond the limit of a finite fission barrier, the RFRM makes, of course, no prediction of any kind as to the shape of the fissioning systems, and the transition state theory used in the analysis may no longer be applied at the saddle in the usual way. Thus, conclusions drawn from data involving angular momenta beyond the limit at which the fission barriers are predicted to vanish should not make any claims regarding the validity of either the RFRM or the RLDM.

References

- *Research supported by the U.S. Department of Energy under contract W-7405-eng-26 with Union Carbide Corporation (ORNL) and under contract with the Los Alamos National Laboratory and Lawrence Berkeley Laboratory.
- ^aPermanent address: Institut de Physique Nucléaire de Lyon, 69622 Villeurbanne, France.
- ^bPermanent address: Los Alamos National Laboratory, Los Alamos, New Mexico 87545.
- ^cPermanent address: Massachusetts Institute of Technology, Cambridge, Massachusetts 02139.
- ^dPermanent address: University of Helsinki, Helsinki, Finland.
- ^ePermanent address: Weizmann Institute, Rehovot, Israel.
- ^fPresent address: National Superconducting Cyclotron Laboratory, Michigan State University, East Lansing, Michigan 48824.
1. J. van der Plicht et al., Phys. Rev. C 28, 2022 (1983); F. Plasil et al., Phys. Rev. C 29, 1145 (1984).
 2. A. Gavron et al., unpublished results.
 3. A. Gavron et al., Phys. Rev. Lett. 52, 589 (1984).
 4. A. J. Sierk, unpublished results.
 5. R. Bass, Phys. Rev. Lett. 39, 265 (1977).

By acceptance of this article, the publisher or recipient acknowledges the U.S. Government's right to retain a nonexclusive, royalty-free license in and to any copyright covering the article.

MASS DEPENDENCE OF THE FUSION OF Ni + Sn

K.T. Lesko, W. Henning, G. Rosner, K.E. Rehm, J.P. Schiffer,
G.S.F. Stephans, B. Zeidman, and W.S. Freeman

Argonne National Laboratory, Argonne, IL 60439

Over the last few years there has been much interest in the fusion of moderate mass systems. These studies have concentrated on essentially three questions: 1) the sub-barrier enhancement of compound nucleus formation (CN), 2) competition between evaporation residue and fission channels and 3) the introduction of new degrees of freedom to the fusion process. [1-4]

The sub-barrier penetration probes the aspects of nuclear structure which determine the shape of the nuclear surface. Recent investigations suggest several possible explanations for the observed enhancement of cross sections above the usual fusion barrier estimates. These suggestions include deformation and collective vibrational effects, Coulomb distortion and rotation effects, valence neutrons, and finally, the introduction of new degrees of freedom (extra-push). The fission excitation functions and the competition between fission and evaporation residues have been shown to yield Rotating Liquid Drop Model parameters. The possibility of confirming some of the popular new Dynamical Models has been, thus far, limited to measuring fusion cross sections.

To address these questions we have undertaken a comprehensive examination of the fusion of $^{64,58}\text{Ni}$ on $^{112-124}\text{Sn}$ over the energy range of 150-200 MeV in the center of mass. In particular, we wished to address the issue of neutron excess as opposed to nuclear collectivity. Consequently, we choose a system with a large variation in neutron number and a system that does not exhibit a strong collective nature. We obtained the evaporation residues [1] and fission cross sections for energies starting well below the classical barrier and extending well beyond it. The wide range of neutron numbers for these systems provides a unique opportunity to investigate the mass dependence of each of these three topics.

The first measurement measured the evaporation residues for the systems $^{58,64}\text{Ni} + ^{112-124}\text{Sn}$ over the energy range of 150-220 MeV in the center of mass. The residues, which were peaked within 5 degrees of the beam, were separated from the beam and the elastically scattered particles using an electrostatic deflector. They were then detected in a gas delta-E solid state-E telescope. The most striking feature of the measured cross sections is the order of magnitude variation in cross sections in going from the most proton rich system to the most neutron rich system. Qualitatively, this difference can be thought to arise either from competition from fission channels or from differences in the compound nucleus formation cross sections. A statistical code analysis (CASCADE) followed the trends mentioned above; however, they underpredicted the effects by about a factor of 2 for the most neutron rich systems.

To address which of these two explanations is correct, we have measured the fission cross sections for the same systems over the same energy range. The data being presented here are from a preliminary analysis which is ongoing. The errors shown are statistical errors only. We estimate that an overall systematic error as large as 20-30% may exist, and further data analysis will reduce this to a more reasonable 10-15%. The data extraction technique was uniform from target to target so that the relative errors should be much less than the overall systematic errors.

We detected coincident fission fragments. One fragment was detected in a gas delta-E solid state-E time of flight spectrometer, which measured the energy, charge, mass, and position of fragment. This was the solid angle determining detector (c. .5msr). The other fragment was detected in a large position sensitive gas detector on loan from M.P.I. (TIC) This counter has a position sensitive delta E region followed by a large E region. The position sensitivity comes from the "saw-tooth" anode. The vertical position of the fragments is measured from the drift time between the anode and cathode. The position resolution was of order 1mm in both directions. The acceptance of the detector was c. 30 degrees in plane and c. 15 degrees out of plane. The fission yields were normalized to a monitor detector which was later calibrated to elastically scattered beam.

We can make several observations about our preliminary results. First, the fission cross sections are (within errors and kinematics) constant for all targets (see figure 1). This would then suggest that the variation in cross sections observed for the evaporation residues is not complemented by the fission fragments, and that the observed differences arise from differences in compound nucleus formation cross sections.

By summing the evaporation residue and fission cross sections and comparing them to the fission cross sections, we can obtain the fission probability as a function of energy and target. We observe the striking feature that the fission probability, rather than rapidly decreasing at the anticipated center of mass energy, flattens out and persists at energies well below the barrier. This would indicate that in addition to the observed enhancement of fusion at energies below the barrier, an enhancement to fission is also observed (see figure 2).

Finally, we can compare the fusion cross sections calculated above to various models (see figure 3). Shown are the model predictions at a single energy of the extra push model (lower solid line), the upper curve is a conventional reaction cross section prediction. The crosses are our data for the target masses 112-124. This would suggest that for the lowest fissility system $(Z/A)_{\text{eff}} = 31.2$ an extra push is important, but as the neutron number decreases $(Z/A)_{\text{eff}} = 32.9$ no extra push is required.

In conclusion, we have observed that the fission cross sections are independent of the target neutron excess and that the observed variations in ER cross sections are manifest of differences in CN formation cross sections. In addition to the enhancement of the ER cross sections at low energies, we also observe an enhancement of fission cross sections. Our choice of targets and projectile allow use to span a range of effect fissilities which are important in the evaluation of some of the new dynamical models.

- 1) W.S. Freeman, et al., Phys Rev Lett 50 1563 (1983)
- 2) W. Reisdorf, et al., Phys Rev Lett 49 1811 (1982)
- 3) M. Blann, et al., Phys Rev C 26 1471 (1982)
- 4) W.J. Swiatecki Nucl Phys A376 276 (1982)

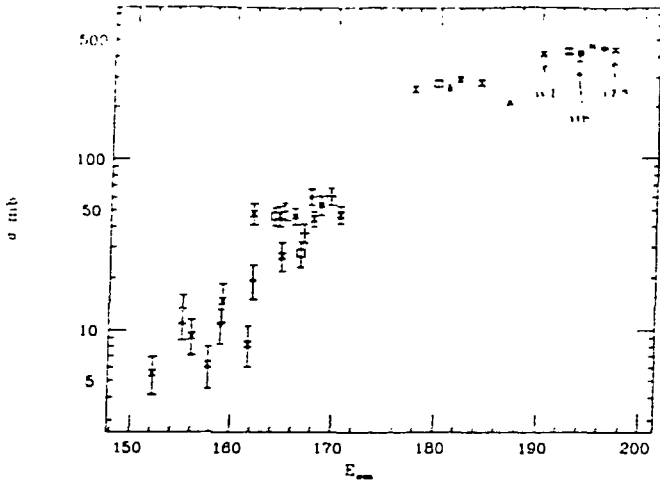


Fig. 1 Fission Excitation Function
Different symbols correspond to different targets as illustrated.

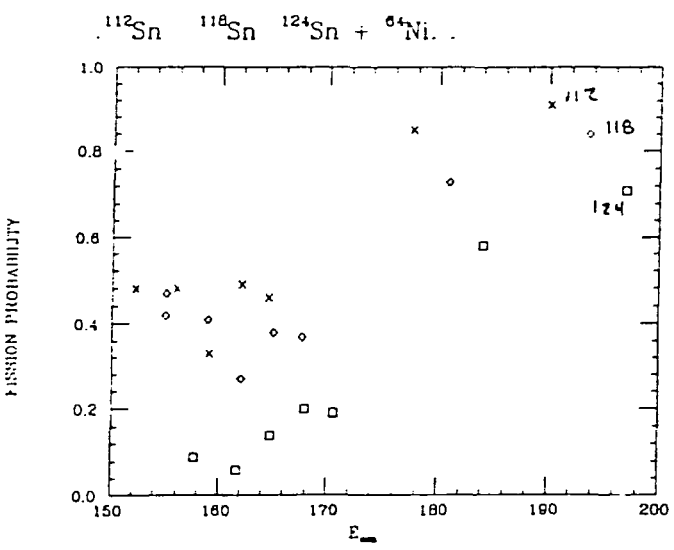


Fig. 2 Fission Probability
Fission probability for three targets, 112, 118, 124 Sn

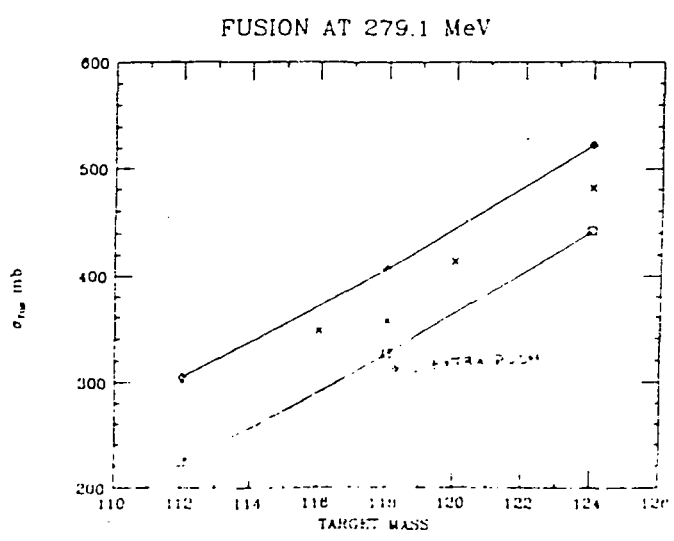


Fig. 3 Fusion Cross Sections at 279 MeV
Lower curve is for extra push model.
Upper curve is for classical fusion model. Data for different targets are shown by x.

NUCLEAR INERTIA FOR FISSION IN A GENERALIZED CRANKING MODEL

J. Kunz and J. R. Nix
Theoretical Division, Los Alamos National Laboratory
Los Alamos, New Mexico 87545

The Inglis cranking model [1] has been widely used to calculate the nuclear inertia associated with collective degrees of freedom. After the inclusion of pairing correlations, theoretical results obtained with the cranking model for nuclear rotations and γ -vibrations were in relatively good agreement with experimental data. Calculations of β -vibrational inertias were also performed in the cranking model for fission deformations. Theoretical results were several times the irrotational values [2] and gave reasonable agreement with experimental spontaneous-fission lifetimes [3,4], although in one study a renormalization factor of 0.8 was required [4].

However, as pointed out by many authors (see ref. 5), the Inglis cranking model possesses two serious deficiencies. First, problems arise when the single-particle potential contains momentum-dependent terms. Second, in the limit of large pairing strength the inertia approaches zero instead of a finite (irrotational) limit.

Alternative approaches to the cranking model which did not lead to such unacceptable results were developed by Migdal [6], Belyaev [7] and Thouless and Valatin [8]. They showed that these deficiencies of the cranking model are due to a lack of self-consistency, since the reaction of the mean field to the collective motion is neglected in the Inglis model. In ref. 5 we used their arguments and developed a generalized cranking model for stationary collective motion. Here we show how to develop a time-dependent formalism appropriate to β -vibrations and fission [9].

We start with the time-dependent equation for the generalized density matrix

$$i\hbar \dot{\mathcal{R}} = [\mathcal{H}, \mathcal{R}] \quad , \quad (1)$$

where it is assumed that the Hamiltonian \mathcal{H} and consequently the generalized density matrix \mathcal{R} depend on the collective variable ε . Furthermore, we assume that the motion is adiabatic, which permits the replacement

$$\frac{\partial}{\partial t} \rightarrow \dot{\varepsilon} \frac{\partial}{\partial \varepsilon} \quad .$$

Choosing the basis so that

$$[\mathcal{H}_0, \mathcal{R}_0] = 0 \quad , \quad (2)$$

we then obtain to lowest order in the collective variable the equation

$$i\hbar\dot{\mathcal{R}}_0 = [\mathcal{H}_0, \mathcal{R}_1] + [\mathcal{H}_1, \mathcal{R}_0] \quad (3)$$

for the generalized density matrix. Here \mathcal{H} and \mathcal{R} symbolize the matrices

$$\mathcal{H} = \begin{pmatrix} h & -\Delta \\ \Delta^* & -h^* \end{pmatrix} \quad \text{and} \quad \mathcal{R} = \begin{pmatrix} \rho & \kappa \\ -\kappa & 1-\rho^* \end{pmatrix} .$$

The usual cranking-model approximation consists of neglecting the \mathcal{H}_1 term in eq. (3). We obtain $\dot{\mathcal{R}}_0$, which appears on the left-hand side of eq. (3), by differentiating eq. (2) with respect to time.

From this point onwards we proceed analogously to ref. 5 and evaluate the first-order correction to the generalized density matrix \mathcal{R}_1 . Its trace with the generalized collective momentum operator then yields the nuclear inertia B . However, in contrast to the stationary formalism, the time-dependent formalism leads to an additional pairing-vibration coupling term [3] because of the implicit dependence of the pairing gap on the collective variable.

Keeping the \mathcal{H}_1 term in eq. (3) gives rise to two additional contributions to the inertia that are proportional to h_1 and Δ_1 . The h_1 contribution arises when the potential contains momentum-dependent terms. In the stationary case one obtains

$$h_1 \propto (1 - m/m^*) \quad , \quad (4)$$

where m^* is the effective mass. This can lead to a considerable change in the inertia [5]. We expect a similar relationship to also hold in the time-dependent case [10]. The additional Δ_1 term, for which an explicit expression is obtained from the continuity equation [6], keeps the nuclear inertia finite in the limit of large pairing strength.

To demonstrate the effect of the Δ_1 contribution on the inertia, we now specialize to the harmonic-oscillator potential. In the limit of zero temperature and a constant pairing gap, we obtain for the inertia

$$B = \hbar^2 \sum_{p,q} |\langle p|i \frac{\partial}{\partial \varepsilon} |q\rangle|^2 \frac{E_p E_q - \hbar_p \hbar_q + \Delta^2}{2E_p E_q (E_p + E_q)} + \hbar^2 \sum_p \frac{1}{8E_p^5} (\hbar'_p \Delta - \hbar_p \Delta')^2, \quad (5)$$

where a prime denotes differentiation with respect to ε . Note the plus sign in front of Δ^2 in the first term, which arises from the Δ_1 contribution.

In fig. 1 we show the first term of the inertia for β -vibrations as a function of pairing strength, calculated with respect to Nilsson's spheroidal deformation parameter ε [2,4,5]. The pairing-vibration coupling term has not been considered here, since it vanishes for large pairing strength. Whereas the Inglis cranking inertia approaches zero for large pairing, the present inertia containing the Δ_1 contribution remains finite and close to

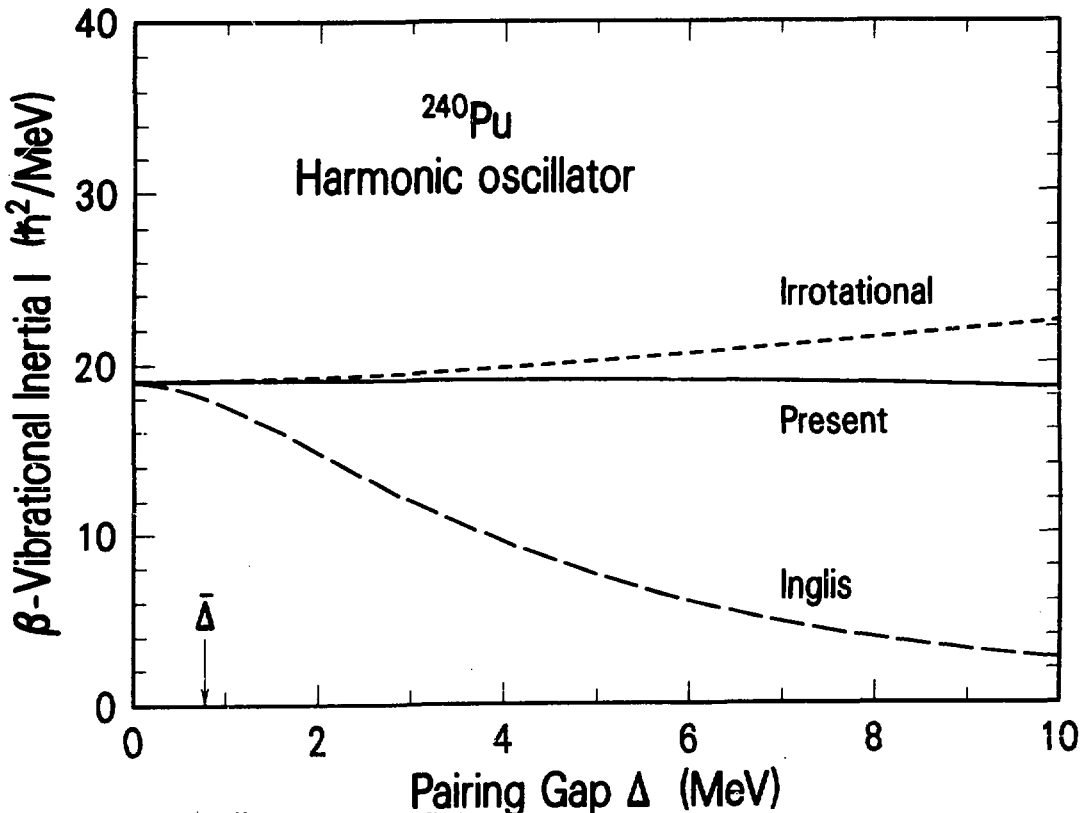


Fig. 1. Dependence of the β -vibrational inertia upon the pairing gap Δ for ^{240}Pu in a harmonic-oscillator potential at the equilibrium deformation $\varepsilon = 0.318$. The solid curve gives the present result calculated in the generalized cranking model with 15 oscillator shells, the long-dashed curve gives the corresponding result calculated in the Inglis cranking model and the short-dashed curve gives the irrotational result.

the limiting irrotational value. The deviation arises from the slow convergence of the cranking inertia with increasing basis size [5].

For a harmonic-oscillator potential with an effective mass, relation (4) holds, and the reaction of the pairing field to the collective motion is given by

$$\Delta_1 \propto Y_{20} .$$

For a more realistic modified-harmonic-oscillator potential we expect similar results. In particular, we expect that the proper inclusion of the effective-mass term h_1 for β -vibrational inertias may account for the renormalization factor of 0.8 that was originally needed to reproduce experimental spontaneous-fission lifetimes [4].

REFERENCES

- 1) D. R. Inglis, Phys. Rev. 96 (1954) 1059 and 97 (1955) 701.
- 2) A. Sobiczewski, Z. Szymański, S. Wycech, S. G. Nilsson, J. R. Nix, C. F. Tsang, C. Gustafson, P. Möller and B. Nilsson, Nucl. Phys. A131 (1969) 67.
- 3) M. Brack, J. Damgaard, A. S. Jensen, H. C. Pauli, V. M. Strutinsky and C. Y. Wong, Rev. Mod. Phys. 44 (1972) 320.
- 4) J. Randrup, S. E. Larsson, P. Möller, S. G. Nilsson, K. Pomorski and A. Sobiczewski, Phys. Rev. C13 (1976) 229.
- 5) J. Kunz and J. R. Nix, Los Alamos Preprint LA-UR-83-3624 (1983).
- 6) A. B. Migdal, Nucl. Phys. 13 (1959) 655.
- 7) S. T. Belyaev, Nucl. Phys. 64 (1965) 17.
- 8) D. J. Thouless and J. G. Valatin, Nucl. Phys. 31 (1962) 211.
- 9) J. Kunz and J. R. Nix, to be published.
- 10) M. J. Giannoni, F. Moreau, P. Quentin, D. Vautherin, M. Veneroni and D. M. Brink, Phys. Lett. 65B (1976) 305.

A STUDY OF $^{11}\text{B} + ^{12}\text{C}$ AND $^{10}\text{B} + ^{13}\text{C}$ FUSION CROSS SECTIONS

J. F. Mateja

Tennessee Technological University, Cookeville, Tennessee

A. D. Frawley

Florida State University, Tallahassee, Florida

D. G. Kovar, D. Henderson, H. Ikezoe, R. Janssens,

G. Rosner, G. Stephans, B. Wilkins, and K. Lesko

Argonne National Laboratory, Argonne, Illinois

In an effort to understand the mechanism responsible for fusion cross section limitations in light heavy-ion systems, four entrance channels which form the ^{23}Na compound nucleus have been studied¹⁻³. In these studies we have found that a limitation mechanism based on a critical density of compound nucleus states does not appear to be responsible for the fusion cross section limitation at energies from approximately one to three times the Coulomb barrier energy. The possibility exists, however, that such a process becomes important at higher energies. To address this question, measurements which utilize the Argonne tandem-linac accelerator have now been completed which extend the energy range for two of the previously studied entrance channels, the $^{11}\text{B} + ^{12}\text{C}$ and the $^{10}\text{B} + ^{13}\text{C}$. The preliminary findings of this work are reported here.

Beams of ^{11}B and ^{10}B were produced by the ANL inverted sputter source and then accelerated at laboratory energies of 42.5-, 60-, 80-, and 100 MeV and 42.5-, 62.3- and 80.9 MeV, respectively. The boron beams were incident on self-supporting ^{12}C and ^{13}C targets. The residues were mass identified with a micro-channel plate, surface-barrier, time-of-flight system. Angular distributions of the residues were measured from 3° to 40° in the laboratory. A contour mass versus energy plot for one of the measurements, the 80.9 MeV $^{10}\text{B} + ^{13}\text{C}$ reaction at 8° , is shown in Fig. 1.

The absolute cross sections were determined by comparing the elastic scattering yields, obtained simultaneously with the reaction residues, with optical model predictions of the elastic scattering. The optical model parameters which were used were taken from Ref. 2. At the overlap energies of 42.5 MeV, the total fusion cross section determined from the ANL $^{10}\text{B} + ^{13}\text{C}$ ($^{11}\text{B} + ^{12}\text{C}$) data agreed to within 2% (5%) with the total fusion cross section measured earlier^{1,2}.

In evaluating the total fusion cross section for any system, care must be taken to insure the proper identification of fusion events. The energy spectra of all exit channel mass groups were inspected for evidence of non-fusion events, e.g. direct transfer, inelastic scattering, or fragmentation,

before any mass was included in the calculation of the total fusion cross section. To assist in the identification of fusion events, the results of the Monte Carlo evaporation code Lilita have been compared on a mass-by-mass basis with the data. The energy domain predicted by the calculation for the $^{10}\text{B} + ^{13}\text{C}$ fusion yield at 80.9 MeV and 8° is enclosed by the solid line in Fig. 1. It is readily apparent that most of the yield in masses 12 to 22 arises from the fusion-evaporation process. Such is not the case for the lighter masses. These mass groups contain substantial direct transfer, inelastic, and, in the case of masses 6 and 7, breakup components. These yields have been carefully excluded in computing the $^{10}\text{B} + ^{13}\text{C}$ total fusion cross section. In the $^{11}\text{B} + ^{12}\text{C}$ study, results very similar to those found in the $^{10}\text{B} + ^{13}\text{C}$ work were obtained.

The total $^{10}\text{B} + ^{13}\text{C}$ and $^{11}\text{B} + ^{12}\text{C}$ fusion cross sections, found by summing the fusion cross sections in masses 9 to 22, are listed in Table 1 (masses 6 and 7 were not included as little evidence was found for fusion yield in these mass groups, see Fig. 1). Using the usual sharp cutoff approximation, the cross sections listed in Table 1 have been used to extract the critical angular momenta for these systems. The critical angular momenta from the ANL experiment are presented along with those from our earlier work^{1,2} in Fig. 2. For each entrance channel, one finds in Fig. 2 that the critical angular momentum for each system continues, as it did at lower energies, to diverge from its grazing angular momentum line (solid curve). This, of course, simply indicates that less and less of the incident flux is being channeled into fusion as the energy of the system is increased. What is particularly interesting about this new data is that the two systems still do not approach a common critical angular momentum line, a condition one expects to find if the limitation is due to a critical density of compound nucleus states. The latest results appear to rule out a compound nucleus limitation even at high energies. As with our earlier work, it is anticipated that much of the "missing" cross section will be accounted for when the non-fusion components of the present data are taken into account³. The conclusion must again be drawn that the limitation mechanism is not related to a critical density of compound nucleus states.

1. J. F. Mateja, A. D. Frawley, L. C. Dennis, K. Abdo, and K. W. Kemper, Phys. Rev. Lett. 47, 311 (1981).
2. J. F. Mateja, A. D. Frawley, L. C. Dennis, K. Abdo, and K. W. Kemper, Phys. Rev. C25, 2963 (1982).
3. J. F. Mateja, J. Garman, and A. D. Frawley, Phys. Rev. C28, 1579 (1983).

Table 1. Total Fusion Cross Sections

System	Energy (MeV)	Cross Section (mb)
$^{11}\text{B} + ^{12}\text{C}$	42.5	953
	60	1019
	80	917
	100	843
$^{10}\text{B} + ^{13}\text{C}$	42.5	971
	62.3	988
	80.9	892

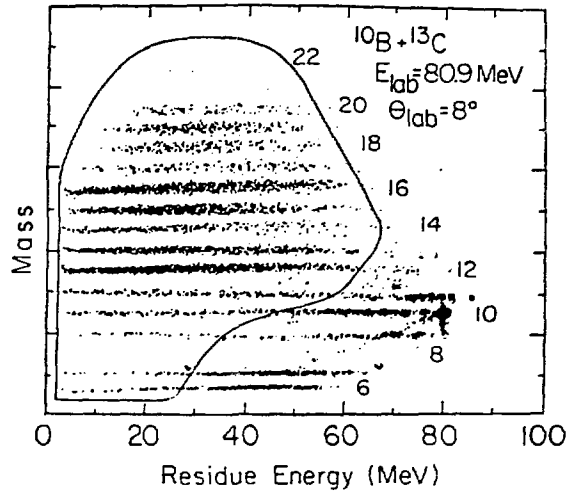


Fig. 1. Mass versus energy contour plot for $^{10}\text{B} + ^{13}\text{C}$. The solid curve indicates the fusion energy region predicted by the computer code Lilita.

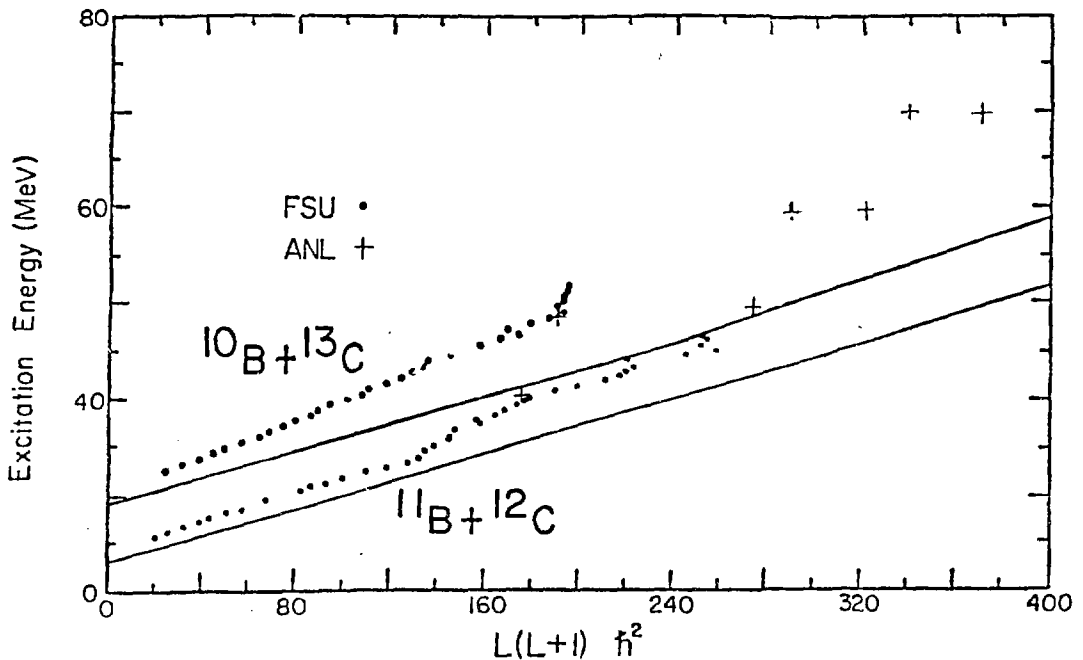


Fig. 2. The critical angular momentum versus ^{23}Na excitation energy. The upper solid curve is the $^{10}\text{B} + ^{13}\text{C}$ grazing angular momentum line while the lower solid curve is the $^{11}\text{B} + ^{12}\text{C}$ grazing angular momentum line.

MEASUREMENT OF NUCLEAR POTENTIALS FROM FUSION EXCITATION FUNCTIONS*

J.R. Huizenga and J.R. Birkelund

Department of Chemistry and Physics
and Nuclear Structure Research Laboratory
University of Rochester
Rochester, New York 14627

It has been shown that information about the internuclear potential can be obtained from fusion excitation functions at above-barrier^{1,2} and sub-barrier energies.³ In this talk I will only discuss data at energies in excess of the barrier. If friction is neglected, the fusion cross section (at energies where barrier penetration is negligible) at incident energy E is given by

$$\sigma_{fus}(E) = \pi R_B^2 (1 - V_B/E) \quad (1)$$

where R_B is the s-wave barrier radius and V_B is the s-wave barrier height obtained from the combination of the Coulomb potential $V_C(R_B)$ and the nuclear potential $V_N(R_B)$. Barrier parameters are obtained from the low-energy data (although well above the barrier) by fitting a straight line through a plot of $\sigma_{fus}(E)$ vs. $1/E$. The intercept of this line with the $1/E$ axis leads to the barrier V_B while the slope of this line

$$d\sigma_{fus}(E)/d(1/E) = -\pi R_B^2 V_B \quad (2)$$

leads to a value of the s-wave barrier radius R_B . The validity of such an analysis requires that all ℓ waves contributing to the fusion cross section have the same barrier radius R_B , a condition that is probably not fulfilled for most reactions.

Bass¹⁾ extended the above technique to regions where the $\sigma_{fus}(E)$ vs. $1/E$ curve is no longer a straight line. Now the intercept and slope of the tangent drawn to the $\sigma_{fus}(E)$ vs. $1/E$ curve is assumed to give a barrier height and barrier position inside the $\ell=0$ barrier. The values of these parameters vary

with energy and are extremely model dependent, insofar that no account is taken of the effects of friction at these close distances.

Recently, Gomez de Campo and Satchler⁴ have proposed the measurement of the internuclear potential at even smaller separations by analysis of the high energy part of fusion excitation functions by a technique similar to that proposed by Bass. Utilizing the measured slope and intercept, this technique leads to values of the total internuclear potential and nuclear surface separation, which have been interpreted as the critical values applicable to the Glas and Mose⁵ model of the fusion excitation function. Hence, in Fig. 1 the barrier radius is replaced by R_{cr} and the barrier height by V_{cr} .

Although initially attractive, and apparently leading to measurements of the nuclear potential at small separations of the nuclear centers, the procedure suggested by Gomez del Campo and Satchler⁴ suffers from several experimental and conceptual problems some of which have been previously discussed.²

The first and most obvious difficulty, the only one to be discussed here, is the problem of experimental errors. This is especially troublesome for systems at high energies, where the measurement of fusion cross sections is complicated by the presence of incomplete fusion reactions, which may yield fragments not easily distinguished from those produced by complete fusion reactions. This is illustrated in Fig. 1, where the excitation function for the reaction $^{27}\text{Al} + ^{20}\text{Ne}$ is shown. We concentrate here on this reaction because its high energy excitation function data⁶ have been corrected for the presence of incomplete fusion reactions.

The analysis of this reaction by Gomez del Campo and Satchler is based on high energy excitation function data⁷ that have not been corrected for the presence of incomplete fusion reactions. This analysis is illustrated by line (a) which leads to values of R_{cr} and $V(R_{cr})$ equal 4.17 fm and -73 MeV, respectively, and a value of $V_N(R_{cr})$ equal to approximately -110 MeV at $s = R_{cr} - R_T - R_P = -1.67$ fm (assuming $b = 1$ fm). Utilizing the uncorrected data of Morgenstern et al. (line b) gives values of R_{cr} and $V(R_{cr})$ equal to 3.57 fm and -123 MeV, respectively, and a value of $V_N(R_{cr})$ equal to approximately -162 MeV at $s = -2.27$ fm. If one performs the above analysis on the fusion excitation functions corrected for incomplete fusion, line (c) results. This analysis leads to a critical radius of zero, and a critical potential of $-\infty$, which illustrates that the model dependent technique applied to the

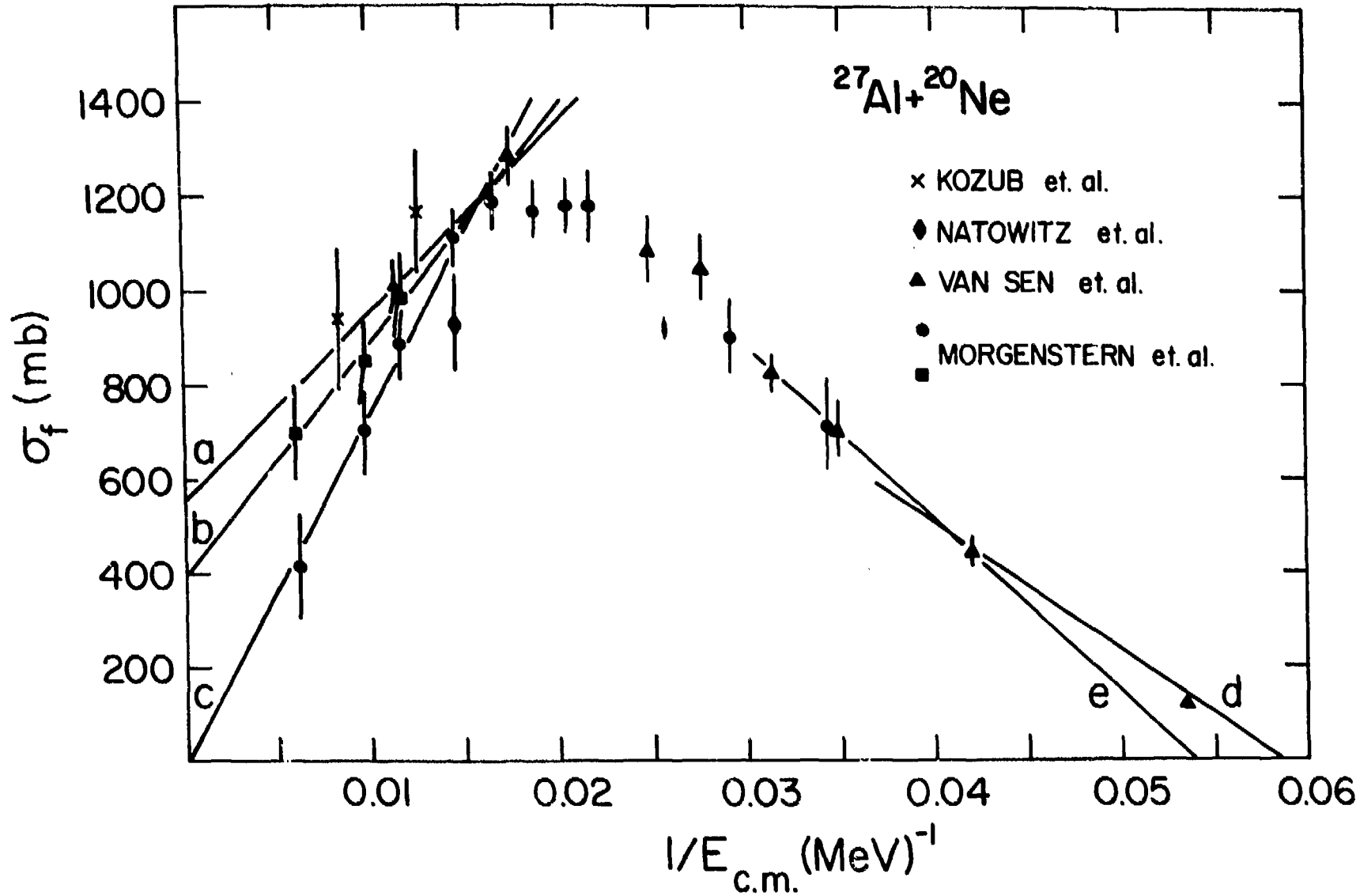
high energy part of the fusion excitation function fails to give a sensible value for the nuclear potential.

The problem of the incomplete momentum transfer correction is present in almost all existing high energy heavy ion fusion data and, when the measurements are corrected, will lead at least to a reassessment of the parameters reported by Gomez del Campo and Satchler, and to further difficulties such as those seen when such an analysis is applied to corrected data (see line (c) in Fig. 1). We conclude that the analysis of fusion excitation functions at high bombarding energies cannot lead to a model independent measurement of the internuclear potential at small separations of the interacting heavy nuclei.

*This work is supported by the U.S. Department of Energy.

1. R. Bass, Phys. Rev. Lett. 39, 265 (1977)
2. J.R. Birkelund and J.R. Huizenga, Proc. Sym. on Heavy Ion Elastic Scattering, Rochester (R. DeVries, Ed.), page 210 (1977); Phys. Rev. C17, 126 (1978)
3. M. Inui and S.E. Koonin, preprint (MAP-54, (1983)
4. J. Gomez del Campo and G.R. Satchler, Phys. Rev. C28, 952 (1983)
5. D. Glas and U. Mosel, Phys. Rev. C10, 2620 (1974)
6. H. Morgenstern et al., Z. Physik A313, 39 (1983)
7. N. Van Sen et al., Phys. Rev. 27, 194 (1983)

Fig. 1 Excitation function for fusion of $^{27}\text{Al} + ^{20}\text{Ne}$, plotted as a function of $1/E_{\text{cm}}$. The data of Morgenstern et al. are shown as dots when corrected for the presence of incomplete momentum transfer processes, and as squares when uncorrected.



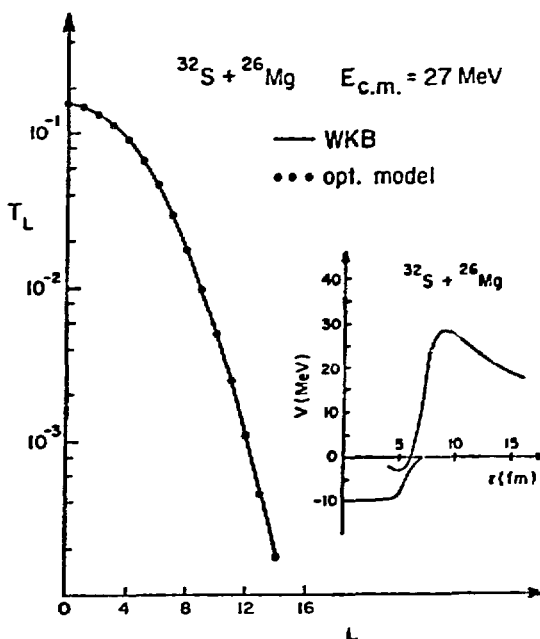
A SELF CONSISTENT APPROACH TO LOW ENERGY HEAVY-ION REACTIONS

M.J. Rhoades-Brown
 Department of Physics
 State University of New York at Stony Brook
 Stony Brook, N.Y. 11794

Recently several attempts have been made to study the role of surface degrees of freedom in grazing heavy ion collisions and separately the role of these degrees of freedom on fusion reactions. In particular the inadequacy of one-dimensional fusion models has been taken as evidence for the influence on the fusion process of ground state fluctuations of the surfaces of the colliding nuclei.

The recent development of numerical techniques for solving large scale coupled-channels problems and the realization that this technique can be used to calculate multi-dimensional barrier penetration probabilities¹⁾ has meant that simultaneous description of fusion-fission, transfer, elastic and inelastic processes in a single reaction model are now possible. A unified approach of this kind would provide more insight in that physically transparent mechanisms determine the distribution of flux between different reaction processes. Our calculations are based on a model in which a 'bare' potential between projectile and target is taken to be the real component of a full optical potential plus a short ranged absorption potential constructed to simulate compound nucleus formation in a one dimensional barrier penetration picture. The 'full' potential between projectiles and target is constructed by adding surface excitations to the bare potential within a multi-dimensional coupled-channels framework.

To study any enhancement of barrier penetrabilities due to coupling to intrinsic degrees of freedom we first demonstrate that in the limit of no coupling the one-dimensional version of our model accurately agrees with the WKB result for penetration of a typical nuclear potential. Such a 'bare' potential is shown in fig. 1 for the system $^{32}\text{S} + ^{26}\text{Mg}$. For the nuclear part of the potential we used the prescription of Akyuz and Winther²⁾ which was designed to reproduce elastic scattering data at energies just above the interaction barrier. Also shown in fig. 1 are the results of penetrability calculations for transmission through the effective barrier at $E_{c.m.} = 27$ MeV about 1.5 MeV below the top of the potential. The solid line is the result of a standard WKB-calculation for the penetrabilities p_L^{WKB} . The solid points are transmission



coefficients $T_L^{\text{OPT}} = |-|S_L(E_{\text{cm}})|^2$ obtained by directly integrating the radial Schrodinger equation in a potential which included the short ranged absorptive potential displayed in fig. 1. The close agreement between the two approaches justifies the use of such 'bare' potentials to calculate barrier penetrabilities.

To describe fusion-fission in the presence of strong inelastic excitations the multidimensional Hamiltonian of interest is reduced in the usual way to a set of coupled equations,

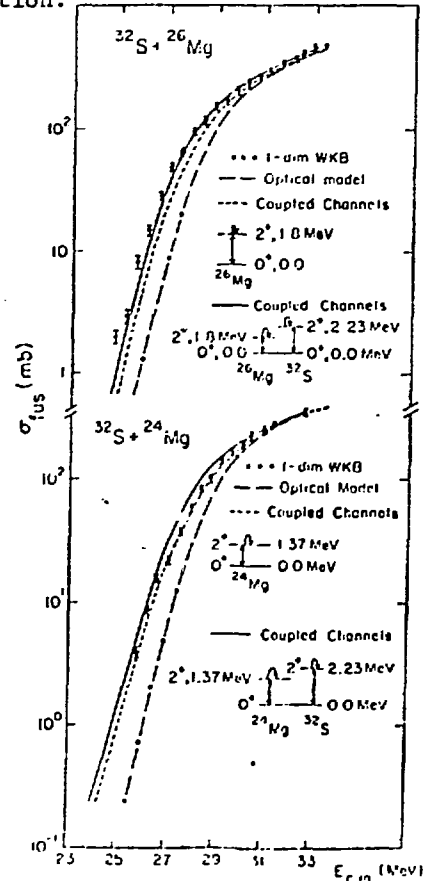
$$\left(\frac{d^2}{dr^2} - \frac{l_\alpha(l_\alpha+1)}{r^2} - U_\alpha^{\text{OPT}} + k_\alpha^2 \right) R_\alpha^{J\pi}(r) = \sum_\beta V_{\alpha\beta} R_\beta^{J\pi}(r) \quad (1)$$

For U_α^{OPT} the bare potential described above was used. The transition potential $V_{\alpha\beta}$ was calculated using the intrinsic coordinates of projectile or target excited during the inelastic process. From the S-matrix elements for elastic or inelastic processes the fusion cross section is given by

$$\sigma_F(E) = \pi\lambda^2 \sum_{l,c} (2l+1) (|-|S_l^c|^2) \quad (2)$$

where c is a generic index for channel specification. Of course with eqs. (1)-(2) we can calculate elastic, inelastic and fusion within the same reaction model. We ignore the transfer component of inelastic scattering for now and only include surface collective excitations. Transfer is under consideration within a zero range approximation.

In figure 2 we show results of our calculations for the fusion reactions $^{32}\text{S} + ^{26}\text{Mg}$ and $^{32}\text{S} + ^{24}\text{Mg}$ measured recently at Stony Brook. The dashed line is the result for the fusion cross section of the one-dimensional WKB or bare potential calculation. Also shown are the effects of coupling to the low lying 2^+ states of $^{24,26}\text{Mg}$ and ^{32}S using a static rotor model. Our investigations show that the basis expansion over low lying collective states converges rapidly at sub-barrier energies. Because transfer is not thought to be important for these nuclei the only uncertainties associated with our approach are the choices of the real component of the bare potential and the nuclear structure wavefunctions.



We have also applied our model to the complete set of data on $^{16}\text{O} + ^{208}\text{Pb}$ measured by Vidabaek et. al.³⁾ at energies just below the Coulomb barrier (80 MeV) to 18 MeV above the barrier (102 MeV). Here transfer is important so we can study the sensitivity of our model knowing a large component of the reaction mechanism is missing. Using straight Akyuz-Winther potentials we find $\sigma_{\text{FUS}} = 23$ mb at 80 MeV whereas experimental measurements indicate 40 mb. At 102 MeV we find adequate description of both fusion and elastic scattering within our approach. Increasing the depth of the Akyuz-Winther potential from 60 to 70 MeV gave excellent agreement with elastic and fusion data at 80 MeV even though transfer contributes up to 40% of the reaction cross section at this energy. This implies the real component of the bare potential may contain some of the included elastic and inelastic processes and thus caution should be used in deducing the role of transfer and surface collective effects on sub-barrier fusion. In a recent paper⁴⁾ we have extended this analysis and shown that the fission-anisotropy function usually denoted $W(\theta)/W(90^\circ)$ is a far more sensitive measure of the reaction mechanism than a single fusion excitation function. In calculating the fission anisotropy we assumed the entrance channel spin distribution is given by equation (2) and the probability for decay of the compound radius state into fission fragments is given by usual transition state theory⁴⁾. The increased sensitivity of fission anisotropy over fusion excitation functions may be understood by changing the potential parameters as described above. When this is done the mean squared value of the spin distribution does not change only the overall magnitude. Hence the ratio $W(\theta)/W(90^\circ)$ can only be changed by reaction mechanisms which change the shape of the spin distribution itself. Application of this idea to $^{16}\text{O} + ^{208}\text{Pb}$ data has now been completed.⁴⁾

In summary it now seems that a unified description of low energy heavy ion reactions is possible within a coupled channels framework.

- [1] M.J. Rhoades-Brown and P. Braun-Munzinger, Phys. Lett. B136 (1984) 19.
- [2] R.O. Akyuz and A. Winther, Enrico Fermi Intern. School (1979) on Nuclear Structure and Heavy Ion Reactions.
- [3] F. Vidabaek et al. Phys. Rev. C15 (1977) 954.
- [4] M.J. Rhoades-Brown and M. Prakash. submitted to Phys. Rev. Lett.

THE NEARSIDE/FAR SIDE DECOMPOSITION OF
HEAVY ION ELASTIC SCATTERING AMPLITUDES*

K. W. McVoy

University of Wisconsin
Physics Department
Madison, WI 53706

If many partial waves are active ($kR \gg 1$), so that the ℓ -sum can be converted into an ℓ -integral, semi-classical arguments show that heavy ion elastic scattering arises from a peripheral ℓ -window, within which the ℓ -dependence of the S -matrix elements is rapid enough to satisfy the stationary-phase condition $2d\delta/d\ell = \theta$. Then the large- ℓ approximation to $P_\ell(\cos\theta)$ suggests a useful split of the scattering amplitude into two parts:

$$\begin{aligned} f(\theta) &= \sum f_\ell P_\ell(\cos\theta) \approx \left(\frac{2}{\pi \bar{\ell} \sin\theta} \right)^{1/2} \sum f_\ell \cos(\ell\theta - \pi/4) \\ &\approx \left(\frac{1}{2\pi \bar{\ell} \sin\theta} \right)^{1/2} \left\{ \sum f_\ell e^{i(\ell\theta - \pi/4)} + \sum f_\ell e^{-i(\ell\theta - \pi/4)} \right\} \\ &\equiv f_F(\theta) + f_N(\theta), \end{aligned} \tag{1}$$

thus defining the farside and nearside components of the amplitude. Considered as running waves in θ , they "turn" (in the scattering plane) in opposite directions about the scattering center, as Fig. 1 indicates. Provided that absorption eliminates trajectories passing near this center, the nearside and farside amplitudes are cleanly separated, and describe, physically, the "edge waves" generated within two ℓ -windows on opposite sides of the target. The "cross-section" $\sigma_{N,F}(\theta) \equiv |f_{N,F}(\theta)|^2$ for each such edge wave has a simple "single slit" diffraction pattern, often exponential in shape [$\exp(-\beta\theta)$], with a "width" β^{-1} inversely proportional to the width ka of the ℓ -window. It is precisely the interference between these two single-slit patterns (from ℓ -windows separated by $\Delta\ell \approx 2kR$) which produces the Fraunhofer interference pattern; the angular spacing between its minima is $\Delta\theta = \pi/kR$, exactly as in the case of peripheral reactions, and for the same reason.

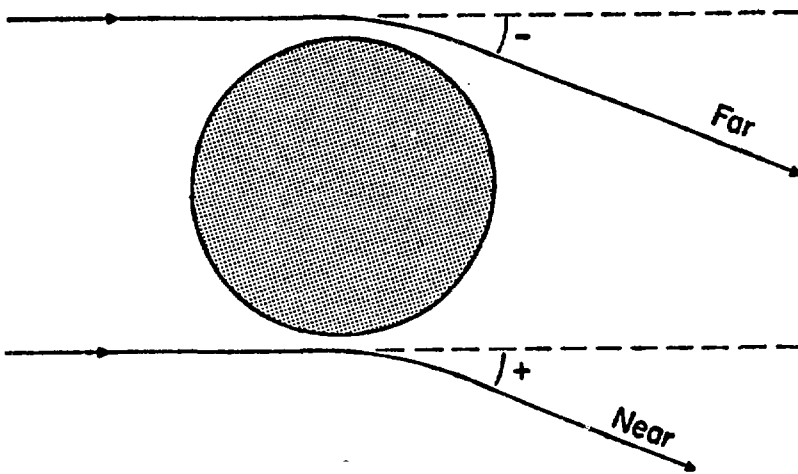


Figure 1

In the case of a pure absorber, the angular falloffs of $f_N(\theta)$ and $f_F(\theta)$ are equal, $\beta_N = \beta_F$, resulting in many equally-spaced Fraunhofer minima, as seen in Fig. 2, which shows scattering by a purely imaginary potential as well as $|f_N(\theta)|^2$ and $|f_F(\theta)|^2$. Adding refraction (through

V- 0.00, R- 5.89, A-0.640, VI- 42.00, RI- 5.89, AI-0.640

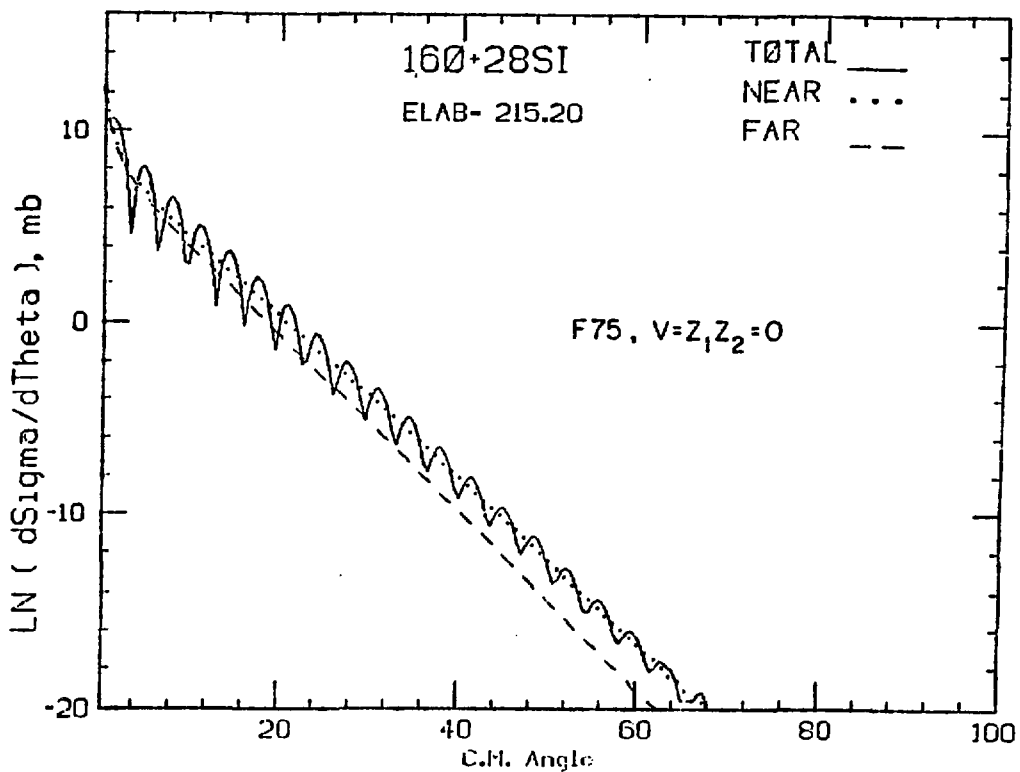


Figure 2

the real part of the optical potential) increases β_N and decreases β_F , thus restricting the Fraunhofer oscillations to the narrow angular range where $f_N(\theta)$ and $f_F(\theta)$ cross, producing the familiar type of heavy-ion angular distribution seen in Fig. 3 (which differs from Fig. 2 only in the addition of refraction to the potential).

1/4-THETA-11.5, K=AI- 5.22,

V-100.00, R- 5.89, A-0.640, VI- 42.00, RI- 5.89, AI-0.640

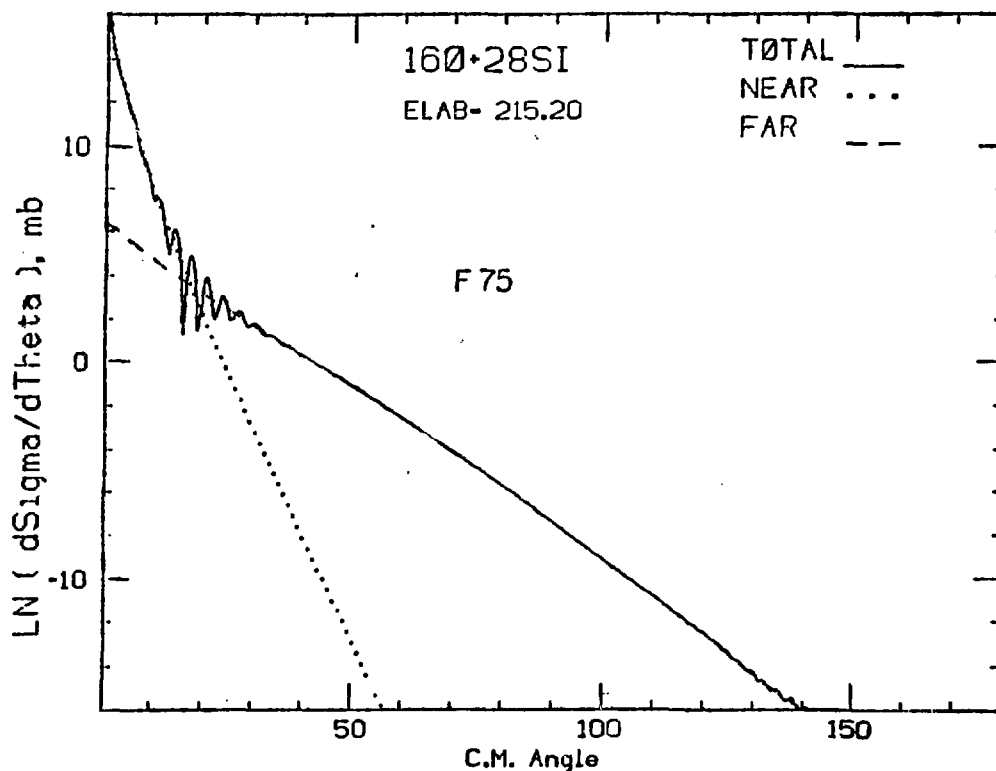


Figure 3

The moral of this tale (as Frahn has observed¹) is that the spectacular Fraunhofer oscillations so often seen in heavy-ion angular really carry no more information than the diameter of the scattering system. The interesting physics is all in the ℓ -dependence of S_ℓ across the ℓ -window, and this information resides precisely in $f_N^\ell(\theta)$ and $f_F(\theta)$. For this reason, their extraction, from the optical model phase shifts, promises to offer an incisive tool for the analysis of such angular distributions. It is, e.g., of crucial importance to the question of "shadowing" of reaction products by the target, whose understanding is clearly predicated on knowing whether the reaction products were generated on a nearside or a farside trajectory.

As a simple example of its usefulness, Fig. 4 shows the N/F decomposition of the elastic $\alpha + {}^{40}\text{Ca}$ scattering at 50 MeV,²⁾ exhibiting N/F Fraunhofer diffraction around 30° and beyond 120° . The remarkably deep dip shown by the data at 120° is seen not to be part of this N/F interference, but to be a minimum in $|f_F(\theta)|^2$ itself. This is a particularly spectacular example of rainbow scattering (the rainbow angle is around 180°), with the 120° dip being one of the "Airy minima" on the bright side of the rainbow; it arises from an interference between two farside ℓ 's, one peripheral and one which penetrates deeply inside the potential. In contrast, the farside of the ${}^{12}\text{C} + {}^{12}\text{C}$ angular distribution ($E_L = 289$ MeV) for the potential³⁾ shown in Fig. 5 is seen to be entirely smooth; the internal ℓ has been completely absorbed away in this case, leaving only the peripheral ℓ -window which describes ordinary, garden-variety diffraction, without refractive rainbow effects.

1/4-THETA- 4.7, K*AI- 4.44,

V- 0.00, R- 3.21, A-0.870, VI- 68.00, RI- 4.40, AI-0.690

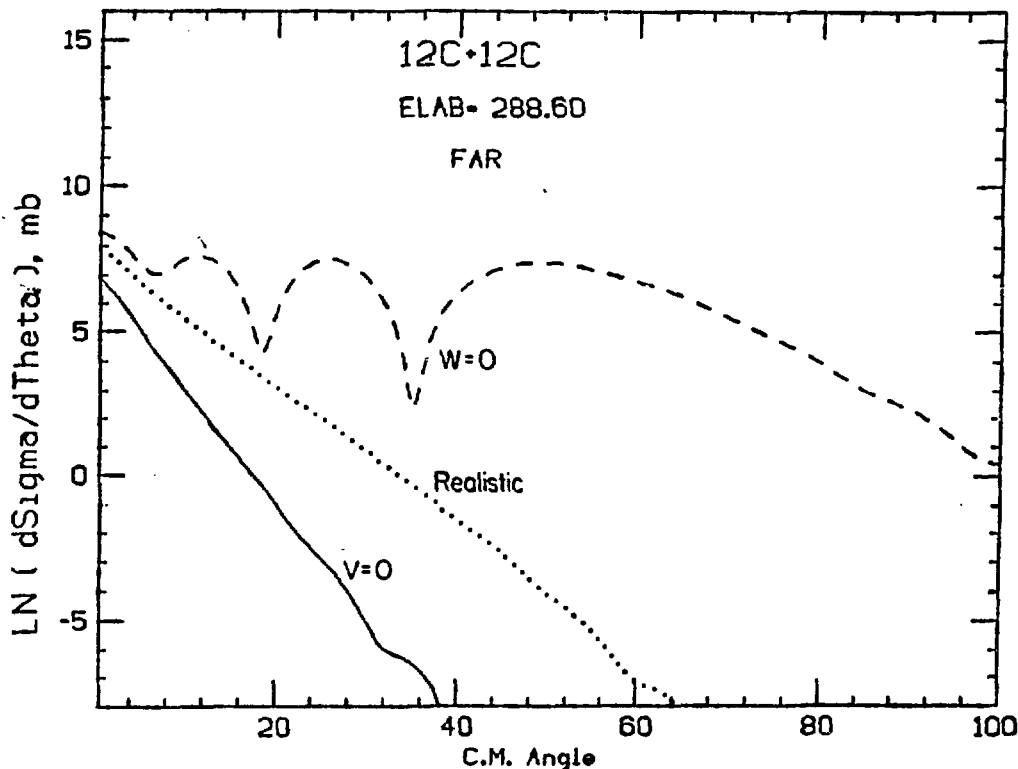


Figure 4

V-181.0 R= 4.69 A-1.290 VI- 17.3 RI- 5.99 AI-1.000
 THETA(INR)--114. AT LINR)- 13

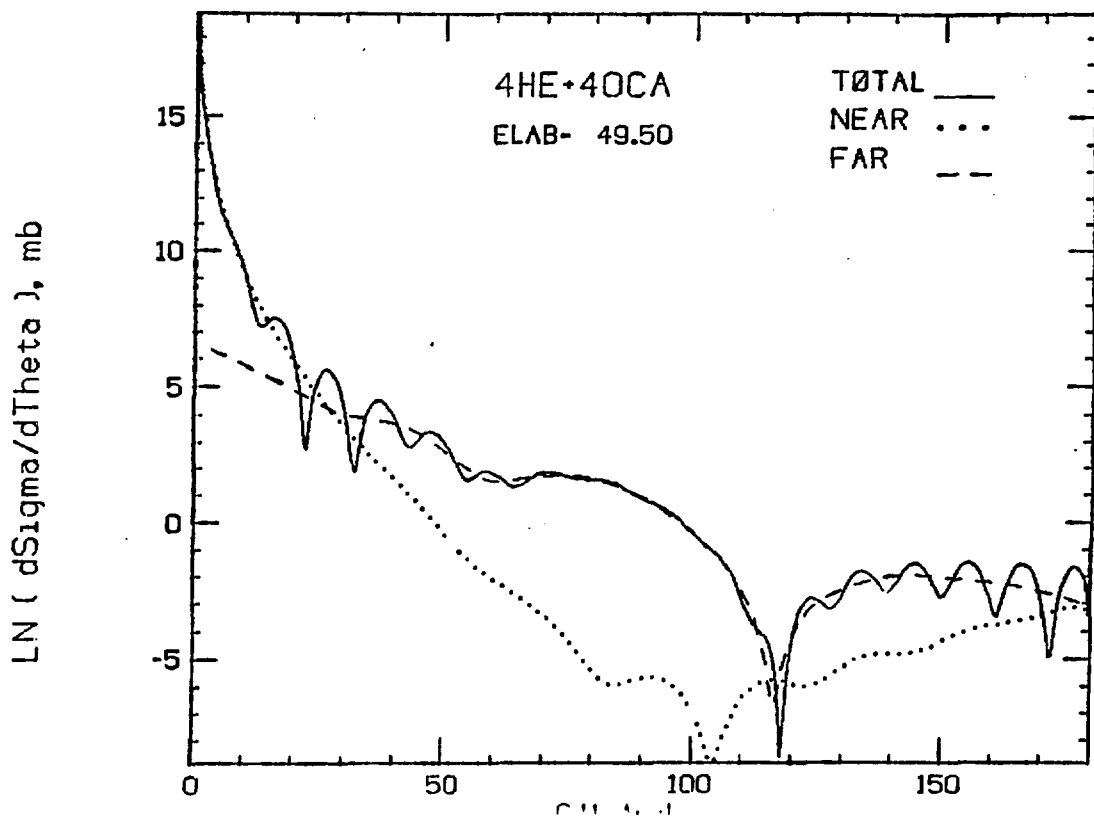


Figure 5

*Further details regarding the N/F decomposition, and other applications can be found in Ref. 4.

Supported in part by the National Science Foundation.

- (1) W.E. Frahn, in Heavy-Ion Science, Vol. 1, 1 ed. D.A. Bromley, Plenum Press, 1982).
- (2) Th. Delbar et al., Phys. Rev. C18 (1978) 1237.
- (3) M.E. Brandan, Phys. Rev. Lett. 49 (1982) 1132.
- (4) M.S. Hussein and K.W. McVoy, to be published in Prog. in Particle and Nuclear Physics (ed. D.H. Wilkinson, Pergamon Press, 1984).

NUCLEAR MASS FORMULA WITH A NEUTRON SKIN DEGREE OF
FREEDOM AND FINITE-RANGE MODEL FOR THE SURFACE ENERGY*

P. Möller and W. D. Myers

Nuclear Science Division, Lawrence Berkeley Laboratory
University of California, Berkeley, CA 94720

We study the possibility of extending the model used by Möller and Nix in 1980 to calculate nuclear masses and fission barriers for nuclei throughout the periodic system, to include provision for the existence of a neutron skin.

The calculation [1] in 1980 yielded an r.m.s. deviation in the ground-state mass of 0.835 MeV and an r.m.s. in the fission barrier height of 1.331 MeV. This calculation used the approach where the energy as a function of shape is calculated as a sum of a macroscopic term and a microscopic term. The macroscopic term varies smoothly with particle number and deformation and changes by about 200 MeV during the fission of a heavy system. The microscopic term, which arises due to the non-uniform distribution of single-particle levels is a rapidly fluctuating term, where the magnitude of the fluctuations are typically a few MeV but may reach values of about 12 MeV at doubly closed shells.

The values above, of the r.m.s. deviations, imply that the model of ref. [1] was very successful in describing ground state masses and fission barriers. In particular it was able to give correctly, for the first time, the fission barriers of medium heavy nuclei with $A \approx 110$ and $A \approx 160$. Also, in a survey of various mass models in ref. [2] the above model was the only one that yielded a smaller r.m.s. deviation, for a set of new masses determined in recent experiments, than was obtained in the original adjustment.

This model is fully discussed in refs. [1,3]. For orientation we give here its main features before we discuss our study of its generalization to include the description of compressibility effects and the neutron skin. The microscopic single-particle and pairing effects were determined from single-particle levels calculated for a Folded-Yukawa single-particle potential. The macroscopic model used was similar to the standard liquid-drop model [4] with the following important modifications:

- 1) In the surface energy expression the surface area was replaced by an expression that takes into account the reduction in surface energy due to the finite range of the nuclear force. This is important, for instance, for saddle point shapes with a well developed neck. The expression used was the Yukawa-plus-exponential model.
- 2) The Coulomb diffuseness correction was calculated exactly.
- 3) A charge asymmetry term and a proton form factor correction was added.
- 4) An A^2 term was included.

We have studied the possibility of generalizing the above model to describe compressibility effects and the effect of a neutron skin. These effects have been extensively studied earlier by Myers and Swiatecki [5] in the framework of the macroscopic "Droplet Model."

Arguments similar to those used to derive the "Droplet Model" may be used to generalize the model studied in ref. [1] to include neutron skin and compressibility effects. However, we found that the inclusion of a compressibility term with the standard choice of the compressibility coefficient $K = 240$ MeV, considerably increased the r.m.s. deviations.

We subsequently found that if we permitted the value of K to be determined by the masses themselves it was so large that its influence on nuclear properties became negligible. Consequently, we have chosen to limit our studies, for the moment, to the effects of including the neutron skin thickness as a degree of freedom in the model. No new parameters are introduced. The previously determined surface symmetry energy term is simply written in a slightly different form. This new form, taken from the Droplet Model theory, allows the generalization of the model of ref. [1] to give a fairly accurate description of isotopic trends in nuclear charge radii.

Below we give the expression for the nuclear potential energy, both the expression used by ref. [1] and the generalized expression we use here. Terms specific to the model of ref. [1] are written to the left, the modified terms specific to the generalized model studied here are written to the right, and terms common to both models are written across the page below.

Model of ref. [1]

Present work

$$\begin{aligned}
& -a_1 (1 - k_V I^2) A + a_2 (1 - M_S I^2) A^{2/3} F_S \\
& + f(k_f r_p) \\
& + M_H Z + M_N N + a_0 A^0 + C_1 (Z^2/A^{1/3}) F_C - C_4 Z^{4/3}/A^{1/3} - C_a(N-Z) - a_e I Z^{2.39} \\
& + W \left[|I| + \frac{1}{0}, \quad Z = N \text{ odd} \right. \\
& \quad \left. \text{otherwise} \right] + E_{\text{shell}}(Z, N, \text{Shape}) + E_{\text{pair}}(Z, N, \text{Shape}) + E_{\text{zp}}(Z, N, \text{Shape})
\end{aligned}$$

$$\begin{aligned}
& + (-a_1 + J\delta^2) A + (a_2 + kJ\delta^2 B_S^2/F_S^2) A^{2/3} F_S \\
& + f_0(k_f r_p) - C_2 Z^2 A^{1/3} B_r - C_5 Z^2 (B_W B_S/F_C) \\
& + \begin{cases} [\Delta/A^{1/2} - \frac{1}{2} \delta/A], & Z \text{ and } N \text{ odd} \\ \frac{1}{2} \delta & , Z \text{ or } N \text{ odd} \\ [\delta/A^{1/2} - \frac{1}{2} \delta/A], & Z \text{ and } N \text{ even} \end{cases}
\end{aligned}$$

In the above expression F_S , F_C , f and f_0 are given by:

$$F_S = - \frac{A^{-2/3}}{8\pi^2 r_0^2 a^3} \iint_V \left(\frac{|\bar{r} - \bar{r}'|}{a} - 2 \right) \frac{e^{-|\bar{r} - \bar{r}'|/a}}{|\bar{r} - \bar{r}'|} d^3 r d^3 r',$$

$$F_C = \frac{15}{32\pi^2} \cdot \frac{1}{(r_0 A^{1/3})^5} \iint_V \frac{d^3 r d^3 r'}{|\bar{r} - \bar{r}'|} \left\{ 1 - \left[1 + \frac{1}{2} \frac{|\bar{r} - \bar{r}'|}{a_{\text{den}}} \right] e^{-\frac{|\bar{r} - \bar{r}'|}{a_{\text{den}}}} \right\},$$

$$f(k_f r_p) = -\frac{1}{8} \frac{r_p^2 e^2}{r_0^3} \left[\frac{145}{48} - \frac{327}{2880} (k_f r_p)^2 + \frac{1527}{1209600} (k_f r_p)^4 \frac{Z^2}{A} \right],$$

f_0 simply keeps the first term in this expression.

The quantity $k_f = [(9/4)\pi Z/A]^{1/3}/r_0$ is the Fermi wave number. The quantities F_S , F_C and f are discussed in refs. [1,2]. We have in this work chosen the constants that multiply the integrals in the expressions for F_S and F_C such that F_S and F_C are 1 for a sphere in the limit the diffuseness constant goes to zero. The quantity f accounts for the effect of the finite size of the proton.

In this study we have truncated the expression f and keep only the first term. In the mass formula we investigate here (right column in the expression above for the potential energy) there enters the quantity $\bar{\delta}$. The quantity $\bar{\delta}$ represents the bulk nuclear asymmetry, it is defined by $\bar{\delta} = [(\rho_n - \rho_p)/\rho_{\text{bul}}]k$, and it is related to the overall asymmetry $I = (N-Z)/A$ by the "geometrical" relationship, $\bar{\delta} = I - \frac{3}{4}(t/R)$, where t is the neutron skin thickness and R the nuclear radius. When the energy of the nucleus is minimized with respect to the skin thickness the following expression for $\bar{\delta}$ is obtained:

$$\bar{\delta} = \left[I + \frac{3}{16} \cdot \frac{C_1}{Q} \cdot Z A^{-2/3} (B_V B_S/F_S) \right] / \left[1 + \frac{9}{4} \cdot \frac{J}{Q} \cdot A^{-1/3} (B_S^2/F_S) \right].$$

This expression should be considered as auxiliary to the mass equation itself since it must be used to calculate $\bar{\delta}$ for subsequent substitution.

The quantities B_S , B_V , B_r and B_W are the Droplet Model surface, neutron skin, volume redistribution and surface redistribution energies respectively [5]. Furthermore we have

$$C_1 = \frac{3}{5} \frac{e^2}{r_0}, \quad C_2 = \frac{C_1}{336J}, \quad C_4 = \frac{5}{4} \frac{3^{-2/3}}{2\pi} C_1, \quad C_5 = \frac{1}{64} \frac{C_1^2}{Q}, \quad \text{and } k = \frac{9}{4} \frac{J}{Q}.$$

To determine the parameters of the mass formula we minimize the quantity

$$F = \alpha \left[\sum_{i=1}^N m_i^{\text{calc}} - m_i^{\text{exp}} \right]^2 / N_m + \frac{(1-\alpha)}{2} \left[\sum_{i=1}^{N_b} (b_i^{\text{calc}} - b_i^{\text{exp}})^2 \right] / N_b$$

Here m stands for ground-state mass and b for the fission-barrier height. Thus F is a weighted sum of the r.m.s. deviation for the ground-state masses and for the fission-barrier heights. Because of the strong coupling between the volume and surface energy term it was not possible to determine a few parameters from an adjustment to fission-barrier heights alone, as was done in ref.[1] where the surface energy coefficient a_s and the surface symmetry coefficient a_s^2 could be determined from an adjustment to fission barriers alone. In our investigation here we take from ref.[3] the values of the following parameters:

M_H	= 7.289034 MeV	hydrogen-atom mass excess δ	= 20 MeV	pairing-asymmetry constant
M_n	= 8.071431 MeV	neutron mass excess	r_p = 0.80 fm	proton room-mean-square radius
e^2	= 1.4299764 MeV fm	square of electronic	r_0 = 1.16 fm	nuclear-radius constant
a_{den}	= 0.99/2 ^{1/2} fm	range of Yukawa function in Coulomb energy calculation	a = 0.68 fm	range of Yukawa-plus exponential potential
a_{e1}	= 1.433x10 ⁻⁵ MeV	electronic-binding constant	c_a = 0.212 MeV	charge-asymmetry constant
Δ	= 12 MeV	pairing-energy constant		

The adjustment procedure for determining the remaining parameters is fairly involved.

As input we use shell and pairing corrections and zero-point energies calculated at the appropriate ground-state and saddle-point deformations. These are taken from the work of ref.[1]. We have also calculated the shape-dependent functions F_s, F_c, B_s, B_r, B_v and B_w at these same ground-state and saddle-point shapes. We then minimize the function F with respect to some set of parameters with prescribed initial values. We have checked that, although the function F is non-linear, the same result is obtained with very different sets of initial values. We consider the same set of experimental ground state masses and fission barriers as did ref. [1]. We have determined the remaining parameters of the model from adjustment to data by performing the minimization in the following steps. First we observe that the Wigner term was introduced to account for a V-shaped kink in the mass surface (see discussion in ref [7] for $N = Z$). Thus its magnitude is best determined by considering nuclei with $N = Z$. We therefore determine the Wigner coefficient by considering only nuclei with $A \leq 70$. The resulting value of W is 22 MeV. In the following we therefore keep W fixed at 20 MeV. We now determine the parameters a_1, a_2, J, Q and a_0 by minimizing F with 1323 masses and 28 fission barriers taken into account. For the remaining parameters we find:

a_1	= 15.9837 MeV	volume energy constant	k	= 1.7029	surface symmetry factor
a_2	= 20.9406 MeV	surface energy constant	a_0	= 6.73 MeV	constant term
J	= 28.6275 MeV	symmetry energy			

and as discussed above, $W = 20$ MeV.

The resulting barrier r.m.s. deviation is 1.245 MeV and ground-state r.m.s. deviation is 0.843 MeV. We show, in fig. 1, plots of experimental and calculated ground-state shell corrections and their difference (which is identical to the difference between experimental and calculated masses). In fig. 2 we show experimental and calculated fission barriers and their difference. There seem to be no systematic increases in the deviations far from stability in these figures. We have, in addition, investigated the predictions of this model by calculating masses far from stability and comparing the calculated results to newly available data on masses that were not used in the determination of the model parameters. We find, for instance, that the model gives -51.26 MeV for the mass excess of ⁹⁹Rb (one of the most neutron-rich nuclei known) compared to an experimental value [8] of -50.60 MeV. Also other calculated results far from stability show very good agreement with new experimental data.

The effect of adding the neutron skin degree of freedom can be seen in fig. 3, from ref. [9]. The quantity plotted against the charge number Z is $A^{2/3}$ times the slope governing the increasing size of the charge distribution with increasing neutron number, ΔR_n . As can be seen in the figure the Liquid Drop Model predicts that this quantity should be a constant, $(r_0/3)$, which is about twice as large as the measured values for nuclei throughout the periodic table. The Droplet Model of ref. [7] is represented by the dashed line in the figure, and the predictions of the combined model described here are given by the dot dashed line.

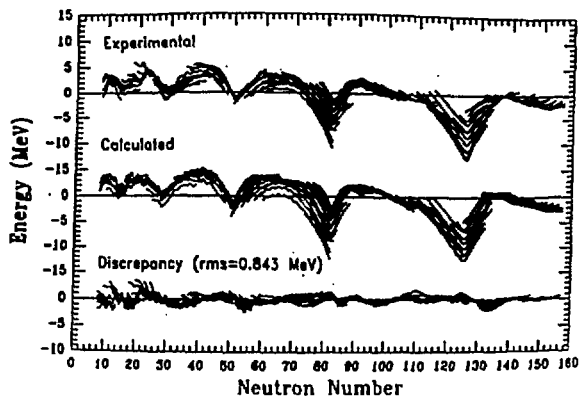


Figure 1.

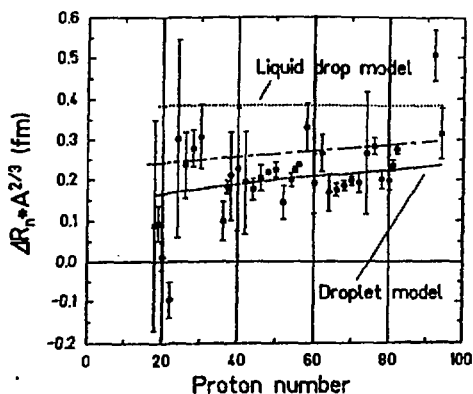


Figure 3.

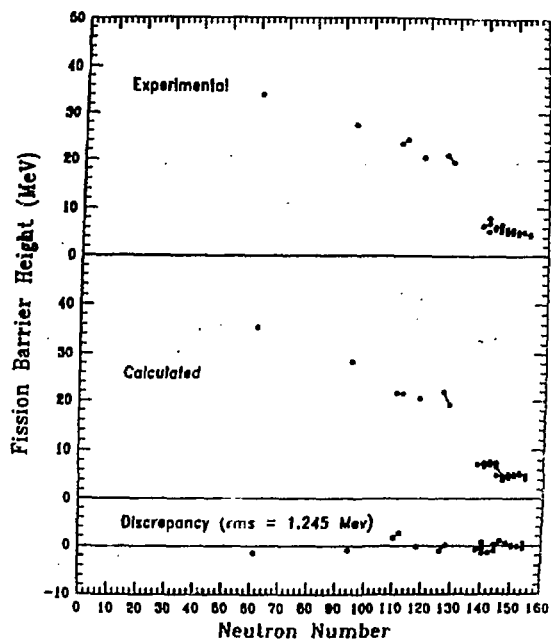


Figure 2.

By adding the neutron skin thickness degree of freedom from the Droplet Model we have been able to extend the results of ref.[1] to include a substantially improved prediction of the isotopic trends in charge radii. The excellent fit to masses and fission barriers is retained and no additional parameters are introduced. In addition, a number of important, and unresolved, issues are raised by this work. For example, we find no indication of curvature or compressibility effects even though there is substantial evidence in the literature that such effects should be present. At the moment we view the approach outlined here as an improvement over ref.[1] but phenomenological in nature because important physical effects have been suppressed to improve the fit to data.

We are grateful to J. R. Nix, W. J. Swiatecki, H. J. Krappe and J. Treiner for stimulating discussions and to D. Strottman for assistance in transferring data files from the Los Alamos computer center to tape.

*This work was supported by the Director, Office of Energy Research, Division of Nuclear Physics of the Office of High Energy and Nuclear Physics of the U.S. Department of Energy under contract DE-AC03-76SF00098, and the Swedish Natural Science Research Council.

- [1.] P. Möller and J. R. Nix, Nucl. Phys. A361 (1981) 117
- [2.] P. Haustein, private communication (1982)
- [3.] P. Möller and J. R. Nix, At. Data and Nucl. Data Tables, 26 (1981) 165
- [4.] W. D. Myers and W. J. Swiatecki, Ark. Fys. 36 (1967) 343
- [5.] W. D. Myers and W. J. Swiatecki, Ann. of Phys. 55 (1969) 395
- [6.] W. D. Myers and W. J. Swiatecki, Ann. of Phys. 84 (1974) 186
- [7.] W. D. Myers, Droplet Model of Atomic Nuclei (IFT/Plenum, New York, 1977)
- [8.] A. H. Wapstra, 1981, mass evaluation, private communication (1982)
- [9.] W. D. Myers and K.-H Schmidt, Nucl. Phys. A410 (1983) 61

PARTICLES + CORE REDUCTION OF THE FISSION EQUATIONS IN THE TIME
DEPENDENT MEAN FIELD APPROXIMATION

Y. Boneh

Nuclear Research Centre - Negev

S. Levit

Weizmann Institute of Science - Rehovot

A mean field theory was obtained for the spontaneous decay of unstable nuclei by applying the stationary-phase approximation to a functional integral expression for $T_r(H-E)^{-1}$, [1]. The decisive step in making the description of fission possible was to introduce an imaginary time into the expression for the evolution operator. For a one spatial dimension model problem the resulting equations of motion can be written as:

$$\left(\frac{\partial}{\partial \tau} + h_\sigma(\tau)\right) u_k(\tau) = \epsilon_k u_k(\tau) \quad (1.a)$$

$$\left(-\frac{\partial}{\partial \tau} + h_\sigma(\tau)\right) u_k(-\tau) = \epsilon_k u_k(-\tau) \quad (1.b)$$

where:

$$h_\sigma(\tau) = \frac{-\partial^2}{\partial x^2} + \int V(x-x')\sigma(x',\tau)dx' + V_3\sigma^2(x,\tau) \quad (2)$$

$$\sigma(x,\tau) = M \sum_k u_k(x,\tau)u_k(x,-\tau) \quad (3)$$

(M - "spin-isospin degeneracy)

$V(x)$ is a given function of x ,

V_3 is a (given) parameter,

and the boundary conditions are:

$$u_k(x, T/2) = u_k(x, -T/2) \quad (4)$$

The computational difficulty in solving even the relatively simple model problem is evidently far greater than the corresponding static HF, due to the introduction of the time variable, τ . Thus it seems imperative to find better techniques for solving the ITMFE (imaginary time mean field equations) to enable a progress towards a study of a more realistic case.

We propose here to apply the particle + core reduction of ordinary TDHF as proposed by Jensen and Koonin [2]. First we note that equations (1) can be obtained by a variational principle:

$$\delta S = 0 \quad (5)$$

where: (In the following, repeated indices implies summation)

$$S = \int_{-T/2}^{T/2} L(\tau) d\tau \quad (5.a)$$

$$L(\tau) = \int dx u_k(x, -\tau) \left(\frac{\partial}{\partial \tau} \right) u_k(x, \tau) - H + \varepsilon_k \int dx u_k(x, -\tau) u_k(x, \tau) \quad (5.b)$$

$$H = M \int dx u_k(x, -\tau) \left(\frac{\partial^2}{\partial x^2} \right) u_k(x, \tau) + \frac{1}{2} \int dx dx' \sigma(x, \tau) v(x-x') \sigma(x', \tau) + \frac{1}{3} V_3 \int dx \sigma^3(x, \tau) \quad (5.c)$$

Subject to the boundary condition (4). The Lagrange multipliers ε_k serve to insure the normalization constraints:

$$\int dx u_k(x, -\tau) u_{k'}(x, \tau) \delta_{kk'} = 1 \quad (6)$$

A straightforward variation of S with respect to $u_k(-\tau)$, or $u_k(+\tau)$, with $\delta S=0$, leads to equations (1.a) or (1.b) respectively, see also Ref. [3].

Now introduce a basis:

$$|\lambda\rangle = \phi_\lambda = \phi_\lambda(\alpha_n(\tau), x) \quad (7)$$

The basis functions ϕ_λ depend on the time, τ via a set of (few) parameters α_n .

The "wavefunctions" $u_k(x, \tau)$ are divided into core functions:

$$|a\rangle = u_a(x, \tau) = \phi_a(\alpha_n(\tau), x) \quad a \leq b \quad (8)$$

and valence:

$$|i\rangle = u_i(x, \tau) = c_{i\lambda}(\tau) \phi_\lambda(\alpha_n(\tau), x) \quad \lambda > b \quad (9)$$

b denotes the number of core functions.

A scalar product is defined as:

$$\langle u | \lambda \rangle = \int dx \phi_u(-\tau, x) \phi_\lambda(\tau, x) \quad (10)$$

The basis is constructed in a way to insure that for any τ :

$$\langle u | \lambda \rangle = \delta_{u\lambda} \quad (11)$$

It will be convenient to use also the following notation:

$$d_{\lambda u}^n(\tau) = \int dx \phi_\lambda(-\tau) \left(\frac{\partial}{\partial \alpha_n(\tau)} \right) \phi_u(\tau) \quad (12.a)$$

$$d_{\lambda\mu}^n(-\tau) = \int dx \phi_\lambda(\tau) \left(\frac{\partial}{\partial \alpha_n(+\tau)} \right) \phi_\mu(-\tau) \quad (12.b)$$

$$h_{\lambda\mu}(\tau) = \int dx \phi_\lambda(-\tau) h_\sigma(\tau) \phi_\mu(\tau) \quad (12.c)$$

From (11) follows the "antihermiticity" of d:

$$d_{\lambda\mu}^n(\tau) = -d_{\mu\lambda}^n(-\tau) \quad (13)$$

The "hermiticity" of $h_\sigma(\tau)$ is demonstrated by:

$$h_{\lambda\mu}(\tau) = h_{\mu\lambda}(-\tau) \quad (14)$$

Upon using the basis (7) with the notation (12) the Lagrangian (5) is:

$$\left(\cdot \equiv \frac{\partial}{\partial \tau} \right)$$

$$L(\tau) = - \left[d_{aa}^n \dot{\alpha}_n + \dot{c}_{i\lambda}(\tau) c_{i\lambda}(-\tau) + c_{i\lambda}(\tau) c_{i\mu}(-\tau) d_{\mu\lambda}^n(\tau) + H(\tau) \right] + \varepsilon_i c_{i\lambda}(-\tau) c_{i\lambda}(\tau) \quad (15)$$

A gauge transformation:

$$c_{i\lambda}(\tau) \rightarrow c_{i'\lambda}(\tau) e^{-\beta_{i'} \tau \delta_{i',i}} \quad (16)$$

does not affect $L(\tau)$ except for changing the values of the Lagrange multipliers from ε_i to $\varepsilon_i - \beta_{i'}$. Thus by choosing $\beta_{i'} = \varepsilon_i$, the last term in the r.h.s of equation (15) is eliminated, where now $L(\tau)$ is a function of the transformed coefficients $c_{i\lambda}(\tau)$.

The appropriate equations for α and c are derived [2] from the Lagrange equations:

$$\frac{d}{d\tau} \frac{\partial L}{\partial \alpha_n} - \frac{\partial L}{\partial \alpha_n} = 0 \quad (16.a)$$

$$\frac{d}{d\tau} \frac{\partial L}{\partial c_{j\lambda}(-\tau)} - \frac{\partial L}{\partial c_{j\lambda}(-\tau)} = 0 \quad (16.b)$$

With the result:

$$\dot{c}_{j\lambda}(\tau) = - [d_{\lambda\mu}^n(\tau) \alpha_n(\tau) + h_{\lambda\mu}(\tau)] c_{j\mu}(\tau) \quad (17.a)$$

$$\begin{aligned}
& \left[d_{av}^m(\tau) d_{va}^n(\tau) - d_{av}^n(\tau) d_{va}^m(\tau) \right. \\
& \left. - d_{ia}^n(\tau) d_{ai}^m(\tau) + d_{ia}^m(\tau) d_{ai}^n(\tau) \right] \dot{\alpha}_n = \quad (17.b) \\
& = -d_{av}^m(\tau) h_{va}(\tau) + d_{va}^m h_{av}(\tau) - d_{ia}^m(\tau) h_{ai}(\tau) + d_{ai}^m(\tau) h_{ia}(\tau)
\end{aligned}$$

Up to now nothing has been said about the choice of the basis (7). For a truncated basis, the accuracy achieved depends on the good choice of the parameters $\alpha_n(\tau)$. As in Ref. [2] these parameters are divided into coordinate like parameters, $q_n(\tau)$, and momentum like parameters, $p_m(\tau)$.

$$q_n(\tau) = q_n(-\tau). \quad (18.a)$$

$$P_m(\tau) = -P_m(-\tau) \quad (P_m(0) = 0) \quad (18.b)$$

The basis build upon $q(\tau)$ and $p(\tau)$ is chosen to be:

$$\phi_\lambda(x, \alpha_n(\tau)) = \exp[P_m(\tau) \cdot \xi_m(x, q_n(\tau))] \cdot g_\lambda(x, q_n(\tau)) \quad (19)$$

$\{g_\lambda\}$ is a set of orthonormal basis functions, and from the requirement (18), so is the basis ϕ_λ , namely equation (11) is automatically fulfilled. The (common) phase of the basis may depend on x and $q(\tau)$ through the functions ξ_m .

The periodic boundary conditions (4) (together with (18.b)) impose on the momentum like coordinates the equality:

$$P_m(-T/2) = P_m(T/2) = 0 \quad (20)$$

Due to (18.a) we then have:

$$\phi_\lambda(-T/2) = \phi_\lambda(T/2) \quad (21)$$

To insure also the periodicity of the valence functions, the transformed coefficients $c_{i\lambda}(\tau)$ should satisfy the boundary condition:

$$c_{i\lambda}(T/2) = \Gamma_i c_{i,\lambda}(-T/2) \delta_{ii}, \quad ; \quad \Gamma_i = e^{\epsilon_i T} \quad (22)$$

where Γ_i is an eigen-value of equations (17).

The inherent difficulty of the ITMFE is evidently still present in equations (17). Considered as time-dependent equations they pose a boundary value problem rather than ordinary initial value differential equations, and thus iterative procedures are needed for their solution. Yet, as already mentioned, by a proper choice of the basis, the number of free parameters may be small enough so as to reduce substantially the amount of the numerical work.

The method is currently tested in one dimension using a two centre basis [4]. The calculations are at a preliminary stage where-by the (two) free parameters of the basis are frozen, all the wave-functions are valence and equations (17) reduce to a system of equations for the expansion coefficients c , subject to the boundary conditions (22). A good agreement was obtained between the present results and those obtained [1] by the grid method.

The crucial stage should come next when we release the restriction on the parameters and let them evolve in time according to the complete set of equations (17).

- [1] S. Levit, J.W. Negele and Z. Paltiel, Phys. Rev. C 22 (1980) 1979
- [2] A.S. Jensen, S.E. Koonin, Phys. Lett. 73B (1978) 243
- [3] A.K. Kerman and S.E. Koonin, Ann. Phys. 100 (1976) 332
- [4] H. Flocard, Phys. Lett. 49B (1974) 129

MACROSCOPIC IMPLICATIONS OF DIVERSE TRANSFER MECHANISMS
IN HEAVY ION COLLISIONS

M. Dworzecka

George Mason University, Fairfax, Virginia 22030

A. Gökmen

Middle East Technical University, Ankara, Turkey

J. J. Griffin

University of Maryland, College Park, Maryland 20742

In the discrete random walk description of nucleon transfer in heavy ion collisions,¹⁻⁴ all of the physical properties of the q^{th} nucleon transfer event are summarized in the transition probabilities $T_{\alpha}(N,Z,q)$, and in the specification of the associated change in total kinetic energy for the emergent fragments. Thus any sharp physical conjecture about the transfer mechanism which can be reduced to a specific set of transition probabilities and energy losses may be converted into an implied (N-Z) evolution and compared with the experimental observations. In such a process one seeks not so much to obtain "a fit" to the data, but to learn which aspects of the physical mechanism most affect which features of the observations, and especially whether (and when) more than one plausible assumption might equally well describe them.

Here⁴ we report calculations based on three assumed forms of transition probability, corresponding to degrees of independence for the transferred nucleon which vary from extreme to minimal. In every case, the Pauli exclusion principle is honored in the allowed final states.

(A) From the most extreme independent particle viewpoint, we assume that a nucleon transferred across the neck of the dinucleus leads to a one-particle, one-hole final state of excitation energy $\Delta_q(\alpha)$ (equal to the increase in E^* due to the transfer, α), and that the state of every other nucleon remains unaltered. The corresponding transition probability, proportional to the weighted density of such final states, is given by

$$T_{\alpha}^{\text{PH}}(N,Z,q) \propto \rho_{\text{PH}} = g^2 \Delta [\exp(\Delta/2\tau)] / \text{Sinh}(\Delta/2\tau), \quad (1)$$

where $\tau_q = \tau_q [E_q^*(N_{\alpha}, Z_{\alpha})]$ is the temperature of the system before the transfer event in the final state nucleus, (N_{α}, Z_{α}) . This assumption must be augmented implicitly by the further assumption that before the next transfer even the energy Δ_q is spread into a new equilibrium distribution characterized by the new temperature, τ_{q+1} .

(B) Our intermediate assumption is that during each nucleon transfer event one additional particle and one additional hole may be created, and that all the previously created particles and holes may be rescattered into new states. Then the transition probabilities are proportional to the "pre-equilibrium" level density, as follows:

$$T_{\alpha}^{\text{PE}}(N,Z;q) \propto \rho_{\text{PE}} = \sum_{s=1}^q \rho_{\text{SS}} [E_q^*(N_{\alpha}, Z_{\alpha})], \quad (2)$$

where ρ_{ss} is the density of s-particle s-hole states.⁵ Since for large q , this pre-equilibrium density approaches the total ("Exponential") level density assumed in (C) below, the implications of this assumption are expected to converge to those of assumption (C) below for large q , or large TKEL, values. (And, in fact, does so, as the present results show.)

(C) Our third assumption specifies that in the process of transfer, as many other nucleons may scatter into new states as are necessary to reach any final state of the system. Then the transition rate is proportional to the total (here taken to have the exponential form, whence the label "EX") level density, as follows:

$$T_{\alpha}^{\text{EX}}(N, Z; q) \propto \rho_{\text{EX}}[E_q^*(N_{\alpha}, Z_{\alpha})] \propto (E^*)^{-5/4} \text{Exp}[gE^*]^{1/2}. \quad (3)$$

Here $E^* = E_q^*(N_{\alpha}, Z_{\alpha})$. This is the form used in the earlier analyses of Ref. 2.

(D) The equations (1), (2), and (3) above refer only to the transition probabilities for nucleon transfer (i.e., $\alpha = 1, 2, 3, 4$). In addition, earlier analyses^{1, 2} have shown that a finite (and substantial) value should also be assigned to the probability, T_0 , that no transfer actually occurs during the transfer event, or q -step. This probability, T_0 , then describes an event in which kinetic energy is lost into excitation energy by some mechanism not associated with the transfer of a nucleon. In the present⁴ calculation we have assumed that T_0 has in each reaction a fixed constant value, γ .

For both of the reactions analyzed⁶⁻⁷, (Fe+Ho (464 MeV), and Fe+U (464 MeV)), the behavior of the overall width in A , σ_A^2 , was first fit as well as possible by a specific choice of γ , which then was retained unchanged. This process is recommended by the fact that the behavior of σ_A^2 is most sensitive to the value of γ , and quite insensitive to the choice of level density (as one can see in Figs. 1a, 2a,), and also by the fact that our precise knowledge of the alternative excitation processes is meager.

In Fe+Ho and Fe+U, the best values of γ are found to be 0.67 and 0.82, respectively. Figures 1a and 2a show that these choices provide an excellent fit to σ_A^2 , independent of the level density assumed. Figures 1b and 2b show that σ_Z^2 is also reasonably well described, but with somewhat more dispersion among the various level densities, which, however, does not strongly favor any particular choice.

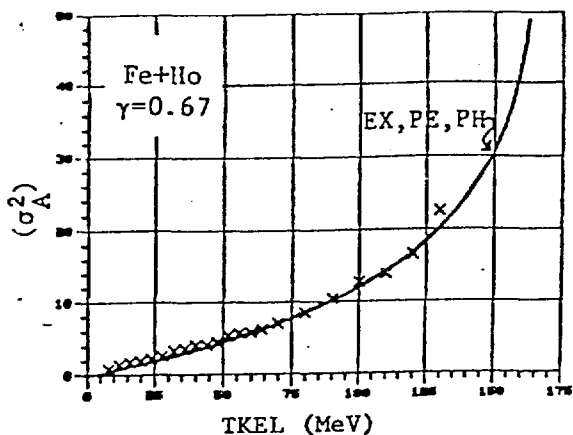


Fig. 1a: Fe+Ho (464 MeV): σ_A^2

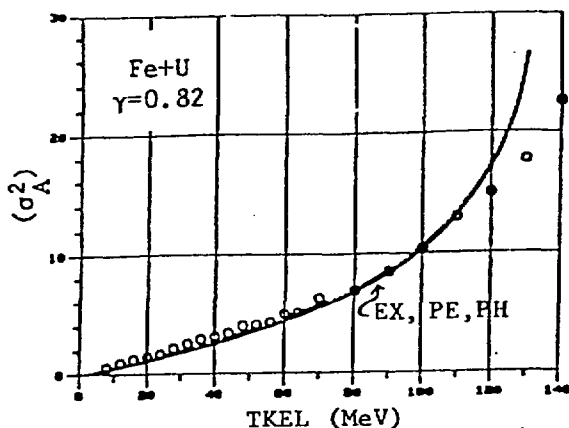


Fig. 2a: Fe+U (464 MeV): σ_A^2

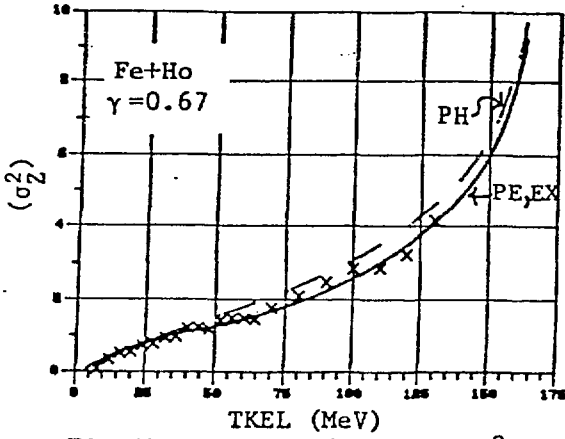


Fig. 1b: Fe+Ho (464 MeV): σ_Z^2

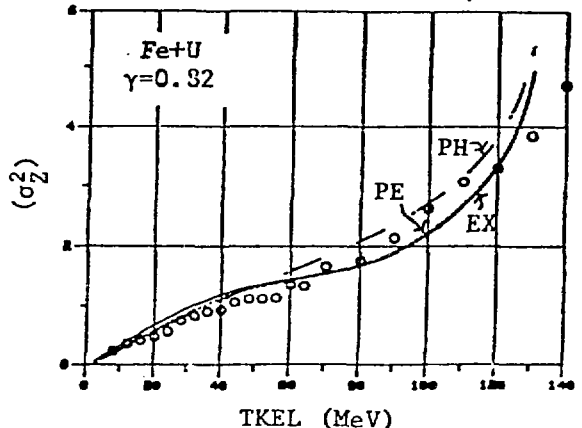


Fig. 2b: Fe+U (464 MeV): σ_Z^2

For the cut-widths, Figs. 1c, 1d, 2c and 2d show σ_Z^2/A and σ_A^2/Z for Ho and U, respectively. Again one finds that the EX and PE assumption yield nearly the same predictions, whereas the PH density differs substantially except for the smallest TKEL values.

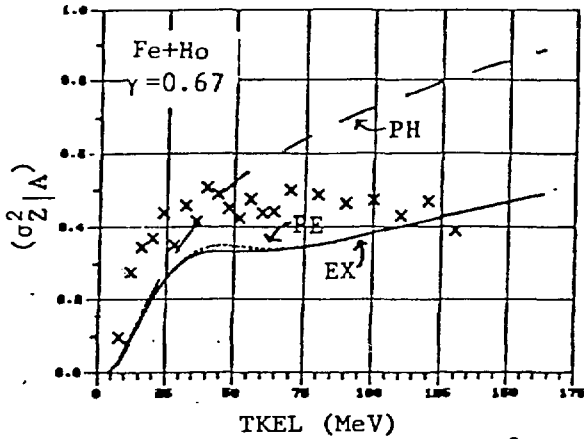


Fig. 1c: Fe+Ho (464 MeV): σ_Z^2/A

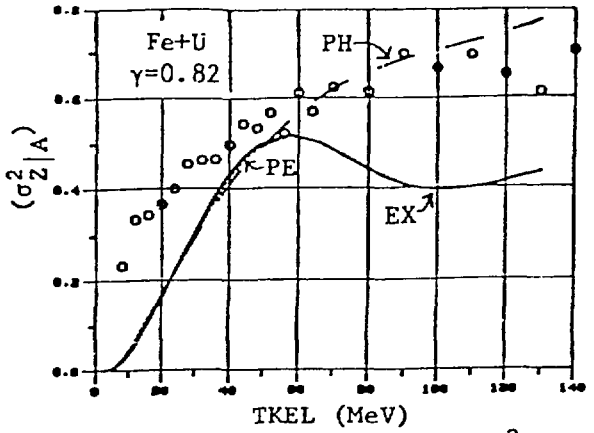


Fig. 2c: Fe+U (464 MeV): σ_Z^2/A

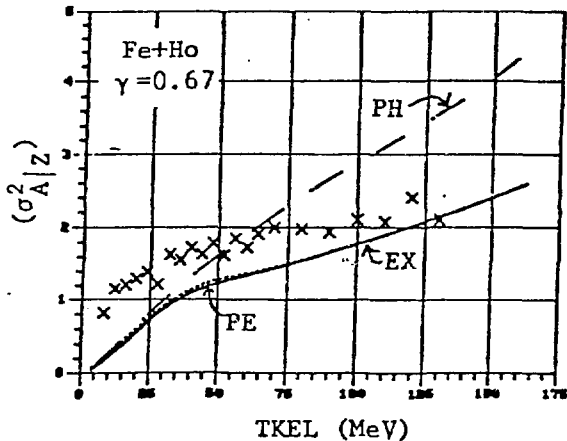


Fig. 1d: Fe+Ho (464 MeV): σ_A^2/Z

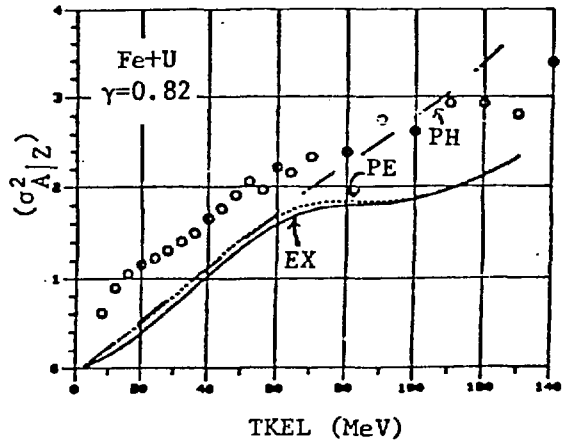


Fig. 2d: Fe+U (464 MeV): σ_A^2/Z

Figure 1e exhibits the observed⁸ and calculated values of \bar{Z} vs. TKEL in the $^{165}\text{Ho}+^{56}\text{Fe}$ reaction. The agreement is slightly better for the Particle-Hole level density than for the Pre-equilibrium, but both are in good semi-quantitative agreement with the data. Because of the Coulomb barrier against proton emission, no emission corrections have been applied to these \bar{Z} values.

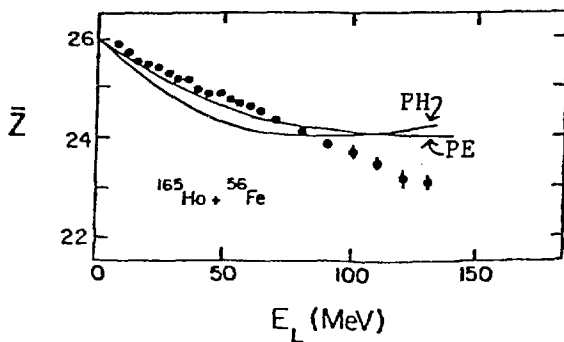


Fig. 1e: Fe+Ho: \bar{Z} vs. TKEL

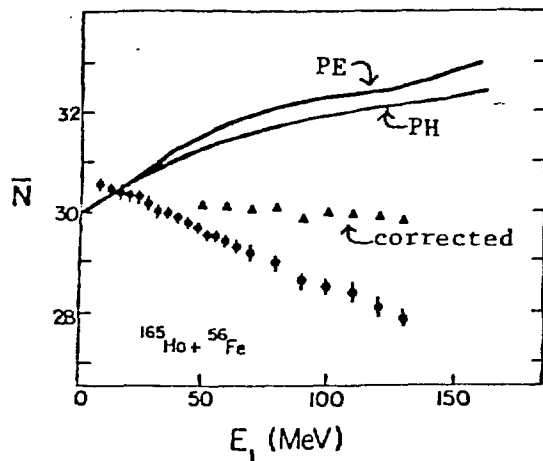


Fig. 1f: Fe+Ho: \bar{N} vs. TKEL

On the other hand, neutron emission will tend to shift the observed values of \bar{N} to lower values, as is shown in Fig. 1f, where the circles represent the raw data and the triangles the values after correction for neutron emission.⁸ Also plotted in the figure are the calculated values of \bar{N} . The disagreement between the theory and experiment in Fig. 1f is qualitative. Whereas the data seems to specify that the prompt value of \bar{N} is nearly constant with TKEL, the calculations exhibit a definite increase.

The situation is similar for the reaction Fe+U, as exhibited in Figs. 2e and 2f. Results for the particle-hole calculation, not shown, are similar to the pre-equilibrium results plotted.

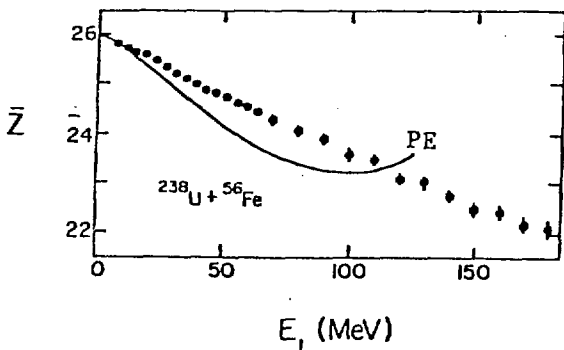


Fig. 2e: Fe+U: \bar{Z} vs. TKEL

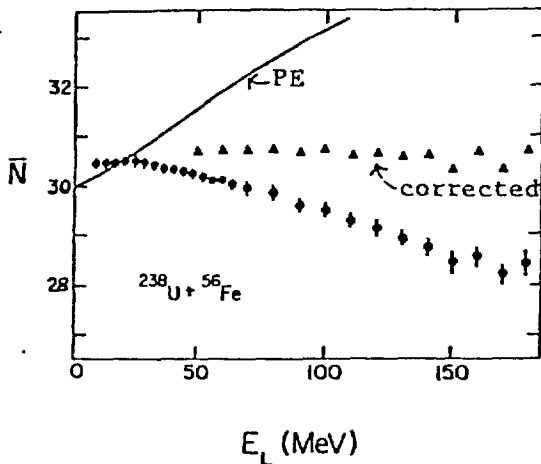


Fig. 2f: Fe+U: \bar{N} vs. TKEL

This discrepancy becomes even more significant when one observes that the source of the theoretical increase in \bar{N} is the dinuclear liquid drop energy surface, shown for Fe+Ho in Fig. 3. Since the transition probabilities favor transitions to states of higher excitation energy, and since the dinuclear ground state energy decreases with increasing N in the neighborhood of the ^{56}Fe projectile, it appears that, inevitably and quite independently of any specific details of the assumed transition rates, the calculation will predict a drift towards larger \bar{N} with increasing TKEL.

In summary, the results for the widths suggest that the careful study of (N,Z) distributions may provide a basis for a qualitative discrimination among various assumptions about the physical nature of the nucleon transfer process. However, none of the assumptions studied can yet claim clear advantage. We believe that such a claim must wait upon a more detailed understanding of the particle emission corrections, and of the systematic remnant discrepancies in the slope of the cut-widths $\sigma_A^2|Z$ and $\sigma_Z^2|A$ at low TKEL. This we expect to be ameliorated by the inclusion of angular momentum effects within the theoretical description.

On the other hand, the behavior of \bar{N} vs. TKEL is qualitatively deviant from the present description, no matter which detailed transfer mechanism is assumed. It follows that this disagreement, unless it can somehow be understood in terms of the neutron emission process, may require a reassessment of the basic energetic considerations which underlie the present description, and in particular, of the role of the dinuclear ground state energy in driving the drift of \bar{N} .

[Support of the U. S. Department of Energy and the University of Maryland Computer Science Center for this research is gratefully acknowledged.]

References

1. J. J. Griffin, Y. Boneh, et al., Nucl. Phys. A369 (1981) 181.
2. J. J. Griffin, Y. Boneh, et al., Nucl. Phys. A382 (1982) 159.
3. D. Schüll, W. C. Shen, et al., Phys. Lett. 102B (1981) 116.
4. A. Gökmen, et al., U. of Md. Tech. Rpt. #ORO 5126-212, to be published.
5. F. Williams, Nucl. Phys. A166 (1971) 231.
6. A. C. Mignerey, et al., Phys. Rev. Lett. 45 (1980) 509.
7. H. Breuer, et al., Phys. Rev. Lett. 43 (1979) 191.
8. A. C. Mignerey, U. of Md. Tech. Rpt. @ORO 5172-0020, September, 1982.

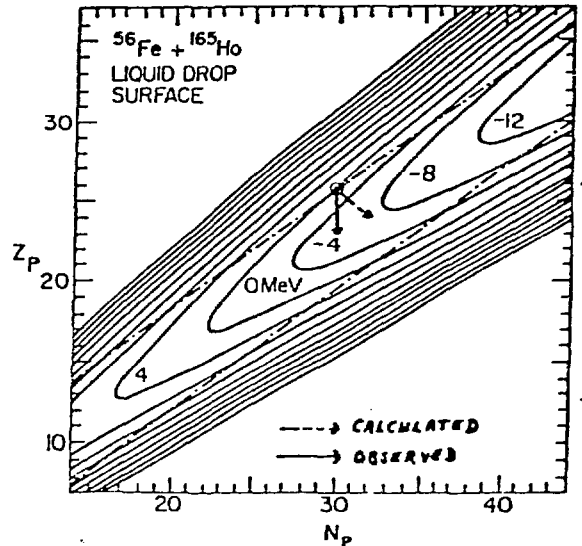


Fig. 3: Fe+Ho Energy Surface. The calculations predict a shift in \bar{N} not verified by the data.

DAMPING OF COLLECTIVE MOTION IN EXTENDED TDHF

S. Ayik

Department of Physics and Astronomy
 University of Maryland, College Park, Maryland 20742

Time-dependent Hartree-Fock theory (TDHF) is regarded as a microscopic basis for describing nuclear collective motion. In particular, the adiabatic limit of TDHF leads to a collective model and provides a microscopic description of collective motion. Since TDHF is a time-reversible theory, the collective model it yields in the adiabatic limit is also reversible and consequently free from dissipation.

A natural possibility for developing a collective model which exhibits dissipation is to consider the extended TDHF (i.e., instead of TDHF) as the underlying microscopic theory and study its adiabatic limit. The extended TDHF theory¹ goes beyond the mean-field approximation by incorporating a collision term into the equation of motion for the single-particle density matrix $\rho(t)$,

$$i \frac{\partial}{\partial t} \rho(t) = [h(\rho), \rho] - i K(\rho) . \quad (1)$$

The two-body collisions described by the collision term $K(\rho)$ provide a mechanism to convert the coherent mean field energy (collective energy) into incoherent intrinsic excitations (heat) in an irreversible manner. Consequently, a collective model based on the extended TDHF theory is irreversible and dissipative. We take a simplified Markovian form for the collision term which is derived in Ref. 1,

$$K(\rho) = \rho \cdot \Sigma(\rho) - (1-\rho) \cdot \tilde{\Sigma}(\rho) + \text{h.c.} , \quad (2)$$

where $\Sigma(\rho)$ is the real part of the self-energy operator for the particle states ($\tilde{\Sigma}(\rho)$ for the hole states) and its diagonal elements determine the width of single-particle states into 2p-1h configurations.

In the present work we develop a formalism suitable to describe low velocity dissipative nuclear collective motion within the framework of the extended TDHF theory in the adiabatic limit.² As a first step in such a development, we consider large amplitude slow collective motion described by a single collective variable $q(t)$ and the conjugate variable $p(t)$. The adiabatic approach is based on the assumption that the time-dependent single-particle density matrix at any value of the collective amplitude is rather close to the local equilibrium density. Following Refs. 3, 4, we parametrize the single-particle density matrix in terms of collective variables q and p as

$$\rho(t) = e^{ip\hat{Q}} \rho_0(q, \tau) e^{-ip\hat{Q}}. \quad (3)$$

Here $\rho_0(q, \tau)$ is the local equilibrium density determined by an appropriate constraint and a temperature τ .

The adiabatic approximation is introduced by assuming the the collective velocity is small and, hence, by expanding the phase factor in (3) in powers of collective velocity to second order. In the same way expanding the mean field and the collision term in powers of collective velocity and equating the same order term separately, we obtain a set of coupled equations for the collective path ρ_0 and \hat{Q} ,

$$i \dot{q} \frac{\partial}{\partial q} \rho_0 = [h(\rho_0), \rho_1] - i(\Gamma_0 \rho_1 + \rho_1 \Gamma_0) \quad (4a)$$

$$0 = [h(\rho_0) + p\hat{Q}, \rho_0] - i K(\rho_0) \quad (4b)$$

$$i \dot{\tau} \frac{\partial}{\partial q} \rho_0 = p\dot{q}[\hat{Q}, \frac{\partial \rho_0}{\partial q}] \quad (4c)$$

where $\rho_1 = ip[\hat{Q}, \rho_0]$ and $\Gamma_0 = \Sigma(\rho_0) + \tilde{\Sigma}(\rho_0)$. The first two equations determine the collective path and \hat{Q} for each value of temperature τ . The third equation

describes the time dependence of the temperature due to the coupling between collective motion and the intrinsic degrees of freedom.

In order to make contact with the collective model, the total energy of the system should be expressed in terms of the collective variables. We assume that the energy in the extended TDHF approximation is given by

$$E = \text{tr } k\rho(t) + \frac{1}{2} \text{tr } \rho(t) v\rho(t) . \quad (5)$$

The expansion in powers of collective velocity yields two contributions,

$$E = U(\rho_0) + T(\rho_0, \dot{\rho}_0) , \quad (6)$$

which consists of zeroth and second-order terms in collective velocity. We identify the zeroth order term $U(\rho_0)$ with the internal energy. The second-order term $T(\rho_0, \dot{\rho}_0)$ is quadratic in collective velocity, therefore it is the collective kinetic energy. The essential difference here, as compared to the usual TDHF, is that the internal energy is not a conservative potential alone. It contains the collective potential energy and also the intrinsic excitation energy. In order to separate the reversible and irreversible contributions, the rate of change of the internal energy should be considered. Two contributions occur in the rate;

$$\frac{d}{dt} U(\rho_0) = \dot{q} \frac{\partial U}{\partial q} + \gamma(q) \dot{q}^2 . \quad (7)$$

The first term determines the conservative force whereas the second term determines the dissipation which is described by the friction coefficient $\gamma(q)$. Using the adiabatic equations (4) the friction coefficient can be evaluated. In the representation which diagonalizes ρ_0 (adiabatic representation) the friction coefficient is given by

$$\gamma(q, \omega) = \sum_{\alpha, \beta} \left| \langle \alpha | \frac{\partial h_0}{\partial q} | \beta \rangle \right|^2 \xi_{\alpha\beta}(\omega) n_{\beta}(1-n_{\alpha}) \quad (8)$$

with

$$\xi_{\alpha\beta}(\omega) = \frac{1}{\omega} \left\{ \frac{\Gamma_{\alpha} + \Gamma_{\beta}}{(\epsilon_{\alpha\beta} - \omega)^2 + (\Gamma_{\alpha} + \Gamma_{\beta})^2} - \frac{\Gamma_{\alpha} + \Gamma_{\beta}}{(\epsilon_{\alpha\beta} + \omega)^2 + (\Gamma_{\alpha} + \Gamma_{\beta})^2} \right\}$$

where $\omega(q)$ is the local frequency of the collective motion, $\epsilon_{\alpha\beta} = \epsilon_{\alpha}(q) - \epsilon_{\beta}(q)$ and $\Gamma_{\alpha} = \langle \alpha | \Gamma_0 | \alpha \rangle$ is the single-particle width. In the same way the mass parameter can be evaluated and it is given by

$$M(q, \omega) = 2 \sum_{\alpha, \beta} |\langle \alpha | \frac{\partial h_0}{\partial q} | \beta \rangle|^2 \frac{\epsilon_{\alpha\beta}}{(\epsilon_{\alpha\beta}^2 - \omega^2)^2} n_{\beta} (1 - n_{\alpha}) . \quad (9)$$

These expressions for the mass parameter and the friction coefficients are also valid in small amplitude and high frequency limit, and in zero frequency limit, they reproduce the results of linear response theory.⁵

[Support of the U. S. Department of Energy for this research is gratefully acknowledged.]

References

1. S. Ayik, Z. Phys. A398 (1980) 83 and Lecture Notes in Physics, ed. K. Goeke and P. G. Reinhard (Springer-Verlag, 1982).
2. S. Ayik, Nucl. Phys., in press (1984).
3. F. Villars, Nucl. Phys. A285 (1977) 269.
4. M. Baranger and M. Veneroni, Ann. Phys. (N.Y.) 144 (1978) 123.
5. H. Hofmann and P. J. Siemens, Nucl. Phys. A257 (1976) 165 and A275 (1977) 464.

DISSIPATION AND FLUCTUATIONS IN NUCLEUS-NUCLEUS COLLISIONS*

H. Feldmeier**

Max-Planck-Institut für Kernphysik, Heidelberg, W. Germany

H. Spangenberg and F. Beck

Institut für Kernphysik, Technische Hochschule Darmstadt, W. Germany

One of the outstanding features of heavy ion reactions is the observation of a practical continuous energy loss in the relative motion, and of large fluctuations around the mean of macroscopic variables, such as energy, angular momentum or particle number of the reaction products. This suggests a statistical treatment of the coupling between macroscopic, or collective, and intrinsic variables. Implicit in such an approach is the assumption that the collective degrees of freedom vary much more slowly in time than the intrinsic ones.

In this work we investigate collisions between two nuclei whose relative velocity is much smaller than the Fermi velocity. Nuclear matter then is assumed to behave not much different from ordinary nuclei, i.e. the colliding partners are still leptodermous and of uniform density distribution in the interior. Therefore we characterize the macroscopic appearance of the nuclear system by families of shapes with sharp surfaces, which we restrict to axial symmetry [1,2]. In addition to the shape degrees of freedom, we use three rotational degrees of freedom. These are our macroscopic variables [3].

For the coupling of the fast intrinsic variables to the macroscopic ones, the novel feature in heavy ion reactions is the fact that at the beginning of the reaction the intrinsic system is completely cold (two nuclei in their ground states), and all the energy brought in resides in the relative motion. Consequently, the coupling between the two sets of variables cannot be characterized by a temperature alone, and application of equilibrium statistical mechanics is not possible.

In order to avoid a neglect of terms which are unimportant for macroscopic systems, and which normally are not retained in the Fokker-Planck equation, we derive equations of motion for the first and second moments of the reduced phase space distribution of the macroscopic variables directly from the Langevin equation [4]. Denoting the macroscopic variables which determine the collective dynamics of heavy ion scattering by $\{\vec{p}(t), \vec{q}(t)\}$, where the vector notation refers to the space of the chosen macroscopic parameters (6-dimensional in our case), the Langevin equation reads

$$\begin{aligned} \dot{\vec{p}} &= \vec{K}(\vec{p}, \vec{q}) + \vec{X}(t) \\ \dot{\vec{q}} &= \overleftarrow{M}^{-1} \cdot \vec{p} \end{aligned} \quad (1)$$

$\vec{K}(\vec{p}, \vec{q})$ denotes the forces among the macroscopic variables themselves, while $\vec{X}(t)$ arises from the interaction with the intrinsic degrees of freedom and produces time-irregular perturbations of the macroscopic momenta. \overleftarrow{M}^{-1} denotes the inverse of the mass tensor.

It is possible to derive closed equations of motion for the phase space averages (first moments) of the macroscopic variables by integration of equ. (1) over a short time interval τ under three basic assumptions:

(1) The time interval τ can be chosen such that

τ is $\left\{ \begin{array}{l} \text{short} \\ \text{long} \end{array} \right\}$ on the $\left\{ \begin{array}{l} \text{macroscopic} \\ \text{microscopic} \end{array} \right\}$ time scale.

(2) The phase space distribution $f(\vec{p}, \vec{q}; t)$ is sharply peaked around the averages $\vec{P}(t) = \int d^n p d^n q f(\vec{p}, \vec{q}; t) \vec{p}$, and $\vec{Q}(t)$.

(3) The momentum change caused by the interaction with the intrinsic system over time interval τ

$$\vec{\eta} = \int_t^{t+\tau} \vec{X}(t') dt' \quad (2)$$

is a stochastic variable and can be characterized by a probability distribution such that

$W(\vec{p}, \vec{q} | \vec{\eta}; \tau) d^n \eta$ is the conditional probability to find the macroscopic system at time $t + \tau$ with the momentum $\vec{p} + \vec{\eta}$, if it resided in (\vec{p}, \vec{q}) at time t .

The fact that $W(\vec{p}, \vec{q} | \vec{\eta}; \tau)$ does not depend on t implies that the intrinsic variables behave Markovian after time steps τ .

The importance of the third assumption lies in the fact that $W(\vec{p}, \vec{q} | \vec{\eta}; \tau)$ can be calculated on the basis of microscopic models of various sophistication, e.g. in the simplest case by assuming stochastic exchange of nucleons through the window connecting the two colliding objects.

The equations of motion for the phase space averages of the macroscopic variables (first moments) contain, besides the conservative forces, a dissipative friction force given by

$$\vec{F}(\vec{P}, \vec{Q}) = \frac{1}{\tau} \int d^n \eta W(\vec{P}, \vec{Q} | \vec{\eta}; \tau) \vec{\eta} \quad (3)$$

On the same basis (and with no further assumption) one can derive equations of motion for the second moments of the deviation from the mean (variances) which describe the fluctuations of the macroscopic variables. Their inhomogeneity is the diffusion tensor defined as

$$\vec{D}(t) = \frac{1}{\tau} \frac{1}{2} \int d^n \eta W(\vec{P}, \vec{Q} | \vec{\eta}; \tau) \vec{\eta} \otimes \vec{\eta} \quad (4)$$

The fact that the friction force \vec{F} and the diffusion tensor \vec{D} follow from the same probability distribution W is the content of the general dissipation-fluctuation theorem in our case.

Application to heavy ion scattering

For explicit calculations we have to specify the set of macroscopic variables, the conservative forces, the mass tensor, and the probability distribution $W(\vec{P}, \vec{Q} | \vec{\eta}; \tau)$ in order to solve the equations of motion for the first and second moments.

(1) Macroscopic variables: We employ the family of shapes as defined in [1, 2] with: s = distance between the spheres; σ = percentage of volume in the neck; Δ = asymmetry. In addition, there are three angles of rotation describing relative and intrinsic rotations.

(2) Conservative forces: For each shape a folding potential energy is calculated consisting of a Coulomb and a nuclear part

$$V(s, \sigma, \Delta) = \frac{Z_C}{2} \int_{\text{shape}} d^3 r d^3 r' \frac{1}{|\vec{r} - \vec{r}'|} + \frac{\gamma_S}{2} \int_{\text{shape}} d^3 r d^3 r' \left\{ \frac{1}{a} - \frac{2}{|\vec{r} - \vec{r}'|} \right\} e^{-\frac{|\vec{r} - \vec{r}'|}{a}} \quad (5)$$

with parameters a, γ_S taken from Krappé, Nix and Sierk [5].

- (3) Mass tensor: We adopt a Werner-Wheeler flow $\vec{v}(\vec{r})$ inside the shapes generated by changes in (s, σ, Δ) . The kinetic energy then reads

$$T = \frac{\rho_0}{2} \int_{\text{shape}} d^3r [\vec{v}(\vec{r})]^2 = \frac{1}{2} \sum_{ij} M_{ij} \dot{Q}_i \dot{Q}_j \quad (6)$$

- (4) Dissipation mechanism: We use the window-plus-wall dissipation which is a specific model to transform momentum from the intrinsic (nuclear) motion to the collective momentum of the macroscopic variables. Both, the well-known window and wall formulas, can be derived by following the time evolution, for small time steps τ , of the one-body phase space distribution close to the window or close to the wall. This then is a specific evaluation for the probability distribution $W(\vec{p}, \vec{Q}; \vec{\eta}, \tau)$ [2].

The momentum diffusion tensor, equ. (4), has up to now only been evaluated in a reduced macroscopic parameter space where window friction is the only dissipation mechanism. (For mass diffusion, see the contribution to this workshop by H. Feldmeier.)

For small mismatch velocities \vec{u} ($|\vec{u}| \ll v_F$) and small temperatures T ($T \ll \epsilon_F$) the momentum diffusion tensor can be written as

$$D_{ij} = |\vec{u}| m v_F D_{ij}^u(\alpha) + T D_{ij}^T(\alpha, \omega) \quad (7)$$

It consists of a "velocity-driven" part, proportional to the mismatch velocity \vec{u} plus a "temperature-driven" part, proportional to the nuclear temperature T . Note that a corresponding temperature part of the friction force vanishes, because of the skew-symmetry of the first moments.

The reduced tensors $D_{ij}^u(\alpha)$ and $D_{ij}^T(\alpha, \omega)$ reflect the geometry of the problem which is defined by the normal to the window, \hat{n} , and by the unit vector in the direction of the mismatch velocity, \hat{u} . $\cos \alpha = \hat{n} \cdot \hat{u}$, and the parameter $\omega = m v_F |\vec{u}| / T$ specifies the relative contribution of the two parts. In the limit stated above, one can derive analytic expressions for both tensors [6]. They are both proportional to the one-sided flux of particles through the window.

Fig. 1 shows the non-vanishing components of the diffusion tensor, taking a typical value of $C = 2 \cdot 10^{22} \text{ s}^{-1}$ for the one-sided flux, and a symmetric collision with an available kinetic energy of 1 MeV per nucleon. The coordinate system points with its 3-axis in the direction of the window normal. The four parts correspond to different partitions of the total energy into heat and kinetic energy. Only when all kinetic energy has been transformed to heat ($\vec{u} = 0$, $T = 3.6 \text{ MeV}$) the diffusion tensor does not depend on α , and the Einstein relation between diffusion and friction tensor holds.

Most important is the fact that the total strength of the fluctuations does not decrease with smaller temperature, but rather increases, quite in contrast to the Brownian motion picture. This shows the importance of the "velocity-driven" part.

Fig. 2 finally gives the calculated Wilczynski diagram for the reaction $^{136}\text{Xe} + ^{209}\text{Bi}$ at $E_{\text{lab}} = 1422 \text{ MeV}$ in comparison to experimental results from ref. [7]. Only a qualitative comparison is possible since the present calculation does not allow for deformations in the exit channel, and consequently cannot lead to energy losses below the Coulomb barrier. The size of the fluctuations, however, is represented in a quite satisfactory way, even in the region of small energy losses. This is a consequence of the velocity dependent diffusion, as can be seen from the lower inset where D^u has been set to zero.

In summary we have presented a model on dissipation and fluctuations in low energy heavy ion reactions which is based on known macroscopic properties of nuclei, and contains otherwise no adjustable parameters. The general formulation can serve as a starting point for a more refined treatment of the coupling between macroscopic and microscopic variables.

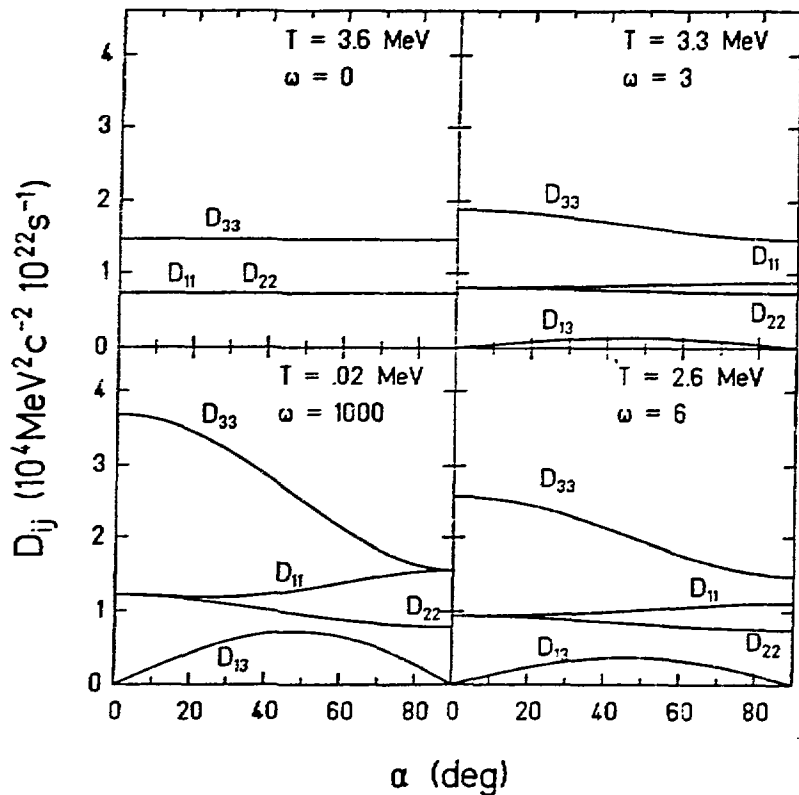


Fig. 1

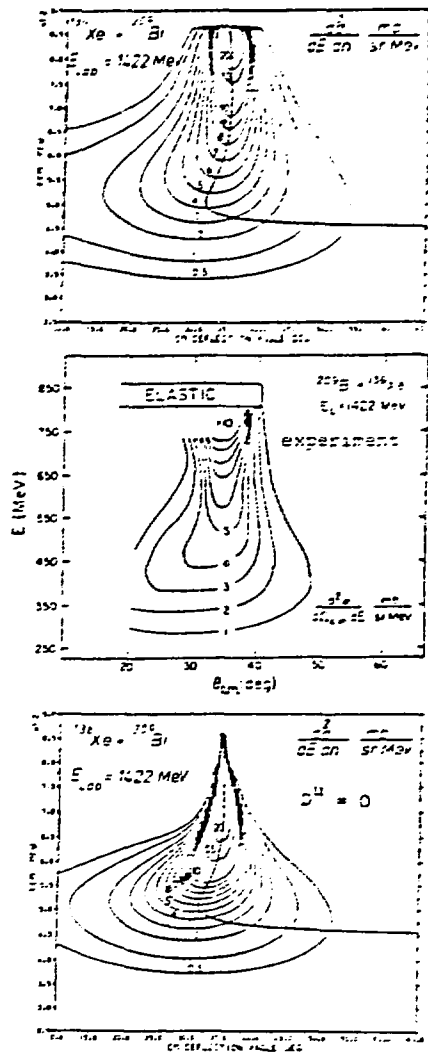


Fig. 2

* Work supported by Gesellschaft für Schwerionenforschung, Darmstadt, W. Germany

** Heisenberg Fellow; present address: Gesellschaft für Schwerionenforschung, D-6100 Darmstadt, W. Germany

- [1] J. Blocki, W.J. Swiatecki, Preprint LBL-12811 (1981).
- [2] H. Feldmeier, Proc. Int. School on Physics "Enrico Fermi", 1982, to be published; IKDA 82 (1982).
- [3] J. Blocki, M. Dworzecka, F. Beck and H. Feldmeier, Phys. Letters 99 B, 13 (1981).
- [4] S. Chandrasekhar, Rev. Mod. Phys. 15, 1 (1943).
- [5] H.J. Krappe, J.R. Nix, A.J. Sierk, Phys. Rev. C 20, 992 (1979).
- [6] H. Feldmeier, H. Spangenberg, GSI Annual Report 1983.
- [7] H.J. Wollersheim et al., Phys. Rev. C 24, 2114 (1981).

EXCHANGE OF PARTICLES, MOMENTUM AND ENTROPY

H. Feldmeier

Gesellschaft für Schwerionenforschung mbH, D-6100 Darmstadt

A moving Fermi gas is completely specified by the following three extensive quantities

$$\begin{aligned} \text{excitation energy} & \quad E^* = \langle \underline{H} \rangle - E_{gs} \\ \text{number of particles} & \quad N = \langle \underline{N} \rangle \\ \text{center of mass momentum} & \quad \vec{P} = \langle \underline{\vec{P}} \rangle \end{aligned}$$

Hence, the statistical operator which contains only this information is of the form

$$\underline{R} = 1/Z \exp\{ -\beta \underline{H} - \alpha \underline{N} - \vec{\xi} \underline{\vec{P}} \} \quad (1)$$

The Lagrange parameters are composed of three intensive quantities:

$$\begin{aligned} \text{temperature} & \quad T = 1/\beta \\ \text{chemical potential} & \quad \mu = -\alpha/\beta + \frac{1}{2} m \vec{u}^2 \\ \text{center of mass velocity} & \quad \vec{u} = -\vec{\xi}/\beta \end{aligned} \quad (2)$$

Here, m denotes the mass of one nucleon.

The basic idea of the model is to regard each nucleus as a Fermi gas described by a statistical operator as given in eq.(1). However, there is no a priori equilibration between the two nuclei. Thus, one considers two temperatures $T_{1,2}$, two chemical potentials $\mu_{1,2}$, and two c.m. velocities $\vec{u}_{1,2}$. If we make the idealization that the nucleus can be described by an ideal Fermi gas it is sufficient to consider only the velocity distribution of the particles which can be deduced from the statistical operator as

$$\begin{aligned} g(\vec{v}, \alpha_i, \beta_i, \vec{\xi}_i) &= \{1 + \exp(\beta_i \frac{1}{2} m \vec{v}^2 + \vec{\xi}_i m \vec{v} + \alpha_i)\}^{-1} \\ &= \{1 + \exp([\frac{1}{2} m (\vec{v} - \vec{u}_i)^2 - \mu_i] / T_i)\}^{-1} \end{aligned} \quad (3)$$

Here, the index $i=1,2$ refers to nucleus 1 and 2, respectively. Therewith, the intensive quantities depend on position in space in such a way that they are uniform in each nucleus but show a finite discontinuity at the "window" between the two nuclei. The particle exchange between the two gases will tend to equilibrate the mismatch in temperatures, chemical potentials and velocities by means of a flux of entropy, particles and momentum between the gases.

The flux of $\ln Z$ through a hole in the container enclosing the gas, which is given by

$$\Omega(\alpha, \beta, \vec{\xi}) := f_0 a_w \int_{\vec{v} \cdot \vec{n} > 0} d^3v P \vec{v} \cdot \vec{n} \ln\{1 + \exp(-\beta \frac{1}{2} m \vec{v}^2 - \vec{\xi} m \vec{v} - \alpha)\}, \quad (4)$$

is a quantity from which all other desired fluxes can be calculated. Here, f_0 is the phase space density, a_w is the window area and \hat{n} its normal vector. If there is a potential barrier in the window then the particles have a certain probability, P , to cross the barrier. The particle flux out of nucleus 1 into nucleus 2 is the negative of the first derivative with respect to α :

$$-\frac{\partial \Omega}{\partial \alpha}(\alpha_1, \beta_1, \vec{\gamma}_1) = \int_0 a_w \int_{\vec{v} \cdot \hat{n} > 0} d^3v P \vec{v} \hat{n} \frac{1}{1 + \exp(\beta_1 \frac{m}{2} \vec{v}^2 + \vec{\gamma}_1 m \vec{v} + \alpha_1)} \quad (5)$$

Similarly the momentum and entropy currents can be written as:

$$-\frac{\partial \Omega}{\partial \vec{\gamma}}(\alpha_1, \beta_1, \vec{\gamma}_1) = \int_0 a_w \int_{\vec{v} \cdot \hat{n} > 0} d^3v P \vec{v} \hat{n} \frac{m \vec{v}}{1 + \exp(\beta_1 \frac{m}{2} \vec{v}^2 + \vec{\gamma}_1 m \vec{v} + \alpha_1)} \quad (6)$$

$$\dot{S}_1 = \left[\Omega - \alpha \frac{\partial \Omega}{\partial \alpha} - \beta \frac{\partial \Omega}{\partial \beta} - \vec{\gamma} \frac{\partial \Omega}{\partial \vec{\gamma}} \right] (\alpha_1, \beta_1, \vec{\gamma}_1) \quad (7)$$

It is easy to verify that the corresponding fluxes from nucleus 2 into nucleus 1 are given by:

$$-\frac{\partial \Omega}{\partial \alpha}(\alpha_2, \beta_2, -\vec{\gamma}_2); + \frac{\partial \Omega}{\partial \vec{\gamma}}(\alpha_2, \beta_2, -\vec{\gamma}_2); \left[\Omega - \alpha \frac{\partial \Omega}{\partial \alpha} - \beta \frac{\partial \Omega}{\partial \beta} - \vec{\gamma} \frac{\partial \Omega}{\partial \vec{\gamma}} \right] (\alpha_2, \beta_2, -\vec{\gamma}_2) \quad (8)$$

The net fluxes are then the mutual differences. For example the net particle flux which is also the rate of change of the particle number in nucleus one can be expressed as

$$\dot{A}_1 = \frac{\partial \Omega}{\partial \alpha}(\alpha_1, \beta_1, \vec{\gamma}_1) - \frac{\partial \Omega}{\partial \alpha}(\alpha_2, \beta_2, -\vec{\gamma}_2) \quad (9)$$

If the difference in the intensive quantities are small one can use a Taylor expansion around the mean values in order to linearize eq. (9) and the corresponding equations for the momentum and entropy flux. In addition we express everything with (μ, T, \vec{u}) instead of $(\alpha, \beta, \vec{\gamma})$ and neglect all terms which are of higher order. The result is a set of coupled thermodynamic equations:

$$\dot{A}_1 = g_{AA} \Delta \mu + g_{AS} \Delta T \quad (10)$$

$$\dot{S}_{21} = g_{SA} \Delta \mu + g_{SS} \Delta T \quad (11)$$

$$\dot{\vec{p}}_1 = \vec{g} \Delta \vec{u} \quad (12)$$

with $\Delta \mu = \mu_2 - \mu_1$, $\Delta T = T_2 - T_1$ and $\Delta \vec{u} = \vec{u}_2 - \vec{u}_1$. The mobility coefficient for particle transfer is given by:

$$g_{AA} = \frac{1}{T_0} \left. \frac{\partial^2 \Omega}{\partial \alpha^2} \right|_0 \quad (13)$$

the equality between the Peltier and the Seebeck coefficient reflects the Onsager relation:

$$g_{As} = g_{sA} = \frac{1}{T_0^2} \left[\left. \frac{\partial^2 \Omega}{\partial \alpha \partial \beta} \right|_0 - \varepsilon_F \left. \frac{\partial^2 \Omega}{\partial \alpha^2} \right|_0 \right]; \quad (14)$$

the entropy conductivity is calculated as:

$$g_{ss} = \frac{1}{T_0^3} \left[\left. \frac{\partial^2 \Omega}{\partial \beta^2} \right|_0 - 2 \varepsilon_F \left. \frac{\partial^2 \Omega}{\partial \alpha \partial \beta} \right|_0 + \varepsilon_F^2 \left. \frac{\partial^2 \Omega}{\partial \beta^2} \right|_0 \right]; \quad (15)$$

and finally the momentum transport coefficients turn out to constitute the well known¹⁾ window friction tensor:

$$\vec{g} = \frac{1}{T_0} \left. \frac{\partial^2 \Omega}{\partial \vec{y} \partial \vec{y}} \right|_0 \quad (16)$$

The symbol $|_0$ means that all the derivatives have to be taken at the mean values:

$$\alpha_0 = -\frac{\varepsilon_F}{T_0}, \quad \beta_0 = \frac{1}{T_0}, \quad \vec{y}_0 = 0 \quad \text{with} \quad \varepsilon_F = \frac{1}{2} (\varepsilon_{F1} + \varepsilon_{F2}), \quad T_0 = \frac{1}{2} (T_1 + T_2) \quad (17)$$

Herewith, we have calculated within a unified microscopic model transport coefficients for four different phenomena: A gradient in chemical potential, $\Delta\mu$, drives the particle flux. The temperature mismatch, ΔT , drives the entropy flux. The velocity mismatch, $\Delta \vec{u}$, sets in motion the momentum flux. In addition there is a coupling between particle and entropy flux in such a way that the hotter gas is giving away particle to the colder one. This effect, as has been pointed out by Moretto²⁾, counteracts the driving force towards symmetry in mass number. In how far it can be made responsible for the lack of mass drift seen in heavy ion collisions will be discussed later. We have worked out analytical expressions for all derivatives of Ω for the case of a classical single particle penetrability P ($P=1$ above, $P=0$ below the barrier).

Before discussing results of trajectory calculations³⁾ in which we have implemented eqs. (10) and (11) we have to specify the origin of excitation energies. The two entropy producing sources in our model are the wall and window friction. The wall friction is assumed to share the dissipated energy according to the surfaces of the two nuclei. The window friction deposits equal amounts of heat in each nucleus. Herewith, the rate of excitation energy in the nuclei is given by:

$$\frac{d}{dt} E_1^* = \dot{Q}_1^{\text{wall}} + \frac{1}{2} \dot{Q}^{\text{window}} + T_0 \dot{S}_{21} \quad (18)$$

$$\frac{d}{dt} E_2^* = \dot{Q}_2^{\text{wall}} + \frac{1}{2} \dot{Q}^{\text{window}} - T_0 \dot{S}_{21} \quad (19)$$

with

$$\dot{Q}_{1,2}^{\text{wall}} = \frac{3}{4} \rho \rho_F \int_{\text{surface of } 1,2} df u_I^2 \quad \text{and} \quad \dot{Q}^{\text{window}} = \Delta \vec{u} \vec{g} \Delta \vec{u} \quad (20)$$

In fig. 1 the counteracting effect of the thermal force (g_{AS}/g_{AA}) ΔT , in comparison to the driving potential, $\Delta\mu$, is depicted. (Please note that $-\Delta\mu$ has been plotted.) In the early stage of the reaction the temperature difference, ΔT , builds up and the thermal force takes away an appreciable fraction of the driving force. During the first 10^{-21} s the mean mass number is not drifting at all. After 10^{-21} s the temperatures are equilibrated and the thermal force is close to zero. Despite this fact the mean mass number drifts only very slowly. The reason is the smallness of the mobility coefficient or since its inverse is the friction coefficient the very large window friction against mass drift.

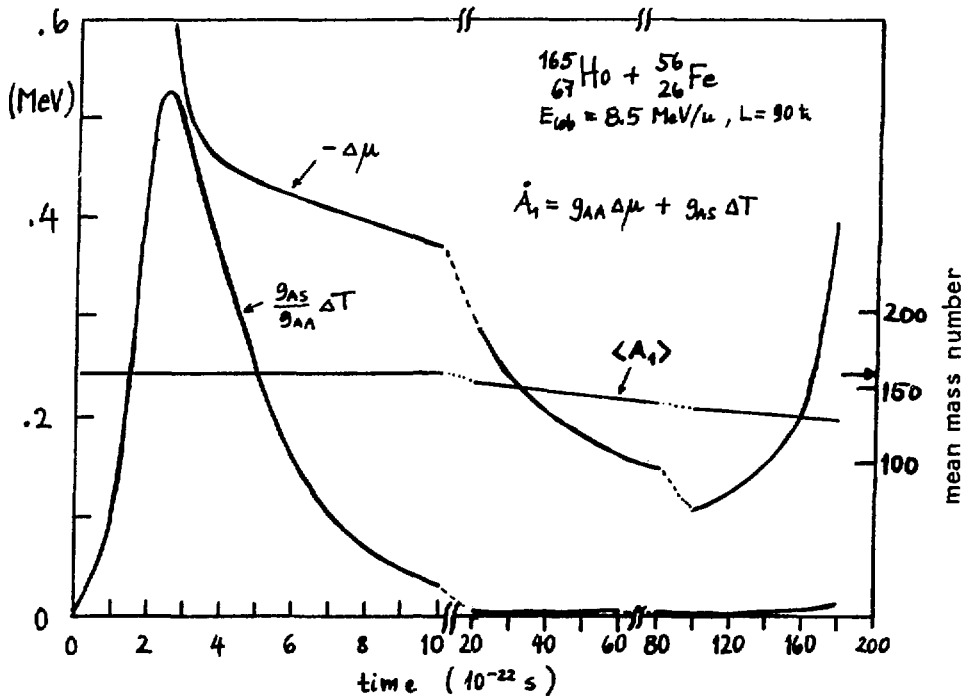


Fig. 1 Driving force, $\Delta\mu$ (the negative of which has been plotted), thermal force, $(g_{AS}/g_{AA})\Delta T$, and mean mass number, $\langle A_1 \rangle$, as function of time along the trajectory.

For a window without barrier and zero temperature $1/g_{AA}$ becomes

$$\frac{1}{g_{AA}} = \frac{4}{3} \frac{p_F}{\rho a_w} \quad \text{for } T_0 = 0, P = 1 \quad (21)$$

Here, p_F is the Fermi momentum, ρ the number density and a_w the window area. The very same expression has also been found independently by Randrup and Swiatecki⁴⁾. The first to note is that the friction coefficient is inversely proportional to the window area, a_w , which leads to a very strong hinderance in mass drift for peripheral collisions. If we assume a typical value of 1 MeV for $\Delta\mu$ and 15 fm^2 for a_w the time scale for mass equilibration is of the order of

$$(g_{AA} \Delta\mu)^{-1} = 0.5 \cdot 10^{-21} \text{ s per mass unit.} \quad (22)$$

This shows that one should not expect the mass number to drift by more than a few units within typical reaction times of the order of 10^{-21} s. In fig. 2 we display the result of a trajectory calculation together with experimental data for the change of the mean charge number. The important outcome is the lack of mass drift for total kinetic energy losses up to the Coulomb barrier. Once the energy loss is greater than that, the window is widely open during a very long reaction time so that even a very slow motion can make some progress. This seems to indicate that the particle exchange model is in accord with experimental findings. In order to study the influence of the thermal force on the final numbers we set $g_{AS} = 0$. The resulting change in the final charge numbers is so little that it can hardly be seen in fig. 2. As discussed already in fig. 1 the thermal force can not be neglected throughout but it assumes large values only in the first 10^{-21} s, then during the long remaining reaction time when the motion in mass asymmetry advances its influence becomes negligible.

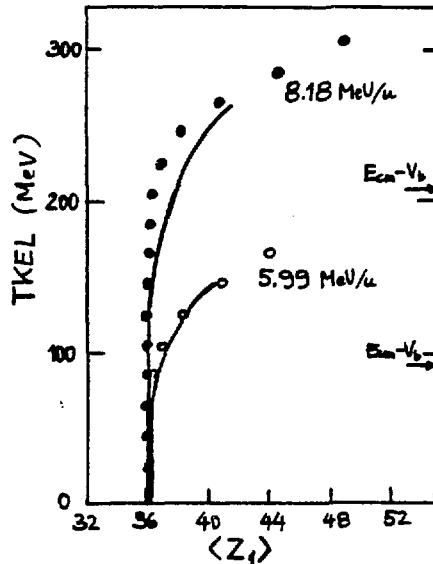


Fig.2 Mean total kinetic energy loss, TKEL, versus mean charge number, $\langle Z_1 \rangle$ for the reaction $\text{Kr} + \text{Er}$ at $E_{\text{lab}} = 8.18$ and 5.99 MeV/u . Experimental data from Rudolf et al., Nucl. Phys. A330, 243 (1979).

In those collisions of Fe+Ho where not all the available kinetic energy has been dissipated the model predicts reaction times up to $1.5 \cdot 10^{-21}$ s for $L = 200$ fm and $TKEL = 175$ MeV. From fig. 3 one sees that the ratio of the temperatures, T_H/T_L , deviates from 1 for smaller energy losses (shorter reaction times). As in the Kr+Er case the drift in asymmetry sets in only below the barrier (denoted by V_b) of two touching spheres (cf. fig. 3). The particle exchange model does not yield complete equilibration of the excitation energies which is in contrast to the findings inferred from spectra of evaporated neutrons. The r.h.s. of fig. 3 compares the effective temperatures extracted from neutron data with the calculated ones. Theory and data seem to disagree. However, it is not so evident that velocity distributions of evaporated neutrons reflect uniquely the intrinsic excitation energies. At this workshop Vandenbosch showed fission data which support our and also Randrup's⁴⁾ theoretical predictions.

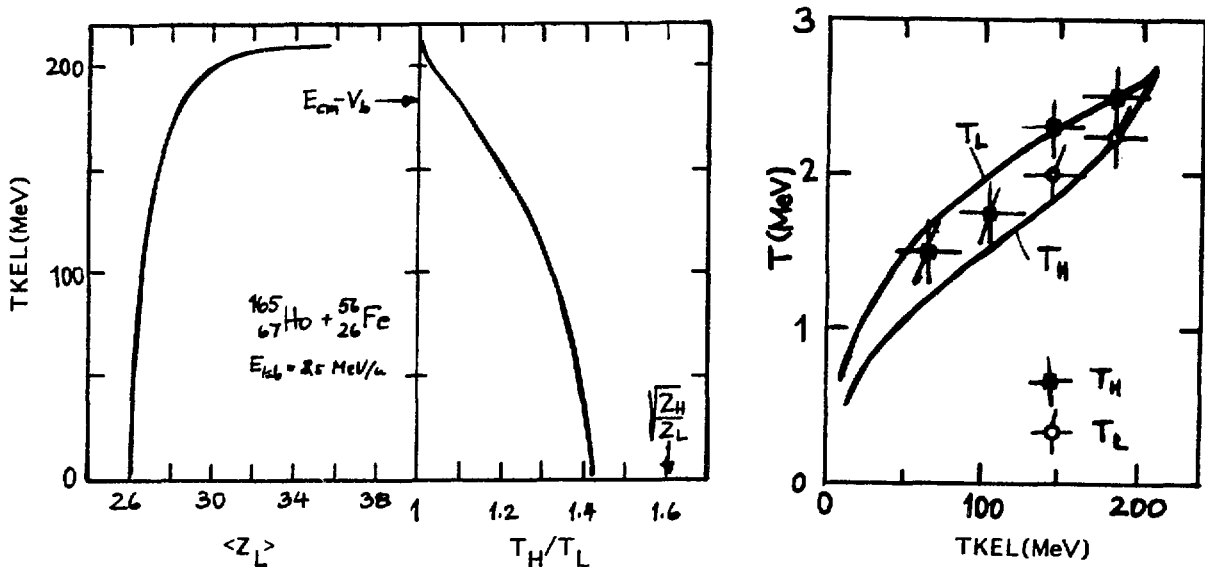


Fig. 3 Correlation between mean charge number, $\langle Z_L \rangle$, ratio of temperatures, T_H/T_L , and effective temperatures for neutron spectra, $T_i = 11/12 \sqrt{8 \text{ MeV } E_i/A_i}$, versus TKEL. Experimental data from Hilscher et al., Phys. Rev. C20, 576 (1979).

The question arises if a small mobility in mass drift should be accompanied by small fluctuations in mass number. Referring to the contribution by Feldmeier et al. in these proceedings the diffusion coefficient in mass number derived from the particle exchange picture can be written as:

$$D_{AA} = g_{AA} (|\Delta \vec{u}| p_F D^U(\alpha) + T D^T(\alpha, \omega)) \quad (23)$$

where $D^U(\alpha)$ ranges between 0.3 and 0.2 and $D^T(\alpha, \omega)$ between 0 and 1 depending on the arguments. Here, one realizes that even for zero temperature the diffusion coefficient does not vanish due to the "velocity part" which is proportional to the velocity mismatch, $\Delta \vec{u}$, at the window. Randrup⁵⁾ derived from the same physical picture the same coefficient using somewhat different approximations as:

$$D_{AA}^{\text{Randrup}} = g_{AA} \frac{1}{2} |\Delta \vec{u}| p_F \coth \left\{ \frac{|\Delta \vec{u}| p_F}{4T} \right\}. \quad (24)$$

For peripheral collisions ($\alpha=90^\circ$) this becomes $0.25 g_{AA} |\Delta \vec{u}| p_F$ compared to $0.21 g_{AA} |\Delta \vec{u}| p_F$ in our case. In any case for grazing collisions $|\Delta \vec{u}| p_F$ is large compared to the temperature T which allows for large fluctuations even at small energy losses and short reaction times. In fig. 4 we display the mean mass number and the variance in mass number, σ_{AA}^2 , as a function of the total kinetic energy loss. To illustrate the importance of the non-equilibrium "velocity part" the mass variance which one would get by assuming the Einstein relation for the diffusion coefficient,

$$D_{AA} = g_{AA} T, \quad (25)$$

is shown as the dashed line. It is evident that for energy losses below the Coulomb barrier, where the mass number does not drift the "velocity part" contributes appreciably.

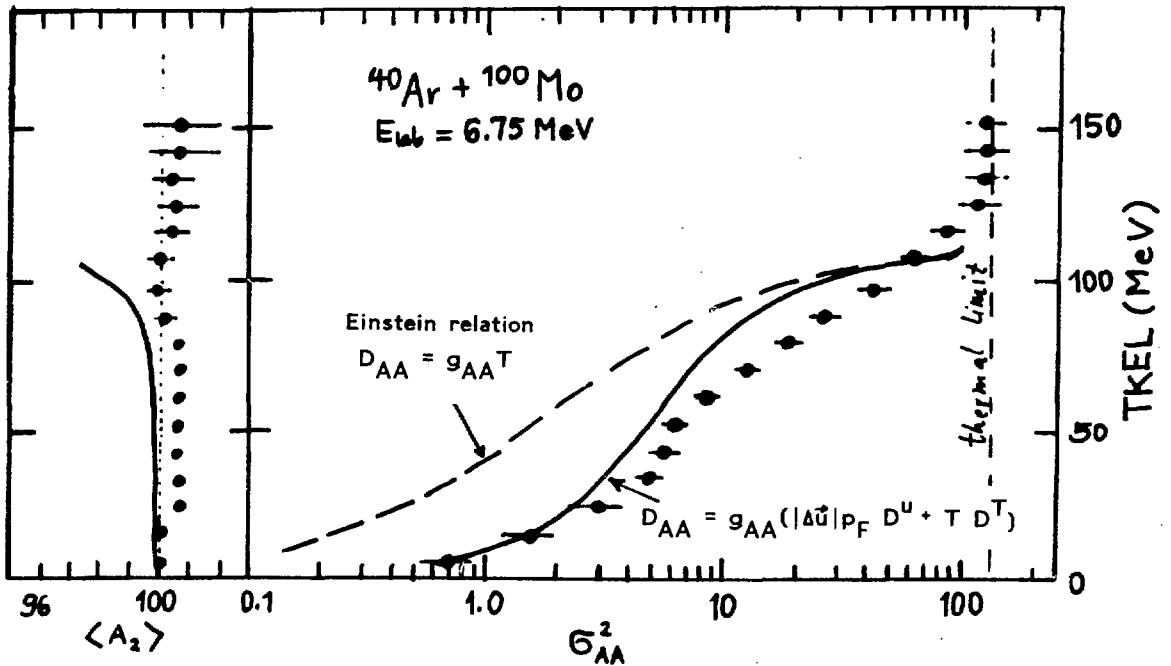


Fig.4 Correlation between mean mass number, $\langle A_2 \rangle(L)$, variance in mass number, $\sigma_{AA}^2(L)$, and mean total kinetic energy loss TKEL(L). Please keep in mind that the experimental data from Bohne et al. (Z. Physik A313,19(1983)) are achieved by cuts in $d^2\sigma/dE dA_1$ so that a direct comparison is questionable.

Before drawing any conclusions from the agreement or disagreement with experimental data let us illustrate in fig. 5 that the relation between mean energy and mass variance for one trajectory

$$\langle \sigma_{ZZ}^2 \rangle(L) \leftrightarrow \langle E \rangle(L) \quad \text{yields} \quad \langle \sigma_{ZZ}^2 \rangle(\langle E \rangle)$$

might be quite different from

$$\sigma_{ZZ}^2(E) := \frac{\int dZ \frac{d^2\sigma}{dE dZ} (Z - \langle Z \rangle)^2}{\int dZ \frac{d^2\sigma}{dE dZ}} \quad (26)$$

Due to fluctuations in energy a range of impact parameters contribute to the same final energy E . Therefore, $\sigma_{ZZ}^2(E)$ is a weighted superposition of many $\langle \sigma_{ZZ}^2 \rangle(L)$. On the left hand side of fig. 5 we have calculated theoretically⁷⁾ $d^2\sigma/dE dZ$ and deduced $\sigma_{ZZ}^2(E)$ by means of eq. (26). This is compared with $\langle \sigma_{ZZ}^2 \rangle(\langle E \rangle)$ on the right hand side. The remarkable difference should be a warning.

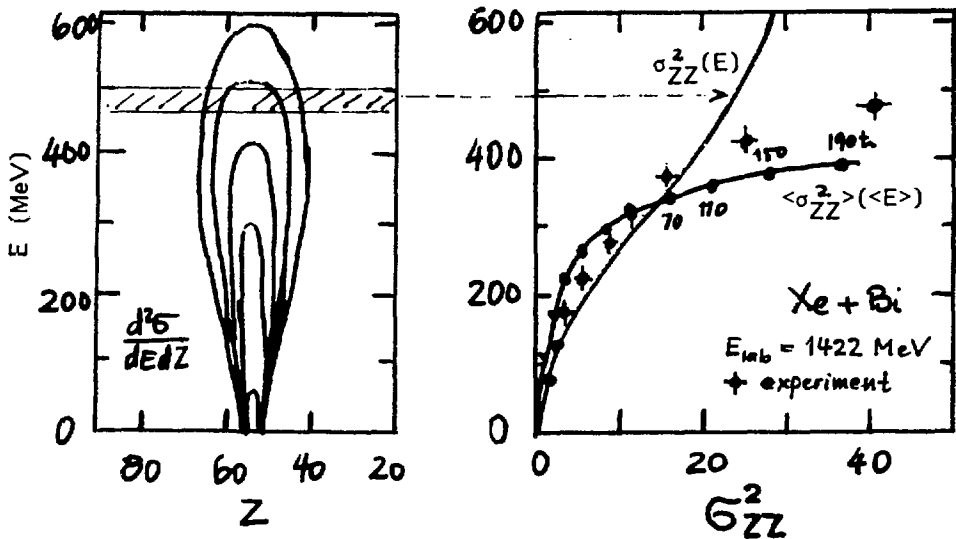


Fig.5 The difference between $\langle \sigma_{ZZ}^2 \rangle(\langle E \rangle)$ and $\sigma_{ZZ}^2(E)$.

I should like to acknowledge many fruitful discussions with L. Moretto at the Max-Planck-Institut in Heidelberg which initiated the present investigations.

References

- 1) J. Blocki et al.: Ann. Phys. (N.Y.) 113, 330 (1978)
- 2) L.G. Moretto: Z. Physik A310, 61 (1983)
- 3) H. Feldmeier: Proc. International School of Physics "Enrico Fermi" Varenna, June 27 - Aug. 6, 1982
- 4) J. Randrup, W.J. Swiatecki: accepted by Nucl. Phys., LBL-17273 (1984)
- 5) J. Randrup: Nucl. Phys. A383, 468 (1983)
- 6) R. Randrup: Nucl. Phys. A327, 490 (1979)
- 7) H. Spangenberg, H. Feldmeier: to be published

NUCLEON AND ENERGY EXCHANGE IN LOW ENERGY HEAVY-ION REACTIONS

H. Breuer, A. Gökmen, C. J. Kulesza, G. Lavelle, A. C. Mignerey, U. Maryland; K. K. Kwiatkowski, V. E. Viola, U. Indiana; J. R. Birkelund, A. D. Hoover, J. R. Huizenga, W. U. Schröder, W. W. Wilcke, H. J. Wollersheim, U. Rochester; R. R. Betts, B. G. Glagola, C. Davids, and K. L. Wolf, Argonne National Lab.

A detailed analysis of the processes relevant for heavy ion reactions requires experimental data which provide information about mass, charge and energy of the reaction fragments. Particularly questions concerning the dynamics of charge equilibration, differences in proton and neutron exchange, and energy loss processes other than statistical nucleon exchange are dependent on such data.

A recent systematic study¹ of the neutron (N) and proton (Z) number distributions of projectile-like fragments observed in 8.3 MeV/u ⁵⁶Fe induced reactions on targets of ⁵⁶Fe, ¹⁶⁵Ho, ²⁰⁹Bi, and ²³⁸U has been extended to further projectile-target combinations and beam energies. Data for the ²³⁸U+⁴⁰Ca reaction and 8.4 and 7.2 MeV/u have been taken at the LBL SuperHILAC and for the ²⁰⁹Bi, ⁴⁰Ca+³⁷Cl reactions at 6.0 (Ca) and 7.3 MeV/u (Ca,Bi) at the ANL-LINAC. Total energy, energy loss and time-of-flight were determined with a solid state detector telescope (ΔE and E detectors separated by a flight path) with sufficient accuracy¹ to allow the identification of each projectile-like fragment uniquely by mass and charge in all reactions.

The experimental analysis of these data is based on two-dimensional Gaussian fits on N-Z distributions of projectile-like fragments as a function of energy loss (E_L). The procedures are described in detail in Ref. 1. For all reactions these fits gave an adequate representation of the experimental results, with the exception of the ²³⁸U+⁴⁰Ca reactions. These show a statistically significant asymmetry (compare Fig. 1) at all E_L . Thus, the results for the ⁴⁰Ca induced reactions derived from Gaussian fits discussed here are preliminary until an appropriate fit procedure has been developed. The qualitative results, however, are not expected to change.

Figure 1 shows examples of experimental N-Z distributions at several E_L . Contour lines of constant cross section demonstrate the evolution of fragment yield in a narrow band approximately parallel to the line of beta stability. With increasing E_L the distributions rotate and increase in width while their centroids drift away from the injection point ⁴⁰Ca (full circles). These properties are common to all reactions mentioned.

In all reactions the average mass of projectile-like fragments decreases with E_L for $E_L > 20$ MeV. For the (nearly) symmetric $^{40}\text{Ca}+^{37}\text{Cl}$ and $^{56}\text{Fe}+^{56}\text{Fe}$ reactions this is mostly due to post-reaction nucleon evaporation. Since simultaneous proton and neutron corrections are extremely difficult to perform, centroids of these reactions will not be discussed. In the asymmetric reactions, where the predominant neutron decay can be corrected for, a net nucleon stripping (on the average) from the projectile is responsible for the mass drift. The contributions of protons and neutrons to the mass drift varies strongly from reaction to reaction as can be observed from the average neutron to proton ratios, \bar{N}/\bar{Z} , of the fragments shown in Fig. 2.

All reactions demonstrate the charge equilibration process: increasing \bar{N}/\bar{Z} -ratios with increasing E_L (and interaction time). For the U+Fe and both U+Ca reactions the increase is nearly linear, possibly with saturation at high E_L in the U+Ca reactions at \bar{N}/\bar{Z} -values of about 1.30. For Bi+Cl \bar{N}/\bar{Z} reaches a maximum of about 1.23 and even decreases at high E_L . Even though the N/Z-values of the combined systems are similar in all these four reactions, the equilibrium N/Z-value given by the potential energy surface is expected to decrease with fragment mass (projectile mass). The maximum \bar{N}/\bar{Z} -value for Bi+Cl as compared to Ca+U is

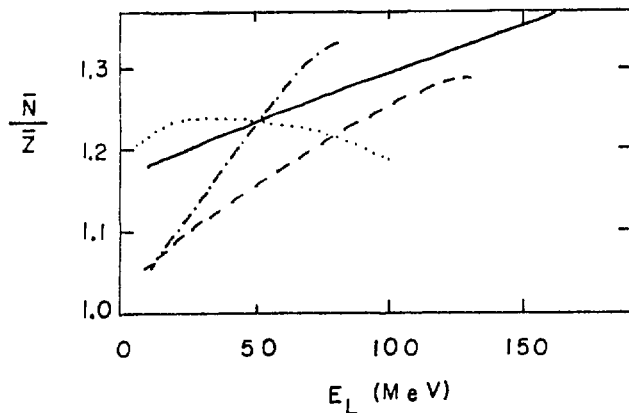
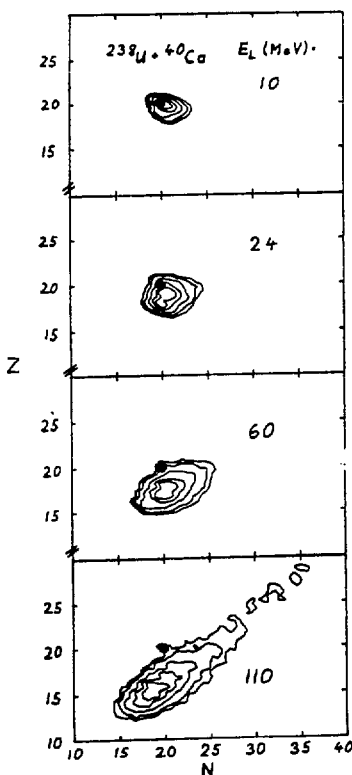


Fig. 2 (above): Average proton to neutron ratios as a function of E_L (corrected for neutron evaporation).

— = $^{238}\text{U} + ^{56}\text{Fe}$, 8.3 MeV/u
 --- = $^{238}\text{U} + ^{40}\text{Ca}$, 8.4 MeV/u
 -.- = $^{238}\text{U} + ^{40}\text{Ca}$, 7.2 MeV/u
 ... = $^{209}\text{Bi} + ^{37}\text{Cl}$, 7.3 MeV/u

Fig. 1 (left): Contour lines of constant cross section as a function of proton and neutron number and E_L .

still surprisingly low, indicating strong influences of shell-structure effects or the differences of N/Z of the incident projectile. A comparison of the results for the Ca+U energies shows a much faster charge equilibration process in terms of E_L for the lower beam energy, which may translate into similar absolute relaxation times. The faster rise of the \bar{N}/\bar{Z} -ratios of the 7.2 MeV/u U+Ca reaction is produced mainly by a stronger neutron pickup rather than an increased proton stripping as compared to the higher energy.

The ratios of the total neutron to proton variances, σ_N^2/σ_Z^2 , are compared in Fig. 3 for reactions of ^{40}Ca and ^{56}Fe with the ^{238}U target. Increased ratios are apparent at low E_L , not inconsistent with the other reactions studied. These high ratios are due to increased neutron rather than small proton variances, indicating preferential neutron exchange at the early stages of the interaction. The spectacularly large σ_N^2/σ_Z^2 -ratios in the 7.2 MeV/u U+Ca reaction may be due to shell effects in connection with the pronounced increase in average neutron fragment number in this reaction. This may create a divergence of paths along the gradient of the potential energy surface during the reaction, although it does not explain the minimum near $E_L = 15$ MeV.

The linear correlation coefficient, $\rho_{NZ} = \sigma_{NZ}/\sigma_N\sigma_Z$ (σ_{NZ} = covariance), quantifies how correlated the N-Z cross section distributions (i.e., Fig. 1) are with

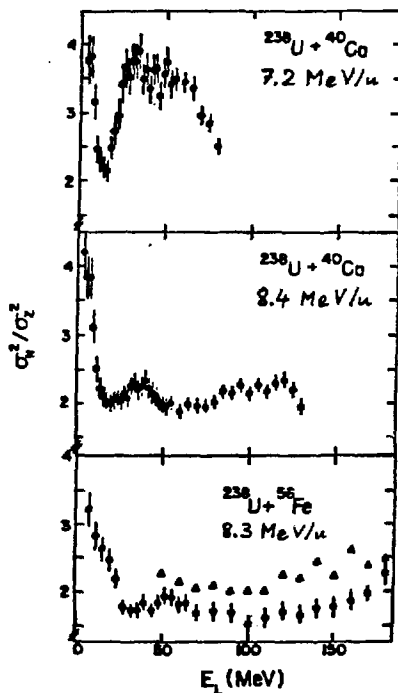


Fig. 3: Ratios of neutron to proton variances as a function of E_L . Triangles represent data corrected for neutron evaporation.

respect to the independent variables proton and neutron number. Figure 4 verifies the expectation that for high E_L , where wide distributions are confined to a narrow tilted band, ρ_{NZ} approached +1.0. For more symmetric reactions as well as for lower beam energies, where the proton and/or neutron variances increase more rapidly with E_L , the ρ_{NZ} -values increase also more rapidly, as expected. Unexpected and not yet understood is the result, that most reactions investigated here exhibit (or are consistent with) negative ρ_{NZ} at low E_L . This corresponds to the negative tilt of the 10 MeV N-Z distribution in Fig. 1. As is apparent from Fig. 4, good statistical significance combined with small E_L steps for the data are required to verify the rapid decrease of the correlation coefficient to negative values (see also Ref. 1). The exception to the consistent presence of negative ρ_{NZ} in this set of data appears to be the Bi+Cl reaction (Fig. 4), which is also the only case without a dramatic charge equilibration process (Fig. 2). Possibly the negative ρ_{NZ} -values give evidence for energy-loss processes other than statistical nuclear exchange, e.g., pion exchange.

¹H. Breuer et al., Nucl. Instrum. & Methods 204 (1983) 419;
H. Breuer et al., Phys. Rev. C 28 (1983) 1080

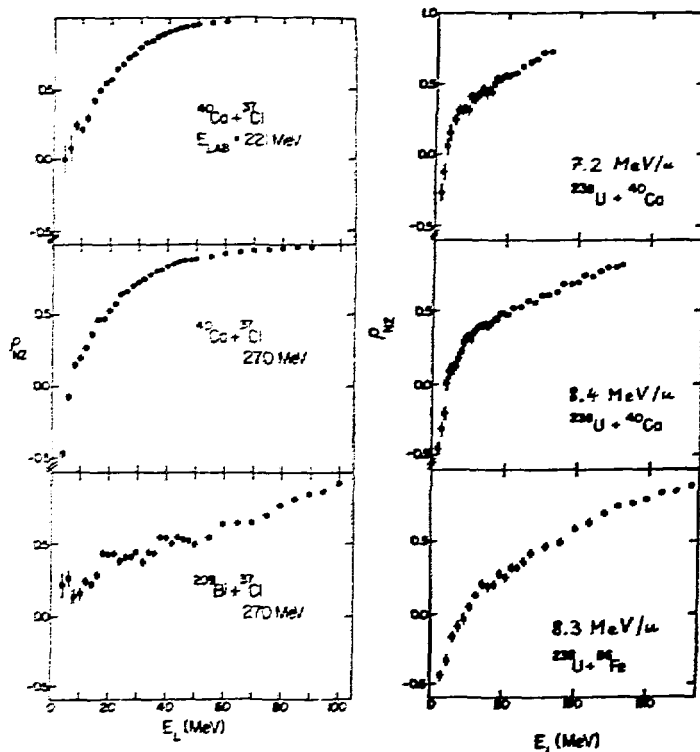


Fig. 4: Correlation coefficients as a function of E_L .

EXACT QUANTAL SCHRÖDINGER MODEL OF DINUCLEAR FLOW:
IMPORTANCE OF KINETIC PRESSURE FOR FLUX RATES

James J. Griffin and W. Broniowski
Department of Physics and Astronomy
University of Maryland, College Park, MD 20742

A one-dimensional two-square-well independent particle model^{1,2} of the heavy ion dinucleus is analyzed by obtaining its exact time-dependent solutions numerically, and computing the time dependence of the number, $N_R(t)$, of nucleons on the right side, and of its dispersion, $\sigma_R(t)$. Then one inquires which features of the model system determine the time dependence of these quantities. The "kinetic pressures", $P_K = -\partial E_{TOT}/\partial L$, of the interfacing Fermi gases emerges as a key determinant of the nucleonic fluxes. Consequently, finite translational velocities for the colliding nuclei also exert a strong influence on time derivatives of the quantities, N and σ^2 .

However, a potential energy difference between nucleons in the two wells exerts a much weaker influence, distinguishing this Schrödinger model from phenomenological statistical formulations³⁻⁵ which imply that the nucleon drift rate, N_R , is non-zero only when the "driving force", $-\partial \langle E_0 \rangle / \partial N_R$, is non-zero. In the present model, even when this "driving force" is zero, guaranteeing zero nucleon drift within the present statistical descriptions, a kinetic pressure difference leads to a finite drift. It presents, therefore, a flat contradiction between the behavior of this Schrödinger model system and the predictions of the statistical models. This contradiction bears especially upon the difference between the behavior of protons, whose kinetic pressure generally favors the drift of protons towards the more neutron excessive nuclide, and that of neutrons for which the kinetic pressure differences and, therefore, the drifts, are here much smaller.⁶

Extrapolation of these qualitative results to the experimental dinucleus indicates that in a reaction⁷ such as Fe+Ho, neutrons should drift at a nearly zero rate, whereas protons should drift out of the Fe-like nucleus much more rapidly. Thus the present model conforms better with the (neutron emission corrected⁸) observations⁷ for this case than do the statistical descriptions³⁻⁵ in which total (i.e., kinetic plus potential) energy differences, rather than kinetic pressures, are the primary determinant of nucleonic flow, and which, therefore, predict in addition to the proton flow out of the Fe-like nucleus also a significant neutron flow into the Fe-like nucleus.

These results are summarized here in a series of figures. We note that only the earliest time behavior of the present model is considered to be relevant to the dinuclear process. (At later times indicated by arrows on the figure abscissas, reflections alter the flow in a manner not extrapolable to the realistic three-dimensional case.) During these early times both N and σ^2 exhibit generally a linear change in time, characterized by the slopes $d=N$ and $s=\dot{\sigma}^2$, respectively. Figure 1 depicts the two-well model potential, $V(x)$, and the initial conditions for the time-dependent Schrödinger equation

$$\{ (T_1 + V_1) \Psi(x, t) = i \hbar \dot{\Psi}(x, t) .$$

i

DOUBLE WELL PROBLEM
and INITIAL CONDITIONS

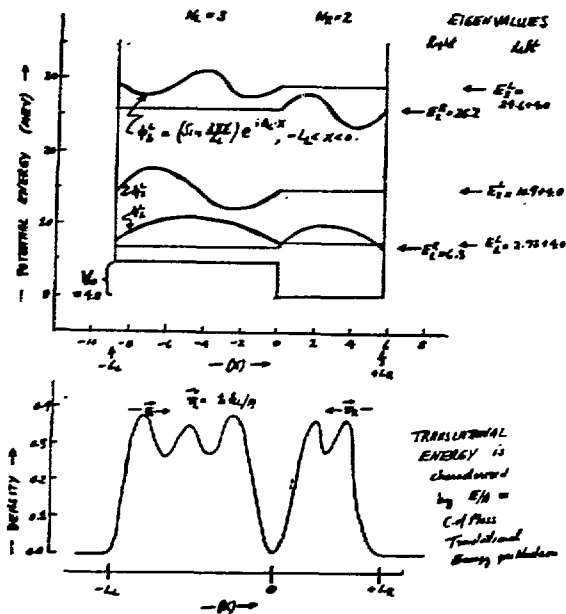


(Fig. 1)

The parameters L_R , L_L and V_0 fix the potential, and the values N_R , N_L , and E/A define the two-ground state initial condition.

Figure 2 shows the time dependence of $\sigma^2(t)$ for cases with $N_R=N_L$, when the size of the nucleidic potential is given by $L_L=CN_L$. This prescription specifies Fermi kinetic energies, K_F , and nuclear densities, N/L , which are independent of N .

From Fig. 2, concludes that the nucleon efflux diminishes with increasing N , leading to smaller slopes, $s = \dot{\sigma}^2/dt$, for larger $N_R=L_L$, and implying a net nucleon drift from smaller N sub-systems into larger N sub-systems (which is verified in calculations not presented here).

Figure 3 shows results for the alternative prescription for the volume,

$$L_R = CN_R [1 + 3/(2N_R) + 1/(2N_R^2)]^{1/3},$$

which fixes the total kinetic pressure to be independent of N , and maintains the average central density of the system, rather than the overall density, at a constant value.⁹⁻¹² One finds here that $\dot{s} = \dot{\sigma}^2$ is essentially independent of N ,

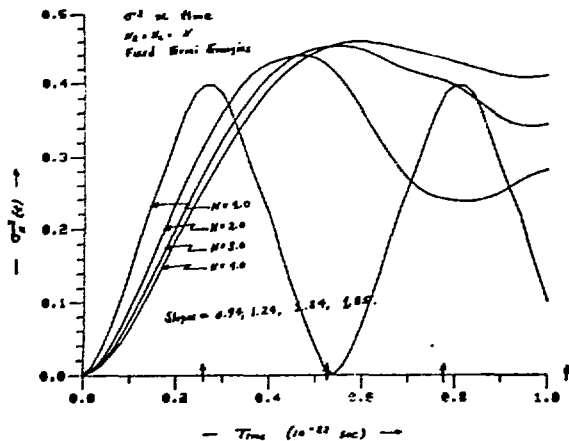


(Fig. 2)

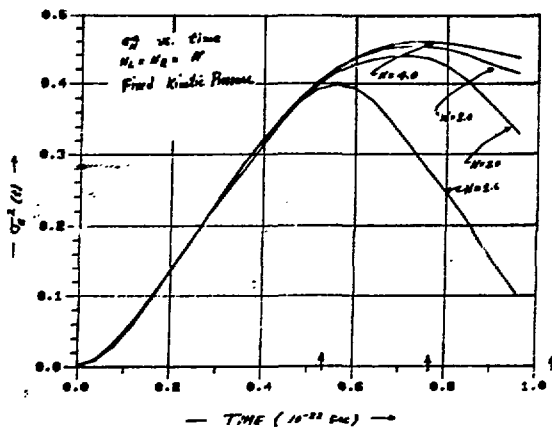


(Fig. 3)

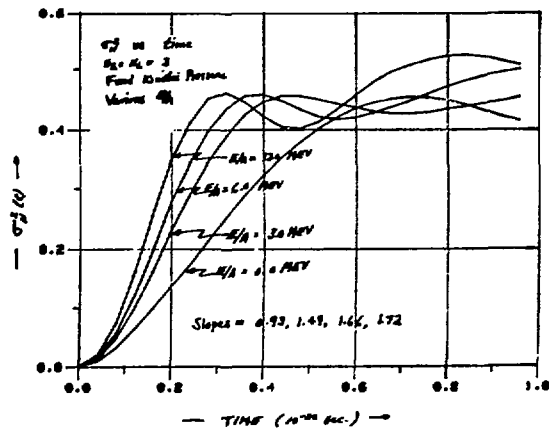
so that a given increase in the translational velocity is somewhat more effective than the same increase in the Fermi velocity in increasing the slope, s .

Figure 5 shows how s depends upon the difference, V_0 , between the potential energy for a nucleon in the left and right wells. One finds that even potential differences of 32 MeV, somewhat larger than the Fermi kinetic energy itself, alter the slope, s , hardly at all whereas a much smaller translational kinetic energy $E/A=3.0$ MeV, had in Fig. 4 a noticeable effect. Also, we have found that the drift rate, $d=\dot{N}_R$, induced by such a 32 MeV per nucleon potential difference is

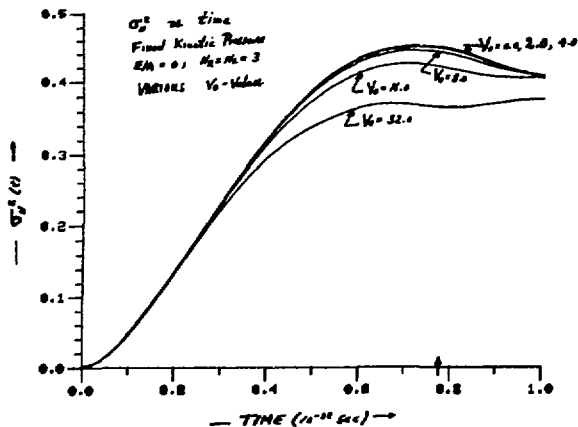
implying that no drift should occur between such systems of different N (when $V_0=0$ and $E/A=0$). (This implication was also verified.)

Figure 4 exhibits the rather strong dependence of $\dot{\sigma}^2$ on the translational energy, E/A . In terms of the (center-of-mass) translational velocity of each nucleon, one finds that the slope, $s=\dot{\sigma}^2$ increases linearly, for small E/A , with the translational velocity, u ; i.e., roughly as

$$s = C[(v_F/\sqrt{3}) + u]$$

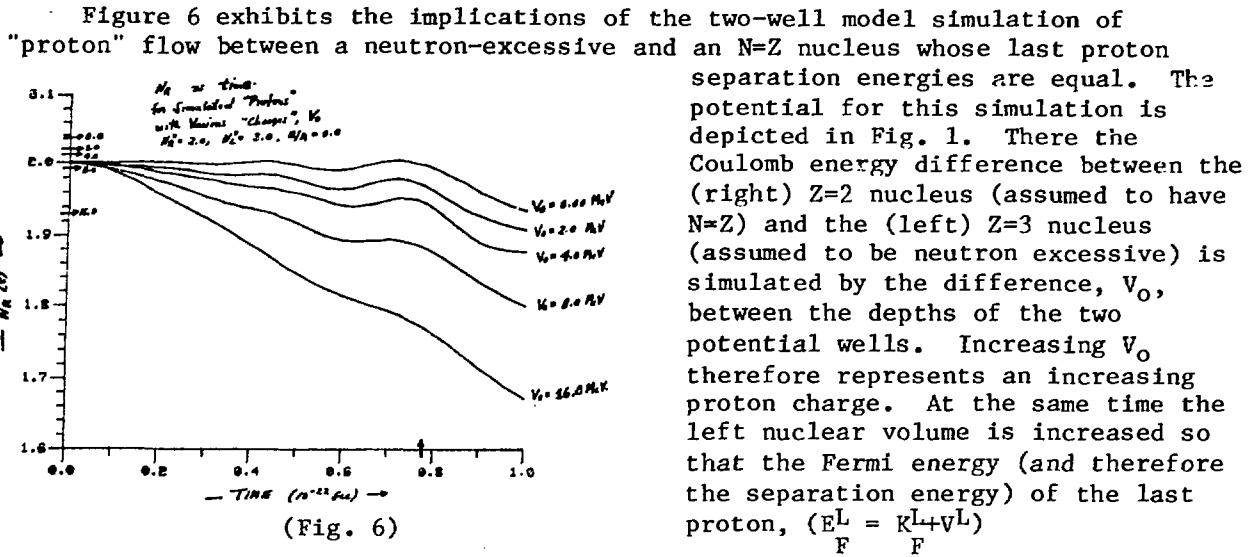


(Fig. 4)



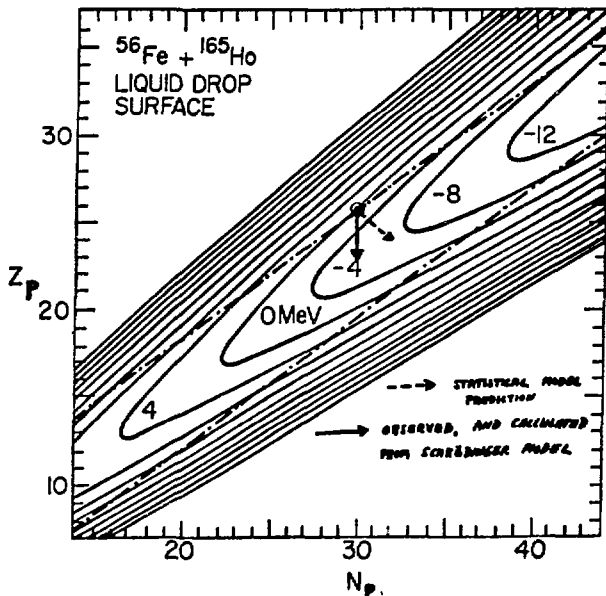
(Fig. 5)

of roughly the same magnitude as the rate induced by the kinetic pressure difference corresponding to an increase in the average kinetic energy of only 8 MeV per nucleon. One concludes that a given increase in the kinetic energy per nucleon is much more influential on the nucleon drift rate than the same increase in the potential energy per nucleon. It follows that any description in which the drift is proportional to a driving force which depends only on the sum of kinetic and potential energies must contradict the present model.



has precisely the same value as it had for $V_0=0$. In this way we model the interfacing protons of a neutron excessive and an N=Z nucleus whose last protons have nearly the same separation energy. The ground state equilibrium values of N_R for the various V_0 -values are indicated as arrows on the ordinate scale in Fig. 6. Since the proton separation energies are nearly identical, the statistical "driving force" is small, and current statistical theories predict that the proton drift here must be small. In fact, the driving force in Fig. 3 favors a slight flow into the right.

However, the Schrödinger model shows (in Fig. 6) a net drift of "protons" into the (left) neutron excessive nucleus: This flow results from the greater kinetic



pressure, P_K , of the protons in the (right) N=Z nucleus and occurs here in spite of the fact the energetic "driving force", $\partial\langle E\rangle/\partial N_R$, is oppositely directed. Since this condition is sufficient to guarantee a rightward drift in the statistical descriptions³⁻⁵ of this process, the present calculations flatly contradict these models. Of these two contradictory predictions, we note that the present Schrödinger model yields an N-Z drift similar to that observed,^{7,8} whereas the statistical descriptions (as shown in Fig. 7) fail to do so.⁶

In summary, the time dependence of the macroscopic variables N and σ^2 as calculated in the present exact Schrödinger model exhibits a greater sensitivity to the kinetic energy differences between nucleons on the two sides of the dinucleus than to their potential energy differences.

Since the "driving forces" of current statistical formulations depend only upon sums of such kinetic and potential energies (via the chemical potential⁴, λ , or the overall dinuclear Binding Energy^{3,5} they would seem to omit a physical distinction which the Schrodinger model shows to be of substantial practical importance.

[Support of the U. S. Department of Energy and the University of Maryland Computer Science Center is gratefully acknowledged.]

REFERENCES

1. C. Yannouleas first applied such a model to the heavy ion problem in unpublished notes of May, 1977.
2. H. Feldmeier et al. have considered also the role of two-body interactions in such a model: Nucl. Phys. A394 (1983) 334.
3. J. Griffin, et al., Nucl. Phys. A369 (1981) 181; A382 (1982) 159; and U. of Maryland PP #84-105.
4. J. Randrup et al., Nucl. Phys. A307 (1978) 319; A327 (1979) 490; A383 (1982) 468; Phys. Lett. 98B (1981) 355.
5. D. Schüll, et al., Phys. Lett. 102B (1981) 116.
6. L. Moretto has discussed these drifts from a different viewpoint: Z. f. Phys. A310 (1983) 334; and Proc. XXI Int. Winter Meeting on Nuclear Physics, Bormio, Italy, p. 396, ed. I. Iori (U. of Milano and INFN, Milano, 1983).
7. A. C. Mignerey, H. Breuer, et al., Phys. Rev. Lett. 45 (1980) 509; 43 (1979) 191; and U. of Maryland PP #83-135.
8. H. Breuer, et al., Nucl. Instr. and Methods 204 (1983) 419; Phys. Rev. C28 (1983) 1080.
9. W. Swiatecki, E. Hilf and C. F. Tsang have considered the related problem of evaluating the surface part of the energy of the static Hill-Wheeler box. See Refs. 10, 11, 12.
10. W. Swiatecki, Proc. Phys. Soc. (London) A64 (1951) 226.
11. E. Hilf, et al., Phys. Lett. 23 (1966) 711; 21 (1966) 564.
12. C. F. Tsang, Ph.D. thesis, U. of California, Berkeley, 1969; UCRL Report #18899.

HOW IS THE EXCITATION ENERGY DIVIDED
IN PARTIALLY DAMPED COLLISIONS?

R. Vandenbosch, A. Lazzarini, D. Leach, D.-K. Lock,

A. Ray and A. Seamster

Nuclear Physics Laboratory, University of Washington, Seattle, WA 98195

We now have a fairly complete understanding of most features of the collisions between heavy ions at energies of 10 MeV/A or less. One-body dissipation, which arises from the real and virtual exchange of nucleons between the two collision partners, is able to account for the competition between fusion and two-body channels, and for the latter channels to describe the dependence of energy dissipation on angle, the variances of the charge and mass distributions, and the magnitude and alignment of the transferred angular momentum. One of the principal remaining open questions concerning quasi- and deeply-inelastic collisions is the division of the excitation energy between the two fragments. The nucleon exchange mechanism leads one to expect rather similar fluxes of exchanged particles in each direction and thus similar excitation energies for each fragment. This should be particularly true for the partially damped events. For more fully damped events the contact time may be sufficiently long that thermal equilibrium can be attained, in which case the excitation energy is expected to divide according to the mass ratio.

These two limiting possibilities lead to a distinguishable difference only when there is a significant mass asymmetry in the exit channel. There are not many experimental observations¹⁻³⁾ which bear on this issue, but those that exist tend to indicate that thermalization is reached more rapidly than might have been expected. The temperatures characterizing the neutron spectra from light and heavy fragments from the $^{56}\text{Fe}+^{165}\text{Ho}$ reaction are the same within experimental error for total kinetic energy losses of the order of 50 to 100 MeV.¹⁾ The uncertainties are sufficiently large that the necessity to square the temperatures to obtain the excitation energy leads to the possibility that the excitation energy could have been divided

considerably more equally than according to the mass ratio. In addition to the temperatures of the evaporation spectra, the ratio of the neutron multiplicities for the light and heavy fragments has been used to deduce information about the division of excitation energy between the two fragments. Studies¹⁻³⁾ of the $^{63}\text{Cu}+^{197}\text{Au}$, $^{86}\text{Kr}+^{166}\text{Er}$ and $^{56}\text{Fe}+^{165}\text{Ho}$ systems have been interpreted as supporting thermal equilibrium for all energy losses studied, including energy losses as low as 30 MeV in the latter system. Awes et al.⁴⁾ however have recently pointed out that the interpretation of both the neutron multiplicity results for the $^{56}\text{Fe}+^{165}\text{Ho}$ system and more recent⁵⁾ charge and mass data for the same system is sensitive to the assumed primary N and Z distributions due to evaporation effects. They find that a consistent account of both sets of data implies more nearly equal excitation energy sharing for total kinetic energy losses of ~50 MeV.

It is clear that an independent measurement by a technique not as sensitive to evaporation effects is desirable to clarify this important question of whether there is non-equilibrium energy partition in such collisions. We have made such a measurement for the very mass asymmetric entrance channel system $^{56}\text{Fe}+^{238}\text{U}$. We determine the total excitation energy from the kinetic energy of the projectile-like fragment and the excitation energy appearing in the heavy fragment from the fission mass asymmetry of the coincident sequential fission fragments from the target-like partner. The relative yields of symmetric and asymmetric fission fragments is a very sensitive function of energy for excitation energies below about 60 MeV.

The experiment was performed using a 480-MeV beam of ^{56}Fe produced by the Lawrence Berkeley Laboratory SuperHILAC. The beam was incident on a self-supporting 0.8 mg/cm^2 ^{238}U target, and the projectile-like fragments were detected in a ΔE -E detector telescope located at 45° where there is a good yield over a broad range of inelasticities. The mass distribution of the fission fragments were determined by their time-of-flight. The mass resolution was very good, with peak-to-valley ratios of over 20 observed at the smallest inelasticities. Samples of the mass yield distributions at several values of the total kinetic energy loss are shown in Fig. 1. These

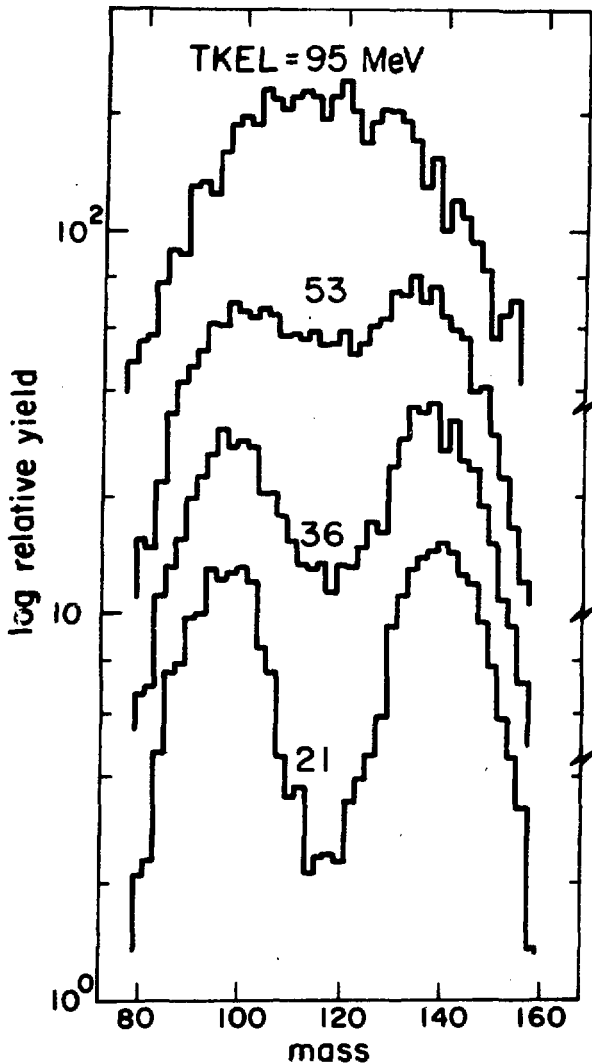


Fig. 1 Samples of fission fragment mass distributions (lab system) at several different total kinetic energy losses.

are the laboratory-system distributions which exhibit a kinematic enhancement of the heavy-mass fragments. This effect is corrected for during the final analysis.

The Z distribution of the projectile-like fragments broaden and drift to lower values as the energy loss increases, as has also been previously observed by Breuer et al.⁵⁾ Some examples of the Z-distributions of the

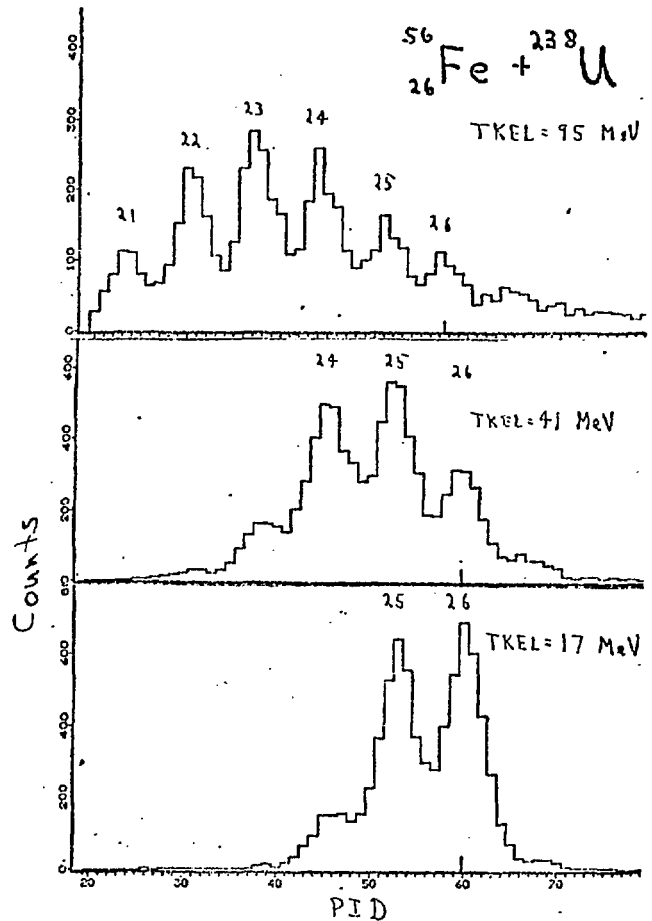


Fig. 2 Examples of Z distributions at several different total kinetic energy losses.

projectile like fragment in coincidence with fission fragments at different total kinetic energy losses are shown in Fig. 2. We have restricted our analysis to those events with $Z=24, 25,$ and $26,$ corresponding to Pu, Np, and U complementary fragments. These are fissioning systems for which we have good calibration data on the dependence of the mass asymmetry on excitation energy.⁶⁾

Our results for the ratio of the excitation energy in the heavy fragment divided by the excitation energy in the light fragment are plotted as a function of total kinetic energy loss in Fig. 3. The total excitation energy is taken as 3 MeV larger than the total kinetic energy loss, reflecting the average Q_{gg} value of the dominant transfer channels. The upper horizontal line is the expectation for equal temperatures (excitation energy partitioned according to mass ratio) and the lower horizontal line is the expectation for equal division of excitation energies. Our results are intermediate between these two expectations but closer to the latter. It is clear that the present results preclude a division based on thermal equilibrium. Our results are in fact in good agreement with a dynamical transport model calculation of Randrup.⁷⁾ He has calculated the time evolution of temperature equilibration for several different partial waves (and hence different energy losses) and found that equilibration is not achieved until less peripheral collisions with energy losses over 100 MeV are considered. A small contribution from the deformation energies of the fragments is also included. The driving term for equilibration in this calculation is the temperature imbalance resulting from the initial equal division of excitation energy between the two fragments. It is seen that this driving force is insufficient to equilibrate the temperatures unless the fragments are in intimate contact for an appreciable length of time.

It should be possible to extend our analysis to larger total kinetic energy losses if the calibration data on the dependence of the shape of the mass yield distribution on excitation energy were available for higher energies. I would appreciate being informed about relevant mass yield measurements, particularly for 50-150 MeV alpha particles on Th, U, Np, or Pu targets.

This work was supported in part by the U.S. Department of Energy.

References

1. D. Hilscher et al., Phys. Rev. C20, 576 (1979).
2. B. Tamain et al., Nucl. Phys. A330, 253 (1979).
3. Y. Eyal et al., Phys. Rev. C21, 1377 (1980).
4. T. Awes et al., Phys. Rev. Lett. 52 251 (1984).
5. H. Breuer et al., Phys. Rev. C28, 1080 (1983).
6. See e.g., D. Burnett, UCRL 11006 (unpublished); Z. Frankel et al., Phys. Rev. C12, 1809 (1975); R.L. Ferguson et al., Phys. Rev. C7, 2510 (1973); F. Plasil and H.W. Schmidt, Phys. Rev. C5, 528 (1972); M. Seki, J. Phys. Soc. Japan 20, 190 (1965); H.C. Britt and S.L. Whetstone, Jr. Phys. Rev. 133, B604 (1964); J. Unik et al., Phys. Rev. 134, 90 (1964); R. Vandenbosch et al., Phys. Rev. 111, 1358 (1958); L.J. Colby et al., Phys. Rev. 121, 1415 (1961).
7. J. Randrup, Nucl. Phys. A383, 468 (1982).

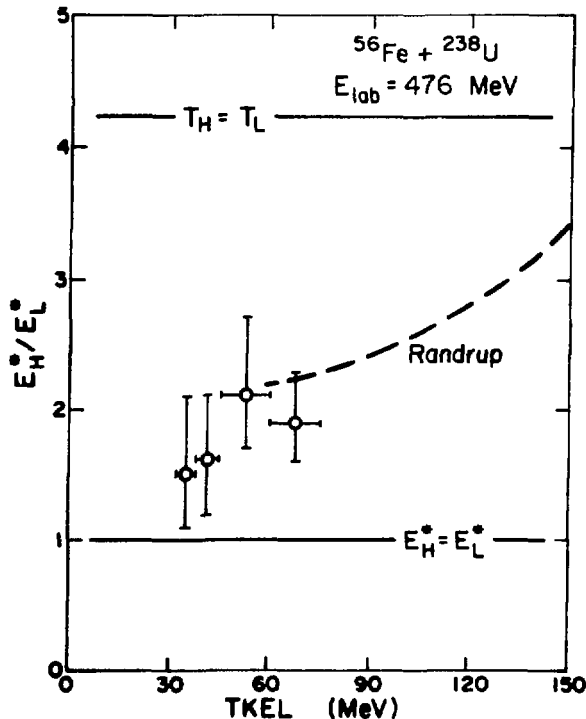


Fig. 3 Dependence of the ratio of the excitation energy of the heavy fragment to that of the light fragment as a function of the total excitation energy. The values expected in the limits of equal division of the excitation energy and of division according to the mass ratio (equal temperatures) are shown by horizontal lines. Also shown are the results of a transport model calculation by Randrup.

EXCITATION ENERGY SHARING IN QUASIELASTIC REACTIONS BETWEEN ^{86}Kr AND $^{208}\text{Pb}^*$

H. Sohlbach, H. Freiesleben

Institut für Experimentalphysik, Ruhr-Universität Bochum †

W. F. W. Schneider, D. Schüll

GSI, Darmstadt

P. Braun-Munzinger

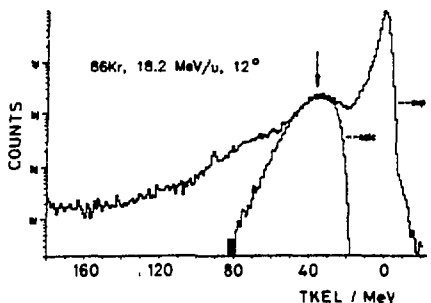
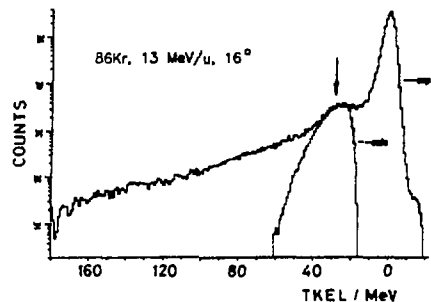
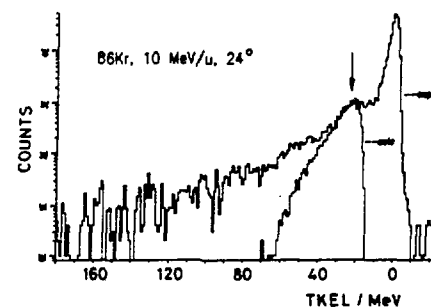
SUNY, Stony Brook

B. Kohlmeier, M. Marinescu, F. Pühlhofer

Fachbereich Physik, Universität Marburg

Experimentally observed neutron multiplicities in strongly damped collisions are clearly indicating, that the emerging fragments have reached the limit of thermal equilibrium corresponding to constant temperature of the combined system [1]. The

excitation energy is then shared among the fragments according to their masses. On the contrary, for quasielastic reactions an equal division of excitation energy is expected on the basis of single-particle state-densities near the Fermi energy. Recent experimental findings seem to support this expectation [2].



In this contribution we present our results of a detailed analysis of energy spectra of Kr-like fragments formed in few-nucleon-transfer reactions on ^{208}Pb at various bombarding energies (10, 13, 18.2 MeV/u). They have been obtained utilizing the GSI magnetic spectrometer which allows for unambiguous identification of emerging fragments in mass and atomic number. Sample spectra of ^{86}Kr measured slightly forward of grazing are displayed in fig. 1. With rising bombarding energy the elastic line exhibits an increasing skewness, indicating the enhancement of inelastic excitations, which are not resolved with the present energy resolution of $\approx 3\%$. These energy spectra are definitely free of target impurities and slit scattering. The tail of each spectrum and in particular the bump hence are bearing physical information. The bump position (indicated by arrows at $Q = -23, -28$ and -36 MeV) moves with increasing bombarding energy toward larger energy losses and is consistent with a picture where it results from neutron emission from particle unstable ^{87}Kr nuclei formed in the neutron pick-up reaction $^{208}\text{Pb}({}^{86}\text{Kr}, {}^{87}\text{Kr})^{207}\text{Pb}$ [3]. The calculated curves included represent the results of a Monte-Carlo simulation of this two step process (see below).

Fig. 1 Energy spectra of ^{86}Kr at three bombarding energies

* presented by H. Freiesleben

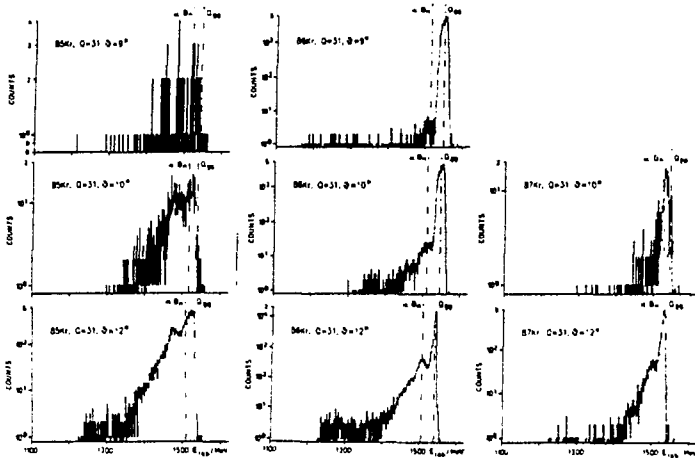


Fig. 2 Energy spectra of three Kr isotopes at various scattering angles (different vertical scales!)

less likely to be excited to states above the n -threshold than ^{87}Kr . At $\Theta_L = 9^\circ$ no ^{87}Kr is observed while ^{85}Kr is still present in the particle stable region. There is also a small bump in the ^{86}Kr spectrum indicating again that all of the primarily produced ^{87}Kr has undergone neutron emission. This behaviour suggests a reaction-channel dependent sharing of excitation energy.

Extensive Monte-Carlo simulations have been performed for the one- and two-neutron decay of Kr spectra taken at $\Theta_L = 12^\circ$. The starting point is the excitation energy spectra of the primary nuclides which have been guessed. We assume those parts of the observed energy spectra being free from sequential decay to resemble primary excitation energy spectra. The total excitation energy

$$E^*_{\text{tot}} = E^*(A_i) + E^*(A - A_i) = \text{TKEL} + Q_{\text{gg}} \quad (1)$$

of the system is then calculated by applying the relation

$$E^*(A_i)/E^*(A - A_i) = A_i/(A - A_i) \pm \exp(-E^*(A_i)/C_i) \quad (2)$$

This dependence reflects thermalization for large total excitation energies. The sign in front of the exponential determines the "direction" and the parameter C_i the "speed" of approach towards equilibrium. Combining eqs. (1) and (2) the primary two-body TKEL is obtained. The portion of the assumed primary excitation energy spectrum above the particle threshold in A_i is subjected to sequential decay (only one- and two-neutron emission has been considered). The kinematics of the neutron decay is calculated taking into account the primary TKEL, a Maxwell-distribution for neutron energies and the geometry of the experimental set up.

The shape and the width of the resulting sequential decay bumps in the secondary energy spectra of the fragments with $(A_i - 1)$ and $(A_i - 2)$ are determined by the shape of the guessed primary excitation energy spectrum of A_i above its neutron threshold. However, the position of the bumps are only controlled by C_i and the neutron threshold in A_i and $(A_i - 1)$ for one- and two-neutron emission, respectively. Hence, C_i is considered to be a free parameter which has been adjusted in order to reproduce the position of the bump in $(A_i - 1)$ thereby establishing

In fig. 2 energy spectra for three Kr isotopes are shown at three lab angles. At $\Theta_L = 10^\circ$ two regions can be clearly distinguished in all spectra, one representing the primary reaction around the ground-state-mass Q -value, Q_{gg} , which reflects the shape of the spectra undisturbed by evaporation, the other at more negative Q -values resulting from sequential decay. At $\Theta_L = 12^\circ$ ($\Theta_{\text{gr}} = 12.5^\circ$) this sequential bump in ^{86}Kr represents nearly the same cross section as the primary part of the ^{87}Kr spectrum, indicating that a large fraction of primary ^{87}Kr was excited above the particle threshold. The intensity of the sequential decay bump in ^{85}Kr is rather small as compared to that of primary ^{86}Kr . Hence ^{86}Kr is

the excitation energy sharing via eq. (2). We note in passing that evaporation calculations have shown charged particle emission to be negligible.

Fig. 3 shows the result for Kr isotopes. From the shape of the primary spectra (right hand side) it is obvious, that C_i differs for all channels and, hence various bump widths and cross sections result. The position and width of the bump in all secondary spectra (left hand side) are nicely reproduced; no further adjustment for the cross section was undertaken. In particular, the ^{86}Kr spectrum exhibits no high excitation energy structures, which are not accounted for by sequential decay. For $\text{TKEL} > 100$ to 120 MeV three or more neutron decay may contribute to the spectra. With the same procedure the bump in the secondary energy spectra of some Rb and Br isotopes are also accounted for in position and width.

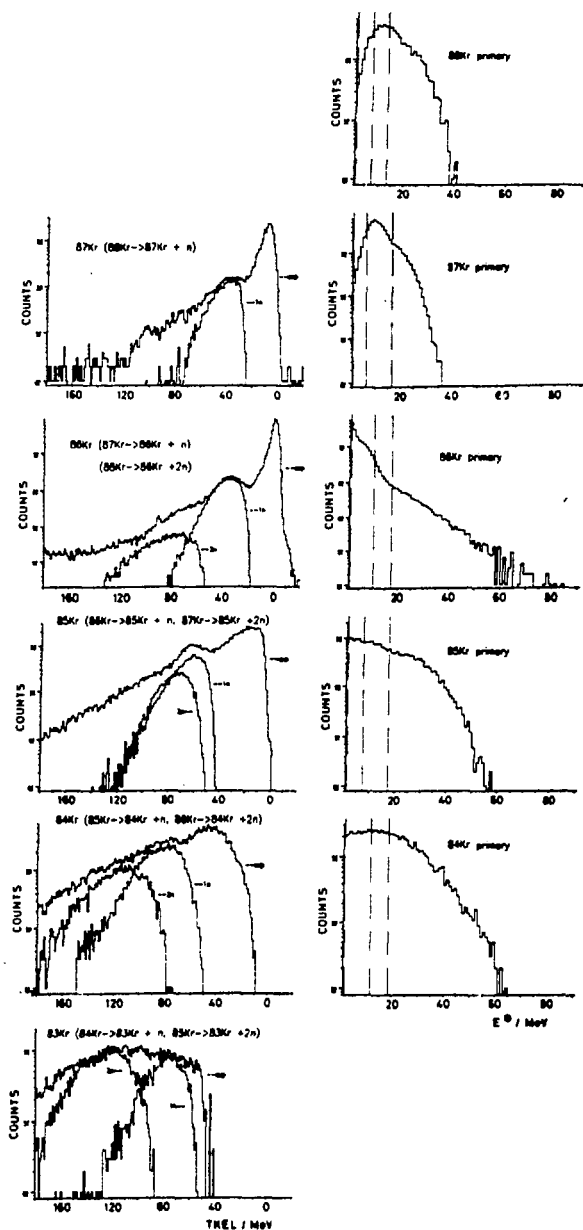


Fig. 3 Primary Kr spectra as function of Kr excitation energy (right) and resulting sequential decay contribution (1n, 2n) in comparison with experimental TKEL spectra (left)

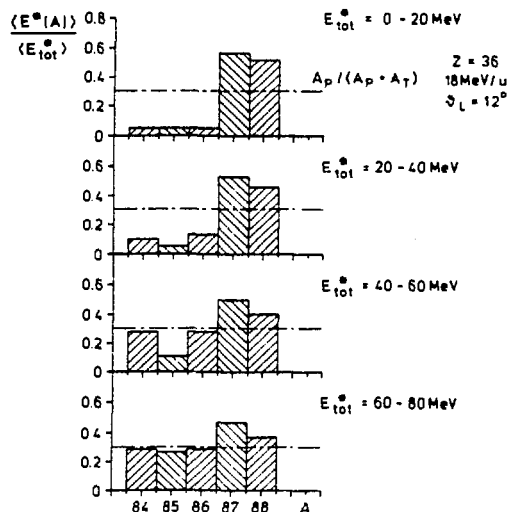


Fig. 4 Percentage of total excitation energy (E_{tot}^*) allocated to various Kr isotopes for consecutive bins in E_{tot}^*

The quantitative results are displayed in fig. 4 for the energy allocated to Kr isotopes for various cuts in the total excitation energy. A tendency seems to emerge: for projectile-stripping reactions the acceptor nucleus receives the lar-

ger fraction of excitation energy while the donator gets the smaller portion. The same holds - to a lesser extent - for pick-up reactions by the projectile, with an energy sharing clearly off the mass ratio and closer to an equal distribution. With increasing values of E^*_{tot} these characteristic differences vanish and the system approaches the equal temperature limit.

We would like to add a few words of caution. The method used to obtain the values presented in fig. 4 relies on the relation between excitation energy in the light fragment and the total excitation energy as implied by eq. (2). It is presently not clear how sensitive the results are on the particular choice of this function as well as on variances of the excitation-energy division, hence "errors" in fig. 4 cannot be quoted. However, the reaction channel dependent sharing of excitation energy is already apparent from fig.2 and will certainly persist if an other procedure would be used to analyse and interpret secondary energy spectra of fragments from quasielastic heavy ion reactions.

† supported by Bundesministerium für Forschung und Technologie, Bonn, Germany

- [1] Y. Eyal et al., Phys. Rev. Lett. 41(1978)625
D. Hilscher et al., Phys. Rev. C20(1979)576
- [2] T. C. Awes et al., Phys. Rev. Lett. 52(1984)251
R. Vandenbosch, these proceedings
- [3] P. Braun-Munzinger et al., Int. Conf. on Heavy Ion Physics,
Stony Brook, 1983

QUASIELASTIC STRUCTURE IN THE REACTION $^{56}\text{Fe} + ^{56}\text{Fe}$ AT 14.6 MeV/NUCLEON

A. C. Mignerey, C. Merouane, S. Bradley, D. Benton, H. Breuer and J. D. Silk
University of Maryland, College Park, MD 20742

K. Kwiatkowski and V. E. Viola, Jr.
Indiana University, Bloomington, IN 47405

T. C. Awes, F. E. Obenshain and S. Pontoppidan
Oak Ridge National Laboratory, Oak Ridge, TN 37830

The detailed study of the quasielastic or partially damped region of the energy spectra of isotopically separated products from heavy-ion-induced reactions began several years ago with the study of the symmetric systems $^{40}\text{Ca}+^{40}\text{Ca}$ (1) and $^{56}\text{Fe}+^{56}\text{Fe}$ (2). While projectile-like products from the calcium reaction at 10 MeV/u showed a series of peaks at excitation energies which appeared invariant with angle and product nuclide, the results from the iron reaction at 8.3 MeV/u were less conclusive. In this reaction only the ^{57}Co product nuclide showed clear indications of structure, corresponding to excitation energies E^* of ~30, 45 and 60 MeV. Evaporation calculations show that the $E^*=30$ MeV peak is consistent with the sequential decay of the ^{58}Co primary product, however, the energies and widths of the higher excitation energy structures are inconsistent with this interpretation. Figure 1 shows the laboratory kinetic energy spectrum for ^{57}Co measured at $\theta_{\text{lab}}=8^\circ$ and the corresponding evaporation calculation. The appropriate emission channels which feed the spectrum are indicated by the dashed and dotted curves.

Indications that the structure is enhanced for higher bombarding energies led to the study of the $^{56}\text{Fe}+^{56}\text{Fe}$ reaction at the Oak Ridge HHIRF using the 14.6 MeV/u ^{56}Fe beam. As in the previous studies, emphasis was placed on obtaining unit mass and charge resolution for all projectile-like products. A time-of-flight system for mass identification employed channel-plate-fast-timing devices as the start and stop detectors. These were separated by a 1.5 m flight path and backed by a large four element ΔE -E ion chamber (Snell chamber) for Z identification and total energy measurement. The resulting charge and mass resolutions were <0.4 charge units and ~ 0.8 mass units, respectively. The use of an internal Faraday cup allowed measurements of projectile-like fragments down to laboratory angles of 3° . The majority of the data were taken slightly forward of the grazing angle (estimated to be between $\theta_{\text{lab}}=6^\circ$ and 7°) at $\theta_{\text{lab}}=5^\circ$; however, some data were also collected at $\theta_{\text{lab}}=3^\circ$ and 7° . Slit scattering from channel-plate grid wires precluded clean identification of individual iron isotopes, however, the excellent charge resolution made possible the separation of this component from Z=25 and 27 products.

The total kinetic energy spectra of the cobalt products detected at 3° , 5° and 7° are shown in Fig. 2. Several structures can be tentatively identified. The most striking feature is a strong peak corresponding to a total kinetic energy loss $E_{\text{loss}}=16-18$ MeV (excitation energy E^* of 12-14 MeV). While very prominent in the 5° and 7° spectra, this peak is not seen at 3° and may be interpreted as a proton transfer channel with an angular distribution characteristic of large angular momentum transfer (see Fig. 3). A second peak can clearly be identified at $E_{\text{loss}}\sim 50$ MeV for $\theta_{\text{lab}}=5^\circ$; however, a similar structure appears at $E_{\text{loss}}\sim 45$ MeV for 7° and there are indications of something at

$E_{\text{loss}} \sim 55$ MeV for the 3° data. Evaporation calculations show that this is the region of feeding from the first sequential neutron evaporation of ^{58}Co .

Several other features are discernable at higher excitation energies which are difficult to understand in the framework of particle evaporation. The 7° spectrum shows structure at $E_{\text{loss}} \sim 65$ MeV and 95 MeV. Thus, this angle has an energy distribution characterized by a series of peaks at excitation energies of 14, 40, 60 and 90 MeV. Aside from the two peaks at $E^* = 12$ MeV and 45 MeV, the 5° spectrum also has a broad shoulder at $E^* \sim 90$ MeV. Due to limited statistics the situation at 3° is less defined. There appear to be peaks at $E^* = 50, 65$ and 95 MeV.

The angular distributions of the four peaks defined by the 7° spectrum are plotted in Fig. 3 for 20 MeV bins in E_{loss} . The lowest excitation energy bin, encompassing the $E^* = 15$ MeV structure, has an angular distribution which appears to be bell-shaped while the other excitation energy peaks become progressively more forward peaked with increasing excitation energy. This behavior is consistent with that observed for the Ar+Pb system at 11 MeV/u (3) where the discrete structure observed is being attributed to multiphonon direct excitations of the ^{208}Pb target. In contrast, the angular distributions obtained for the neutron transfer channel in the system Kr+Pb at 13 MeV/u (4) become broader and less forward peaked with increasing excitation energy. In this reaction no structure was observed at excitation energies greater than those corresponding to the first sequential evaporation peak.

While the results of the $Z=27$ energy spectra are encouraging, separation of the 5° data into spectra for individual cobalt isotopes does not greatly enhance the structure. Since the majority of the $Z=27$ cross section is due to ^{57}Co , the spectrum of this nuclide shown in Fig. 4 is not significantly different from the inclusive spectrum. The major difference between the cobalt isotopes is the cross section observed for the first 20 MeV of excitation energy. This region reflects the primary distribution and gives an indication of the dominant direct reaction channels. There is very little ^{56}Co produced in the initial interaction. Due to the relatively poor mass resolution, what cross section is observed at low excitation energy is probably dominated by feedthrough from the strong ^{57}Co peak. A purely statistical exchange of nucleons predicts a much larger initial ^{56}Co cross section (see Fig. 5).

The statistical evaporation of light particles from the primary reaction products significantly modifies the observed energy spectra. Using the assumption of smoothly varying Gaussian mass and charge distributions, the results shown in Fig. 5 were obtained for the secondary spectra of ^{56}Co and ^{57}Co . The assumed overall primary distribution was normalized using the total experimentally measured energy distribution including an average energy correction for particle evaporation. The highest kinetic energy peak can only be the result of the γ decay of the direct production of the primary product. However, the energy of the primary peak appears to be shifted by 6-8 MeV. This corresponds to an effective Q -value higher than Q_{gg} by that amount. A possible explanation for this may be excitation energy which results in γ decay rather than particle emission. In the ^{57}Co case this must correlate with the direct transfer of the proton to form the ^{57}Co .

As seen in the 8.3 MeV/u $^{56}\text{Fe} + ^{56}\text{Fe}$ reaction, the second peak agrees with the position of the sequential peak from neutron emission of ^{58}Co ; however, the 6-8 MeV shift is also apparent. As in the lower energy reaction, there is

no structure produced by the calculation at excitation energies higher than this peak. Due to the folding of the statistical energy distributions and isotropic particle emission, the widths of the evaporation channels increase with increasing excitation energy. This realization leads to several conclusions. First, any structure observed at $E^* > 40$ MeV must have been extremely well defined in energy in the primary spectrum to maintain an observable peak after particle emission. Alternatively, the peak could have resulted from a discrete target excitation which takes the majority of the excitation energy and leaves the detected projectile-like product cold so that particle evaporation cannot broaden the peak. This mechanism has been suggested as the source of the sharp structure observed at high excitation energies in the systems $^{36}\text{Ar} + ^{208}\text{Pb}$ at 11 MeV/u and $^{20}\text{Ne} + ^{208}\text{Pb}$ at 30 MeV/u (3).

The current generation of intermediate energy heavy-ion accelerators has provided new impetus to the study of nucleon transfer and high excitation energy structure. At bombarding energies > 10 MeV/u relatively few reaction channels contribute to the quasielastic region. Due to kinematics the first sequential evaporation peak is well separated from the primary direct reaction peak allowing a detailed study of the initial nucleon transfer process. Compared to the lower energy studies, the excitation energy range available is much larger, with $E^* = 140$ MeV cleanly separated from the damped reaction products in the 14.6 MeV/u Fe+Fe reaction. There is little underlying exponential background from partially damped reactions and the cross sections for product nuclides near the projectile almost vanish before increasing again at fully damped energies. Only a few systems have been studied in this energy regime with varying results; yet, it is clear that if the key to the structure is to be found it will be through studies at these energies.

References

1. N. Frascaria et al., Z. Phys., A249, 167 (1980).
2. A. C. Mignerey et al., University of Maryland Nuclear Chemistry Progress Report ORO-5172-0019, 1981, p. 20 and to be published.
3. Ph. Chomaz et al., preprint (1984).
4. P. Braun-Munzinger et al., Proc. Intl. Conf. on Heavy Ion Physics, Prospects at Energies Below 20 MeV/u, April 1983.

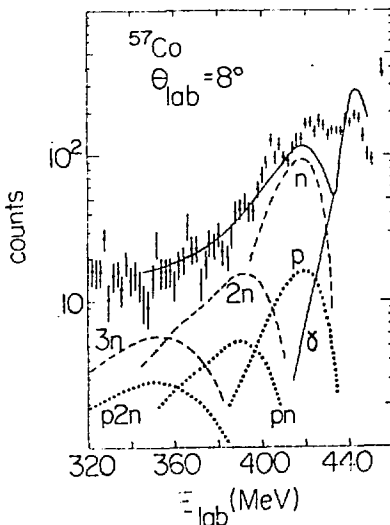


Figure 1 The points show the laboratory kinetic energy spectrum for the ^{57}Co product nuclide detected at $\theta_{\text{lab}} = 8^\circ$ in the reaction of 465 MeV ^{56}Fe with ^{56}Fe . The dashed and dotted curves are contributions to the calculated secondary spectrum (solid curve) from the evaporation channels indicated.

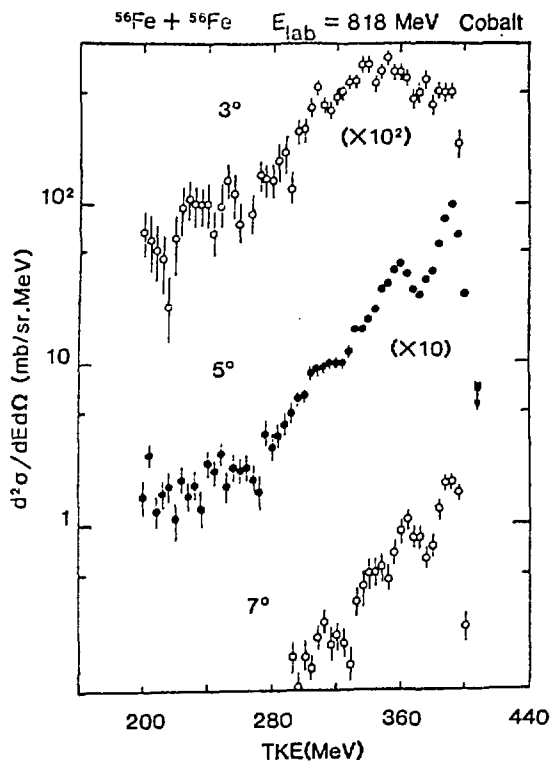


Figure 2 Total kinetic energy spectra of cobalt ($Z=27$) measured at laboratory angles of 3° , 5° , and 7° in the reaction of 818 MeV ^{56}Fe with ^{56}Fe .

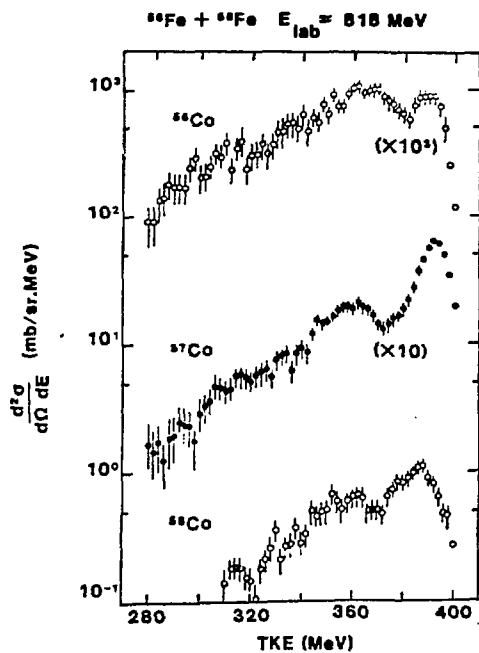


Figure 4 Total kinetic energy spectra of the individual isotopes of cobalt detected at $\theta_{\text{lab}}=5^\circ$.

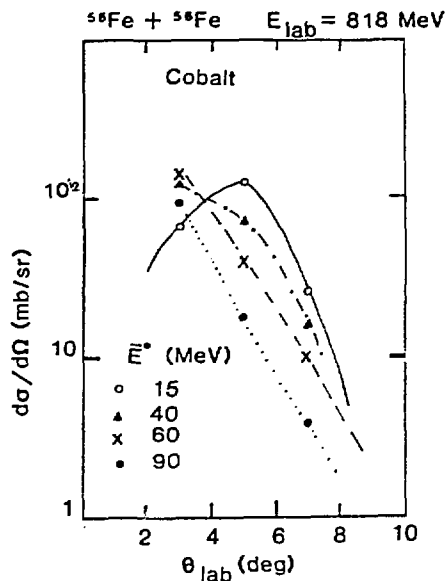


Figure 3 Laboratory angular distributions of the cobalt product for four 20-MeV wide bins in TKE. The average excitation energy corresponding to each bin is indicated.

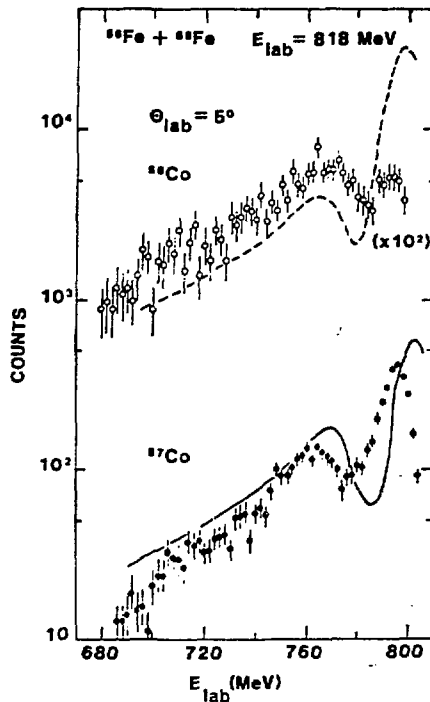


Figure 5 Evaporation calculations (dashed and solid curves) for the ^{56}Co and ^{57}Co compared to the experimental data for $\theta_{\text{lab}}=5^\circ$.

RELAXATION TIMES FOR ANGULAR MOMENTUM IN DAMPED NUCLEAR REACTIONS*

T. Døssing[†] and J. Randrup

Nuclear Science Division, Lawrence Berkeley Laboratory, Berkeley, CA 94720

We discuss in this contribution the evolution of the angular momentum distribution in damped nuclear reactions within the framework of the nucleon exchange transport model.¹⁾ A preliminary treatment of angular momentum transport was given in ref. 2), and a recent more comprehensive study^{3,4)} considers both the angular momentum transport during a reaction and the confrontation with data on sequential decay. Here we present part of this recent development with emphasis on the qualitative features.

The dynamical variables focussed on are the spins of the two nuclei, \vec{S}^A and \vec{S}^B . It is often advantageous to change variables to the total and relative spins of the nuclei, defined as $\vec{S}^+ = \vec{S}^A + \vec{S}^B$ and $\vec{S}^- = \mathcal{I}_- (\vec{S}^A/\mathcal{I}_A - \vec{S}^B/\mathcal{I}_B)$, with associated moments of inertia $\mathcal{I}_+ = \mathcal{I}_A + \mathcal{I}_B$ and $\mathcal{I}_- = \mathcal{I}_A \mathcal{I}_B / (\mathcal{I}_A + \mathcal{I}_B)$ defined in terms of the moments of inertia \mathcal{I}_A and \mathcal{I}_B of the individual nuclei. The types of dinuclear motion associated with the quantities \vec{S}^+ and \vec{S}^- have been given illustrative names by Nix and Swiatecki⁵⁾ in connection with a study of angular momentum excitations in fissioning nuclei, and the thermal excitation of these modes of motion during damped nuclear reactions has been described by Moretto and Schmitt⁶⁾ and by Schmitt and Pacheco.⁷⁾

Within the nucleon exchange transport model, first-order equations are derived for the time evolution of the mean values and covariances of the spin variables. Special care is used in choosing the coordinate system: it has the z-axis aligned with the dinuclear axis and the y-axis aligned with the orbital angular momentum \vec{L} of the relative nuclear motion. Due to the diffusion of the direction of \vec{L} during the reaction, this "L-aligned" coordinate system fluctuates relative to an externally defined system and therefore extra terms arise in the equations. These terms are essential for obtaining the correct stationary solution to the equations

$$\langle S_y^+ \rangle = \frac{\mathcal{I}_+}{\mathcal{I}_0} J - \tau^* \mathcal{I}_+ \frac{\mathcal{I}_0}{\mathcal{I}_R} \frac{1}{J}, \quad \langle S_y^- \rangle = 0, \quad \overleftrightarrow{\sigma}^{+-} = \overleftrightarrow{0} \quad (1)$$

$$\overleftrightarrow{\sigma}^{++} = \tau^* \mathcal{I}_+ \frac{\mathcal{I}_0}{\mathcal{I}_R} (\hat{x}\hat{x} + \hat{z}\hat{z}) + \tau^* \mathcal{I}_+ \frac{\mathcal{I}_R}{\mathcal{I}_0} \hat{y}\hat{y}, \quad \overleftrightarrow{\sigma}^{--} = \tau^* \mathcal{I}_- \hat{I}$$

Here J is the total angular momentum, τ^* is the effective temperature¹⁾, \mathcal{I}_R is the moment of inertia for the relative motion, and $\mathcal{I}_0 = \mathcal{I}_R + \mathcal{I}_+$ is the total moment of inertia. The mean values of the stationary solution correspond essentially to rigid rotation and the covariances to thermal excitation. A proper coordinate transformation of the distribution (1) results in the statistical model distribution described in refs. 6,7).

The spin equations of motion are first-order in time and essentially linear, so the solution will evolve towards the instantaneous time dependent stationary solution with relaxation times obtained by diagonalizing the coefficient matrix. For a symmetric reaction, the equations for \vec{S}^+ and \vec{S}^- are not coupled which reduces the number of relevant relaxation times.

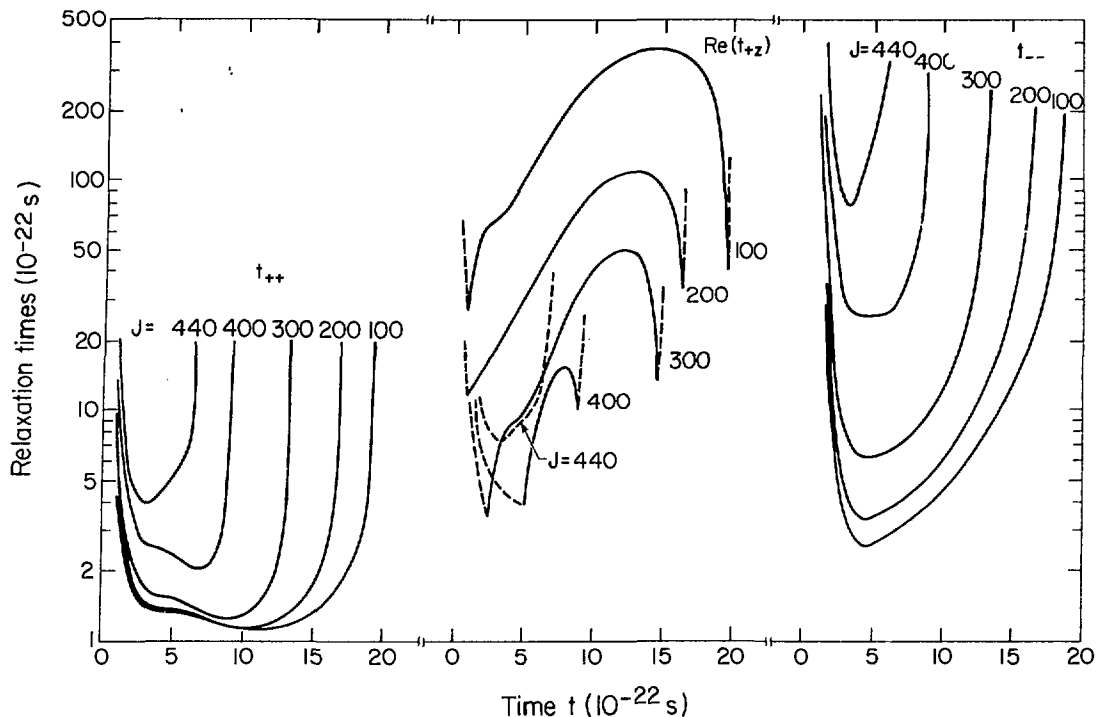


Figure 1 shows the relaxation times for evolution of the covariances as obtained from a complete dynamical calculation which follows the time evolution of the center separation and the neck opening for various values of the total angular momentum for the collision of 1400 MeV ^{165}Ho with ^{165}Ho . Starting initially from zero, the variance tensor for the negative modes, σ^{--} ("bending" and "twisting") develops isotropically with the characteristic time t_{--} , shown in the right hand side of the figure. The characteristic time for the positive mode along the y-axis (one of the "wriggling" modes) is t_{++} , shown in the left hand side of the figure. The equations for the x and z variances are coupled by the tangential motion, and there are essentially two relaxation times involved, t_{++} and t_{+z} , respectively, where t_{+z} is shown in the middle of the figure. The eigenvector for t_{++} is approximately along the x-axis (the other "wriggling" mode) and the eigenvector for t_{+z} is approximately along the z-axis (the "tilting" mode). All relaxation times are infinitely large before the reaction starts, then become finite during the reaction and finally diverge again when the nuclei re separate and the spin distribution is frozen in.

For total angular momenta below 400 \hbar , the wriggling relaxation time remains smaller than $3 \cdot 10^{-22}$ s for a period exceeding $6 \cdot 10^{-22}$ s, so the wriggling variances, σ^{++} and σ^{yy} , will reach the asymptotic value (1) for all but the most grazing collisions. Making a similar comparison between the relaxation times and the duration of the reaction, it is seen that the negative modes will only partially relax and, furthermore, the tilting mode receives little excitation, especially for the most central reactions.

The relative magnitudes of these characteristic time scales can be understood by recalling that the agency for exchange of spin is the quasi-free transfer of nucleons between the two nuclei. The dominant angular momentum exchange is effected by nucleons moving tangentially when transferring. They contribute parallel angular-momentum increments in the two nuclei and thus

preferentially excite the two wriggling modes. The excitation of the negative modes requires a transfer at a distance from the dinuclear axis and is correspondingly weaker. In the present classical treatment the transferred nucleons can not excite directly the tilting mode which is thus only indirectly excited through the Coriolis effect of the relative nuclear motion, which rotates part of the variance built up along the x-direction to the z-direction. These considerations of the basic transfer processes and the relaxation times guide the understanding of results obtained for the variances in complete calculations.

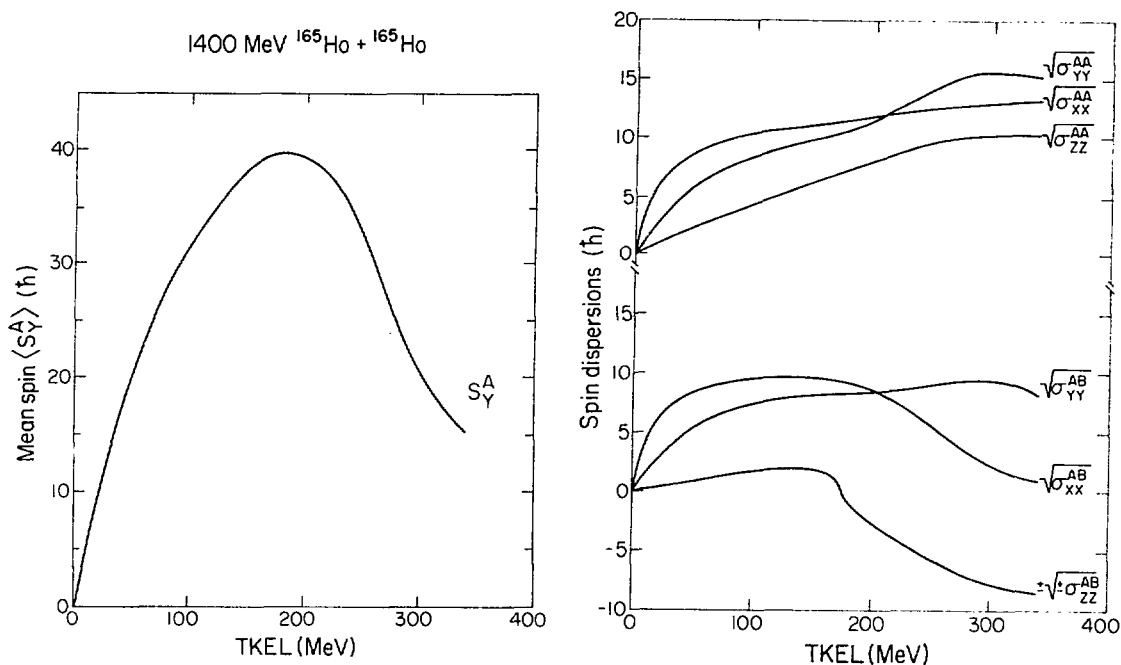


Figure 2 shows the result of the calculation of the spin moments as functions of total kinetic energy loss (TKEL) for the same Ho + Ho reaction. In obtaining the result, the time evolution has been calculated for a grid of values of total angular momentum J , and at the end of each calculation the mean spins and covariances have been transformed from the intrinsic fluctuating coordinate system to the external reference frame. For each J , the average and variance of the total kinetic energy loss and the covariance between energy loss and spins have been calculated, permitting a final integration over J to obtain the moments of the spin distribution gated by TKEL.

The large dispersions and the strong positive correlation between the spins in the two nuclei along the perpendicular directions for small TKEL displayed in fig. 2 are mainly results of the short wriggling relaxation times. The decrease of σ_{XX}^{AB} for large TKEL is due to the decrease of the bending mode relaxation time for small impact parameters. σ_{YY}^{AB} does not display such a decrease because the integration over impact parameter allows the large TKEL to receive contributions from a substantial range of total angular momenta. The dispersion along the z-axis increases more slowly due to the long tilting and twisting relaxation times, t_{+z} and t_{-} , for large J . The negative correlation at large TKEL is due to the relaxation time for twisting being much smaller than for tilting, for central reactions.

The rapid rise of the mean spin vector $\langle S_0 \rangle$ for small TKEL is, loosely speaking, determined by the ratio between tangential and radial friction for near grazing collisions. For these, the window friction is almost exclusively tangential, whereas the wall dissipation associated with the motion of the neck connecting the nuclei effectively produces radial friction. The size of the maximum value of $\langle S_0 \rangle$, reached for medium TKEL, depends upon the cross section (how wide an interval in total angular momentum J contributes to damped reactions), the relaxation time for the mean spin, which is $t_{++}/2$, and how strong a correlation there is between impact parameter and energy loss.

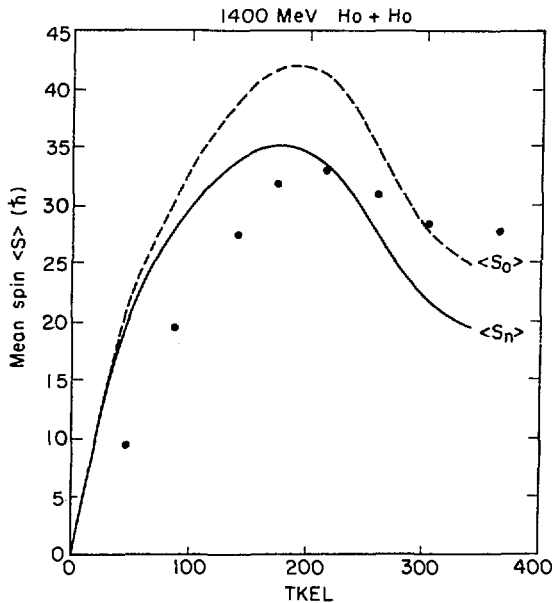


Figure 3 shows the average spin magnitude in one of the nuclei as calculated before (dashed curve) and after (solid curve) neutron evaporation and as extracted from γ -multiplicity data⁸⁾ (dots). The calculated behavior is qualitatively correct but deviates from the data in two respects. The too steep rise for small TKEL presents a significant discrepancy which cannot be remedied by reasonable changes of the few model parameters. The too pronounced decrease for large TKEL is less severe; it probably results from the mean trajectory method employed which prevents dynamical fluctuations from coupling back into the form factors.

From the combined comparison to different kinds of data we conclude in ref. 4) that the spin dispersions are well described by our calculations. The significant spin correlations displayed in fig. 2 can be studied fairly directly though double angular correlation experiments. A separate discussion of this possibility for the case of double fission is given in ref. 4).

Footnotes and References

- * This work was supported by the Director, Office of Energy Research, Division of Nuclear Physics of the Office of High Energy and Nuclear Physics of the U.S. Department of Energy under Contract DE-AC03-76SF00098.
- + Supported by a Niels Bohr Fellowship granted by the Royal Danish Academy of Science.
- 1. J. Randrup, Nucl. Phys. A327 (1979) 490
- 2. J. Randrup, Nucl. Phys. A383 (1983) 486
- 3. T. Døssing and J. Randrup, LBL-16825 (1984)
- 4. T. Døssing and J. Randrup, LBL-16826 (1984)
- 5. J. R. Nix and W. J. Swiatecki, Nucl. Phys. A71 (1965) 1
- 6. L. G. Moretto and R. P. Schmitt, Phys. Rev. C21 (1980) 204
- 7. R. P. Schmitt and A. J. Pacheco, Nucl. Phys. A379 (1982) 313
- 8. R. J. McDonald et al., Nucl. Phys. A373 (1982) 54

A POLARIZATION STUDY OF INCOMPLETE FUSION DYNAMICS[†]

W. Trautmann, P.D. Bond, O. Hansen and H. Tricoire^{*}
 Brookhaven National Laboratory, Upton, NY 11973

and

W. Hering, R. Ritzka and W. Trombik
 Sektion Physik der Universität München, D-8046 Garching, W. Germany

The dynamics of fast charged particle emission in incomplete fusion reactions were studied by measuring the circular polarization of deexcitation γ -rays with respect to the reaction normal. This technique [1] was found to be very useful in its application to quasielastic and deep-inelastic reactions. For the study of incomplete fusion reactions a difficulty arises from the fact that the type of reaction is not uniquely defined by the observation of a fast light particle in a forward direction. Depending on the bombarding energy and the chosen projectile-target combination, sequential ejectile break-up following quasielastic or deep-inelastic interactions may compete with the transfer of a major projectile fragment to the target. We have therefore added an array of seven 3"x3" NaI detectors to the polarimeter setup which allowed us to investigate the dependence of the measured polarization on the γ -ray multiplicity M_γ . By requiring that, e.g., at least one NaI detector has fired (in addition to one γ -ray detected by one of the polarimeters), a weighing in proportion to M_γ is performed which strongly suppresses low multiplicity break-up events as well as reactions with light contaminants in the target. The intensity of the evaporation component, on the other hand, was determined in cross section measurements at backward angles.

In a series of experiments (Table 1) ^{16}O and ^{14}N beams, provided by the Brookhaven two- and three-stage tandem accelerator facility, were used to bombard self supporting Sm and Nb targets of 2-5 mg/cm² areal density. Light charged particles were detected and identified in 300 mm² telescopes consisting of ΔE and E solid state detectors of 150 μ and 2000 μ thickness, respectively, and mounted at distances of 7-8 cm from the target. Projectile-like reaction products were stopped in nickel foils of 75 mg/cm² areal density in front of the detectors. Two forward-scattering polarimeters were positioned perpendicular to the reaction plane in a double-symmetric detector arrangement [1]. The total efficiency of the NaI array to detect a γ -ray in the relevant energy range was $\approx 3.5\%$.

Table 1: Reaction list.

Projectile	E_{lab} (MeV)	Target	θ_{lab} (deg)
^{16}O	140	^{144}Sm	25
^{16}O	140	^{154}Sm	25, 38
^{16}O	110	^{93}Nb	38
^{16}O	120, 140	^{93}Nb	25, 38
^{14}N	95	^{93}Nb	38

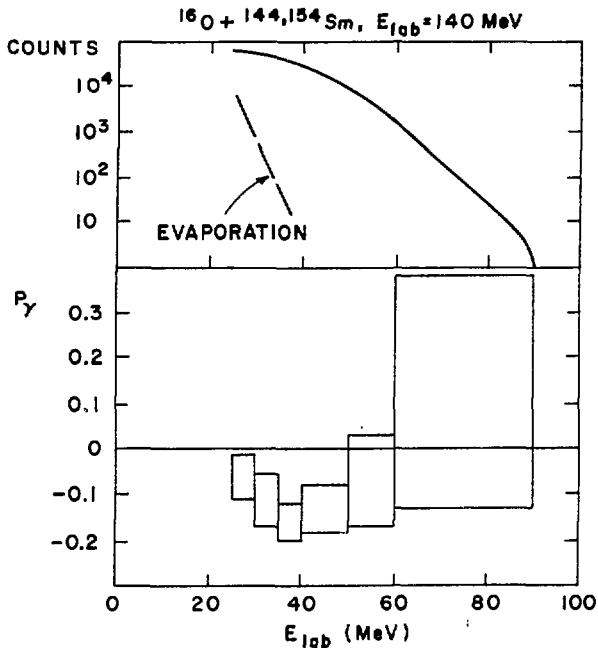


Fig. 1. Spectrum (top) and circular polarization P_γ (bottom) of coincident γ -radiation for α -particles from the reaction $^{16}\text{O} + ^{144,154}\text{Sm}$ at 140 MeV ($\theta_{\text{lab}} = 25^\circ$). The intensity of the evaporation component is indicated.

An example of the obtained results is shown in fig. 1. Here the data from the bombardment of the two Sm isotopes at $\theta_{\text{lab}} = 25^\circ \pm 7^\circ$ were summed since no significant difference was detected. The main result evident from the figure is the small negative γ -ray circular polarization of about 10% to 15% in coincidence with α -particles of energies in the range corresponding to the beam velocity ($E_\alpha \approx 35$ MeV). At the larger angle of $\theta_{\text{lab}} = 38^\circ \pm 8^\circ$ the polarization slightly increases to $P_\gamma \approx -20\%$. The negative sign of the polarization indicates that these α -particles are somewhat deflected away from the beam axis, presumably by the action of the Coulomb force in the entrance and exit channels. This is consistent with the decrease of the polarization with increasing bombarding energy which becomes apparent if these data are seen together with circular polarization for ^{14}N induced reactions on a Tb target which were reported by Ishihara [2].

A negative polarization of beam velocity α -particles is not observed in reactions with the Nb target (fig. 2). However, these data show the same tendency toward a positive polarization with increasing energy of the emitted particle as indicated by the data taken with rare-earth targets (fig. 1, ref. 2). This effect was observed with statistical significance in the measurements at 38° where the polarization associated with α -particles of $E_\alpha > 40$ MeV was found to be $P_\gamma \approx +0.3$ (table 2). Evidently, these particles with velocities larger than that of the beam are predominantly emitted toward negative angles as expected for a PEP (Fermi-jet) or knock-out (piston) process for sufficiently large impact parameters [3,4].

The polarizations measured in coincidence with protons are considerably smaller and essentially consistent with zero (table 2). Apparently there is no evidence for a mechanism (such as shadowing, Coulomb deflection, PEP or knock-out process) which would cause a main direction of emission different from the beam axis.

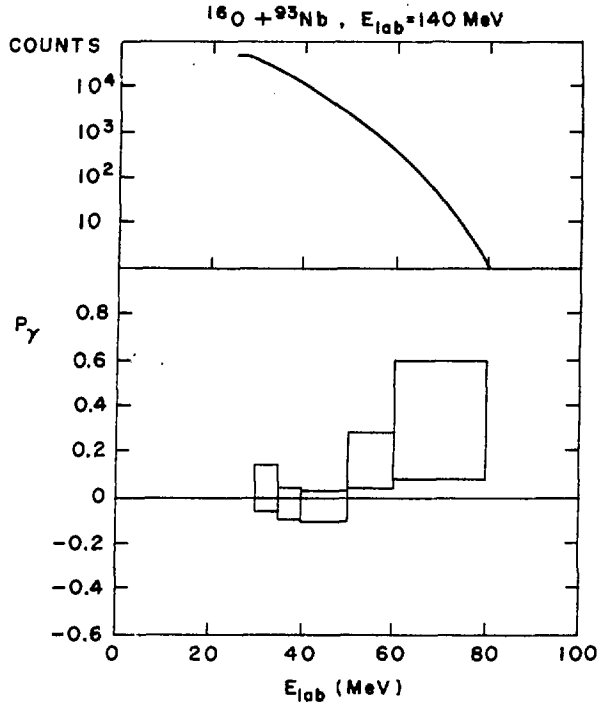


Fig. 2. As figure 1, but for the reaction ^{16}O on ^{93}Nb .

The near zero polarization in the case of proton emission is of particular interest since a considerable spin polarization of the emitted protons was observed in a double scattering experiment, conducted for the $^{14}\text{N}+^{93}\text{Nb}$ reaction at $E_{\text{lab}} = 95$ MeV [5]. A spin polarization of $\approx +20\%$ at $\theta_{\text{lab}} = 20^\circ$ and $\approx +40\%$ at $\theta_{\text{lab}} = 40^\circ$ for the direct proton component was deduced from the data. Since the produced fusion products are essentially unpolarized in these reactions, as shown by the γ -ray circular polarization measurement, a large class of possible explanations for the proton polarization are ruled out. We propose to interpret it as the result of the spin-orbit force acting on tangentially emitted fast protons. Estimates indicate that the l-s force is strong enough to produce the observed proton polarization.

Table 2: Circular polarization P_γ in coincidence with fast α -particles ($E_\alpha > 40$ MeV) or fast protons ($E_p > 15$ MeV) for reactions on Nb; $\theta_{\text{lab}} = 38^\circ$ and at least one hit in the NaI array required.

System	E_{lab} (MeV)	$P_\gamma(\alpha)$	$P_\gamma(p)$
$^{16}\text{O}+^{93}\text{Nb}$	110	$.26 \pm .15$	$.05 \pm .05$
$^{16}\text{O}+^{93}\text{Nb}$	120	$.35 \pm .12$	$.07 \pm .04$
$^{16}\text{O}+^{93}\text{Nb}$	140	$.15 \pm .09$	$.05 \pm .05$
$^{14}\text{N}+^{93}\text{Nb}$	95	$.34 \pm .08$	$.05 \pm .03$

⁺Work supported in part by the U.S. Department of Energy, Division of Basic Energy Sciences, under Contract No. DE-AC02-76CH00016, and by the Bundesministerium für Forschung und Technologie.

*Permanent address: IPN Orsay, France.

- [1] W. Trautmann, et al., Nucl. Instr. and Meth. 184 (1981) 449.
- [2] M. Ishihara, Nucl. Phys. A400 (1983) 153c, and contribution to Intl. Conf. on Nucl. Phys., Florence, 1983.
- [3] D.H.E. Gross and J. Wilczynski, Phys. Lett. 67B (1977) 1.
- [4] H. Tricoire, Z. Phys. A312 (1983) 221.
- [5] T. Sugitate, et al., Nucl. Phys. A388 (1982) 402.

WHAT CAN WE LEARN FROM SPIN DEPOLARIZATION MEASUREMENTS
IN DAMPED NUCLEAR REACTIONS?

J.C. STECKMEYER* and F. LEFEBVRES

Laboratoire de Physique Corpusculaire associé à l'IN2P3

ISMRA - Université de Caen - 14032 CAEN CEDEX France

Communication at the Winter Workshop on nuclear dynamics III

Copper Mountain Colorado

March 5-9, 1984

Since the discovery of the damped nuclear reactions, a great deal of experimental studies has been accumulated. In parallel, various phenomenological models have been proposed, giving generally a good description of the data, i-e the evolution of the mean values of the macroscopic observables such as energy, charge, mass and angular momenta, defining the final state of the nuclei in the binary reaction. The gross features of the damped nuclear reactions are well understood on the basis of the applicability of classical dynamics including phenomenological friction forces. In spite of these successes, the basic reaction mechanisms in terms of the fundamental microscopic nuclear properties are not yet clearly elucidated. Precise and complete measurements of spin transfer process in damped nuclear reactions are certainly important and fruitful in order to discriminate between the theoretical models, currently available, based on the fundamental properties of nuclear matter.

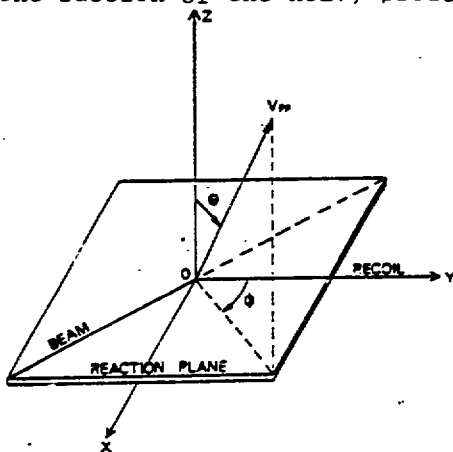
From an experimental point of view, the aims of the spin transfer process measurements are to know with accuracy and without experimental biases the first and second moments of the fragment spin distributions in space. Several experimental methods have been used extensively in a recent past to obtain information on angular momentum transferred into spin to the individual fragments. All these methods are based on the decay studies of highly excited nuclei produced in the primary reaction and the use of

* Thesis, University of Caen to be held.

either the angular distribution of the fission fragments of the heavy recoil , or the angular distribution and multiplicity measurement of γ rays , or the angular distribution of sequentially emitted light particles .

These different methods are complementary. For all of them the out of plane angular distributions contain essentially information on the average spin component mainly aligned along the normal to the reaction plane. Concerning the in-plane angular distributions, γ ray and light particle measurements are rather insensitive to differences between the in-plane spin components . Only the sequential fission method is quite sensitive to such differences and can give rise, if they exist, to measurable anisotropies of the fission fragment angular distribution in the reaction plane. In these conditions, it is possible to measure simultaneously with a reasonable accuracy the spin observables of the heavy nucleus in the reaction plane and along its normal.

The angular momentum transfer into fragments spins has been studied in the damped nuclear reactions Ar+Bi at 255 MeV and 295 MeV and Ni+Pb at 435 MeV from the measurement of the angular distribution of the fission fragments of the heavy recoil nucleus in coincidence with the projectile like fragment. These experiments have been done at Alice accelerator in ORSAY, the projectile like reaction products were detected and identified in charge by a $\Delta E.E$ silicon telescope, the coincident fission fragments and target like products in a position sensitive PPAC giving accurate time of flight measurements. The experimental method and data analysis are described in detail elsewhere¹⁻²⁾, the sequential fission events are easily separated from the other events and we obtain from the fission fragment velocity distribution in the rest frame of the heavy recoil a clear signature of the sequential process, that is a damped nuclear reaction followed by the fission of the heavy product.

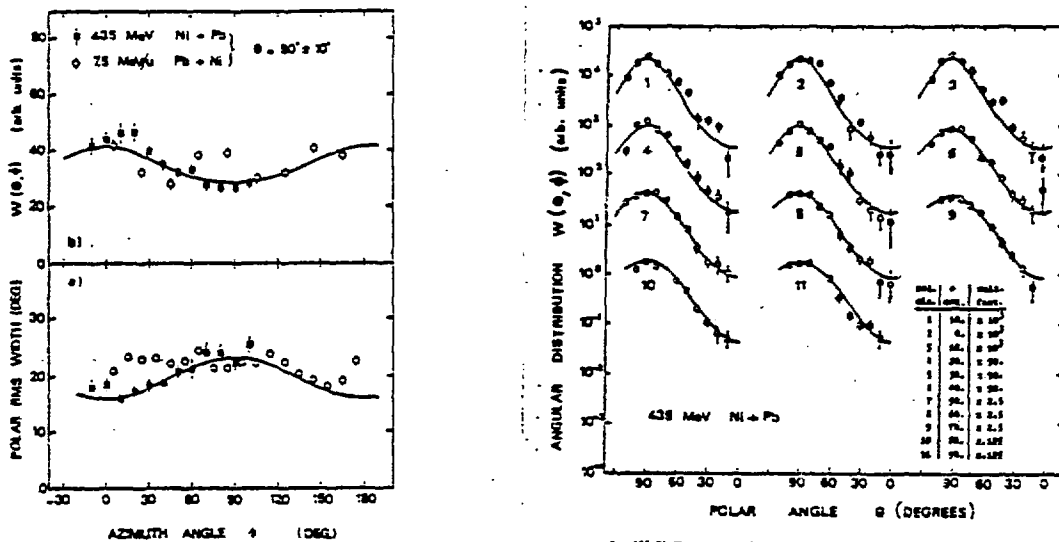


The direction of emission of the fission fragment is defined by the polar angle θ and the azimuth one ϕ in the rest frame of the target like product according to the left figure.

The whole angular distribution (out of plane) and the in plane angular distribution ($\theta = 90^\circ \pm 10^\circ$) are reconstructed in $\Delta\phi$ and $\Delta\theta$ bins from the sequential

fission events and presented without and with Z_L (atomic number of the projectile like product) and TKEL (total kinetic energy loss) selections.

For the lack of place, we present in this communication only the Ni+Pb angular distributions (the whole data are shown in ref. 1 and 2). As observed in previous experiments^{1,3,4,5}, the strong inplane focusing of the fission fragment indicates at once that the spin of the heavy product is large and aligned along the normal to the reaction plane (the 90° to 0° ratio is almost of two orders of magnitude in the recoil direction). Another important observation can be made also from these data, the clear increase of the width of the polar distributions as a function of the azimuth angle ϕ , put in evidence, for the first time in the study of the Ar+Bi at 255 MeV¹⁾.



For 425 Ni+Pb system, polar angular distributions summed in 10° wide θ bins (shown 22, and TKEL cuts. The continuous curves are fits to data (see the next part of the communication).

In the above figures are displayed in a) the ϕ dependence of the polar distribution widths (RMS) together with the results of ref.4 (Pb+Ni at 7.5 MeV/u same total energy in the center of mass system). Our data are at variance with the nearly constant rms polar widths of the Darmstadt experiment.

The in plane distribution (selection $\theta = 90^\circ \pm 10^\circ$) shown in b) exhibit an unambiguous anisotropy :

$$R = \frac{W(\phi=0^\circ, \theta=90^\circ)}{W(\phi=90^\circ, \theta=90^\circ)} = 1.46 \pm 0.9, \text{ slightly weaker than Kr+Bi experiment}^{2)}$$

$$(R=2.0).$$

The fission fragment angular distributions of the Ar+Bi system at two energies 255 and 295 MeV display the same properties as the presented Ni+Pb data in the polar and in plane distributions with the following

We will now spend some times to explain how the extraction of the spin observables has been made from our data.

Within the frame work of the transition model, D. von Harrach has derived the angular distribution of the fission fragment emitted by decaying nucleus. This formula is obtained under the hypothesis of gaussian distribution ($\langle I_i \rangle, \sigma_i$) for the cartesian spin components ($0, \sigma_x$), ($0, \sigma_y$), ($\langle I_z \rangle, \sigma_z$).

$$W(\theta, \phi) \propto \exp - \frac{\langle I_z \rangle^2 \cos^2 \theta}{2N^2}$$

$$N^2 = K_0^2 + \sigma_x^2 \sin^2 \theta \sin^2 \phi + \sigma_y^2 \sin^2 \theta \cos^2 \phi + \sigma_z^2 \cos^2 \theta$$

K_0 is the rms width of the K distribution (K being the projection of fragment spin I on the nuclear symmetry axis) which has been deduced from the light ion induced fission data.

In fitting $W(\theta, \phi)$ to the data, only three quantities among the four spin observables ($\langle I_z \rangle, \sigma_x, \sigma_y$ and σ_z) can be extracted in an independent manner, because there is a scaling law between two different parameter sets ($\langle I_z \rangle, \sigma_i$) and ($\langle I_z' \rangle, \sigma_i'$) that is described in details in réf. 2.

From a pure mathematical point of view, an infinite number of solutions is available, with σ_i values increasing with the increase of the aligned part $\langle I_z \rangle$. Minimum values of three variables are obtained when the fourth one is equal to zero. But, we have to take into account several physical constraints. First, the aligned part $\langle I_z \rangle$ cannot exceed the rigid rotation limit. Secondly, the observed in-plane anisotropies indicate $\sigma_x \gg \sigma_y$. With the unphysical hypothesis $\sigma_y = 0$ \hbar , σ_x values greater than 10 \hbar are needed in order to reproduce such anisotropies. At last, the quantal uncertainties :

$$\sigma_x^2 + \sigma_y^2 \gg \langle I_z \rangle \hbar \quad \text{and} \quad \sigma_x \cdot \sigma_y > \frac{\langle I_z \rangle \hbar}{2}$$

force the σ_i magnitudes to be of the order of a few \hbar units. With such physical constraints applied to our data, unambiguous physical solutions on the spin observables have been obtained.

The following method has been used. A first fitting procedure is realized assuming $\sigma_y = 0$ \hbar . The $\langle I_z \rangle$ values obtained in this way are high, in clear disagreement with the rolling hypothesis of the dinuclear system. Within the experimental error bars, these values agree very well with the theoretical values $\langle I_z \rangle_{RR}$ calculated with the assumption of the rigid rotation of two touching spheroids and the use of the mean weighted ℓ_i -values as initial orbital angular momenta. A second fitting

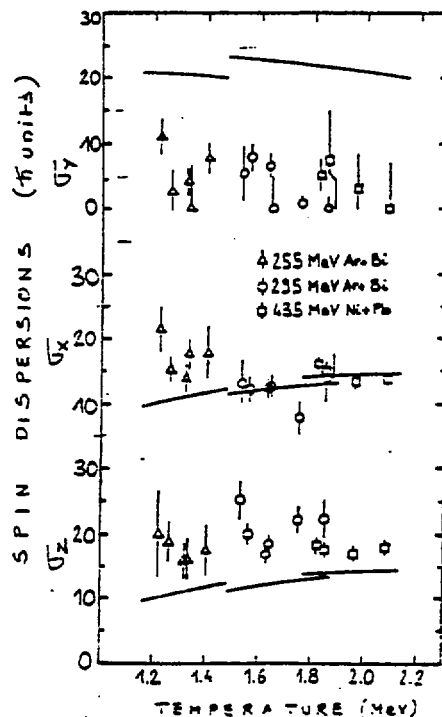
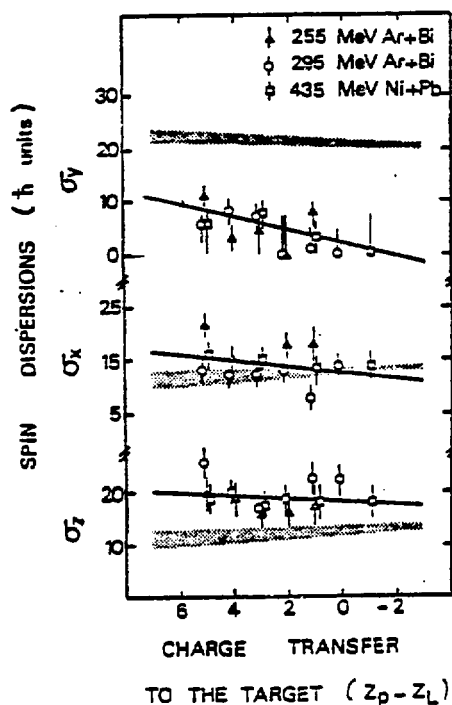
calculated values $\langle I_z \rangle_{RR}$ and physical solutions of the standard deviations σ_i are then obtained.

The spin observables extracted from the whole angular distributions, with the K_0 parameters used in the fitting procedure and the asymmetry and alignment parameters deduced are given in the following table.

EXPERIMENT	E_{lab} (MeV)	$\langle I_z \rangle_{RR}$ (\hbar)	K_0 (\hbar^2)	σ_x (\hbar)	σ_y (\hbar)	σ_z (\hbar)	P_{zz}	P_{xy}
Ar+Bi	255.	45	81	13^{+2}	5^{+2}	14^{+2}	$.88^{+.02}$	$.06^{+.02}$
Ar+Bi	295.	55	113	15^{+1}	7^{+2}	15^{+1}	$.88^{+.02}$	$.05^{+.02}$
Ni+Pb	435.	49	121	16^{+1}	7^{+2}	14^{+1}	$.84^{+.03}$	$.07^{+.02}$

We remark that the σ_i values are equal inside the statistical errors whatever the energy and the projectile target system.

After, we have made a Z and TKEL or temperature analysis of the spin depolarizations that are presented in the figures below, where we put together all the data : Ar+Bi at 255 MeV and 295 MeV and Ni+Pb at 435 MeV.



Concerning the Z analysis, we remark that except some local accident due to poor statistics, the σ_i are rather independent of the projectile and of the incident energy. (The solid lines are linear fits obtained with all the data). The σ_y values lie between 1 μ and 10 μ , they are always smaller than σ_x and σ_z values, σ_x are the order of 15 μ , whereas, the σ_z ones, slightly higher can reach 20 μ .

For the general trends, the spin misalignment is increasing as more protons are transferred from the projectile to the target; the σ_y are growing more rapidly than the σ_x ones, σ_z values being nearly constant. From this observation, we can infer that for large charge transfer (long life time of the dinuclear complex), the spin fluctuations are expected to be distributed isotropically in space and no more longer preferentially located in the plane perpendicular to the recoil direction.

For the temperature analysis, the same remarks as precedently can be applied to the orders of magnitude, inside the error bars, we can say that the σ_z values are rather flat and there is a tendency of the decrease of σ_x and σ_y as the temperature increases.

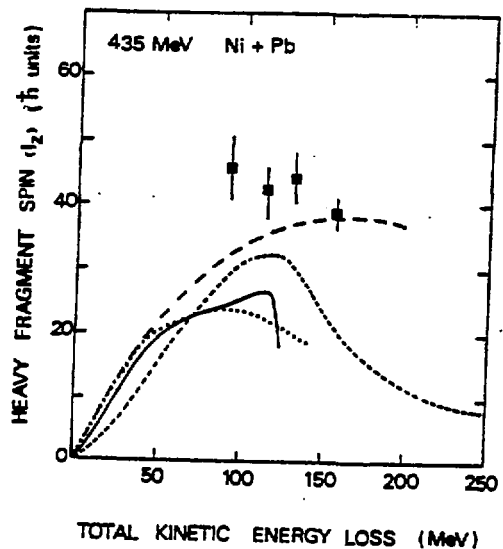
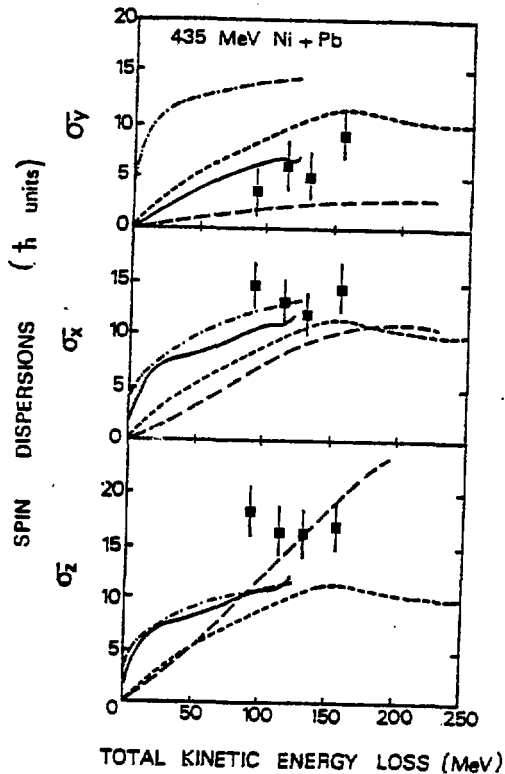
At this point, we can make a comparison of the results with the statistical equilibrium model⁶⁾. In this model, the dinuclear system is assumed to reach the thermal equilibrium limit, that corresponds the long time limit of the dinucleus. The collective rotational modes of the dinuclear system generate random spin components in space, which are then coupled with the spin aligned part to give the final spin distribution. The spin dispersions of the fragment can be calculated at the scission time of the dinucleus and we have to relate these theoretical values of σ_i with the experimental ones measured in our reference system after the coulomb deflexion of the final fragments.

On the figure, we have drawn in the shaded areas the values of σ_i for three systems in the scission frame. Using the dynamical nucleon exchange model⁷⁾, we have estimated for our three systems the rotation angle χ between the scission line and the heavy recoil direction (we found values lying between 30° and 45°). The σ_z values are independent of this rotation and they are not reproduced in absolute value by the statistical equilibrium model. We do not introduce this rotation and make only a qualitative discussion, we note that with this correction the agreement can be rather satisfactory

with σ_x . For σ_y , the data shows a discrepancy by a factor 2-3.

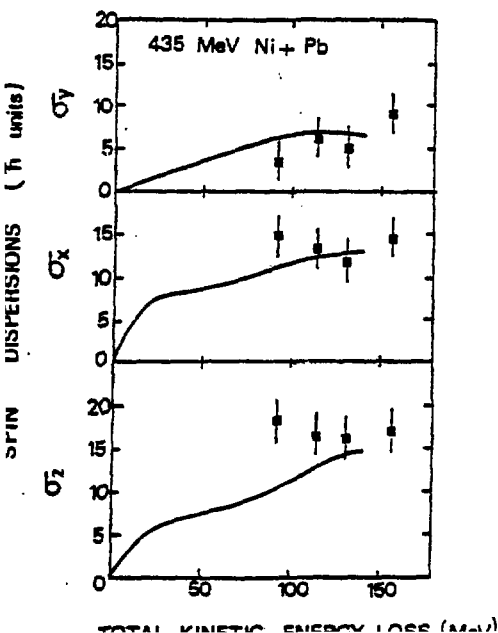
The same remarks can be made on the temperature dependence of the σ_i (the continuous lines represent the predictions of the statistical equilibrium model in the scission frame). So we can conclude at this stage of the analysis that the statistical equilibrium model fails to interpret all our data, meaning at least that the thermal equilibrium is not reached for some collective rotational modes in particular for the tilting one which induces large values of σ_y for such very asymmetric systems as ours.

We will compare, now for the Ni+Pb system our experimental results of $\langle Iz \rangle$, σ_x , σ_y , σ_z , as a function of TKEL with different theoretical models : $-\cdot-\cdot-$ collective model of Broglia ⁵⁾ et al., $-----$ diffusion model of Wolshin, $-\cdot-\cdot-$ thermal equilibrium model ⁶⁾ and finally the dynamical nucleon exchange model of Randrup ⁷⁾ $-----$



Concerning the aligned part of the spin, the heavy fragment spin predictions are shown together with our data. The statistical equilibrium model simply assumes that the rigid rotation limit is achieved in heavy ion reactions, but no theoretical prevision is given since it depends on the dynamics of the reaction. A good agreement is seen with the calculations of the collective model the curve standing for the 610 MeV Kr+Bi system. The diffusion model taking into account for the deformation of the nuclei in the collision, is able to predict the large experimental TKEL-values, but not the magnitude of the aligned part where, at least, 10 \hbar units are lacking. Our calculations based on the dynamical nucleon exchange model and those of Dossing and Randrup give similar predictions and therefore the same discrepancies with respect to the data : aligned spin value is too low, by a factor 2, and the assumption of two spherical nuclei prevents us to get more higher TKEL values.

The calculations that we have performed according to the dynamical nucleon exchange model (solid lines) give a good description for the three σ_i values and agree with what we have inferred previously from the data : σ_x and σ_z values evolving slowly after a rapid initial rise, whereas the σ_y values are linearly increasing as a function of the TKEL. This observation can be understood as follows : the nucleon transfer generates spin components primarily in the plane perpendicular to the line joining the centers of the two nuclei. As this line is rotating during the life time of the dinuclear system, the orbital motion induces σ_y values which are expected to grow up more and more as a function of the interaction time, i.e. the TKEL value of the reaction.



A last comparison is made with the calculation performed by Dossing and Randrup⁽²⁰⁾. They have improved the dynamical model by including angular momentum and energy fluctuations in such a manner that the spin observables are now presented as a function of the TKEL after integration over all the partial waves involved. Another refinement is that correlations between the fluctuations of the angular momenta and the fluctuation of the employed body fixed coordinate system are now accounted for. This final version is compared with our data in the left figure.

In conclusion, with all our systems, the aligned part of the spin $\langle I_z \rangle$ reached the rigid rotation limit, it is not well reproduced by all the theoretical models except the collective one.

The spin dispersions extracted from the data show that the dealignment mechanisms act mainly in a plane nearly perpendicular to the heavy recoil lab direction (within 10° - 20°). Such results are very well accounted for by a dynamical model based on the exchange of individual nucleons between the two ions during the collision. The high values of the aligned part of the spin are reproduced by incorporating both the nucleon transfer and the surface vibration modes.

The spin dispersions along the recoil direction are increasing with the TKEL value and the charge transfer from the projectile to the target. The dispersions in the plane perpendicular to the recoil are rather constant whatever the TKEL and the charge transfer. These results are at variance with the thermal equilibrium model which is seen to fail in the attempt to explain our data, indicating that the thermal equilibrium is not fully reached in the deep inelastic reactions.

The specific study of the Ar+Bi reactions versus the bombarding energy shows that the heavy fragment spin is increasing with the energy, as expected, but the observed spin fluctuations are energy independent, within the precision of the measurements.

REFERENCES

- 1) C. Le Brun, J.F. Lecolley, P. Lefebvres, M. L'Haridon, A. Osmont, J.P. Patry, J.C. Steckmeyer and R. Chechik, Phys. Rev. C25 (1982) 3212
- 2) *Steckmeyer et al. Angular momentum transfer and spin dealignment mechanisms in damped nuclear reactions Ar+Bi and Ni+Pb to be published in Nuclear Physics*
- 3) P. Dyer, R.J. Puigh, R. Vandenbosch, T.D. Thomas, M.S. Zisman and L. Nunnolley, Nucl. Phys. A322 (1979) 205
R.J. Puigh, P. Dyer, R. Vandenbosch, T.D. Thomas, L. Nunnolley and M.S. Zisman, Phys. Lett. 86B (1979) - 24
- 4) D.v. Harrach, P. Glässel, Y. Civelekoglu, R. Männer and H.J. Specht, Phys. Rev. Lett. 42 (1979) 1728
- 5) D.J. Morrissey, G.J. Wozniak, L.G. Sobotka, A.J. Pacheco, C.C. Hsu, R.J. Mc Donald and L.G. Moretto, Z. Phys. A305 (1982) 131
- 6) L.G. Moretto and R.P. Schmitt, Phys. Rev. C21 (1980) 204
R.P. Schmitt and A.J. Pacheco, Nucl. Phys. A379 (1982) 313
- 7) J. Randrup, Nucl. Phys. A383 (1982) 466
- 8) R.A. Broglia, G. Pollarolo, C.H. Dasso and T. Döessing, Phys. Rev. Lett. 43 (1979) 1649
- 9) G. Wolschin, private communication (1980)

OBSERVATION OF A CRITICAL ANGULAR MOMENTUM FOR DEEP INELASTIC PROCESSES
WITH LIGHT HEAVY IONS

S. T. Thornton and R. L. Parks,^a
University of Virginia,^b Charlottesville, VA 22901

D. Shapira, D. Schull,^c J. L. C. Ford, Jr.,^d B. Shivakumar,^e and J. Gomez del Campo,^f
Oak Ridge National Laboratory, Oak Ridge, TN 37830

Studies of collisions between nuclei have shown that the large incoming orbital angular momenta play an important role in systems where Coulomb and centrifugal repulsion for the dominant (near grazing) partial waves are of comparable magnitude ($A_p A_t < 40$). The kinetic energy of the fully damped fragments contains significant centrifugal energy contributions. Recent measurements have shown that the yield of fragments from strongly damped processes dominates the spectra at backward angles, and the angular distributions associated with this yield indicate that the fragments emerge from a long-lived rotating dinuclear complex (orbiting).¹ These measurements at backward angles provide a means for studying the products from deep inelastic processes in the absence of contributions from quasielastic processes. In our study of deep inelastic processes in $^{28}\text{Si} + ^{12}\text{C}$ at backward angles we show here results which demonstrate that the orbital angular momentum of the rotating dinuclear system formed in this collision reaches a critical value beyond which it ceases to increase with increasing bombarding energy. Such a limit on orbital angular momentum is indeed expected to occur when the centrifugal force becomes large enough to cancel the attractive nuclear force. Aside from serving as additional confirmation for the long held semiclassical view of deep inelastic scattering as an orbiting phenomenon,² knowledge of this angular momentum limit can also be used to learn about the strength and range of the nuclear interaction potential.

In the experiment, ^{28}Si beams at several energies ranging from 100 MeV to 190 MeV from the Brookhaven National Laboratory Tandem facility were used to bombard natural carbon foils, and spectra of recoiling target-like nuclei were studied at forward angles.¹ This is equivalent to studying projectile-like products emitted at backward angles in the bombardment of a ^{28}Si target by ^{12}C beams. In Ref. 1 we have shown that all the yield in these spectra and

similar spectra of boron, nitrogen and oxygen nuclei comes from the decay of a long-lived rotating dinuclear complex formed in the collision between $^{28}_{12}\text{Si}$ and $^{12}_6\text{C}$. The most probable Q value (Q) for these spectra does not depend on the angle of emission and has a linear dependence on bombarding energy over the energy range $30 < E_{\text{cm}} < 40$ MeV studied in Ref. 1. Results from similar measurements at higher energies are shown in Fig. 1 for emitted carbon and oxygen nuclei, the two strongest outgoing channels. The figure shows the most probable values for the total kinetic energy of the final fragments as a function of bombarding energy. The kinetic energies were obtained by adding the most probable values of the measured Q value spectra to the center-of-mass bombarding energy ($E_{\text{kin}}^{\text{cm}} = E_{\text{cm}} + Q$). The linear dependence on bombarding energy seen at the lower energy range arises from the centrifugal energy of the rotating dinuclear system prior to scission. Above an incident energy of 45 MeV (c.m.) we see that the final kinetic energy becomes almost independent of bombarding energy.

A simple interpretation of this sudden change stipulates that at this bombarding energy a critical value of the angular momentum has been reached in the entrance channel beyond which formation of a dinuclear system is not allowed because of centrifugal repulsion. A simple analysis of the linear energy dependence seen in Fig. 1 using a proximity type nuclear potential and the semiempirical parameters suggested by Bass³ was presented in Ref. 1. The resulting nucleus-nucleus potential for $^{28}_{12}\text{Si} + ^{12}_6\text{C}$ is shown in Fig. 2.

When the orbital angular momentum of the nuclei in contact exceeds $\ell_c = 22$ the "pocket" in the nucleus-nucleus potential vanishes, and the two nuclei do not attract each other and therefore cannot orbit. The nuclei may collide with higher incident energy and angular momenta (E_{II}), but dissipate enough energy and angular momentum to feel mutual attraction^{II} in their contact configuration so that orbiting can still occur. Eventually at higher bombarding energies, (E_{III}), the incoming orbital angular momentum is so high that even dissipation cannot bring its value at contact down to $\ell_c = 22$ and the flux from these partial waves and higher ones cannot contribute to orbiting.

This classical approach can describe only the most probable values of the measured macroscopic observables (maxima of the measured distributions). Quantum fluctuations in the shape of the nucleus-nucleus potential or in the energy dissipation process cause a spread in the observed kinetic energy (Q-

value) around the maximum value. A quantum mechanical treatment of the nucleus-nucleus potential must also include absorption - which to first order governs the probability of the orbiting nuclei to reparate rather than fuse. With no absorption one would expect the magnitude of the total cross section for orbiting to drop like $1/E_{cm}$ once a limiting angular momentum has been reached. Nucleus-nucleus absorption is expected to modify this behavior and indeed the measured absolute cross section which increases initially very fast with bombarding energy does so at a progressively decreasing rate at higher energies.

We have considered the problems inherent from measuring only inclusive spectra. Sequential α -emission from the excited projectile producing low energy carbon ions and decay of C and O ions in flight lead to incorrect Q-value determinations. Our results indicate that while the data may be slightly weighted by secondary processes the sudden change in the slope of the data near 45 MeV indicates that a fundamental change in the reaction process has occurred.

We therefore suggest that the saturation observed in the kinetic energy of the outgoing fragments reflects a limiting value of angular momentum with which the dinuclear system can rotate. Since the fusion of nuclei must proceed via a contact configuration we expect the limit on angular momentum derived from analysis along the lines outlined above to provide an upper bound for the critical angular momentum that can lead to fusion of these nuclei. Such information could complement ℓ_{crit} for systems of light nuclei derived from absolute cross sections for compound nucleus formation, which are complicated and subject to large uncertainties at high bombarding energies.

We have begun measurements of evaporation residues from the fusion of $^{28}\text{Si} + ^{12}\text{C}$ over the same energy range that we hope will further elucidate the relation between critical angular momenta for fusion and for the orbiting process. A preliminary spectrum for the ^{33}S residue, shown in Fig. 3, seems to show evidence for incomplete fusion for bombarding energies of 6.4 MeV/A. Observation of incomplete fusion for such light systems below 10 MeV/A has not been previously reported and is not expected.⁴ The preliminary results clearly show the advantage of TOF experiments with ΔE -E detectors where both the mass and charge can be determined. The incomplete fusion results were observed at 2° and 3° (lab), but were not observed for 5° or larger angles.

As has been stated before the presence of incomplete fusion will make the

determination of fusion cross sections (and subsequently ℓ_{crit}) even more difficult. The technique outlined in this paper could have great promise in providing important information on angular momentum limitations on nuclear interactions such as fusion.

We acknowledge the assistance of R. A. Cecil in the data taking.

- (a) Present address: E-Systems, Falls Church, Virginia 22046.
 (b) Supported in part by the National Science Foundation.
 (c) Permanent address: GSI, Darmstadt, West Germany.
 (d) Deceased.
 (e) Permanent address: A. W. Wright Nuclear Structure Laboratory, Yale University, New Haven, Connecticut 06520. Supported in part by contract No. DE-AC02-76ER0374 with the U.S. Department of Energy.
 (f) Operated by Union Carbide Corporation under contract W-7405-eng26 with the U.S. Department of Energy.

References

1. D. Shapira et al., Phys. Lett. **114B**, 111 (1982).
2. J. Wilczynski, Phys. Lett. **47B**, 484 (1973).
3. R. Bass, Phys. Rev. Lett. **39**, 265 (1977).
4. S. Kox, et al., Phys. Lett. **119B**, 303 (1982).

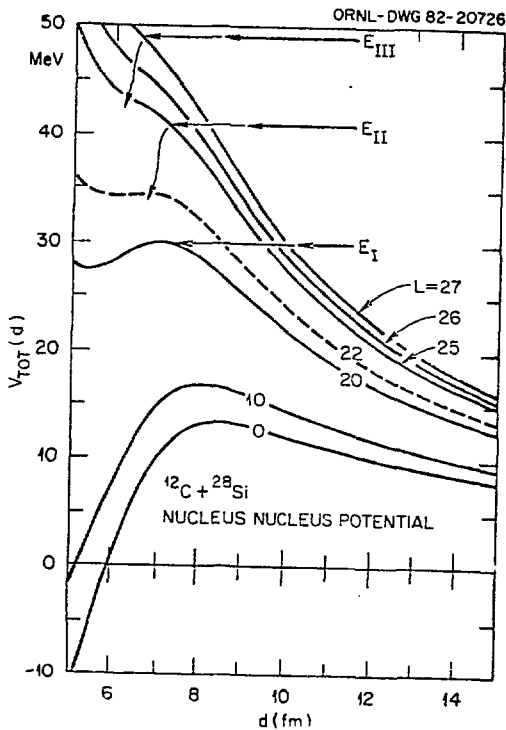


Fig. 2. The $^{12}\text{C} + ^{28}\text{Si}$ total nucleus-nucleus potential

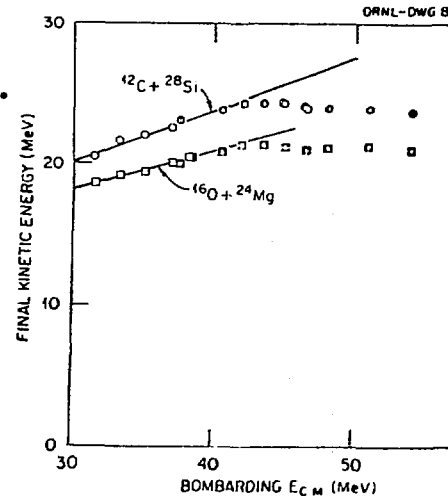


Fig. 1. Bombarding energy dependence of the most probable value of the total kinetic energy of the outgoing fragments for the $^{12}\text{C} + ^{28}\text{Si}$ and the $^{16}\text{O} + ^{24}\text{Mg}$ channels.

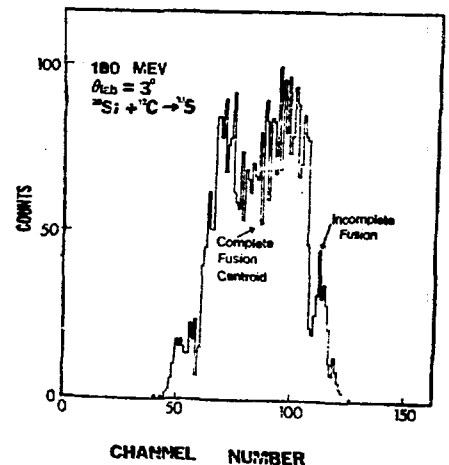


Fig. 3. An energy spectrum of $Z=16$ and $A=33$ (^{33}S) from the bombardment of ^{12}C with 180 MeV ^{28}Si ions. The estimated energy centroids for complete and incomplete fusion ($^{28}\text{Si} + ^6\text{Be}$) are noted.

PROJECTILE FISSION IN ^{58}Ni -INDUCED REACTIONS AT 15.3 MeV/u*

T. C. Awes, R. L. Ferguson, R. Novotny,^a F. E. Obenshain,
F. Plasil, V. Rauch,^b H. Sann,^c and G. R. Young

Oak Ridge National Laboratory, Oak Ridge, Tennessee 37831

The present study was intended as a search for sequential fission of projectilelike fragments for reactions induced by intermediate-mass heavy ions. The objective was to determine the fission probability as a function of excitation energy or energy loss in the first step of the reaction. The experimental configuration was optimized for the detection of three-body sequential fission events over the full range of possible energy losses. The detector arrangement included a large-area ionization chamber which had two independent upper and lower halves, each capable of measuring the energy, E , and the energy loss, ΔE , of reaction products as well as their (x,y) position. A second detector was operated in coincidence on the other side of the beam axis. It consisted of an ionization ΔE section backed by a position-sensitive silicon detector. This telescope covered a fixed in-plane angular range of -12° to -32° , while the large-area ionization chamber was operated at three angles covering the angular range of 4° to 39° .

The inclusive charge distributions measured with the large-area ionization chamber for reactions of $^{58}\text{Ni} + ^{58}\text{Ni}$ at 15.3 MeV/u were found to be dominated by products with $Z < 28$. Very little yield was observed for nuclei with charges greater than that of the projectile. It has been shown¹ that most of the shift toward lighter products is consistent with the effects of equilibrium evaporation. At the largest calculated energy losses, the inclusive charge distributions were found to be slightly asymmetric due to an increasing component of fragments with half or less of the projectile charge. These light fragments were observed to have much broader angular distributions than the corresponding heavier fragments of the same energy loss. These observations from the inclusive measurements already suggest the occurrence of sequential fission of the projectilelike fragment. More conclusive evidence is obtained from the coincidence measurements.

In Fig. 1(a) the distribution of coincident events is shown as a function of $Z_1 + Z_2$ and $E_1 + E_2$. A strong cluster of events appears centered at $Z_1 + Z_2 \approx 40$ and $E_1 + E_2 \approx 440$ MeV. Events in this region originate from binary events. They involve large energy losses and, therefore, large amounts of charged-particle evaporation. The peak represents only a small portion of all binary events due to phase-space restrictions of our experimental geometry. In contrast, events with $10 \lesssim Z_1 + Z_2 \lesssim 30$ and $200 \lesssim E_1 + E_2 \lesssim 750$ MeV are not due to binary reactions between ^{58}Ni nuclei, but must originate either from three-body sequential fission events or from binary reactions between ^{58}Ni projectiles and light target contaminants.

Evidence that these coincident events are not due to reactions on a light target contaminant is obtained by a direct comparison of the results from the ^{58}Ni target with those obtained for the $^{58}\text{Ni} + ^{12}\text{C}$ reaction under

identical experimental conditions. The coincident distributions for reactions on carbon are found to differ significantly from those on nickel.

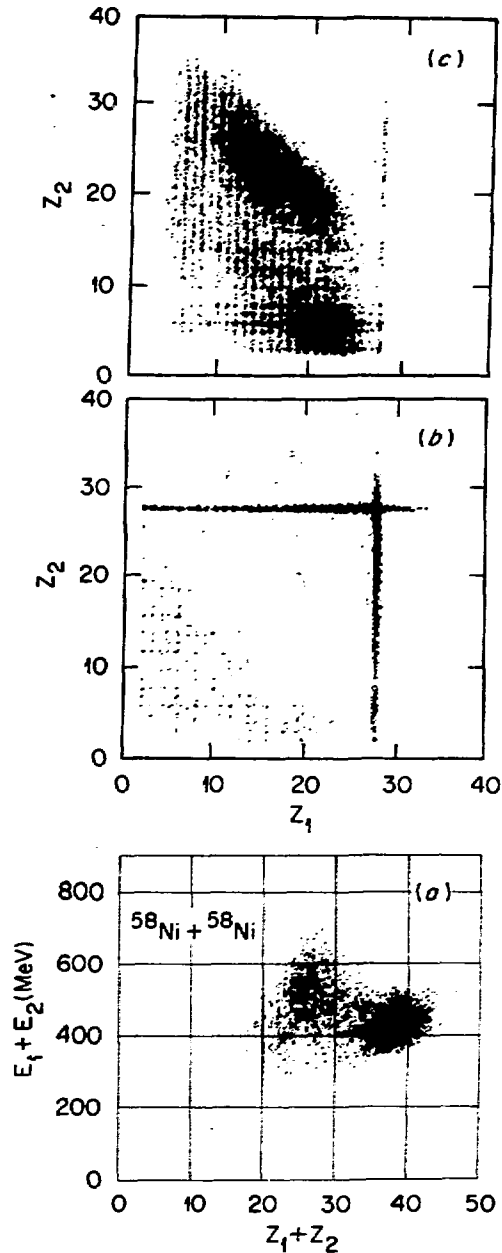


Fig. 1. Distributions of coincident products for reactions of $^{58}\text{Ni} + ^{58}\text{Ni}$ at 15.3 MeV/u. (a) Summed charge versus the summed laboratory energy. (b) Charge of fragment observed in lower half of ionization chamber versus charge observed in upper half. (c) Correlation between fragment charges observed on opposite sides of the beam by two different ionization chambers.

In particular, the rest frame velocity of those events on ^{58}Ni with $Z_1 + Z_2 \lesssim 30$ is peaked near 3.8 cm/ns, which is consistent with a fully damped two-body reaction followed by sequential fission. On the other hand, due to the inverse kinematics, the center-of-mass velocity of the $^{58}\text{Ni} + ^{12}\text{C}$ system is 4.5 cm/ns. From these differences we can conclude that possible contributions from light target contaminants are less than 5%.

Due to the inverse kinematics, it is clear that reactions on a light target contaminant would result in a coincidence distribution which might be interpreted as resulting from three-body sequential fission occurring after little energy loss. Although the experimental geometry and systems studied were different, there is a similarity between our results on ^{12}C and the $^{86}\text{Kr} + ^{89}\text{Y}$ coincidence measurements presented in Ref. 2 in the region of small, apparent energy losses.

Further direct evidence for the three-body interpretation of our results is shown in Fig. 1(b) by the correlation between coincident charges, Z_1 and Z_2 , obtained with the lower and upper halves of the ionization chamber. Thus, both of the detected fragments were observed on the same side of the beam, which, by momentum conservation, immediately implies that a third reaction product must be present on the other side of the beam. The concentration of events with $Z = 28$ is obviously due to random coincidences with elastically scattered ions.

In Fig. 1(c) the correlation between the nuclear charge, Z_1 , observed in the large ionization chamber is shown versus the nuclear charge, Z_2 , observed in the small detector. This presents a less biased selection of coincident events than those of Fig. 1(b), which were constrained to small opening angles due to the angular acceptance of the ionization chamber. The concentration of yield at $Z_1 + Z_2 \approx 40$ due to binary events is again clearly observed. A striking feature of Figs. 1(b) and 1(c) is the broad distribution of three-body events over nearly all possible Z_1, Z_2 combinations with sum charge less than or about equal to ^{58}Ni . Since the sum charge is sometimes much less than 28, it is likely that there are occasionally more than three large fragments in the final state. In Fig. 1(c) two different components are observed to contribute to the coincident events with $Z_1 + Z_2 \approx 28$. One component corresponds to symmetric fission with both fragments observed to have about equal charges. The second component corresponds to an asymmetric decay with the emission of a carbonlike fragment $Z_1 \approx 20, Z_2 \approx 6$. (The corresponding asymmetric decay $Z_1 \approx 6, Z_2 \approx 20$ is biased against by our experimental configuration.)

In Fig. 2 the experimental fission probabilities are shown for all fissionlike events with Z_1 and $Z_2 > 3$ (asterisks) and also for symmetric fission events only [crosses, $|Z_1 - Z_2| \lesssim 0.3 (Z_1 + Z_2)$]. To extract the fission probabilities shown in Fig. 2, we have made a Monte Carlo simulation in order to determine the coincident detection efficiency. To obtain the fission probability, we have divided the efficiency-corrected fission cross section by the total cross section at each energy loss. The excitation energy of the nickellike fragment is assumed to be half of the calculated energy loss. This neglects the effects of particle evaporation and the

width in the sharing of the excitation energy, which will have compensating effects on the actual excitation energy of the fragment.

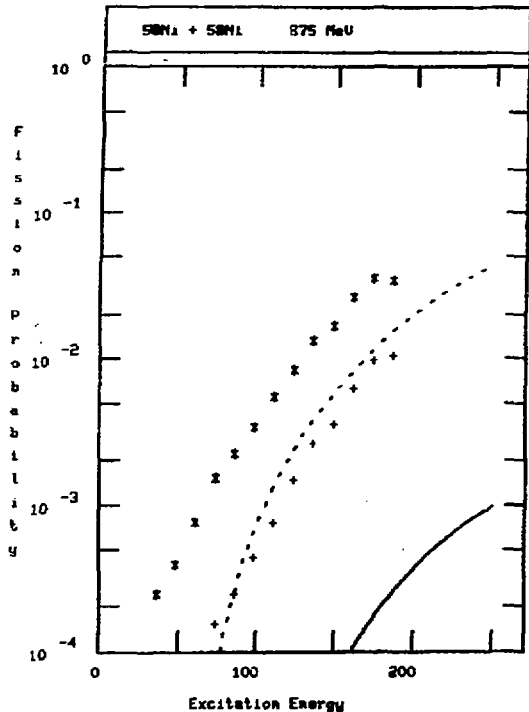


Fig. 2. Excitation function of fission probability. Experimental results are preliminary with an estimated uncertainty of 50% due to uncertainties associated with the simulation process. Experimental points: all fissionlike events (asterisks); symmetric fission events (crosses); calculations: $J = 25$, $B_f = 0.8 B_f^{\text{RLDM}}$, $a_f/a_n = 1.05$ (dashed curve); $J = 25$, $B_f = B_f^{\text{RLDM}}$, $a_f/a_n = 1.00$ (solid curve).

Also shown in Fig. 2 are the results of statistical model calculations of the fission probability of ^{58}Ni using the evaporation code PACE.³ For this calculation an angular momentum of $J = 25$, corresponding to the sticking condition, was assumed, together with a fission barrier corresponding to 0.8 of the rotating liquid drop barrier and a level density parameter $a_f/a_n = 1.05$. This calculation is found to reproduce the probability for symmetric fission surprisingly well. The large probability for asymmetric fission of the projectilelike fragment might be explained by liquid drop calculations which predict a decreasing barrier with increasing mass asymmetry for systems with low fissility. The enhanced yield at carbon might be due to modifications of the liquid drop barrier due to cluster effects for systems this light.

References

- *Research supported by the U.S. Department of Energy under contract W-7405-eng-26 with the Union Carbide Corporation.
- ^aOn leave from Physical Institute, University of Heidelberg, West Germany.
- ^bOn leave from Centre de Recherches Nucléaires, Strasbourg, France.
- ^cGesellschaft für Schwerionenforschung, Darmstadt, West Germany.
1. T. C. Awes, et al., Phys. Rev. Lett. 52, 251 (1984).
 2. A. Olmi et al., Phys. Rev. Lett. 44, 383 (1980).
 3. A. Gavron, Phys. Rev. C 21, 230 (1980).

THREE NUCLEI FRAGMENTATION IN LIGHT-ION REACTIONS AT
11 MeV/u BOMBARDING ENERGY

M. Bühler, A. Gorks, D. Pelte, B. Weissmann and U. Winkler

Physikalisches Institut der Universität Heidelberg and
Max-Planck-Institut für Kernphysik, Heidelberg, F.R. Germany

Heavy-ion reactions at bombarding energies above 10 MeV/u show clear evidence of a direct fragmentation into more than two nuclei¹⁻³). The magnitude of the cross section and the angular distribution of the fragments indicate, that this process cannot be interpreted as a deep inelastic reaction with subsequent fission. In this contribution it is shown that nuclear fragmentation is also observed in light-ion reactions at bombarding energies above 10 MeV/u.

Experimental Methods

The reactions $^{32}\text{S} + ^{58}\text{Ni}$ and $^{35}\text{Cl} + ^{58}\text{Ni}$ were studied at 355 MeV respectively 395 MeV beam energy. The experimental setup employed two large area ionisation chambers for the coincident detection of two heavy fragments and a light particle detector system consisting of twenty independent scintillation counters. The ionisation chambers, which cover a solid angle of 120 sr each, were mounted on opposite sides of the beam at positions ranging from 22 to 58 degrees with respect to the beam. 12 of the scintillation counters were mounted in the backward- and only 8 in the forward hemisphere to avoid shadowing the ionisation chambers.

In the off-line analysis the nuclear charges Z_i , the kinetic energies E_i and the linear momentum vectors \vec{p}_i of the two detected nuclei were deduced. The deficits (marked by delta) of these parameters were obtained using the conservation laws (quantities in the entrance channel are marked by 0):

$$\Delta Z = Z_0 - Z_1 - Z_2 ; \quad \Delta \vec{p} = \vec{p}_0 - \vec{p}_1 - \vec{p}_2 ; \quad Q_t = E_1 + E_2 + \Delta E - E_0 .$$

For the determination of the total Q value Q_t the assumption

$E = (\Delta p)^2 / 2\Delta m$ has to be made, which is valid only for exactly three particles in the exit channel. The deduction of nuclear charges, linear momenta etc. is correct for any number of particles. The distributions of the linear momenta are presented on the event-plane, which is defined by the coplanarity of the three momentum vectors \vec{p}_1 , \vec{p}_2 and $\Delta \vec{p}$ in the center of mass (cm) system. Additional information deduced from the scintillation counters are the multiplicity M of light particles and the ratio F/B of the number of particles detected in the forward and backward counters.

Results

The measured charge deficits clearly indicate the strong deviations from a true binary behaviour of the reactions studied. Fig.1 displays the charge deficit ΔZ of the ^{32}S induced reaction at two different detector positions. The smaller charge deficits with a maximum of the distribution at $\Delta z = 7$ are due to deep inelastic reactions with subsequent light particle evaporation⁴). Events with a charge deficit $\Delta z > 16$ only occur at beam energies larger than 10 MeV/u and indicate the fragmentation into more than two nuclei. The relative contribution of this component relative to the total yield increases from 3.4% (355 MeV) to 10% (395 MeV) and depends slightly on the detector positions.

In order to verify the binary or non-binary nature of the reactions the charge deficit ΔZ is plotted versus the sum of the recoil angles in the cm system (fig.2). The distribution of $\vartheta_1 + \vartheta_2$ should center around π for the normal binary component. Deviations from this requirement are caused by light particle evaporation and by the kinematical cuts due to the finite detector

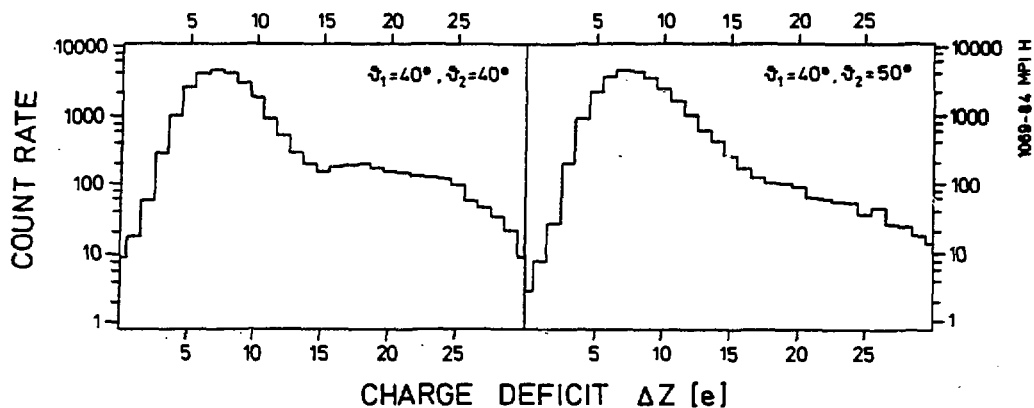


Fig.1 Measured charge deficits from the reaction $^{32}\text{S} + ^{58}\text{Ni}$.

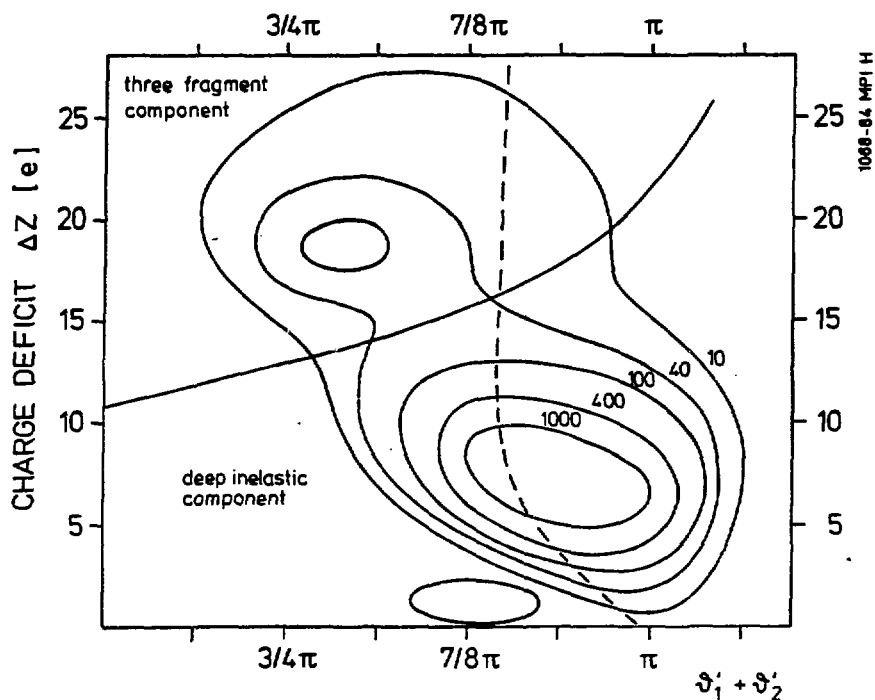


Fig.2 Dependence of the charge deficit on the sum of the recoil angles for the ^{32}S induced reactions.

dimensions. This is confirmed by Monte-Carlo calculations which assume a deep inelastic reaction mechanism with subsequent light particle emission (dashed curve in fig.2). The reactions up to $\Delta Z = 14$ show the predicted behaviour whereas the reactions at larger ΔZ values disagree with the predictions.

The changes in the reaction mechanism are also seen in the distributions of the linear momenta, which are displayed in fig.3. The reactions with $\Delta Z = 5$ show large momenta \vec{p}_1' and \vec{p}_2' of the two detected nuclei, whereas the distribution of the momentum deficit $\Delta\vec{p}'$ is centered near $\Delta p' = 0$. This behaviour is typical for deepinelastic reactions, as the primary fragments both emit light particles,

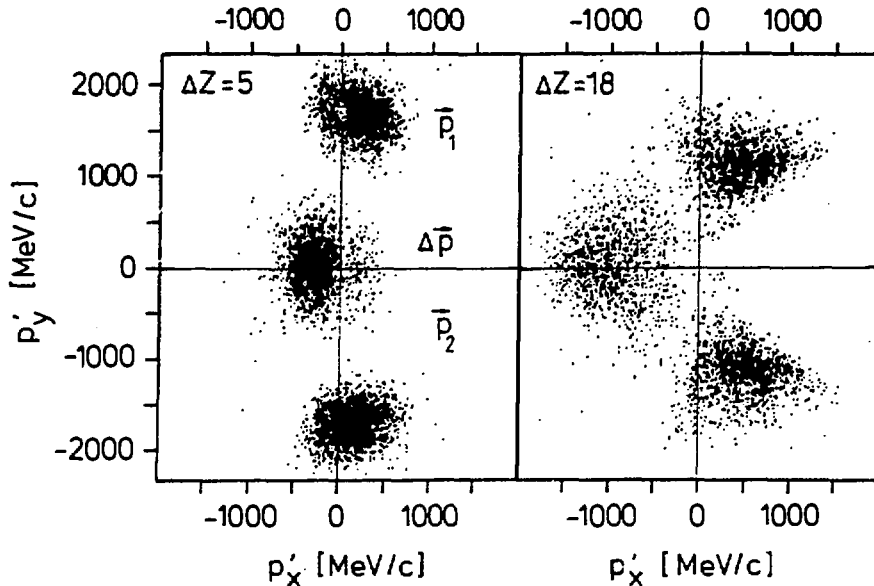


Fig.3 Measured momentum distributions of two exit channels of the reaction $^{32}\text{S}+^{58}\text{Ni}$.

whose linear momentum vectors add up to a distribution near zero. The reactions with $\Delta Z=18$ exhibit large momentum deficits which point against beam-direction. The absolute values of the three momenta are of about equal size and the collinearity of \vec{p}'_1 and \vec{p}'_2 is heavily disturbed. It is concluded that the occurrence of the large momentum deficits is mainly caused by a third heavy fragment.

The emission of some light particles in addition to three heavy fragments is indicated by the light particle data. The average measured multiplicities are $\langle M \rangle = 1.22$ for the reactions with $\Delta Z=5$ and $\langle M \rangle = 0.85$ for the reactions with $\Delta Z=18$. The correction factors caused by the efficiency of the scintillation counters are estimated from Monte-Carlo calculations to be around 4. Values of $\langle M \rangle \neq 0$ prove the emission of light particles, but the number is too small to account for the total missing charge $\Delta Z=18$. A comparison of the ratio F/B between the deep inelastic and the three fragment exit channels shows, that the light particles are emitted from all two respectively three fragments.

In fig.4 the distribution of the total Q value Q_t is displayed for the three fragment exit channels of the reaction $^{32}\text{S}+^{58}\text{Ni}$ at 355 MeV. The mean value indicated by the arrow is $\langle Q_t \rangle = -142$ MeV. This value is estimated to be 10-15 MeV too negative since the additional emission of light particles introduces a systematic shift. Still it can be concluded that three nuclei fragmentation only occurs at large energy losses.

Conclusion

In the reactions studied three fragment exit channels were clearly identified by means of the charge and momentum deficits deduced from two completely measured fragments and by the multiplicities of light particles. The reaction mechanism appears to be that of a direct fragmentation process and not of a normal deep inelastic process with subsequent fission of one of the two primary fragments. The reasons for this hypothesis are: First the observed charge deficit and elemental distributions are broader than the distribution one expects from sequential fission. Second a sequential fission results in a $\Delta \vec{p}'$ distribution

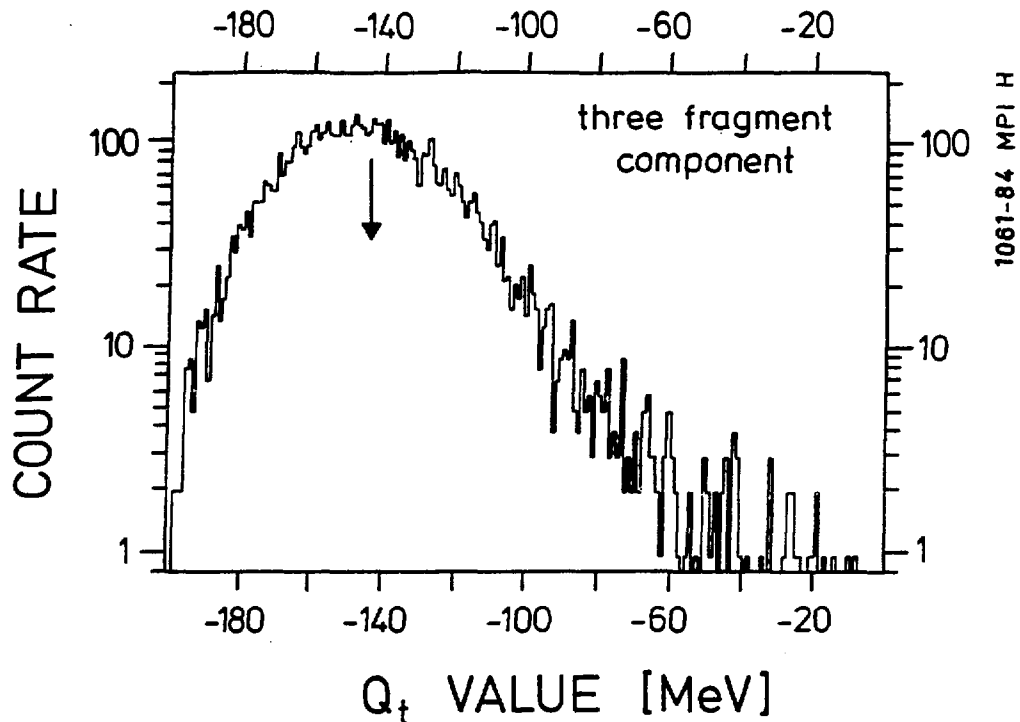


Fig.4 Distribution of the total Q value for the three fragment exit channels of the ^{32}S induced reactions

centred around $\Delta p'=0$ whereas in fig.3 large momentum deficits are observed. Thus we are tempted to believe that all three fragments are emitted in one step.

This work was supported by Bundesministerium für Forschung und Technologie, Federal Republic of Germany

References:

- 1) A. Olmi, U. Lynen, I.B. Natowitz, M. Dakowski, P. Doll, A. Gobbi, H. Sann, H. Stelzer, R. Bock and D. Pelte, Phys. Rev. Lett. 44 (1980) 383
- 2) P. Glässel, D. v. Harrach, H.J. Specht and L. Grodzins, Z. Phys. A310 (1983) 189
- 3) T.C. Awes, R.L. Ferguson, R. Novotny, F.E. Obenshain, F. Plasil, V. Rauch G.R. Young, 11. International Workshop on Gross Properties of Nuclei and Nuclear Excitations, Hirschegg, Austria, 1983
- 4) J. Betz, H. Gräf, R. Novotny, D. Pelte and U. Winkler, Nucl. Phys. A408 (1983) 150

FIRST RESULTS OF 35 MeV/u Kr + Au
EXPERIMENT AT GANIL (Caen)

Collaboration CAEN-SACLAY-STRASBOURG

J.C. ADLOFF⁺, B. BOISHU*, D. DALILI^o, A. GENOUX-LUBAIN*,
A. KAMILI⁺, C. LE BRUN*, J.F. LECOLLEY*, F. LEFEBVRES*,
P. LHENORET^o, M. LOUVEL*, R. LUCAS^o, C. MAZUR^o, C. NGO^o,
R. REGIMBART*, M. RIBRAG^o, G. RUDOLF⁺, F. SCHEIBLING⁺,
T. SUOMIJARVI^o and E. TOMASINI^o.

* Laboratoire de Physique Corpusculaire LA34 - ISMRA
Université de Caen - 14032 CAEN CEDEX - France

^o Service de Physique Nucléaire - Métrologie Fondamentale
CEN SACLAY - 91191 GIF SUR YVETTE CEDEX - France

⁺ CRN Strasbourg - 67037 STRASBOURG CEDEX - France

Communication presented by F. LEFEBVRES
at the Winter Workshop on nuclear dynamics III
COPPERMOUNTAINS - COLORADO
March 5-9 1984


INTRODUCTION

We present here, the preliminary results and interpretations of the first experiment done at GANIL with a 35 MeV/u Kr-beam on Au target (100 $\mu\text{g}/\text{cm}^2$ thickness).

This experiment was conducted by the CAEN-SACLAY-STRASBOURG collaboration which has been established to measure the angular and kinematical correlations between 3 or 4 fragments produced in the heavy ion collisions at intermediate energy. The aims of these studies are linear and angular momentum transfer between the projectile and the target, breaking of the projectile and search for new reaction mechanisms in this rather unknown energy domain.

We know from the past and in particular at low energy (discovery of the deep inelastic reactions) the importance of the size of the projectile and there is some hope that new behaviours of nuclear matter will merge in increasing the projectile energy.

EXPERIMENTAL SET UP

This experiment has been operated with an experimental set up made of large solid angle gaseous detectors, this instrumentation is planned to grow in the future in order to cover a nearly complete solid angle in the forward direction and around the target. In the fig. 1, we present an horizontal schematic view of the experimental set up which operates in the big vacuum reaction chamber called Nautilus¹⁾. This instrumentation is composed of parallel plate avalanche counters (PPAC) 

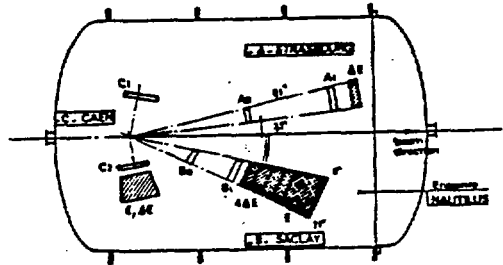




Fig. 1

with XY localisation and time of flight measurements between associated detectors and also the RHF (Radio high frequency) of the last separated sector cyclotron of GANIL and ionization chambers using either transversal electric field collection  or longitudinal electric field collection  compared to the fragment trajectory. Let describe shortly the measured fragment physical parameters.

- The STRASBOURG set of detectors labelled A (two PPAC and ΔE detector) was centered around the grazing angle ($\theta_g \approx 7^\circ$) in an angular range between 3.5° and 9.1° . It gives Z_A and \vec{V}_A the atomic number and velocity vector of the fragment emitted in the forward direction in a solid angle of 1.2×10^{-2} sr.

- The SACLAY MF set of detectors labelled B (two PPAC and a big ionization chamber of Darmstadt type) covered an angular domain above the grazing angle ($8-21^\circ$) and gives $Z_B, A_B, E_B, \theta_B, \omega_B$ of the detected fragment.

- The CAEN set of detectors labelled is composed of two PPAC C_1 and C_2 located at large angle $\bar{\theta}_{1,2} = 80^\circ$ ($100^\circ < \theta_{1,2} < 60^\circ$) with a solid angle $\Delta\Omega_{1,2} \approx 1$ sr, C_2 is followed by a longitudinal electric field ionization chamber that gives either a E_2 or ΔE_2 measurements. C_1, C_2 detectors give respectively \vec{V}_2, Z_2, A_2 and \vec{V}_1 (\vec{V}_i being the velocity vectors, Z, A atomic and mass number of detected fragment).

PRESENTATION OF PRELIMINARY DATA

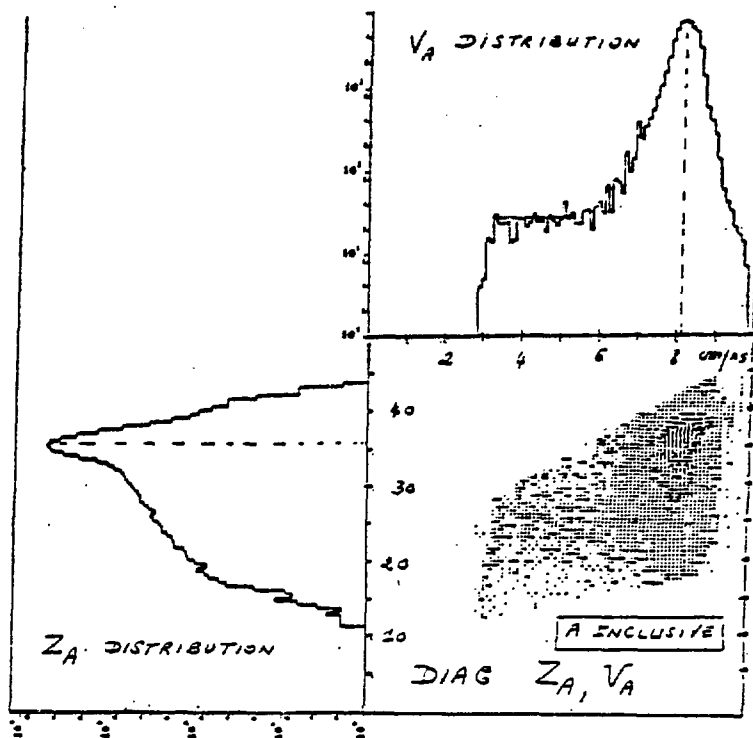


FIG. 2

We present in fig. 2 (only a part of the available data) the diagram Z_A, V_A (atomic number versus velocity in cm/ns) of the fragments detected in the forward direction around the grazing angle in the set of detectors A without conditions on the other detectors that is A inclusive data. At the left and upper parts of this diagram are shown the projected distributions with a logarithmic scale. We see at first the dominance of the elastic peak ($Z_A=36$ with beam velocity 8.2 cm/ns) and the quasi elastic events. Also, we observed the events produced by the fragmentation mechanism which are reduced in Z_A compared to $Z_A=36$ and with a velocity slightly lower than the beam one. Another class of events of particular interest appears in this diagram Z_A, V_A that corresponds to rather important relaxation in velocity $V_A < 6$ cm/ns or in $E/A < 18.5$ MeV/u associated with atomic number less than 30. These events represent approximately 1% of the cross section which is dominated by the elastic, quasi elastic and fragmentation events.

We present in fig. 3 now the same diagram Z_A, V_A under the condition AC_1C_2 inclusive, that corresponds to a fragment emitted in the forward direction around the grazing angle and two fragments detected at large angles in opposite directions. Firstly we remark as it is normal the disparition of the elastic events but also of the class of events which is highly relaxed in velocity and Z . The bulk of the events are associated with beam velocity and with a Z_A distribution that peaks at values around $Z_A=33$, that is fragmentation of the projectile.

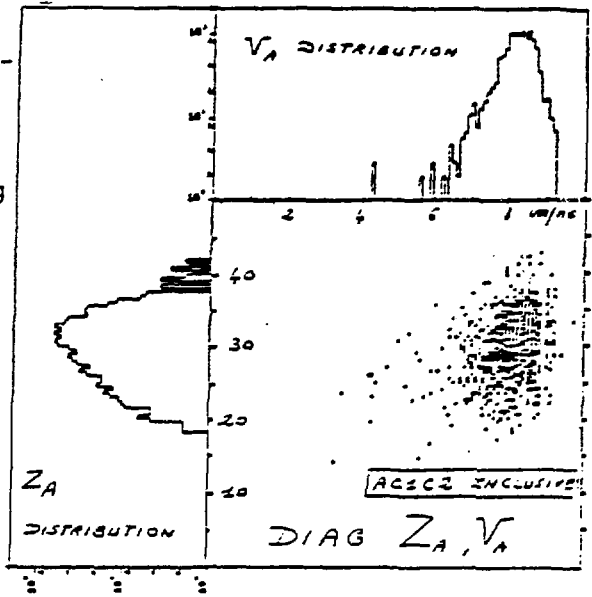


FIG. 3

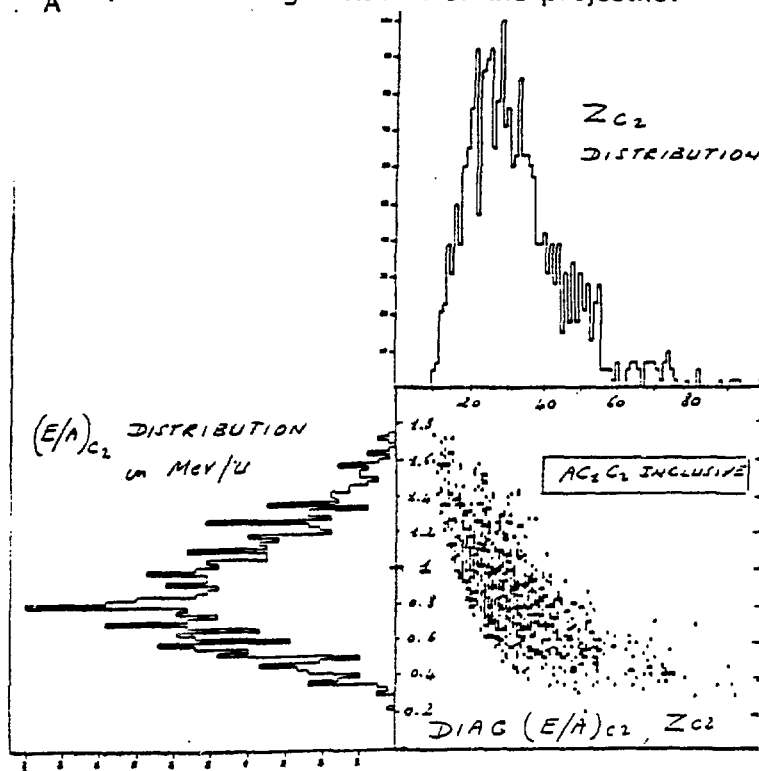


FIG. 4

In fig. 4, we show the diagram $(E/A)_{C_2}, Z_{C_2}$ (Z_{C_2} fragment detected detector C_2 under the condition AC_1C_2 inclusive). We see from the correlation between the velocity and the charge of the emitted fragment at large angle that we have to deal with the fission of the target residue produced in the primary interaction. Z_{C_2} distribution peaked around 30 with an associated $E/A \sim 0.8$ MeV/u. If we take into account the precedent informa-

tions (cf. fig. 3) on the A projectile residue ($\Delta Z_{.3}, \Delta Z_{.4}$ losses) it rea-

reasonable to think that we detected fission fragments after proton and neutron evaporation (more detailed kinematical balance will be done on this class of event in the future).

We present now²⁾ in figures 5 and 6 respectively the kinetic energy per nucleon $(E/A)_B$ of the B products with $E/A > 10$ MeV/u and the associated Z_B distribution under the condition B inclusive (fragments emitted above the grazing angle, $8^\circ < \theta < 21^\circ$, in the forward direction). In the $(E/A)_B$ spectrum, the dominant features are the absence of the fragmentation mechanism and the concentration of nearly all the products for $E/A < 18$ MeV/u and the Z_B distribution is rather flat between $Z=21$ and $Z=26$.

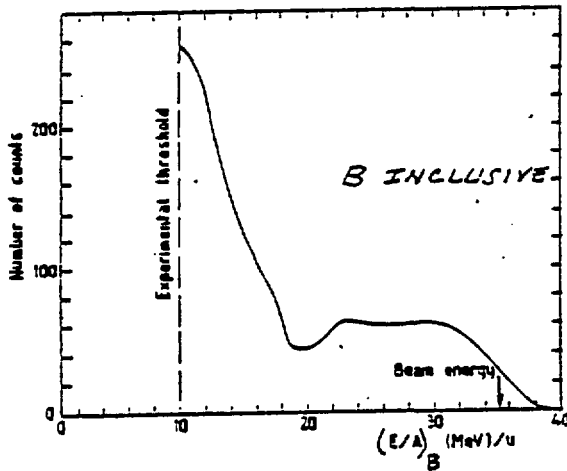


FIG. 5

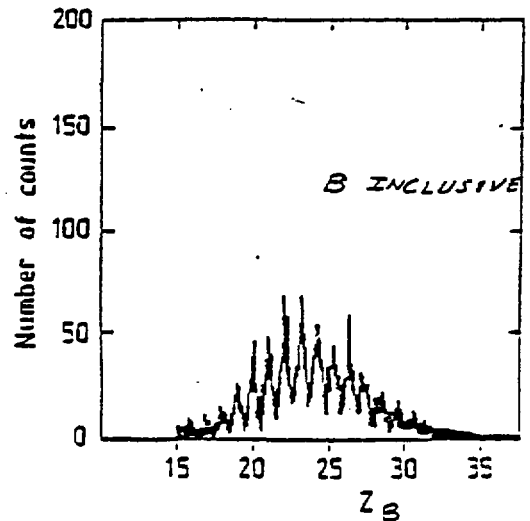


FIG. 6

The fig. 7 presents now the diagram Z_A, V_A under the condition AB inclusive, that means two fragments emitted in the forward direction; we see the fragmentation events with the class of events relaxed in Z and velocity precedently observed in the A inclusive data. If we isolate (rectangular cuts) these events we get after projections the V_A and Z_A distributions in fig. 8. These distributions are peaked at $Z_A = 23$ and $(E/A)_A = 12$ MeV/u)

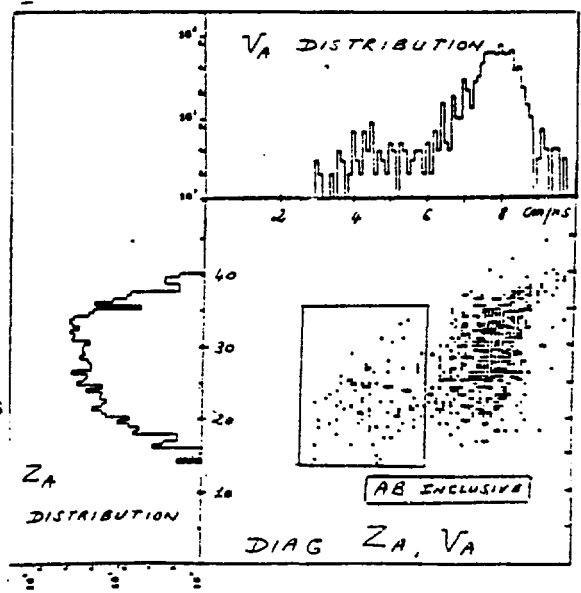


FIG. 7

At the time of this communication, we cannot present the physical parameters of the B fragments in coincidence with the distributions shown in fig. 8. Nevertheless, it is reasonable to associate the Z_A and V_A spectrum with the most probable B events in figures 5 and 6, that is the highly energy relaxed products.

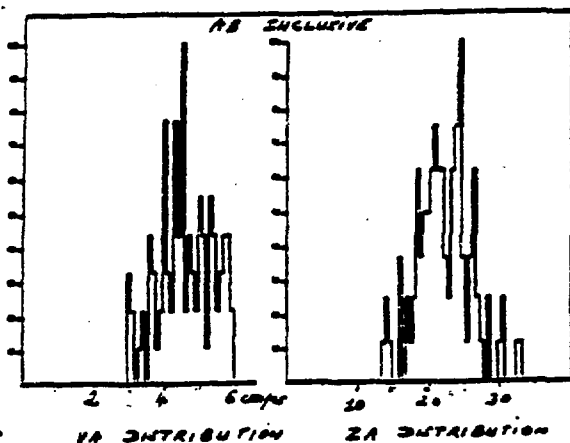


FIG. 8

To explain this interesting part of the data, we have developed simple kinematics based only for the moment on the following simple assumptions : the Kr projectile cuts a piece of the target matter and fuse with it, in this way the velocity of this new nucleus is slowed down in proportion of the size of the removed target part. This highly excited nucleus with a lot of angular momentum decays by a binary symmetrical fission. At this preliminary stage of the interpretation we leave open the internal energy repartition between the fragments involved in the primary stage of the reaction and we have used only the momentum conservation. Because the fission fragment velocities in the rest frame of the decaying nucleus are much lower than the laboratory velocity of the created fragment, the fission fragments are collimated in an angular aperture defined by θ^{\max} and θ^{opening} being respectively the maximum emission angle and maximum opening angle. Due to the properties of the Jacobian, the differential cross section for the detection of one fragment and the opening angle distribution peaked respectively at the corresponding angle θ^{\max} and θ^{opening} . The fig. 9 presents the variation of these angles as a function of the fission fragment atomic number Z_{FF} or its $(E/A)_{FF}$ in MeV/u.

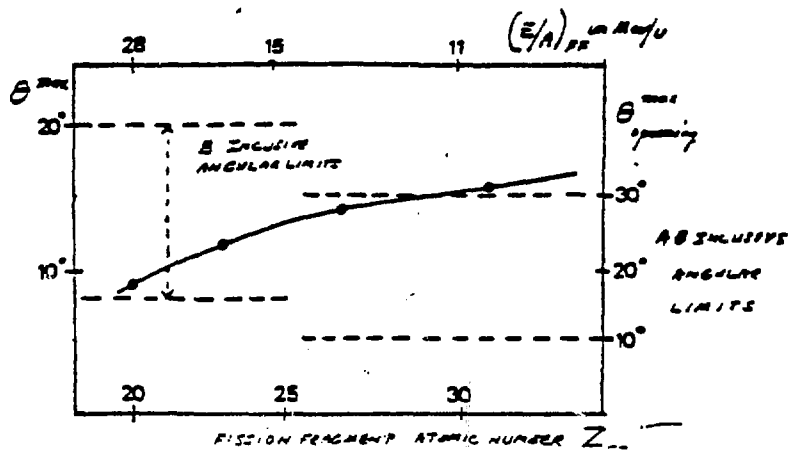


FIG. 9

If we think of the crude approximations used in the kinematics, no corrections for charged particle and neutron evaporations and the fact that we must take into account dynamical effects correlated to the impact parameter, the observed production in the forward direction highly energy relaxed fragments can be explained in a satisfactorily manner by a massive transfer of the order of 35 nucleons from the target to the Kr projectile, the new nucleus created decaying by fission.

In conclusion, the dominant features that merge from our preliminary results and interpretations are that we are dealing with fast binary reactions in the early stage of interaction followed later by sequential decays by fission. These facts are obtained by the short interaction time compared to the low energy domain, the large energy and rather high angular momentum in the entrance channel.

In the forward direction, around the grazing angle we observed the dominance of the Kr fragmentation that disappears above this angle. This fragmentation is associated with the fission of the target residue.

On a small sample of coincident events in the forward direction than we have analysed, we have evidence for the creation of nuclei of mass number A of the order of 120 that decay by fission.

REFERENCES

- 1) A large vacuum reaction chamber NAUTILUS for the GANIL experimental areas.
Internal report - Laboratoire de Physique Corpusculaire - University of Caen - Centre de Recherches Nucléaires - Strasbourg
- 2) Experimental evidence of highly energy relaxed products in the 35 MeV/u Kr+Au reaction.
D. DALILI et al - Submitted to Z. Phys.

LINEAR MOMENTUM TRANSFER STUDIES AT ENERGIES AROUND 100 MeV/u

Y. Cassagnou¹, M. Conjeaud¹, R. Dayras¹, S. Harar¹,
 E. Kankeleit², G. Klotz², R. Legrain¹, M.S. Nguyen¹,
H. Oeschler², E.C. Pollacco¹, F. Saint-Laurent³, C. Volant¹

¹D.Ph.N./B.E., C.E.N. Saclay, France

²Inst. für Kernphysik, TH Darmstadt, Germany

³G.A.N.I.L., Caen, France

INTRODUCTION

In nucleus-nucleus collisions above the Fermi velocity a transition from nucleus-nucleus collisions to nucleon-nucleon interactions is expected¹. The study of this transition is subject of our experimental program at Saturne II which up to now has been carried out using light projectiles and at GANIL with heavy projectiles.

In order to characterize the reaction mechanisms we take the linear momentum transferred from the projectile to the target. This quantity is accessible by the measurement of the angle and velocities of the fission fragments². By the use of heavy targets such as Th nearly all reactions terminate by fission and a general view of the occurring mechanisms can be obtained. Detailed informations are obtained if lighter target nuclei are used whereby fission is less probable and only a selected range of impact parameters leads to fission. Or by precisely measuring all kinematic quantities in order to reconstruct the event. These various aspects mark the structure of my talk: In the first part, based on the measurements on Th, a classification of the reaction mechanisms is proposed^{3,4}, and in the second part, at first, data on lighter nuclei are discussed whereby high transferred momenta are selected and secondly, the precise measurements performed at GANIL are presented.

Before continuing, I would like to clarify that the quantity "linear momentum transfer" is not a measure of the

nuclear stopping power. After the primary reaction between projectile and target, fast particles might be emitted taking away forward momentum. But when equilibrium is reached the recoil velocity is no longer changing and the fission process gives access to this velocity. Hence, we measure the momentum left in the target nucleus at the instant when equilibrium is reached.

By these arguments it is assumed that the two fragments arise from a fission process as known from low-energy experiments. And indeed, all experimental quantities (kinetic energy of fission fragments, width of mass distribution, angular distribution,...) are in agreement with this assumption.

1. CLASSIFICATION OF THE REACTION MECHANISM

The comparison of the angular correlations at incident energies from about 10 MeV/u to 250 MeV/u is given in fig.1 for the α -induced reactions on Th/U nuclei. This figure illustrates the transition from the low-energy behaviour to the typical high-energy domain. The arrows indicate the angles corresponding to full momentum transfer. At low energies, most of the reactions lead to complete fusion and the shoulder at 180° represents the direct processes. At 35 MeV/u, the maximum of the correlation function is no longer at the full-momentum-transfer location. At 70 MeV/u, the maximum moves to larger opening angles and only about half of the available beam momentum is transferred to the target. At even higher energies, the maximum is

close to 180° as only a small fraction of the available beam momentum is transferred, a typical behaviour for high energies and in agreement with intra-nuclear-cascade calculations*.

In fig.2, the mean linear momentum transferred per projectile nucleon is presented as function of the incident energy per nucleon. The full curve indicates complete momentum transfer for all projectiles. From this figure, we suggest a classification of the dominating reaction mechanisms into three energy regimes²:

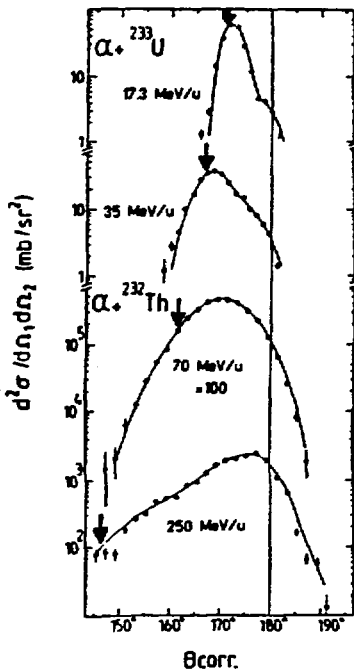


Fig.1: In-plane angular correlations of α -induced reactions on Th/U targets. Full momentum transfer is indicated by an arrow and zero momentum transfer by a thin line at 180° . The data $\alpha + U$ are from ref.5.

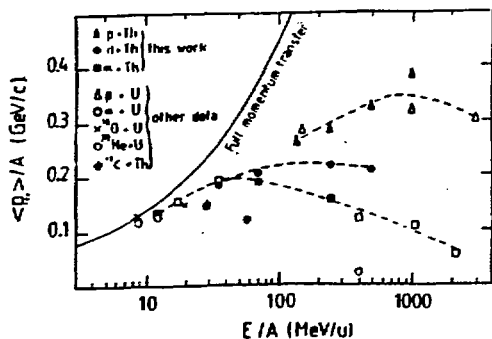


Fig.2: Mean momentum transfer versus energy per nucleon. The other data are from refs.2,5-11.

(i) Below 10 MeV/u, the incident particles transfer their momentum almost completely to the target. Complete fusion is the dominating process even for heavy projectiles like ^{16}O and ^{22}Ne .

(ii) Between 10 MeV/u and about 70 MeV/u, the data points fall below the full-momentum-transfer curve but still more than half of the incident beam momentum is transferred to the target. Furthermore, alpha particles and deuterons exhibit a scaling, i.e., the transferred momentum is proportional to the mass of the projectile.

(iii) The 70 MeV/u to about 1000 MeV/u range correspond to a transition region characterized by several features: The data points fall drastically below the full-momentum-transfer location. While the momentum transferred by protons continues to increase with energy, the momentum transfers induced by deuterons and alpha particles drop with different slopes, i.e. the scaling observed in (ii) is lost.

11. SELECTION OF HIGH P_t

An interesting question concerns the possibility to transfer the full beam momentum. Unfortunately, this can not easily be deduced from the data with the Th target as evaporation from the fission fragments smoothes out the direct connection between correlation angle and linear momentum transfer. The angular correlations have been unfolded in order to correct for this contribution*. This yields the probability for each transfer and hence, the probability for full transfer.

a) α ON MEDIUM-MASS NUCLEI

Another way to study the probability for high p_t consists in using lighter target nuclei. We have bombarded α particles on Au, Ho and Ag at 70 MeV/u and 250 MeV/u. The fission cross section drops drastically for the lighter nuclei as expected due to increasing fission barrier.

It turns out that for less fissile nuclei fission occurs only if relatively high linear momenta have been transferred, a result, which can be understood as fission of light nuclei requires high excitation energies corresponding to high transferred momenta.

The fission fragment mass distribution of $A=100$ nuclei represents an interesting point as it is predicted that the mass splitting becomes broad due to the proximity of the Businaro-Gallone point¹². The existing data concerning this question are summarized in ref.¹¹. A very preliminary analysis of the α on Ag data indicates no effect of the predicted Businaro-Gallone point.

Fig. 3 shows preliminary results evidencing the selectivity in p_{\perp} . For each event p_{\perp} has been calculated from the correlation angle and the velocities of the two fragments. Thereby, the broadening due to evaporation is not corrected. The data at 250 MeV/u show the selectivity in the best way; the peripheral collisions dominating the distribution obtained by the Th target disappear when bombarding a Au target. The fission

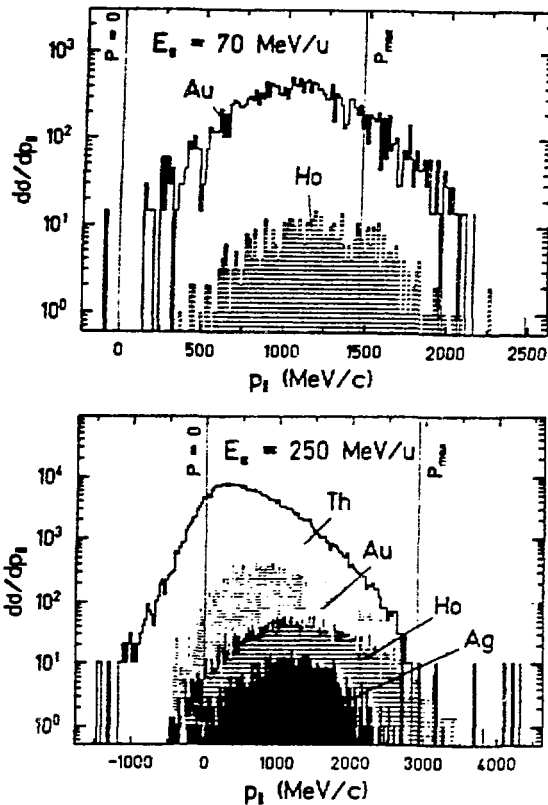


Fig.3: Angular correlation measurements converted into a p_{\perp} scale. The ordinate represent relative yields. (preliminary data).

reactions induced on the Ho target represent even higher transfers. However, the fraction of events fissioning after the bombardment on Ag does not indicate a further selection to high values of p_{\perp} . (in ref.⁶, the selectivity in angular momentum is discussed, too.)

At 70 MeV/u (fig.3a) the reactions induced on the Ho target terminating by fission correspond to nearly full momentum transfer (1.5 GeV/c). Of course, higher values in p_{\perp} can be transferred with heavier projectiles as will be discussed next. But the existence of nearly full momentum transfer can be seen at a beam velocity which is the double Fermi velocity. From the measured mass spectra we can conclude that about 21 nucleons are emitted, a result which accords with the assumption that all beam energy has been converted into internal excitation.

Summarizing this part we can state that full momentum transfer is possible with α particles of 70 MeV/u and it occurs with a probability of a few percent. Compound-like nuclei with high excitation energies are formed.

b) ^{44}Ar OF 44 MeV/u ON HEAVY NUCLEI

The aim of this experiment is to measure precisely the angles, energies, masses and velocities of both fission fragments. This is achieved by two time-of-flight setups each consisting of a channel-plate assembly and a solid-state detector on one side and six surface barrier detectors on the opposite side. The kinematic reconstruction yields p_{\parallel} and p_{\perp} for each event. Fig. 4 shows the measured angular correlation for the two targets Au and Th. Both distributions are characterized by a maximum at 155° and 164° , resp. and an extended tail towards higher transferred momenta. On Au as expected the peripheral collisions are not leading to fission.

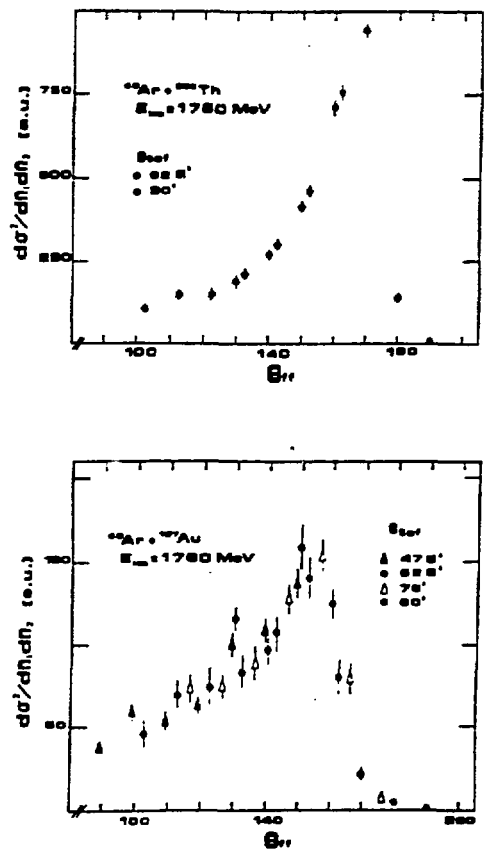


Fig.4: Angular correlation of 44 MeV/u Ar on Th and Au.

The results of these measurements are briefly summarized as follows^{1,2}:

- The velocities between the two fission fragments agree excellently with the Viola systematics. (besides the very high momentum transfer region in the bombardment of Au).
- The sum of the masses of the fission fragments decreases linearly with transferred linear momentum.
- The perpendicular momentum is highest for the peripheral collisions leading to small values of p_{\perp} .

From these facts we conclude that the data points around 85° to 110° are not tails of the maximum smeared out by evaporation but events representing linear momentum transfers of up to 6.5 GeV/c and 4.9 GeV/c, resp. for the nuclei Au and Th, resp.. Consequently, high excitation energies up to 1 GeV are reached in these collisions.

This work is partially supported by the BMFT.

REFERENCES

1. e.g. Proceedings of the International Conference on Nucleus-Nucleus Collisions, MSU, sept. 1982, Nucl. Phys. A400(1983).
2. T. Sikkeland, E.L. Haines and V.E. Viola Jr., Phys. Rev. 125(1962)1350.
3. F. Saint-Laurent, M. Conjeaud, R. Dayras, S. Harar, H. Oeschler and C. Volant, Phys. Lett. 110B(1982) 372.
4. F. Saint-Laurent, M. Conjeaud, R. Dayras, S. Harar, H. Oeschler and C. Volant, Nucl. Phys. in print.
5. W.G. Meyer, H.H. Gutbrod, Ch. Lukner and A. Sandoval, Phys. Rev. C22(1980)179.
6. L.P. Remsberg, F. Plasil, J.B. Cumming and M.L. Perlman, Phys. Rev. 187(1969)1597.
7. A.A. Kotov, G.G. Semenchuk, B.A. Bochagov, B.L. Gorshkov, G.G. Kovshennyi, V.R. Reznik and G.E. Solyakin, Yad. Fiz. 17(1973)950; Sov. J. Nucl. Phys. 17(1973)498.
8. B.B. Back, K.L. Wolf, A.C. Mignerey, C.K. Gelbke, T.C. Awes, H. Brauer, V.E. Viola Jr. and P. Dyer, Phys. Rev. C22(1980)1927.
9. J. Galin, H. Oeschler, S. Song, B. Borderie, M.F. Rivet, I. Forest, R. Bimbot, D. Gardès, B. Gatty, H. Guillemot, M. Lefort, B. Tamain and X. Tarrago, Phys. Rev. Lett. 48(1982)1787; M.F. Rivet, B. Borderie, S. Song, D. Guenreau, H. Oeschler, R. Bimbot, I. Forest, J. Galin, D. Gardès, B. Gatty, M. Lefort, B. Tamain and X. Tarrago, Nucl. Phys. A387(1982)143c.
10. U. Lynen, H. Ho, W. Kühn, D. Palte, U. Winkler, W.F.J. Müller, Y.-T. Chu, P. Doll, A. Gobbi, K. Hildenbrand, A. Olmi, H. Sann, H. Stalzer, R. Bock, H. Löhner, R. Glasow and R. Santo, Nucl. Phys. A387(1982)129c.
11. V.E. Viola Jr., R.G. Clark, W.G. Meyer, A.M. Zebelman and R.G. Sextro, Nucl. Phys. A261(1976)174.
12. U.L. Businaro and S. Gallone, Nuovo Cimento 1(1955) 629 and 1277.
13. H. Oeschler and H. Freiesleben, in: Lecture Notes in Physics Nr.107, Springer-Verlag, Heidelberg
14. E.C. Pollacco, M. Conjeaud, S. Harar, C. Volant, Y. Cassagnou, R. Dayras, R. Legrain, M.S. Nguyen, H. Oeschler and F. Saint-Laurent, to be published.

ENHANCED EMISSION OF NON-COMPOUND LIGHT PARTICLES IN THE REACTION PLANE

M. B. Tsang

National Superconducting Cyclotron Laboratory

Michigan State University

E. Lansing MI 48824

As the bombarding energy is raised above 10 MeV per nucleon processes involving incomplete fusion become increasingly important. These processes can be studied, for example, by measuring the momentum transfer to the composite system or by measuring the accompanying non-compound light particle emission. Little is known at present about the dynamics of reactions which lead to incomplete momentum transfer. In this talk, I will discuss measurements of fission fragment - light particle correlations and light particle - light particle correlations which provide new dynamical information about these reactions and in particular indicate an unexpected enhancement for non-compound light-particle emission in the reaction plane.

In an experiment performed at the K500 cyclotron at Michigan State University we have measured light particles in coincidence with two fission fragments for ^{14}N induced reactions on ^{197}Au at 420 MeV incident energy. The fission fragments were detected with two large area position sensitive parallel plate avalanche detectors. Light particle telescopes consisting of silicon- ΔE and NaI-E detectors were placed both in ($\phi_x = 0^\circ$) and out ($\phi_x = 90^\circ$) of the plane defined by the centers of the two fission detectors and the beam axis where ϕ_x denotes the azimuthal angle about the beam axis between this plane and the light particle telescope.

The momentum transferred to the composite system was determined by measuring the folding angle between the two outgoing fission fragments. Unlike observations with more fissile targets, however, transfer and inelastic reactions characterized by small linear momentum transfers contribute negligibly to the fission cross section for reactions on the ^{197}Au target. For events which lead to fission, the most probable linear momentum transfer corresponded to about 85% of the beam momentum. This is similar to the most probable momentum transfer observed for fusion-like reactions on ^{238}U at the same beam energy¹. Much of the missing momentum is carried away by non-equilibrium light particle emission. In Fig. 1, the component of the momentum parallel to the beam axis for the detected light particle is plotted against the corresponding measurement of the most probable momentum transferred to the fissioning system. If the final state of the reaction consisted of the two fission fragments and only one light particle, conservation of momentum would dictate that the data would lie along a line defined by $P_x + P_R = P_{\text{beam}}$, where P_x is the component of the momentum parallel to the beam for the light particle and P_R is the momentum transfer. For reference, the line defined by $P_x + P_R = .85 \cdot P_{\text{beam}}$ is also indicated. Irrespective of the type or energy of light particle detected, most of the beam momentum (>80%) not carried by the observed light particle is transferred to the fissioning system.

Present experimental information on noncompound particle emission in fusion-like reactions supports the concept of statistical emission from a localized region of high excitation^{2,3}. For angles less than or equal to 70° and light particle energies greater than 25 MeV, noncompound light particle emission is the dominant contribution to the light particle energy spectra. The energy spectra of light particles in coincidence with fission-fragments detected in- and out- of-plane suitably averaged are very similar to the inclusive light particle energy spectra indicating that conclusions drawn from the coincidence data may be generalized to the singles as well. Since the angular momentum of the fissioning system is nearly perpendicular to the entrance channel reaction plane, the

plane of detected fission fragments can be used to indicate the reaction plane. The ratios of out-of-plane to in-plane energy integrated coincidence spectra for p, d, t and alphas scattered to a polar angle of 55° with respect to the beam axis are plotted in Fig. 2 where the energy integration intervals are indicated by the horizontal bars. The ratio decreases significantly with increasing energy and with increasing mass of the coincident light particles. For the highest energy alpha particles, azimuthal anisotropies of up to one order of magnitude are observed.

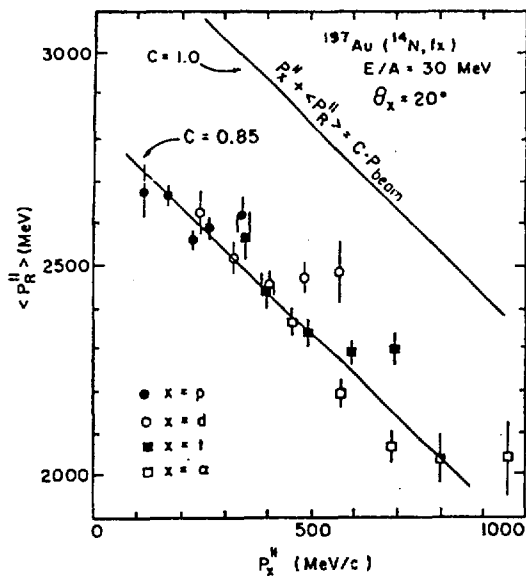


Fig. 1

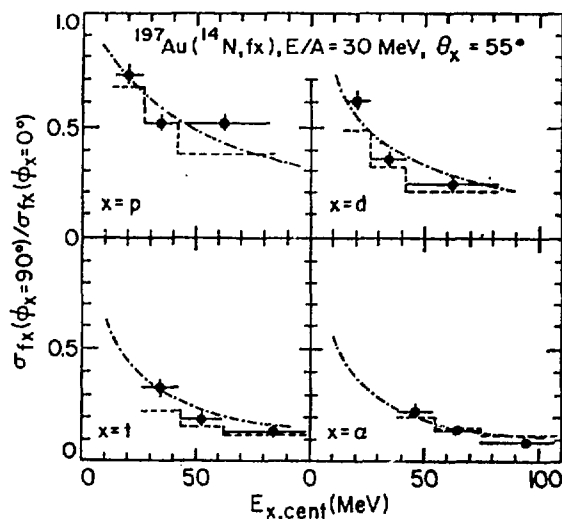


Fig. 2

Although particle emission from such localized regions of excitation may be expected to be azimuthally anisotropic due to geometrical shadowing⁴ or dynamical flow effects, until now, no azimuthal anisotropies have yet been established experimentally. The observed enhanced emission of nonequilibrium particles in the reaction plane can be easily accounted for by assuming the existence of an ordered collective motion of the emitting source in the reaction plane and transverse to the beam. Two schematic calculations adopting a) a model of an emitting source which rotates about an axis perpendicular to the reaction plane while moving parallel to the beam axis; and b) a model of a moving source with parameterization corresponding to a Maxwellian distribution in a rest frame which moves at an angle of 29° with respect to the beam axis. Details of both calculations will be presented in Ref. 5. In both calculations the velocity of the source parallel to the beam axis is assumed to be about .4 of the beam velocity, thus the collective motion here described is obviously quite distinct from a rigid rotation of the compound nucleus. The results of these calculations are compared to the measurements in Fig. 2. Calculations with the rotating source appear as dashed histograms while the dot-dashed lines were calculated assuming a deflected source. Since both of these rather simple models qualitatively describe the data, it is likely that similar agreement could be obtained by other models which superimpose random statistical motion of the participating nucleons upon a transverse collective velocity of approximately .05c.

Such collective flow effects of the emitting source in the reaction plane can be further illustrated with results obtained from light particle - light particle correlations obtained in a measurement of ^{16}O induced reactions on an ^{197}Au target at the Holifield Heavy-Ion Research Facility at ORNL. For simplicity we limit our discussion to data where the light particles are detected at polar angles of $\theta_1 = 40^\circ$, $\theta_2 = 70^\circ$ and have the relative azimuthal angle (ϕ) about the beam axis between the two coincident light

particle detectors which varies from 0° (where the particles are detected on the same side of the beam) to 180° (opposite sides). In Fig. 3, the ratio $\sigma_{12}/\sigma_1\sigma_2$ (where σ_{12} and σ_1, σ_2 are the coincidence and singles cross sections respectively) is plotted against the relative azimuthal angle (ϕ) for pp, pd, dd and dt correlation data. In all cases, suppression of emission of light particles at $\phi=90^\circ$ can be seen clearly. The suppression of emission at $\phi=90^\circ$ becomes more significant with increasing mass of the emitted particles. Neglecting for the moment attenuation of particle emission due to the presence of spectator nucleons surrounding the regions of particle emission, calculations using the rotating emitting source as discussed above reproduce the general features of the data. The calculations are plotted as solid curves in Fig. 3.

The relative magnitudes of the correlations at $\phi=0^\circ$ and $\phi=180^\circ$, however, are not reproduced by the calculation. For the two correlations involving protons, the correlation at $\phi=180^\circ$ corresponding to emission to opposite sides of the beam axis is larger than that at $\phi=0^\circ$ where the particles are detected on the same side of the beam. This type of enhancement can be expected due to the constraint imposed by momentum conservation on a system with a finite number of particles³. In contrast, when both of the detected particles are either deuterons or tritons, the correlation is significantly larger at $\phi=0^\circ$. This suppression of emission at $\phi=180^\circ$ is probably due to shadowing since both of these composite particles have rather short mean free paths and are expected to be extensively shadowed by any surrounding cold target spectator matter.

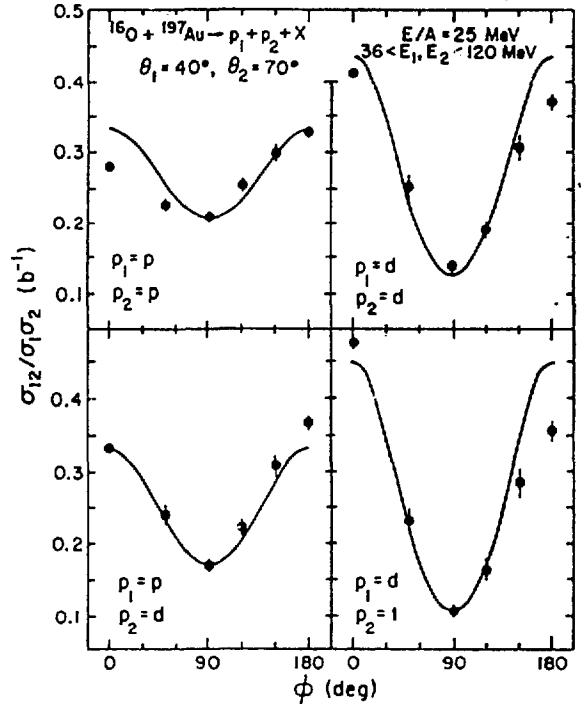
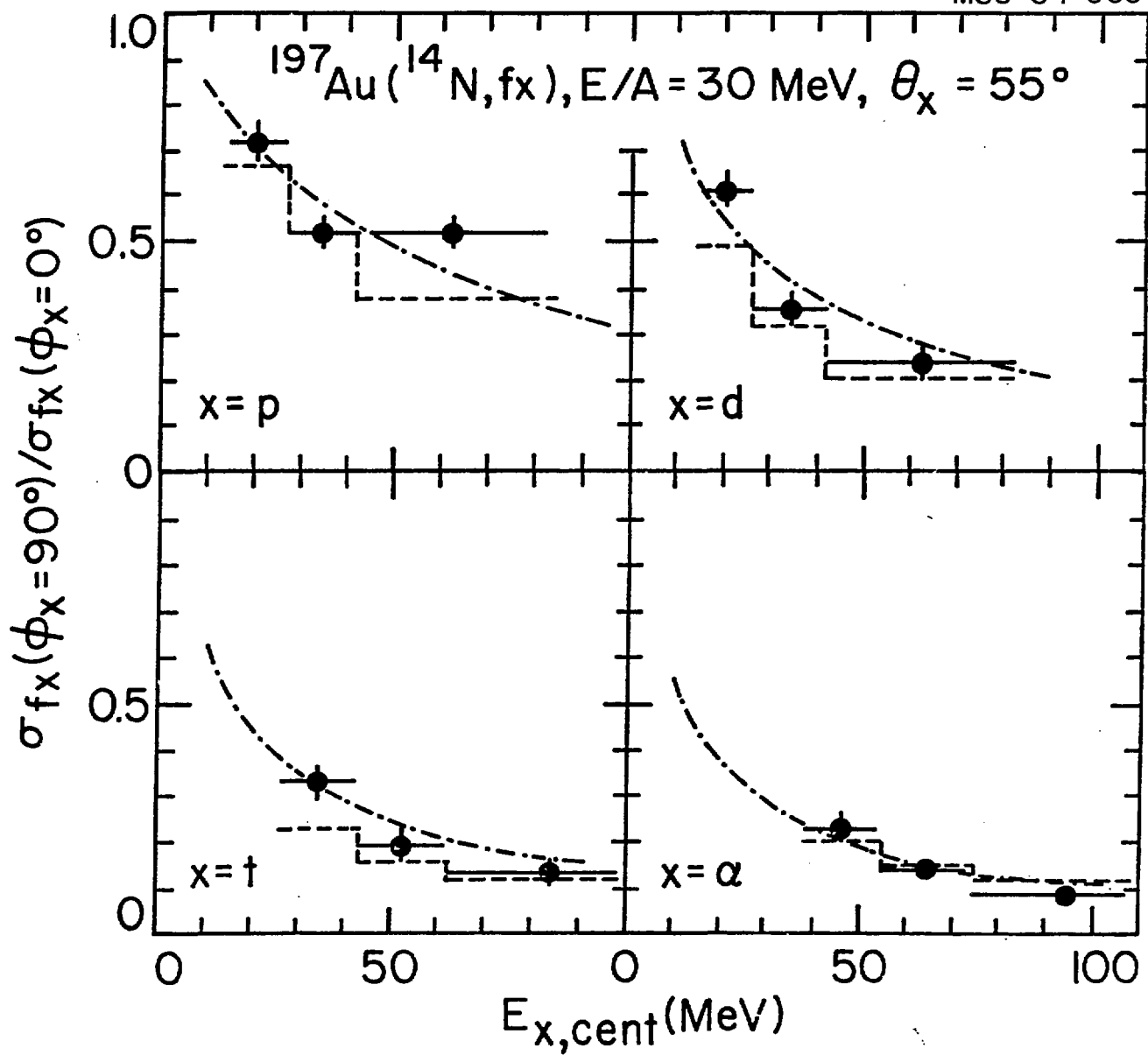


Fig. 3

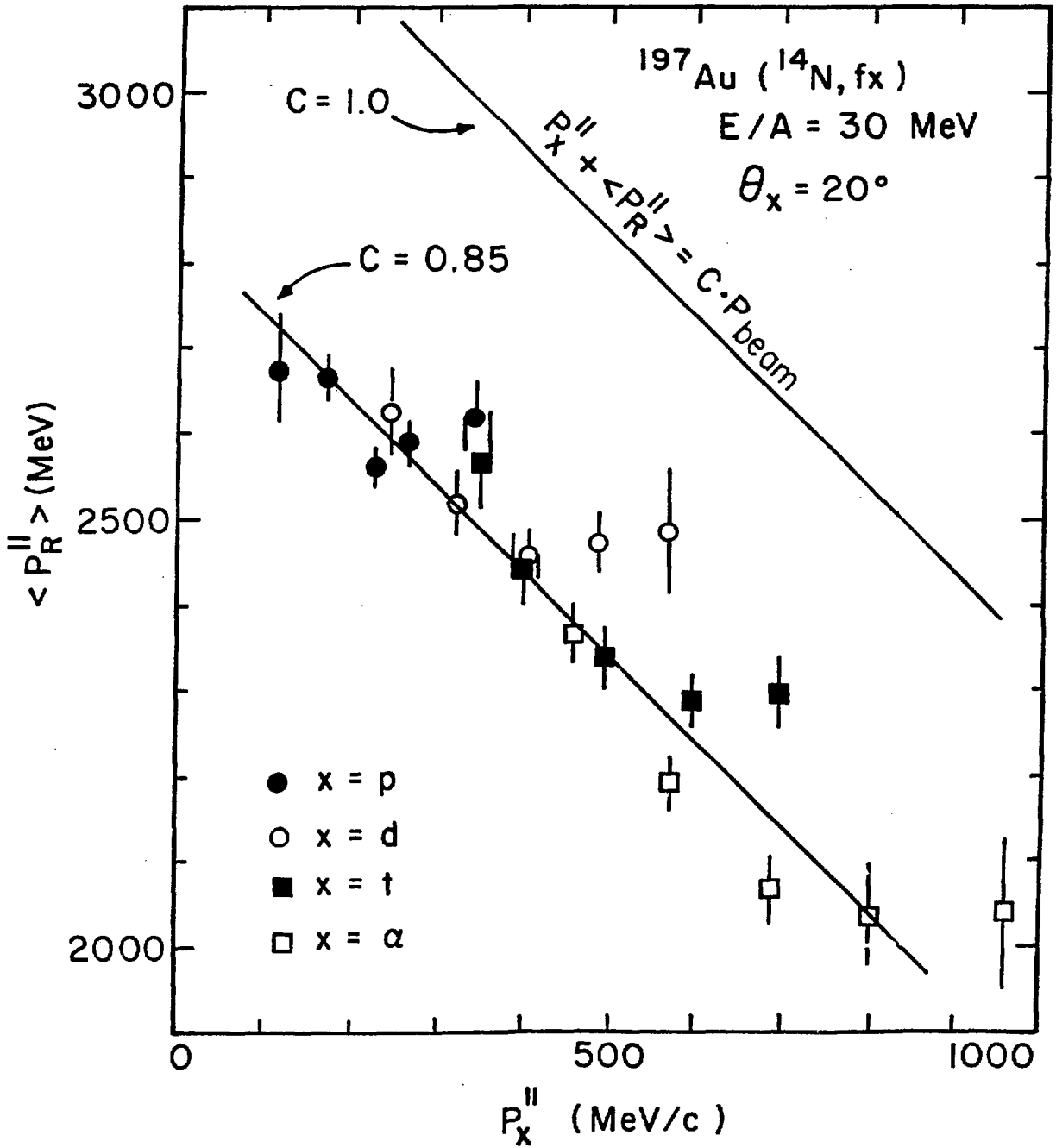
In summary, both the fission fragment - light particle and light particle - light particle correlation data reveal a strong preference for the emission of noncompound light particles in the reaction plane. This can be explained by assuming an ordered transverse motion in the reaction plane superimposed onto the random statistical motion of the individual nucleons. In addition, shadowing may have a significant influence on correlations between light particles when the light particles involved are deuterons or tritons because of the rather short mean free paths of these particles

This material is based upon work supported by the National Science Foundation under Grant No. PHY-80-17605.

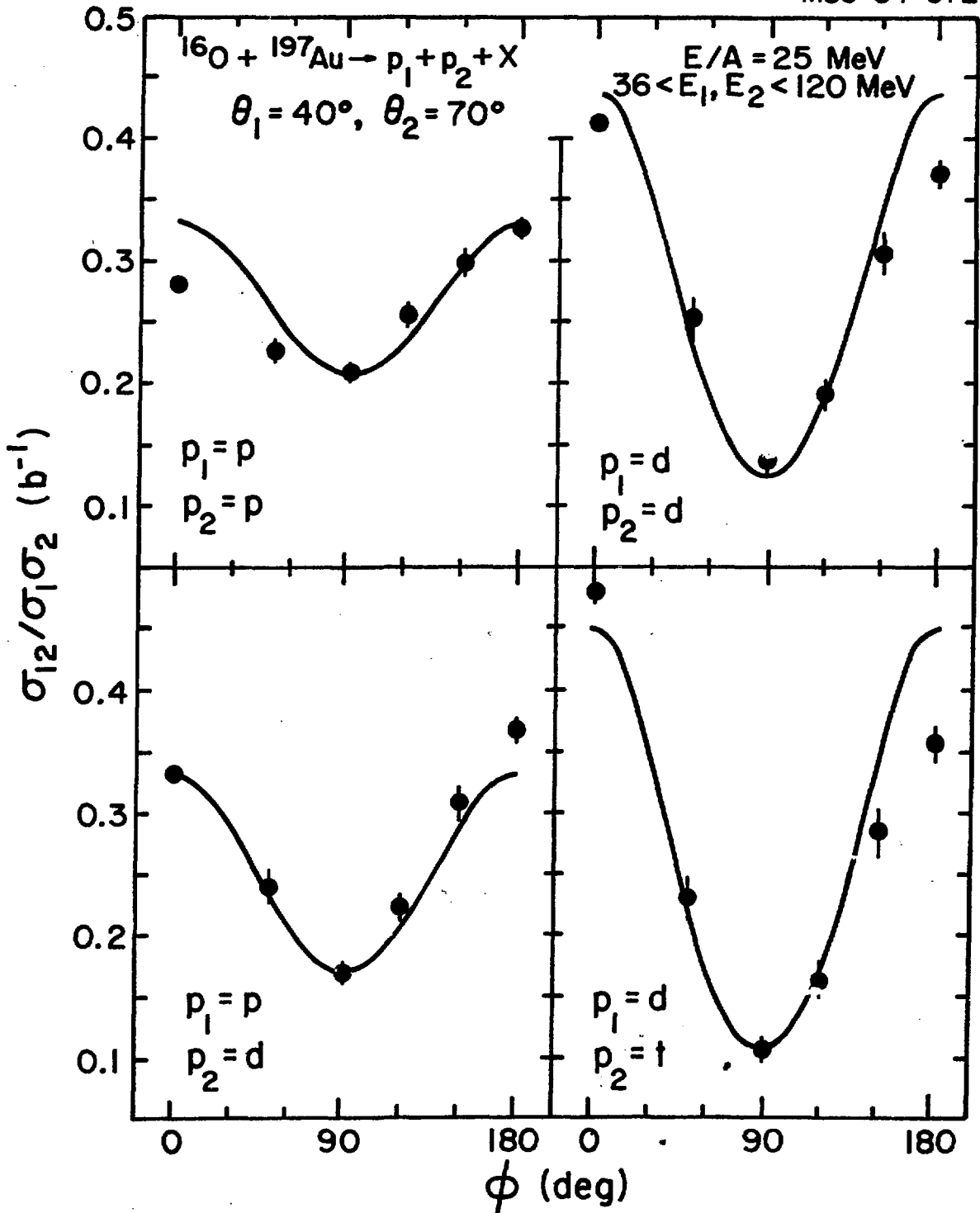
1. M. B. Tsang et al., Phys. Lett. 134B, 169 (1984).
2. C. K. Gelbke, Nucl. Phys. A400, 473c (1983).
3. W. G. Lynch et al., Phys. Rev. Lett. 51, 1850 (1983).
4. W. A. Friedman, Phys. Rev. C 29, 139 (1984).
5. M. B. Tsang, et al., to be published.



MSU-83-644



MSU-84-072



LINEAR MOMENTUM TRANSFER IN
INTERMEDIATE-ENERGY PROJECTILE-NUCLEUS COLLISIONS*

K. Kwiatkowski, M. Fatyga, H. J. Karwowski, L. W. Woo
and V. E. Viola, Jr.

Departments of Chemistry and Physics
and Indiana University Cyclotron Facility
Indiana University
Bloomington, IN 47405

M. B. Tsang, C. B. Chitwood, D. J. Fields, C. K. Gelbke and W. G. Lynch

Department of Physics
National Superconducting Cyclotron Laboratory
Michigan State University
East Lansing, MI 48824

One of the basic observables that must be successfully described by any dynamical theory of nucleus-nucleus collisions is the distribution of linear momentum transferred from projectile to target in the interaction. Such data yield estimates of the relative contribution of complete and incomplete fusion mechanisms, as well as more complex processes, and at the same time complement interpretations of the reaction dynamics provided by studies of light-charged-particle spectra. Taken together, linear momentum transfer (LMT) and coincident light-charged particle (LCP) information permit an evaluation of the total momentum balance in a given reaction, thereby providing more stringent tests of models designed to describe these continuum processes.

As a consequence of advances in intermediate-energy accelerator capabilities, experimental data have recently become available which provide for the first time a systematic picture of the dependence of linear momentum transfer on projectile type and bombarding energy.¹ In this report we examine the behavior of existing LMT data for heavy target nuclei in an effort to gain a better understanding of the mechanisms by which energy is transferred to the nuclear medium over an energy range extending from the mean field (low energy) to nucleon-nucleon (high energy) collision regimes.

For reactions involving highly fissionable target nuclei, linear momentum transfer distributions can be determined experimentally from measurements of the angle

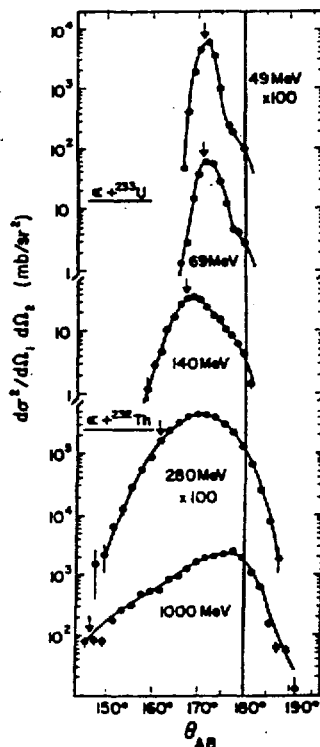


Fig. 1. Fission-fragment angular-correlation data for ^4He -induced reactions as a function of bombarding energy. Data at 490 and 1000 MeV are from Ref. 5; lower-energy data are from Ref. 3. The vertical line represents zero net linear momentum transfer and arrows indicate complete momentum transfer at each energy.

* Work supported by the National Science Foundation and the U. S. Department of Energy.

between binary fission fragments.² The results discussed here have all been obtained consistently with this technique, using a wide variety of projectiles incident on heavy targets. A fundamental assumption in the interpretation of these data is that the fission cross section provides a realistic representation of the total reaction cross section; i.e. $\sigma_f \cong \sigma_R$. This assumption has been shown to be valid for complex projectiles at bombarding energies up to $E/A \approx 40$ MeV.³ For protons, spallation reactions of the type $(p, xnyp)$ have a significant probability, even for uranium targets. Therefore, cross-section data for these processes must be included in order to make appropriate correction to the fission data necessary to yield a global description of the total reaction cross section.

As an illustration of the representative trends observed for fission fragment angular correlation data as a function of bombarding energy, Fig. 1 presents data for ^4He -induced reactions from $E/A = 12$ to 250 MeV.^{3,5} The fission correlation angle θ_{AB} can be readily transformed to a corresponding longitudinal component of linear momentum, $p_{||}$, under the assumption of symmetric mass division and a value of the total kinetic energy release given by systematics.

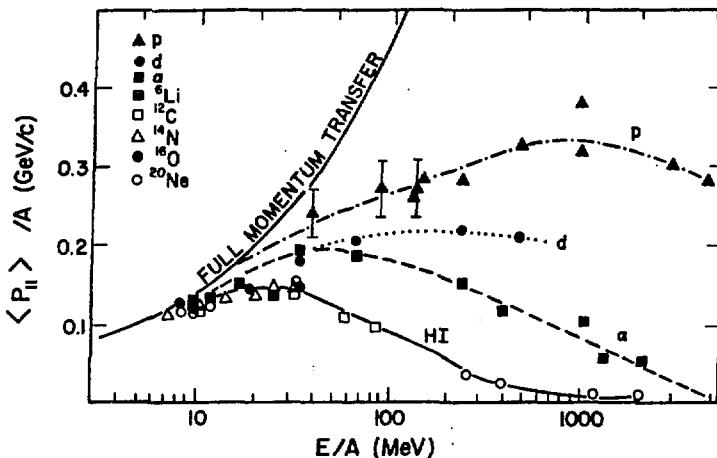


Fig. 2. Plot of the average linear momentum transfer, $\langle p_{||} \rangle / A$, as a function of beam energy per nucleon for projectiles with $1 \leq A \leq 20$. Data are taken from Refs. 1-3 and 5-10, or references therein. Lines for various projectile types are to guide the eye.

10 to 40 MeV, the relative importance of the peripheral-like contribution to σ_R increases, an effect which can be observed more dramatically in heavy-ion-induced reactions.^{1,6} At still higher energies the LMT distribution in which fusion-like processes evolve into a continuous distribution in which fusion-like processes diminish to a negligible level and the most probable $p_{||}$ corresponds to values characteristic of peripheral collisions.

In Ref. 5 it was found that the experimental results could be conveniently summarized in terms of the average linear momentum transfer per projectile nucleon, $\langle p_{||} \rangle / A$, as a function of beam energy, E/A . The average of the linear momentum transfer distribution offers a particularly useful characterization of LMT data in the intermediate energy region in that it is uniquely defined and avoids ambiguities associated with fusion-like and peripheral components of the distributions. Fig. 2 presents such a plot for the existing data (summarized in Ref. 1,

In each case the value of the beam momentum (complete momentum transfer) is indicated by an arrow; the value for zero momentum transfer ($\theta_{AB} = 180^\circ$) is given by the vertical line. One observes that near the Coulomb barrier ($E/A \sim 10$ MeV), complete LMT (or complete fusion) processes dominate the reaction cross section. In the bombarding energy range from $E/A \approx 10$ to 40 MeV, two components appear in the distributions. The major component is associated with fusion-like mechanisms whereas the minor component represents peripheral processes which involve low l values. As the bombarding energy increases from E/A

plus new results for protons and ${}^6\text{Li}$ projectiles⁷ and also for ${}^3\text{He}$ beams.⁸ The heavy solid line on Fig. 2 indicates the expected value of $\langle p_{||} \rangle / A$ for complete linear momentum transfer.

The behavior of $\langle p_{||} \rangle / A$ as a function of projectile type and energy exhibits many distinctive features. Most striking is the observation that on a per nucleon basis, the proton is the most effective agent for linear momentum transfer compared with the other projectiles. Of corresponding interest it is noted that for all heavy ions (i.e. $6 \leq A \leq 20$, or nuclei with particle-stable

excited states), the value of $\langle p_{||} \rangle / A$ as a function of E/A falls on a universal curve, within the limits of error of the data. This result suggests the possibility that at least for projectiles in this mass range, the nucleus-nucleus interaction may be amenable to description in terms of macroscopic models. The deuteron and helium data are observed to fall systematically between the proton and heavy-ion data.

From the dependence of $\langle p_{||} \rangle / A$ on projectile energy, it is apparent that below $E/A \approx 20$ MeV, the data for all ions are consistent with collisions dominated by fusion-like mechanisms. Above this energy the heavy-ion curve reaches a maximum average momentum transfer of ~ 150 MeV/c at bombarding energies of $E/A = 30-50$ MeV and then decreases to very small values above $E/A \approx 100$ MeV. The implication of this result, supported by existing data with relativistic heavy ions,^{9,10} is that binary fission reactions no longer provide a global account of the linear momentum transfer distribution for relativistic heavy ions. Instead, large linear momentum transfer processes initiate complex fragmentation of both the target and projectile nuclei, requiring more complex experimental methods in order to reconstruct the LMT distribution for the total reaction cross section.

While the light-ion data exhibit similar systematic behavior, the maximum values of the average longitudinal momentum transfer, $\langle p_{||} \rangle^{\text{max}} / A$, and the energy at which the maximum occurs are significantly larger. For He ions one finds that saturation occurs in the energy interval $E/A \approx 30-60$ MeV, whereas for deuterons and protons the maxima are near $E/A \approx 200$ MeV and $600-1000$ MeV, respectively. In Fig. 3 the values of $\langle p_{||} \rangle^{\text{max}} / A$ indicated by the data of Fig. 2 are plotted as a function of projectile mass.⁶ As previously pointed out, $\langle p_{||} \rangle^{\text{max}} / A$ is significantly larger for protons, reaching $300-350$ MeV/c, compared to heavy ions, which

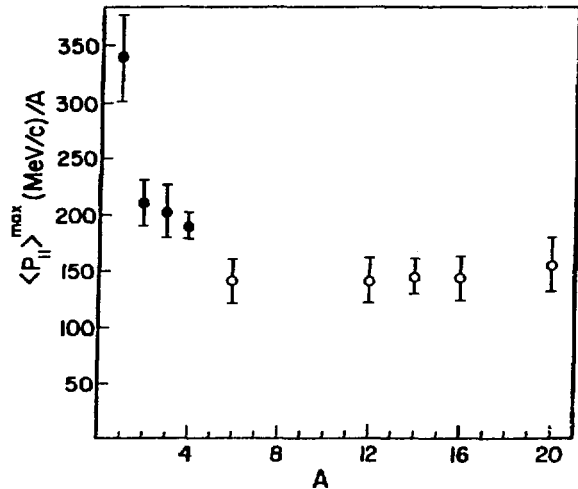


Fig. 3. Plot of the maximum value of the average linear momentum transfer per nucleon, $\langle p_{||} \rangle^{\text{max}} / A$, as a function of projectile mass number. The values of $\langle p_{||} \rangle^{\text{max}} / A$ were determined from the maximum observed value of $\langle p_{||} \rangle / A$ for each system in Fig. 2. Closed circles represent systems for which energy systematics are complete; open circles represent the largest value of $\langle p_{||} \rangle / A$ ever observed for the given system.

have a common value of about 145 MeV/c. Values for d, ^3He and ^4He are intermediate, peaking in the vicinity of 200 MeV/c. Since the per nucleon values of $\langle p_{||} \rangle_{\text{max}}/A$ for all complex projectiles are in the vicinity of the average Fermi momentum of nucleons in nuclear matter, one can speculate that the observed limitations may be associated with Fermi motion. This correlation suggests that theoretical efforts directed along these lines may prove useful in explaining this basic feature of the interaction.

In an attempt to understand the underlying physics responsible for the light-ion results, intranuclear cascade calculations^{11, 12} have been performed for the LMT distributions in these systems. For p, d and α projectiles the CLUST code,¹¹ which contains all combinations of fundamental scattering and reaction cross sections for these particles has been applied.¹³ Pion production is not included in this code. The results are compared with the data in Fig. 4. Qualitative agreement is obtained with the systematic features of

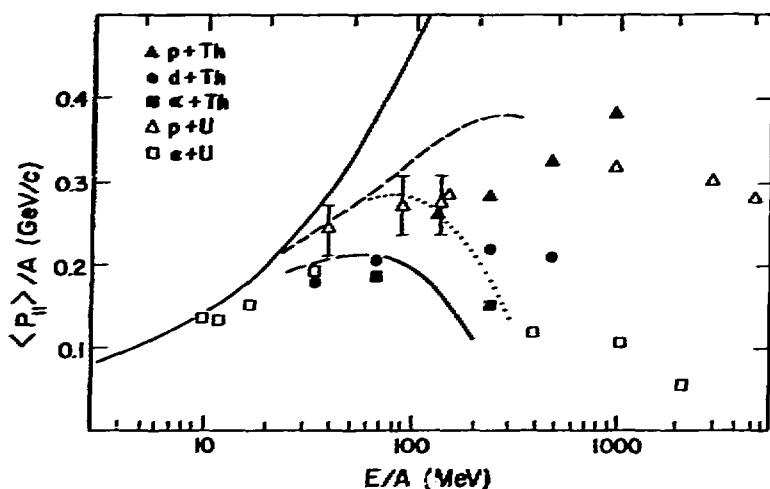


Fig. 4. Comparison of $\langle p_{||} \rangle / A$ data for protons, deuterons and alpha particles with predictions of the intranuclear cascade code:¹² ----, protons; ····, deuterons, and ——— alpha particles.

the data, although for protons the calculations are about 20 per cent too high over much of the energy range and the complex projectiles are poorly described at high energies. The agreement can be understood from an analysis of the average longitudinal momentum transfer characteristics of the fundamental N-N, d-N and α -N differential cross sections which serve as input to the cascade code. Such an analysis¹³ reveals the much greater effectiveness of nucleon-nucleon collisions in the transfer of longitudinal linear momentum

relative to d-N and α -N collisions. Thus, to the first order, the light-ion behavior in Fig. 2 can be interpreted in terms of fundamental scattering and reaction processes between p, d and α projectiles with nucleons in the target medium.

The overestimate of the calculated $\langle p_{||} \rangle$ values for protons relative to the experimental values can be traced to an excess of full momentum transfer events predicted by the intranuclear cascade code. Correspondingly, the code underestimates the probability for fast nucleon emission, especially at small angles (cf. Ref. 14). In contrast, for ^4He -induced reactions in the vicinity of $E/A = 40$ MeV, the CLUST code reproduces both the LMT and fast nucleon emission data rather well.

The major failing of the intranuclear cascade calculations for d and α projectiles - i.e. the strong decrease in $\langle p_{||} \rangle / A$ at high energies - can be attributed to several factors: absorptive and inelastic breakup processes,

target fragmentation and pion production, which are not handled properly in the CLUST code. A particularly serious shortcoming of the code is that complex projectiles are not permitted to break up during the interaction. The net effect of this limitation is that at higher energies, forward angle inelastic scattering is enhanced at the expense of collisions in which one or more nucleons are transferred to the target, which would impart momentum to the struck nucleus.

Preliminary investigations with the ISABEL intranuclear cascade code,¹² which simulates nucleus-nucleus collisions as a series of N-N collisions, have indicated that (1) below $E/A \approx 100$ MeV, the code provides a poor representation of the data and (2) for heavy-ion projectiles the code predicts that $\langle p_{||} \rangle/A$ is projectile dependent rather than falling on the universal curve indicated in Fig. 2.

In summary, fairly complete systematics of linear momentum transfer distributions now exist for a variety of ions up to $A = 20$ and bombarding energies of $E/A \geq 10$ MeV. On a per nucleon basis the proton is the most effective agent of linear momentum transfer and heavy ions the least effective. For heavy ions ($6 \leq A \leq 20$) the average linear momentum transfer scales directly with projectile mass, producing a universal curve in terms of $\langle p_{||} \rangle/A$. For all projectiles the average linear momentum transfer reaches a maximum at intermediate energies and then falls off gradually. For protons this maximum value is about 300 - 350 MeV/c, in contrast with the universal heavy ion value of $\langle p_{||} \rangle^{\max} \approx 145 A$ MeV/c. Many of the qualitative features of the light-ion data can be understood in terms of fundamental N-N, d-N and α -N scattering processes. Intranuclear cascade calculations are consistent with the data although inadequacies in the mode are apparent. Finally, the need for an intensified theoretical effort to explain these data is clearly essential if we are to understand these basic features of nucleus-nucleus collisions in the intermediate-energy regime.

References

1. V. E. Viola, Jr., Proc. XVth Masurian Summer School on Nuclear Physics (Mikołajki, Poland, 1983), to be published in Nukleonika; Indiana University Chemistry Report INC-40007-17 (1983).
2. T. Sikkeland, et al, Phys. Rev. 125, 1350 (1962); V. E. Viola, Jr., et al, Phys. Rev. C26, 178 (1982).
3. W. G. Meyer, et al, Phys. Rev. 20, 1716 (1979).
4. J. J. Hogan, et al, Phys. Rev. C20, 1831 (1979).
5. F. Saint-Laurent, et al, Phys. Lett. 110B, 372 (1982).
6. M. B. Tsang, et al, Phys. Lett. 134B, 119 (1984).
7. M. Fatyga, et al, IUCF 1984 Progress Report, to be published.
8. H. Hicks, et al, *ibid.*
9. U. Lynen, et al, Nucl. Phys. A387, 129c (1982).
10. A. Warwick, et al, Phys. Rev. C27, 1083 (1984).
11. G. J. Mathews, et al, Phys. Rev. C25, 2181 (1982).
12. Yariv and Z. Fraenkel, Phys. Rev. C20, 227 (1979); M. Clover, private communication.
13. L. Woo, et al, Phys. Lett. 132B, 283 (1983).
14. H. W. Bertini, Phys. Rev. C10, 2427 (1974).

VELOCITY DISTRIBUTION OF FUSION-LIKE PRODUCTS
FOR MEDIUM MASS HEAVY-ION SYSTEMS

Y.Chan C.Albiston, M.Bantel, P.Countryman, D.DiGregorio, R.Stokstad, S.Wald,
S.Zhou, Z.Zhou and A.Budzanowski, K.Grotowski, R.Plantel

Nuclear Science Division, Lawrence Berkeley Laboratory
University of California, Berkeley, Ca. 94720

The velocity of the compound nuclei prior to their decay can be determined by studying the invariant velocity distributions of the final residues¹. Thus by comparing the differences between the empirically measured average parent emitter velocity, V_{obs} , to that expected for complete fusion, $V_{c.m.}$, one can learn about the relative importance of incomplete fusion (or massive transfer) processes.

Following the results reported previously² for ^{16}O beams, a series of measurements on a wider range of projectile and target masses was initiated at the 88-inch Cyclotron Laboratory. Time-of-flight techniques were used to measure the velocities directly. Reactions between ^{14}N , ^{16}O , ^{19}F , ^{20}Ne , ^{22}Ne , ^{24}Mg projectiles and ^{24}Mg , ^{26}Mg , ^{27}Al , ^{28}Si , ^{40}Ca , $^{58,60}\text{Ni}$ targets have been studied in the bombarding energy range of 7 - 20 MeV/nucleon (Table 1).

The invariant velocity spectra of the residues can be expressed as^{1,3}:

$$\frac{1}{v^2} \frac{d^2 \sigma_A}{dv d\Omega} \propto \left[\exp \left(-\frac{(v - V_p \cos \Theta)^2 + V_p^2 \sin^2 \Theta}{2s_A^2} \right) \right] \left[\frac{\sqrt{(v - V_p \cos \Theta)^2 + V_p^2 \sin^2 \Theta}}{V \sin \Theta} \right]^{n_A}$$

where v , V_p and Θ are the residue velocity, parent emitter velocity, and detection angle, respectively, in the laboratory frame. The width parameter s_A reflects the dynamics of the decay process, and n_A , parametrizing the anisotropy of the angular distribution in the emitter frame, varies from 0 in the weak coupling limit to 1 in the strong coupling limit. The differences found in the velocity centroids by treating n_A as a free fitting parameter were found to be quite small for the higher mass residues. The present results were obtained by assuming $n_A = 0$, in which case the quantity of interest, $R (= V_{obs} / V_{c.m.})$, is equal to $\langle v \rangle / (V_{c.m.} \cos \Theta)$. Here, $\langle v \rangle$ is the empirical centroid of the invariant velocity spectrum at angle Θ .

A. Global behavior

Fig.1 shows the mass averaged velocity ratio plotted versus the local relative velocity of the reactants at the barrier, $V_{loc} (= [2(E_{cm} - V_C)/u]^{1/2})$. All results here correspond to values of the mass asymmetry $S = (A_T - A_P) / (A_T + A_P)$ that are larger than zero. The deviation of $\langle R \rangle$ from the nominal value of 1.0 (complete fusion) increases with increasing bombarding energy, an expected behavior, since incomplete fusion processes are expected to become more prominent at higher bombarding energies. It is also of interest to expand the comparison and include results from other linear momentum transfer measurements^{4,5,6,7} for fissile system at high bombarding energies (Fig.2). Even though there are certainly variations among the data, the deviation from complete fusion follows an approximately linear fall-off pattern with increasing relative velocity over a very wide range of bombarding energies. The deviation from complete fusion appears to have a threshold of about 5 MeV/nucleon above the barrier.

B. Projectile and target dependence

It is possible that break-up thresholds of the projectile might play an important role in the incomplete fusion mechanism. To see how this is reflected in our data, Fig.3(a) shows the excitation functions for different projectiles (^{14}N , ^{16}O , and ^{20}Ne) on the same Ca target. Within errors there are no drastic differences between these reactions and in fact for $^{14}\text{N} + ^{40}\text{Ca}$, where the projectile is not an alpha-cluster nucleus and has a low threshold for proton emission, the excitation function shows comparable fall-off as for the ^{16}O and ^{20}Ne projectiles. This may imply that particle thresholds of the projectile alone can not pre-determine the fraction of momentum loss in a fusionlike event, but that other dynamical factors can be of equal importance.

There are reasons to expect, however, that the velocity shift should depend on the mass asymmetry of the system for small asymmetries. To investigate this, Fig.3(b) shows a comparison of the $^{20}\text{Ne} + ^{26}\text{Mg}$ and the $^{14}\text{N} + ^{40}\text{Ca}$ reactions (corresponding to $S=0.13$ and 0.48) It is quite clear that the former reaction, which is more symmetric with respect to the projectile and target masses, exhibits a much smaller velocity shift at a comparable value of V_{loc} . This is because, for more symmetric systems, stripping-like and pick-up-like processes can contribute to residue production with comparable probability, reducing the net average velocity shift (but broadening the distribution). In fact, for identical projectile and target nuclei, the

average parent velocity is the same as the center-of-mass velocity. In this case, the centroid approach is no longer sensitive to the underlying reaction mechanism.

D. Relative cross sections

The deduction of the relative cross sections for different processes from the inclusive residue velocity spectra alone is quite difficult as one does not know a priori the number and velocities of parent emitters that are present. The spectra are broad and featureless at high bombarding energies causing fitting procedures with multiple peaks less reliable. Fig.4 shows such an attempt for the $^{19}\text{F} + ^{40}\text{Ca}$ reaction at 184 MeV. The spectra are fitted by a complete fusion component obtained from an evaporation model calculation, LILITA¹, and another Gaussian component whose center, width, and height are allowed to vary. Typical results obtained indicate that close to 20% of the fusionlike cross sections are in fact not coming from a complete momentum transfer process, with slight variations depending on the residue mass. Preliminary studies show that these numbers are larger than what one would have expected from, for instance, the standard Wilcznski sum-rule model.⁸

In summary, the present experimental method appears to be well adapted for measurements of the amount of linear momentum that is transferred in a fusionlike process for medium mass heavy-ion systems. It is quite efficient for studying systematics and provides a complimentary approach to the more conventional method of studying the fast light ejectiles.

References :

1. J. Gomez del Campo et al., Phys. rev. C19 ,2170(1979).
2. Y. Chan et al., Phys. Rev. C27 ,447(1983).
3. H. Morgenstein et al., Z. Phys. A, 313 ,39 (1983).
4. V.E. Viola, Jr., et al., Phys. Rev. C26 ,178(1982) and references therein.
5. E. Duek et al., Z. Phys. A, 307 ,221(1982) and references therein.
6. J. Galin et al., Phys. Rev. Lett., 48 ,1787 (1982).
7. G. Nebbia et al., Z. Phys. A, 311 ,247(1983).
8. J. Wilczynski et al., Phys. Rev. Lett., 45 ,606(1980).

Table I. A summary of reactions studied in this work. The velocity ratio (see text) has been averaged over the higher portion of the residue masses. Errors are preliminary and include systematic errors.

	E_{Lab} (MeV/nucleon)	V_{Inr} (cm/ns)	$\langle R \rangle$ (%)	Reaction
1	8.3	2.99	99.5 ± 3.	$^{26}\text{Mg} + ^{27}\text{Mg}$
2	7.2	3.02	99.8 ± 4.	$^{18}\text{F} + ^{56}\text{Ni}$
3	7.2	3.13	97.2 ± 4.	$^{18}\text{F} + ^{40}\text{Ca}$
4	7.2	3.22	97.3 ± 4.	$^{18}\text{F} + ^{29}\text{Si}$
5	7.7	3.24	97.4 ± 4.	$^{20}\text{Ne} + ^{40}\text{Ca}$
6	7.2	3.25	97.8 ± 4.	$^{18}\text{F} + ^{27}\text{Al}$
7	7.5	3.34	100.5 ± 3.	$^{20}\text{Ne} + ^{27}\text{Al}$
8	8.8	3.56	98.0 ± 4.	$^{16}\text{O} + ^{40}\text{Ca}$
9	8.8	3.68	97.0 ± 4.	$^{16}\text{O} + ^{56}\text{Ni}$
10	9.7	3.73	96.6 ± 4.	$^{18}\text{F} + ^{40}\text{Ca}$
11	9.7	3.81	94.0 ± 4.	$^{18}\text{F} + ^{29}\text{Si}$
12	8.7	3.89	95.8 ± 4.	$^{18}\text{F} + ^{27}\text{Al}$
13	9.7	3.92	97.3 ± 4.	$^{22}\text{Ne} + ^{24}\text{Mg}$
14	10.4	4.10	98.5 ± 3.	$^{22}\text{Ne} + ^{26}\text{Mg}$
15	10.4	4.11	97.0 ± 3.	$^{22}\text{Ne} + ^{56}\text{Ni}$
16	11.4	4.13	95.8 ± 4.	$^{14}\text{N} + ^{56}\text{Ni}$
17	11.0	4.21	98.5 ± 3.	$^{50}\text{Ne} + ^{24}\text{Mg}$
18	11.0	4.23	97.5 ± 3.	$^{20}\text{Ne} + ^{26}\text{Mg}$
19	11.4	4.23	93.0 ± 4.	$^{14}\text{N} + ^{40}\text{Ca}$
20	11.4	4.31	92.2 ± 4.	$^{14}\text{N} + ^{29}\text{Si}$
21	11.4	4.34	95.3 ± 4.	$^{14}\text{N} + ^{27}\text{Al}$
22	12.5	4.36	94.0 ± 4.	$^{50}\text{Ne} + ^{56}\text{Ni}$
23	12.5	4.45	94.0 ± 4.	$^{20}\text{Ne} + ^{40}\text{Ca}$
24	12.5	4.53	95.5 ± 4.	$^{50}\text{Ne} + ^{27}\text{Al}$
25	12.6	4.57	96.0 ± 3.	$^{50}\text{Ne} + ^{26}\text{Mg}$
26	13.6	4.60	92.0 ± 4.	$^{16}\text{O} + ^{60}\text{Ni}$
27	13.6	4.68	89.5 ± 4.	$^{16}\text{O} + ^{40}\text{Ca}$
28	13.6	4.78	91.0 ± 4.	$^{16}\text{O} + ^{27}\text{Al}$
29	14.3	4.84	88.0 ± 4.	$^{14}\text{N} + ^{40}\text{Ca}$
30	17.9	5.43	85.6 ± 4.	$^{14}\text{N} + ^{56}\text{Ni}$
31	17.9	5.50	81.0 ± 4.	$^{14}\text{N} + ^{40}\text{Ca}$
32	19.6	5.73	81.0 ± 4.	$^{16}\text{O} + ^{27}\text{Al}$
33	19.6	5.80	79.0 ± 4.	$^{16}\text{O} + ^{40}\text{Ca}$
34	19.6	5.87	83.0 ± 4.	$^{16}\text{O} + ^{60}\text{Ni}$

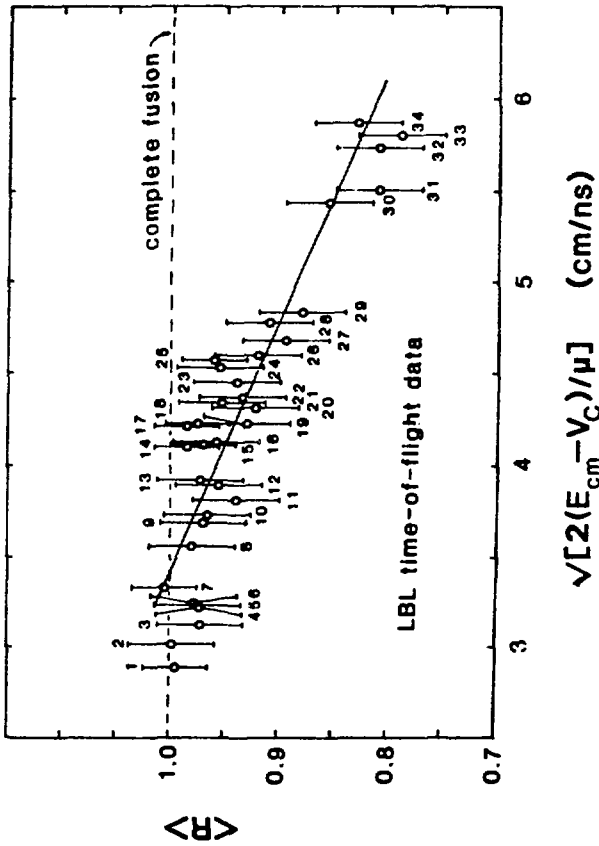


Fig. 1. Systematics of the average parent emitter velocity, expressed as a ratio R to the velocity corresponding to complete fusion.

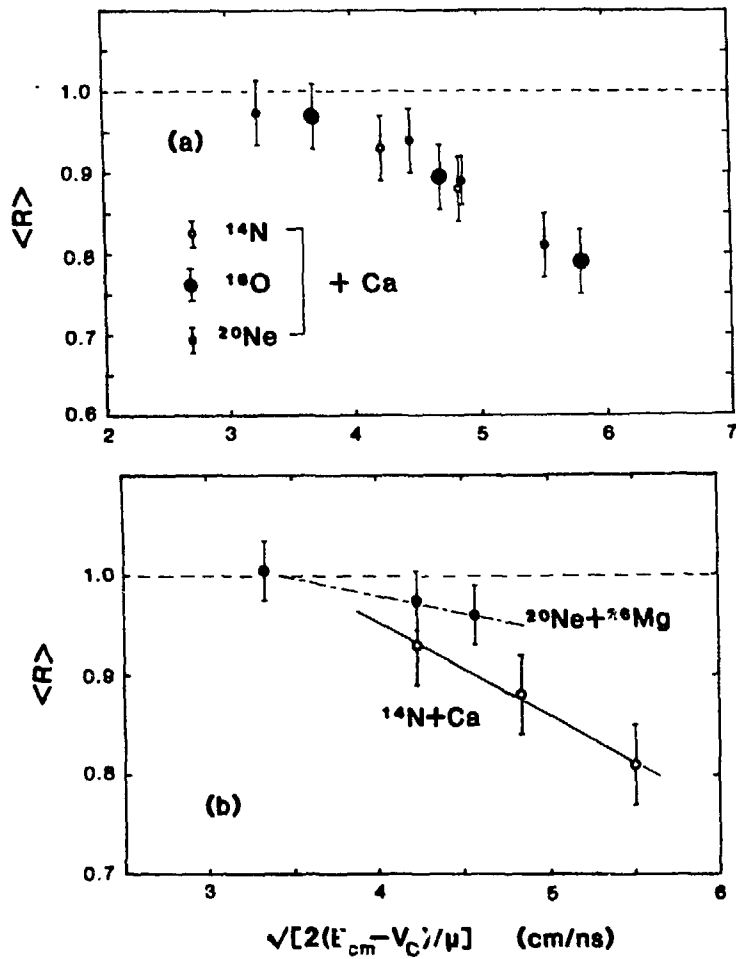


Fig. 3. Comparison of velocity shifts as a function of bombarding energy for (a) different projectiles on the same target and (b) systems with different mass asymmetry in the entrance channel. -

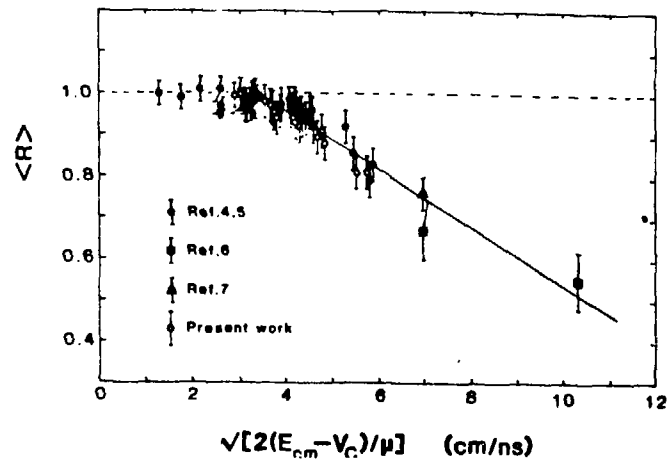


Fig. 2. Comparison including results from other linear momentum transfer measurements (refs. 4-7).

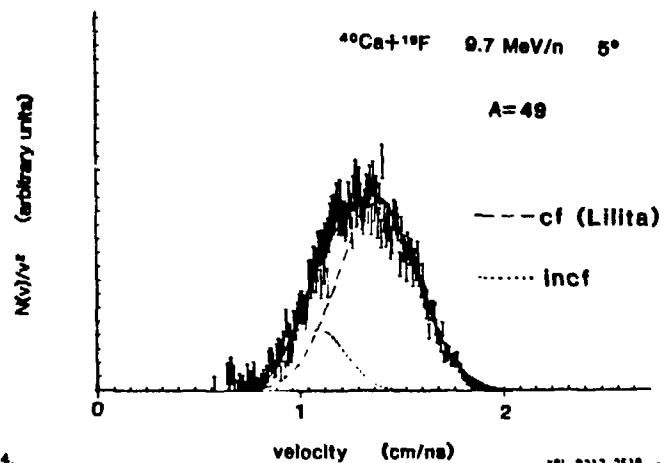


Fig. 4. Relative ratio for complete and incomplete fusion contributions to the velocity spectrum from peak shape fitting. The complete fusion component is calculated by the evaporation code, LILITA.¹

SIMPLE ESTIMATES FOR FERMI JETS*

K. Moehring[†] and M. Zielinska-Pfabe^{††} **

Nuclear Science Division, Lawrence Berkeley Laboratory, Berkeley, CA 94720

Window friction [1] is one of the proposed mechanisms to understand a deep inelastic heavy ion reaction. Several authors [2,3,4] investigated the implication that an early opening of the window allows the prompt emission of nucleons: Due to the still high ion-ion relative velocity adding to the Fermi motion, some nucleons might get enough momentum not only to cross the window but actually to leave the system ("Fermi jets," "PEPS").

If this mechanism could be checked experimentally, this would provide, among other things, valuable information on the approach phase of the reaction process. Relying on the early opening of a window, it might also help to decide between different proposed mechanisms for the slowing down of the colliding nuclei [1,5].

There are rather detailed calculations of the Fermi jetting process reported in the literature [2,3,4], limited however to just a very few specific reactions. The inclination as to experimental identification of Fermi jets is not clear.

In order to get a more schematic overview, we present a simple model which allows for an approximate estimate of the expected cross sections for a wide variety of heavy ion reactions.

The model represents the collision as the conventional coming together of two sharp-surfaced potential wells filled with classical Fermi gases. After contact, a window opens and time dependent fluxes of nucleons begin to irradiate the two wells. These fluxes are elementary in terms of the velocity distributions of the Fermi gases and the instantaneous relative velocity $\vec{u}(t)$ of the collision partners. They are proportional to the window area $a(t)$. A small fraction of the traversing nucleons have velocities high enough to escape over the back sides of the wells and produce Fermi jets. The bulk part of the fluxes is captured in the wells and causes a decrease of $\vec{u}(t)$ (window friction). The corresponding equations of motion for the radial and the tangential component of $u(t)$ read

$$\frac{d}{dt} u_r(t) = -\frac{1}{4} \rho_0 \bar{v}_F a(t) \frac{2}{M} u_r(t) + \frac{u_t^2(t)}{r} - \frac{1}{M} \frac{\partial V}{\partial r}, \quad (1)$$

$$\frac{d}{dt} u_t(t) = -\frac{1}{4} \rho_0 \bar{v}_F a(t) \frac{1}{M} u_t(t) + \frac{u_r(t) u_t(t)}{r}. \quad (2)$$

$\frac{1}{4} \rho_0 \bar{v}_F$ is a universal flux factor [1].

Because, provided the original collision velocity is not too high, the decrease of \vec{u} will soon prohibit the possibility of jetting, we are limited to a rather small part of the trajectory. Assuming that contact establishes at the interaction barrier, we neglect the conservative force $-\partial V/\partial r$. Since window friction relies on a first order expansion in the ratio u/v_F , also the centrifugal terms in eqs. (1,2) are considered as negligible. Consequently, $u_t(t) \sim [u_r(t)]^{1/2}$ and $du_r \sim dt/a(t)$.

Integrating the jetting over the proper time interval along the trajectory and changing the time integration to integration over u_r , we find the complicated window area $a(t)$ canceling out. As a result we obtain elementary integrals over velocities, approximately independent of the detailed collision dynamics. This simplifies the calculations considerably.

For the geometry of the potential wells we restrict ourselves to two touching spheres (fig. 1).

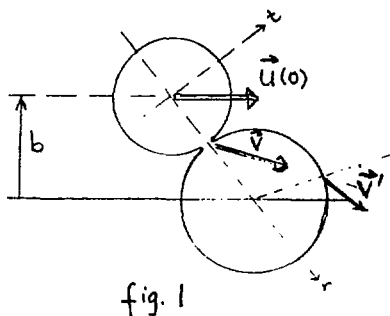


fig. 1

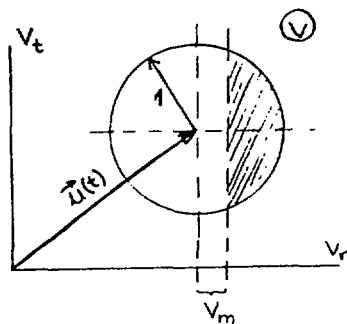


fig. 2

The orientation of the axis joining the centers is defined by the impact parameter b and assumed to stay approximately fixed during the short time interval jetting takes place. (It is only with this approximation that the window area $a(t)$ really does not enter the calculation.)

For a small window, the possibility for a nucleon to jet is then entirely defined by its radial velocity at the window

$$V_r \geq V_{esc} = \left(\frac{E_F + S + E_c}{E_F} \right)^{1/2}. \quad (3)$$

(Henceforth, we give all velocities in units of the Fermi velocity v_F , $E_F = 32.32$ MeV.) S is the separation energy, E_c the Coulomb barrier as seen by the jetting protons. Eq. (3) implies that out of the Fermi sphere in velocity space a cap defined by

$$V_m = V_{esc} - u_r(t) \leq V_r \leq 1 \quad (4)$$

contributes to jetting (fig. 2). The range of $u_r(t)$ allowing for jetting is therefore

$$V_{esc} - 1 \leq u_r(t) \leq u_r(0). \quad (5)$$

$u_r(0)$ is the radial velocity at barrier. For the interaction barriers we use

$$B_{cm} \cong \frac{Z_p Z_T}{A_p^{1/3} + A_T^{1/3}} \text{ MeV}. \quad (6)$$

The resulting expressions are to be integrated over a proper range of impact parameters. For the results presented below we consider reactions leading to compound formation followed by evaporation, thereby confining ourselves to rather central collisions where jetting should be most favoured. Estimates for the corresponding cut-off angular momenta \bar{l} are taken from ref. [6].

For the separation energy S we use the nominal value 8 MeV. Jetting protons have to overcome an additional Coulomb barrier. Because they see the combined charge of projectile and target rather than the barrier of the isolated nucleus, we use

$$E_c = (Z_p + Z_T - 1) e^2 / 1.22 \left(A^{1/3} + \left(1 - \frac{A}{A_{tot}} \right) (A_p^{1/3} + A_T^{1/3}) \right). \quad (7)$$

This is the value of the monopole field of the combined charge at the tip of the nucleus the proton is going to leave. The same monopole field is used for the Coulomb scattering of the proton after jetting.

With these (admittedly drastic) approximations all quantities of interest are easily calculated. We calculate the velocity distributions and the double differential cross sections $d\sigma/dE d\Omega$ for jetting of neutrons or protons through either projectile or target.

The total cross sections can be given in closed form

$$\sigma_{\text{tot}} = \frac{\pi \bar{\ell}^2}{R^2} \cdot A_{\text{red}} \cdot f \cdot \begin{cases} N_{\text{tot}}/A_{\text{tot}} \\ Z_{\text{tot}}/A_{\text{tot}} \end{cases} \quad \text{for } \begin{cases} \text{neutrons} \\ \text{protons} \end{cases} \quad (8)$$

where f is an analytic function of the velocities involved.

Calculating cross sections for some 40 reactions, we find that in all cases the distributions of velocities can fairly be approximated by two-dimensional Gaussians,

$$\frac{d^3\sigma}{2\pi dv_{\parallel} dv_{\perp}} = \frac{\sigma_{\text{tot}}}{\pi^{3/2} w_{\parallel} w_{\perp}} \alpha \exp\left\{-\frac{1}{w_{\parallel}^2}(\alpha v_{\parallel} - \bar{v}_{\parallel})^2 - \frac{1}{w_{\perp}^2} \alpha^2 v_{\perp}^2\right\}, \quad \alpha = \left[1 - \frac{E_c/E_F}{v_{\parallel}^2 + v_{\perp}^2}\right]^{1/2} \quad (9)$$

v_{\parallel} and v_{\perp} are the velocities parallel and perpendicular to the beam. α exploits the fact that the protons as contrasted to the neutrons essentially suffer an additional shift in energy due to the final state Coulomb scattering. With $\epsilon = E/E_F$, $\epsilon_c = E_c/E_F$,

$$\frac{d\sigma}{dE d\Omega}_{\text{cm}} = \frac{1}{2} \frac{\sigma_{\text{tot}}}{\pi^{3/2} w_{\parallel} w_{\perp}} \frac{1}{E_F} \sqrt{E - \epsilon_c} \exp\left\{-\frac{1}{w_{\parallel}^2}(\sqrt{E - \epsilon_c} \cos\theta - \bar{v}_{\parallel})^2 - \frac{1}{w_{\perp}^2}(E - \epsilon_c) \sin^2\theta\right\}. \quad (10)$$

The parameters σ_{tot} (or rather f , cf eq. (8)), \bar{v}_{\parallel} , w_{\parallel} , w_{\perp} are calculated in the model and plotted in figs. 3 against the maximal velocity

$$v_M = [(1 + u_0)^2 - v_{\text{esc}}^2]^{1/2} \quad (11)$$

a nucleon can leave leaving the specific nucleus with respect to the latter. v_M^{cm} is this quantity in the center of mass.

In order to get some idea to what extent absorption within the potential well might change the results, we included an attenuation factor for the traversing nucleons, using for both neutrons and protons the mean free path as given by ref [7]. We find that the total cross sections get reduced by up to a factor 2 (fig. 3); the forms of the distributions (\bar{v}_{\parallel} , w_{\parallel} , w_{\perp}) almost stay unchanged. One should however keep in mind that the proper treatment of absorption in the present context is not very well understood.

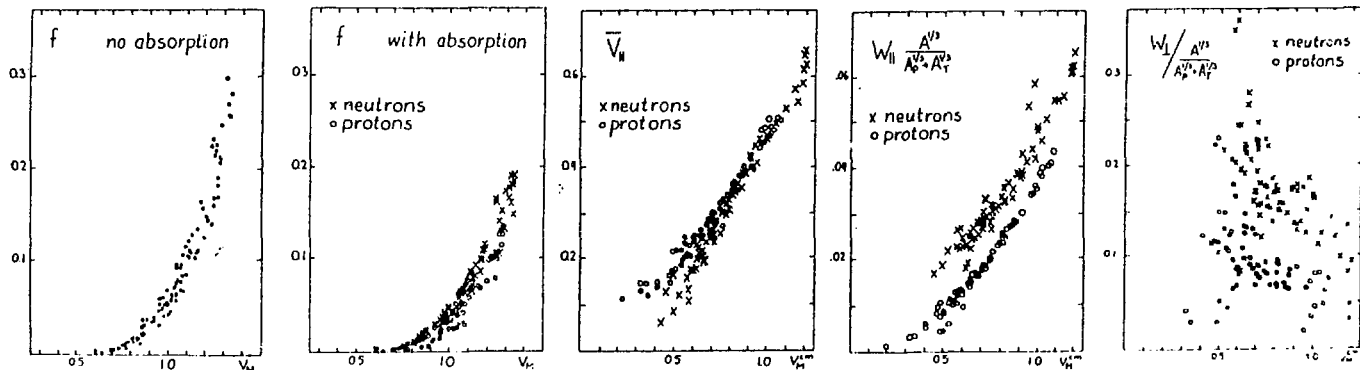


fig. 3

The parameters clearly show some systematic behavior. A more detailed investigation of this systematics is under way. In any case, the present model should help the discussion if and under what conditions Fermi jets might be observed experimentally.

We finally mention that one of the original motivations for this work was the question to what extent Fermi jets can account for the loss of linear momentum observed in a variety of heavy ion reactions. The results show that only a small fraction of the observed effects might be attributed to jets.

*This work was supported by the Director, Office of Energy Research, Division of Nuclear Physics of the Office of High Energy and Nuclear Physics of the U.S. Department of Energy under Contract DE-AC03-76SF00098.

**In collaboration with W. J. Swiatecki.

+On leave from Hahn Meitner Institut fuer Kernforschung, Berlin-West, Germany.

++Department of Physics, Smith College, Clark Science Center, Northampton, MA 01063.

- [1] J. Blocki et al., *Ann. Phys.* 113 (78) 330
- [2] J. P. Bondorf et al., *Nucl. Phys.* A333 (80) 285
- [3] K. T. R. Davies et al., preprint ORNL (83)
- [4] M. Robel, Ph.D. thesis, preprint LBL 8181 (79)
- [5] D. H. E. Gross and H. Kalinowski, *Phys. Rep.* 45 (78) 177
- [6] S. Bjørnholm and W. J. Swiatecki, *Nucl. Phys.* A391 (82) 471
- [7] A. Bohr and B. R. Mottelson, *Nuclear Structure I*, W. A. Benjamin Inc., 1969

FORMATION OF DECAY OF A LOCALIZED REGION OF HIGH
EXCITATION IN HEAVY-ION REACTIONS

William G. Lynch
National Superconducting Cyclotron Laboratory
Michigan State University
East Lansing, Michigan 48824

The de-excitation and disassembly of highly excited hadronic many-body systems produced in medium and high energy nuclear reactions presents one of the more challenging problems in nuclear physics. One exciting opportunity is the possibility of studying the decay of nuclear systems at temperatures and densities at which the thermodynamic properties of the nuclear medium are unknown. Such a program is complicated by the degree to which the dynamical and statistical aspects of the reaction become intertwined as the excitation energy per particle is increased. For heavy ion reactions, relevant time scales such as the time scale for particle emission, the time scale for equilibration, and the time scale for the dynamical evolution of the collision all become comparable at intermediate energies. This talk will concentrate on aspects of light particle correlations and complex fragment emission in which the near equivalence of these time scales appears to be particularly relevant.

1. Space-time localization information from light particle correlations

Inclusive measurements have established quite clearly the importance of nonequilibrium light particle emission in heavy ion reactions. Systematic studies have revealed that the inclusive light-particle cross sections may be described in terms of thermal emission from a hot source of nucleons having an apparent temperature considerably higher than that of the compound nucleus and moving with slightly less than half the beam velocity.¹ Information about the spacial and temporal features of this source may be obtained by a measurement of the importance of final state interactions between correlated light particles at small relative momenta. For the case of two protons emitted at close proximity in space and time, the strong attractive nuclear interaction in the singlet s partial wave causes a characteristic enhancement in the two-proton correlation at relative momenta of about 20 MeV/c. Emission from a source of large dimensions or long source lifetimes will result in a reduced final state effect.

One can define a two-proton correlation function $R(p_1, p_2)$ in terms of the singles cross sections, $\sigma(p_1)$, $\sigma(p_2)$, and coincidence cross section $\sigma(p_1, p_2)$, by

$$\sigma(p_1, p_2) = C\sigma(p_1)\sigma(p_2)(1 + R(p_1, p_2)) \quad (1.)$$

where the p 's denote the momenta of the particles and the normalization constant C is experimentally determined by the condition $R(p_1, p_2) = 0$, for sufficiently large relative momenta where final state interactions are not important. For a source of negligible lifetime, $R(p_1, p_2)$ depends principally upon the magnitude of the relative momentum $\Delta p = |p_1 - p_2|/2$.²

In an experiment performed at the Holifield Heavy Ion Research Facility light particle correlations produced in ^{16}O induced reactions on C, Al, and Au targets were measured using a close-packed hodoscope centered at a scattering angle of 15° .³ The experimental correlation functions, shown in fig. 1, were obtained by inserting the experimental cross sections in Eq. 1 and by summing both sides of the equation over all energies and angles corresponding to a given relative momentum. The solid curves drawn in the figure are the results of calculations using a model developed by Steve Koonin for the case of incoherent emission from a source of negligible lifetime and a 4 fm gaussian

radius parameter r_0 .² Nonnegligible decay times will reduce the correlations, therefore values for r_0 deduced by comparison with the calculations performed in the limit of zero source decay time will represent upper limits on the average source sizes.

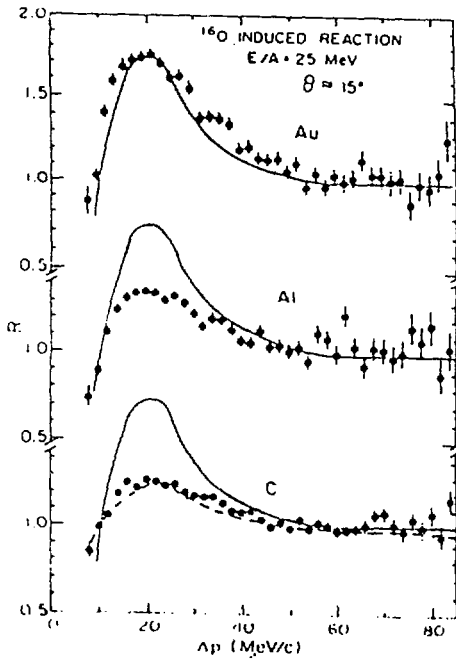


Fig. 1

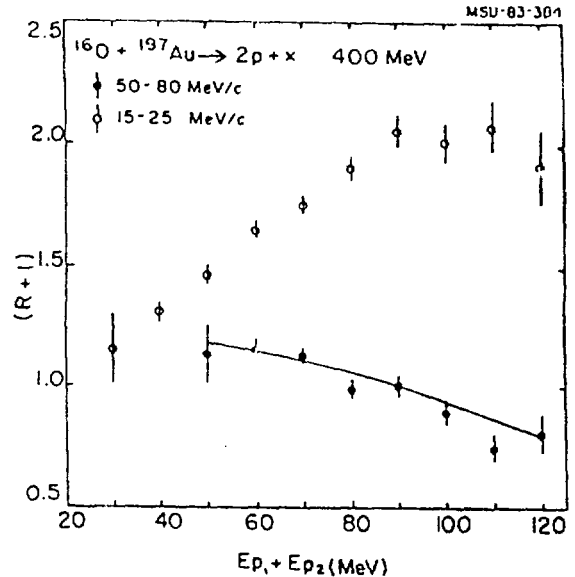


Fig. 2

If one compares the magnitude of the experimental correlation at $\Delta p = 20$ MeV/c for the three targets, it will be noted that the correlation decreases with the size of the target. In the limit of zero source decay time, this result would imply that the spatial radius parameter r_0 associated with the largest target is smaller than the r_0 associated with the smallest target. When an appreciable fraction of the correlated protons originates from the decay of a long lived system (e.g. a compound nucleus), however, the source lifetime must be taken into account. From measured inclusive proton angular distributions, one can determine that protons evaporated from the compound nucleus contribute negligibly to the Au data of Fig. 1. For reactions on C or Al, however, the large velocity of the center of mass kinematically focuses the protons which are evaporated from the compound nucleus to forward angles. Because of the rather long emission time associated with the compound nucleus, in the model developed by Koonin, these evaporated protons would be only weakly correlated.

Further insight may be gained by investigating the dependence of the measured correlation function $1+R(\Delta p)$ on the total energy of the two coincident protons. This energy dependence for reactions on the Au target is shown in Fig. 2 for the relative momentum intervals of $\Delta_1 p = 15-25$ MeV/c (where $R(\Delta p)$ is maximum) and $\Delta_2 p = 50-80$ MeV/c (where $R(\Delta p)$ should be negligible). For the lowest proton energies, the difference between the two correlations is small, corresponding to emission from a source of rather large space time extent. With increasing proton energies the difference between the two correlations increase and for the highest energy protons are consistent with a source of rather limited space time extent. For proton energies above $E_1 + E_2 = 90$ MeV the ratio $(1+R(\Delta_1 p))/(1+R(\Delta_2 p))$ yields an upper limit of $r_0 = 3.1$ fm.

In fig. 2, the correlation function corresponding to $\Delta p = 50-80$ MeV/c decreases slightly for increasing energy of the coincident protons. This decrease may be understood

in terms of the phase space constraints imposed by energy and momentum conservation. In order to assess these effects, we assume for simplicity that only a subset of nucleons have interacted strongly during the time in which the two protons are emitted. These protons are assumed to be emitted isotropically with a Maxwell-Boltzman distribution in the rest frame of this subset of nucleons. The solid line in Fig. 2 shows the correlation expected from energy and momentum conservation with a subset having an apparent temperature (7.1 MeV) and source velocity (.087c) chosen to provide an adequate description of the inclusive data and consistent with the overall features of the coincidence data. While these kinematic correlations do not significantly affect conclusions drawn from the energy gated correlations shown in fig. 2, such kinematic correlations may reduce or render misleading conclusions drawn from comparison of the energy averaged correlations with calculations which do not include these energy and momentum conservation constraints.

As an alternative interpretation, the strong enhancement of the two proton correlation at $\Delta p = 20$ MeV/c may be attributed to the sequential decay of particle unstable ${}^2\text{He}$. In many statistical models these particle unstable nuclei are considered to lie within the phase space of decay configurations. Protons from the sequential decay of these particle unstable nuclei have been predicted to contribute as much as 25% to the inclusive proton yield.⁴ The proton correlations for the C and Al targets have been reproduced by assuming the statistical emission of particle unstable ${}^2\text{He}$ from the compound nucleus.⁴ Indicated by the dashed line in Fig. 1 is the proton correlation for the C target calculated within the framework of this assumption. While the proton correlations observed on the C and Al targets are comparable to the predictions from compound emission of ${}^2\text{He}$, a compound nucleus produced in reactions on the Au target emits only a negligible number of ${}^2\text{He}$ due to the considerably lower temperature and larger nuclear charge of this system. The application of a thermal ${}^2\text{He}$ emission mechanism to reactions on the Au target appears to require as well the additional assumption that the emission occurs predominantly from an excited subsystem during the early stages of the collision.

Final state interactions can influence the correlations at small relative momenta between any two emitted particles. Examples of other correlations can be seen in preliminary data shown in Fig. 3. It is clear that any comprehensive final state interaction theory must eventually be able to describe simultaneously correlations (such as dt and pt) which display prominent resonance as well as correlations (such as dd and pd) in which the importance of resonances is minimal.

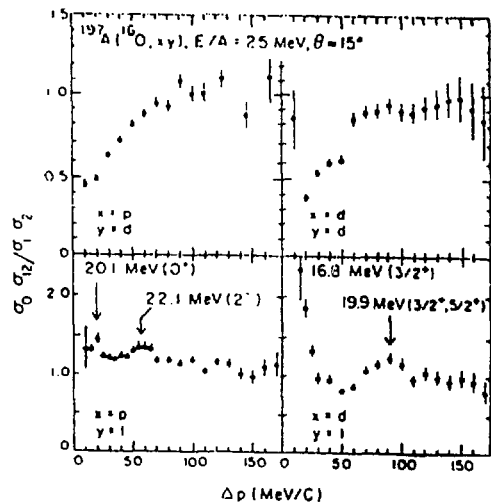


Fig. 3

2. Pre-equilibrium aspects of complex fragment emission

The emission of complex nuclei has been observed in nucleus-nucleus collision over a large range of incident energies. These observations have suggested that the emission of complex nuclei (fragmentation) may be a general characteristic of highly excited nuclear

systems. The assumption of sequential binary decay from the compound nucleus has been successful in reproducing the elemental yields and energy dependence of fragmentation cross sections in intermediate energy heavy ion reactions.⁵ The fragmentation cross sections induced by relativistic protons have been reproduced as well by a variety of differing statistical calculations including a very stimulating interpretation in terms of statistical cluster formation near the critical point of the liquid-gas phase diagram of nuclear matter.⁶ These differing calculations correspond to differing dynamical configurations at which statistical partitioning must be performed; the correctness of these dynamical assumptions and their influence on the experimental observables is yet to be clarified.

The fragmentation spectra produced in heavy ion reactions at intermediate energies may reflect as well the dynamics of the equilibration process. Fig. 4 shows energy spectra for fragments with $Z_f=5-10$ which were measured at the K500 cyclotron at Michigan State University in ^{12}C induced reactions on Au at $E/A = 30 \text{ MeV/A}$.⁵ For the lighter elements, the angular distributions are forward peaked indicating that these elements are emitted prior to the attainment of full statistical equilibrium of the composite nucleus. With increasing element number the angular distributions become less forward peaked more characteristic of a higher degree of equilibration for the emitting system. If one characterizes these energy spectra by fitting with the simple moving source parameterization the apparent temperatures and source velocities one obtains are considerably larger for the lighter fragments than for the heavier fragments. This would suggest that the heavier particles originate on the average from larger and colder sources.

This may be consistent with the existence of some localized region of excitation in a reaction evolving towards an equilibrium configuration provided two conditions are met: 1) the time scales for equilibration and particle emission are comparable, and 2) the hotter and smaller sources of the initial stages of the reaction emit relatively more of the lighter fragments than do the later fully equilibrated stages. To illustrate this possibility, we have generalized a statistical formulation of compound nucleus decay to describe the statistical emission from an excited subsystem.⁷

In our calculation we assume that the entire projectile merges with some number of target nucleons to form a source of A_S nucleons with a velocity and excitation energy calculated from energy and momentum conservation. The entire projectile momentum is assumed either to remain with the source or to be carried away by the statistically emitted fragments. Nucleons are accreted by the source from the target spectator. This adds additional excitation energy to the source and

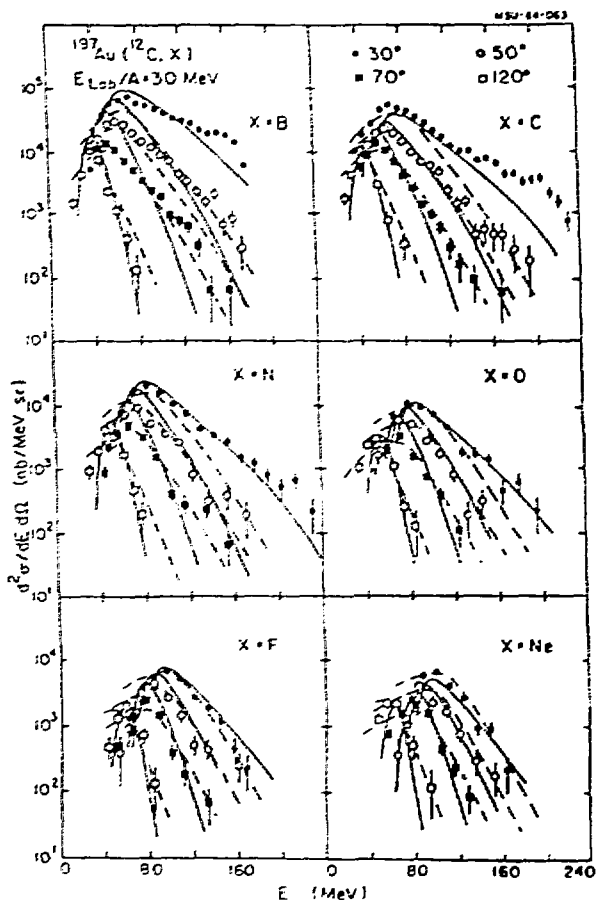


Fig. 4

lowers its velocity. During its entire evolution this idealized source emits particles at rates determined by the available phase space with the level density of excited subsystem approximated by an expansion of the fermi gas level density expression evaluated at normal nuclear matter density.

The particles are assumed to be emitted isotropically in the rest frame of the source with a thermal distribution generalized from the Weisskopf formula. The calculation also considers the division of kinetic energy between the emission partners as well as a random component of momentum introduced by the net fermi momentum of the target participant nucleons. With these considerations in mind, the distribution is transformed to the laboratory with the coulomb acceleration taking place in the center of mass frame. (The coulomb barrier is averaged over a range of values about the centroid in order to mitigate the effects of sharp cutoffs on the distributions.)

The solid curves in Fig. 4 were produced by summing the appropriately normalized spectral contributions which describe the fragment emission at each stage of the reaction. In this calculation the mean coulomb barrier is taken to be .9 of the touching sphere value. The rate at which the source accretes nucleons from the cold target spectator region is taken to be a constant 2. nucleons per fm/c. It is important to note here that curves for all six elements were produced with the same set of input values including the overall normalization, given by the reaction cross section.

In summary, the spectra and multiplicities of light particles and complex fragments produced in intermediate energy heavy ion reactions are strongly influenced by the near equivalence of the time scales for equilibration and particle emission. In addition, there exist supporting evidence for the assumption of a statistical emission mechanism, particularly for the description of complex fragment emission. One may reasonably hope that refinements in both measurements and theories will eventually enable the study in detail of the response of the nuclear many body system to localized and transient excitations.

1. C.K. Gelbke, Comments Nucl. Part. Phys. 11, 259 (1983), and references given therein.
2. S.E. Koonin Phys. Lett. 70B, 43 (1977).
3. W.G. Lynch, et al., Phys. Rev. Lett. 51, 1850 (1983).
4. M.A. Bernstein, et al., Phys. Rev. C29 132 (1984).
5. C.B. Chitwood, et al., Phys. Lett. 131B, 289 (1983).
6. J.E. Finn, et al., Phys. Rev. Lett. 49, 1321 (1982).
7. W.A. Friedman and W.G. Lynch, Phys. Rev. C28, 16 (1983).

ENTROPY PRODUCTION IN HIGH ENERGY NUCLEAR COLLISIONS

G.D. Westfall, B.V. Jacak, C.K. Gelbke, L.H. Harwood, W.G. Lynch,
D.K. Scott, H. Stöcker, and M.B. Tsang
National Superconducting Cyclotron Laboratory
Michigan State University, East Lansing, MI 48823-1321 USA

T.J.M. Symons
Lawrence Berkeley Laboratory, Berkeley, California 94720

The study of the entropy produced in proton- and heavy ion- induced reactions on heavy nuclei can provide a method of studying the collective behavior of nuclear matter.^{1 2} Hydrodynamical^{3 4} and intranuclear cascade calculations⁵ have demonstrated that the entropy per baryon, S/A , created in high energy nucleus-nucleus collisions remains constant during the expansion of the system. Information concerning the entropy produced in these reactions can be obtained by comparing the fragment production cross sections with a quantum statistical model.⁶ Thus fragments observed experimentally can carry information concerning not only the late stages of the reaction but also the hot, compressed stage of the reaction.

The idea that the entropy created in a nucleus-nucleus collision could be extracted from observed data was put forth the Siemens and Kapusta in 1979.¹ Entropies in the range of 4-6 were extracted from the observed deuteron to proton ratios based on the formula $S/A = 3.945 - \ln(\langle d \rangle / \langle p \rangle)$. The disagreement between these results and the expected entropy was interpreted as evidence for a soft equation of state. However more recent calculations indicate that heavier fragments must be included in the analysis in order to extract the entropy produced.⁶

We have recently reported systematic measurements² for complex nuclear fragments emitted at intermediate rapidities from reactions of ^{40}Ar with Au at 42, 92, and 137 MeV/nucleon. The observed fragments with $A=1-14$ are explained by emission from a common thermal source and the mass distributions are analyzed using a quantum statistical model to deduce the entropy created in the collision.

Measured energy spectra of ^{10}Be are shown in Figs. 1a, 1b, and 1c for 137, 92, and 42 MeV/nucleon $^{40}\text{Ar}+\text{Au}$. These spectra are typical of fragments with $A>6$. The solid lines are fits to the spectra assuming particle emission from a single moving source. The source temperature and velocity and the fragment cross section are obtained by fitting the double differential cross sections with a relativistic Boltzmann distribution in the rest frame of the source using a least squares method. This parameterization is used to isolate the component of inclusive spectra arising

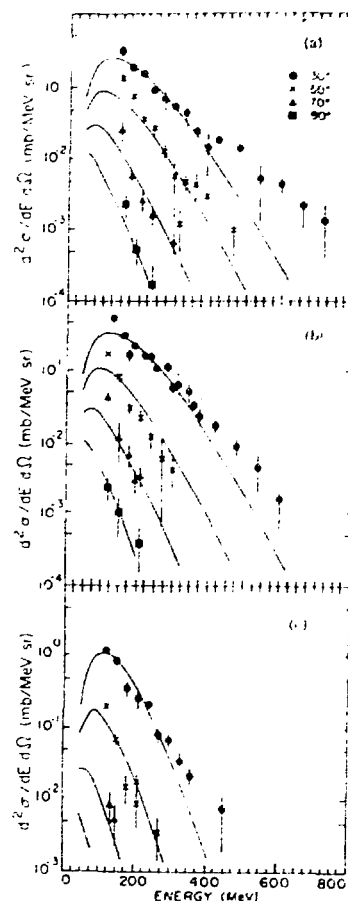


Fig. 1

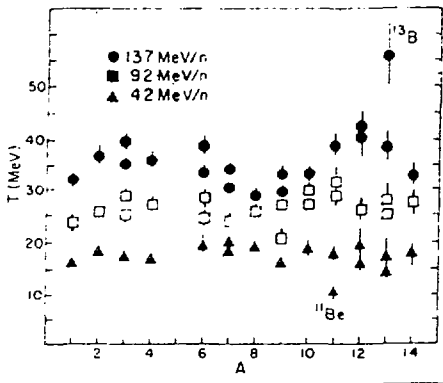


Fig. 2

thus sampling only a portion of the intermediate rapidity data. It would be difficult to account for the production of $A=14$ fragments at intermediate rapidity with models based on few nucleon-nucleon scatterings. Therefore we believe that our results convey evidence for thermalization of the emitting system.

Fig. 3a shows the relative mass yields as a function of mass. The cross sections are obtained by integrating the moving source fits in order to focus on the intermediate rapidity source and exclude particles originating from the projectile and target. The solid histograms show the results of a quantum statistical calculation of the mass yield. The quantum statistical model assumes a system of N neutrons and Z protons in thermal and chemical equilibrium at a given S/A and nuclear density, ρ , which then specifies the temperature. Included in the calculation are nucleons, pions, delta resonances, stable and γ -unstable nuclei up to $A=20$, and the known particle unstable nuclear states up to $A=10$. The N and Z of the initial system are chosen to be those of the target nucleus for proton-induced and peripheral nucleus-induced reactions. For nucleus-nucleus reactions the overlapping volume of the two nuclei at the impact parameter with the most weight is used. Interactions are taken into account via the excluded volume of the fragments. The shape of the calculated mass yield is well determined by the total entropy in the system for $\rho=0.3-0.7\rho_0$, where $\rho_0=0.15/\text{fm}^3$. This method allows extraction of the entropy from the experimentally determined mass yield through a least squares fit of the calculated yields. The histograms are results for $\rho=0.3\rho_0$.

from an intermediate velocity source. The resulting temperature for each fragment is shown in Fig. 2 as a function of the fragment mass.

The similarity of the temperatures over the measured range of fragment masses suggests that the fragments originate from a thermal source and that the same type of source gives rise to the heavy and the light fragments. The average source temperatures are 18, 25, and 35 MeV at the bombarding energies of 42, 92, 137 MeV/nucleon respectively. The fluctuations in the temperatures for the 137 MeV/nucleon case could be due to the fact that the telescopes only measured particles up to 80 MeV/nucleon

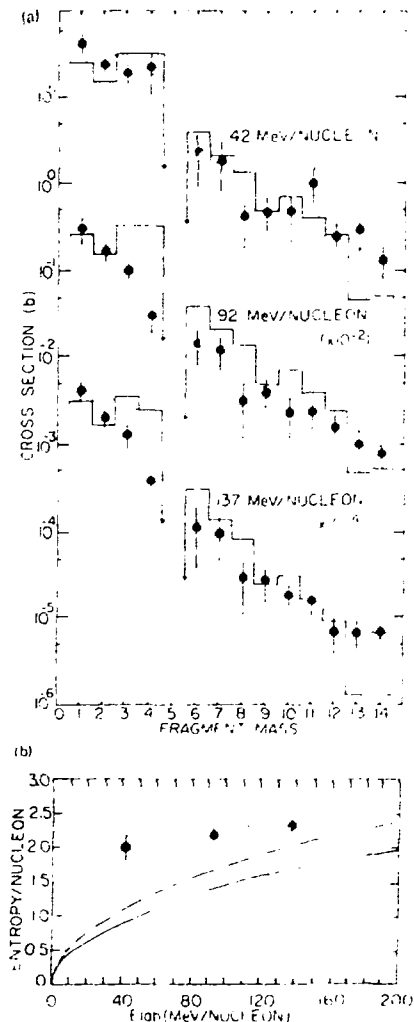


Fig. 3

The solid line in Fig. 3b shows the average entropy/nucleon expected for participants using a conventional hydrodynamic calculation and the dashed line the result for a viscous fluid. The extracted entropies are much lower than those derived from deuteron/proton ratios, but are still larger than theoretical values. This discrepancy may be due to several effects. The detection of a heavy fragment at intermediate rapidity correlates with a high multiplicity, so the measured fragments arise from central collisions, but some averaging over impact parameter remains. This averaging has been shown to alter the extracted entropy.⁷ Another possible factor would be a liquid-vapor phase transition, which would cause the expansion to be no longer isentropic and additional entropy to be produced.

One can also extract the entropy from target rapidity fragments as well as from intermediate rapidity fragments. The results of fitting the above quantum statistical model to target-like fragments are shown in Fig. 4a for a variety of proton- and nucleus-induced reactions.⁸ The fits generally encompass fragments with $3 \leq Z \leq 10$ and appear to be independent of both projectile type and energy. The average value for S/A in these cases is 1.84 ± 0.16 . This constant value of 1.84 for the extracted S/A coincides with the entropy necessary to excite the target nuclei to their binding energy. Shown again in Fig. 2b are the extracted entropies for intermediate rapidity fragments ($1 \leq A \leq 14$) from the reaction of Ar+Au at 42, 92, and 137 MeV/nucleon. These values are higher than those extracted from target fragments and increase with bombarding energy. No data exist for intermediate rapidity fragments with $A \geq 6$ at energies above 137 MeV/nucleon. The data of Gosset et. al.⁹ do not extend to intermediate rapidities for fragments heavier than ${}^4\text{He}$.

The extracted entropies from intermediate rapidity fragments with $1 \leq A \leq 3$ and $1 \leq A \leq 4$ from high energy nucleus-nucleus reactions are also shown in Fig. 4b. The average value of S/A for fragments with $1 \leq A \leq 3$ and $1 \leq A \leq 4$ are 4.24 ± 0.32 and 3.60 ± 0.12 respectively, independent of the incident energy and projectile nucleus. The difference between the entropy extracted using the same quantum statistical model compared to light particle cross sections and cross sections for fragments with $1 \leq A \leq 14$ appears to be a paradox because these fragments seem to have common origins. The apparent temperatures of these fragments are similar to each other at a given bombarding energy while the extracted source velocities vary from 0.5 times the projectile velocity for $A \leq 3$ to 0.3 times the projectile velocity for

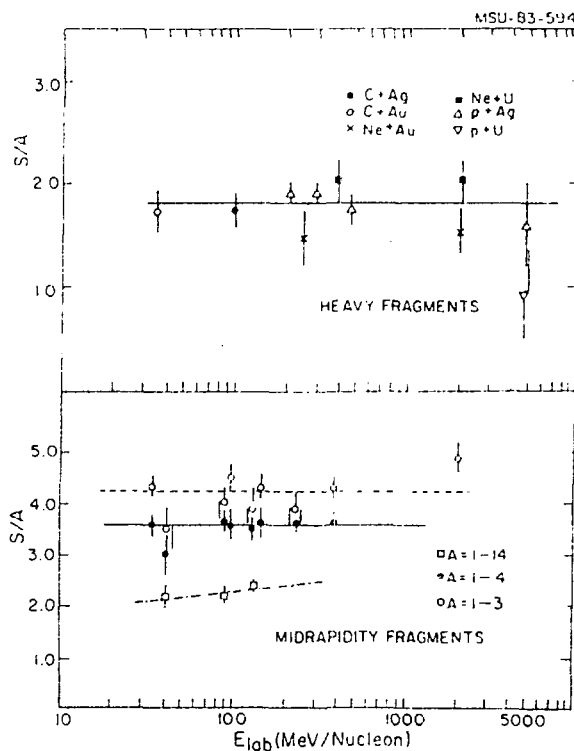


Fig. 4

the heavier fragments. However the present light particle inclusive data are dominated by more peripheral collisions where the small number of nucleons contained in the interaction volume between the two nuclei exclude the formation of heavier emitted fragments. The macrocanonical approach inherent in the quantum statistical model requires many particles in the system and is inapplicable for peripheral collisions. In contrast the thermodynamic limit is approached for near-central collisions which is where medium mass fragments are produced.

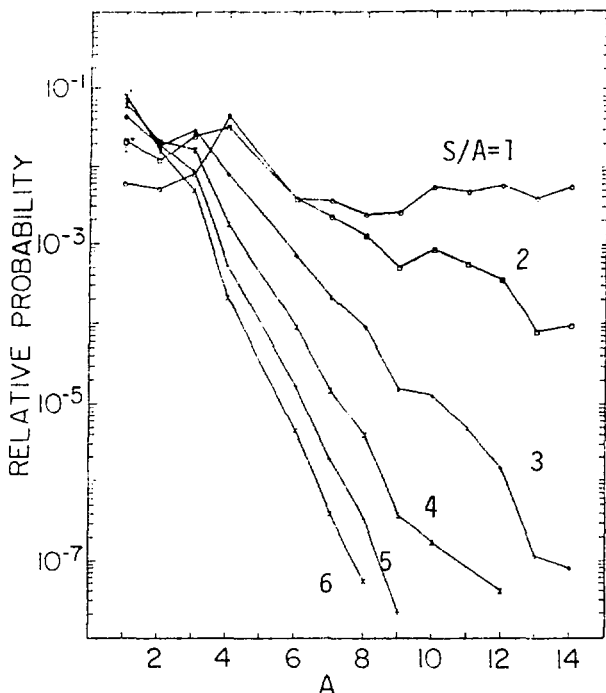


Fig. 5

The remaining question is what happens to the intermediate rapidity intermediate mass fragments from nucleus-nucleus collisions at energies above 137 MeV/nucleon. In Fig. 5 the mass distributions for these fragments predicted by the quantum statistical model are plotted for values of S/A ranging from 1 to 6. These entropy values correspond roughly with incident energies from 10 to 2000 MeV/nucleon. To establish conclusively whether the extracted entropy is a meaningful quantity one must compare with data for fragments with $1 \leq A \leq 14$ from reactions between 200 and 1000 MeV/nucleon.

This work is supported by the National Science Foundation, Grant No. PHY 83122455.

References

1. P. Siemens and J.I. Kapusta, Phys. Rev. Lett. 43, 1486 (1979).
2. B.V. Jacak, G.D. Westfall, C.K. Gelbke, L.H. Harwood, W.G. Lynch, D.K. Scott, H. Stöcker, M.B. Tsang, and T.J.M. Symons, Phys. Rev. Lett. 51, 1846 (1983).
3. H. Stöcker, J. Hofmann, J.A. Maruhn, and W. Greiner, Prog. Part. Nucl. Phys. 4, 133 (1980).
4. J.I. Kapusta and D. Strottman, Phys. Rev. C23, 1282 (1981).
5. G. Bertsch and J. Cugnon, Phys. Rev. C24, 2514 (1981).
6. H. Stöcker, G. Buchwald, G. Graebner, P. Subramanian, J.A. Maruhn, W. Greiner, B.V. Jacak, and G.D. Westfall, Nucl. Phys. A400, 63c, (1983).
7. H.H. Gutbrod, H. Löhner, A.M. Poskanzer, T. Renner, H. Reidesel, H.G. Ritter, A. Warwick, F. Wiek, and H. Wieman, Phys. Lett. 127B, 317 (1983).
8. B.V. Jacak, H. Stöcker, and G.D. Westfall, Phys. Rev. C, in press, (1984).
9. J. Gosset, H.H. Gutbrod, W.G. Meyer, A.M. Poskanzer, A. Sandoval, R. Stock, and G.D. Westfall, Phys. Rev. C16, 629 (1977).

DROPLET MODEL OF NUCLEAR FRAGMENTATION AT HIGH ENERGIES -
APPLICATION TO FRAGMENT NUCLEAR CHARGE DISTRIBUTION

N. T. Porile, A. Bujak, J. E. Finn^a, L. J. Gutay, A. S. Hirsch,
R. W. Minich^b, R. P. Scharenberg, and B. C. Stringfellow

Departments of Physics and Chemistry, Purdue University,
W. Lafayette, IN 47907

and

F. Turkot

Fermi National Accelerator Laboratory, Batavia, IL 60510

An inclusive experiment in which nuclear fragments from helium to aluminum were produced in collisions between high energy protons (30-350 GeV) and heavy nuclear targets (xenon, krypton) has motivated the description of fragment production as a critical phenomenon.¹⁻³ The observation that the mass yield of fragments obeys a power law in fragment mass number, A_f ,

$$Y(A_f) \propto A_f^{-\tau} \quad (1)$$

with τ about 2.6 for both targets, was recognized as a possible signature for fragment formation near the critical point of nuclear matter.¹ (Fig. 1) The power law describes the frequency distribution for clusters (fragments) having A_f constituents. Clustering according to a power law with an exponent between 2 and 3 is displayed by many systems near their critical point.⁴⁻⁶ Away from the critical point, the yield is expected to be damped exponentially, thereby suppressing the creation of large clusters.

In pursuing this description of fragment production, we have generalized the classical droplet model by M. E. Fisher for a one component system undergoing a liquid-gas phase transition near its critical point.⁷ For a single species substance, the probability to form an l -particle cluster depends on the Helmholtz free energy and the chemical potential per particle

$$Y(l) \propto e^{-(f(l)-\mu l)/kT} \quad (2)$$

The Helmholtz free energy

$$f(l) = U(l) - TS(l) \quad (3)$$

contains bulk and surface contributions to both the cluster binding energy, $U(l)$, and entropy, $S(l)$. Fisher stated that there existed a term in the free energy which contained the parameter τ . At the critical point, nearly exact cancellation between $f(l)$ and μ leaves only the term containing τ and so the power law (1) emerges from (2). This simple description works surprisingly well for real gases from the triple point up to the critical point.⁴

From this point of view, nuclear fragments are formed when the remnant of the proton-nucleus collision approaches its critical point. Precisely how this state is attained cannot be answered at present, but for the sake of argument let us accept the power law (1) as evidence that the remnant is at

or in the neighborhood of its critical point. Thus, large density fluctuations occur giving rise to clusters of nucleons, or fragments. The surface free energy is substantially reduced near the critical point, and so the system of fragments is free to disassemble under the influence of Coulomb repulsion. Fragmentation is therefore viewed as a multi-body breakup of the remnant near the critical temperature. We expect that inclusive fragment measurements and those obtained with a heavy fragment trigger will display the same characteristics, since the observation of a fragment is, within this picture, a signature for the multi-body break up of the remnant near its critical point. This has recently been confirmed by the data of Warwick et al.

The first step in applying Fisher's model to our data is to parameterize the binding energy term in (3). The natural choice is the Weizsacker semiempirical mass formula. The coefficients are in general temperature and density dependent. Following Fisher, the entropy term, S , in (3) contains a bulk term proportional to the number of constituents in the cluster, and a surface term, proportional to the surface area of the cluster of $A_f^{2/3}$. Therefore, we can absorb the heat contribution to the cluster free energy into the appropriate terms in the binding energy parameterization. The Helmholtz free energy becomes

$$f(Z_f, A_f) = a_v A_f - a_s A_f^{2/3} - a_c Z_f^2 / A_f^{1/3} - a_{\text{sym}} (A_f - 2Z_f)^2 / A_f - \delta \quad (4)$$

where $\delta = a_p / A_f^{.75}$ for odd-odd nuclei, zero for odd-even nuclei, and $-a_p / A_f^{.75}$ for even-even nuclei. The coefficients in (4) represent the volume, surface, Coulomb, symmetry and pairing contributions to the free energy.

Fisher's condensation theory dealt with unimolecular liquids, and thus is not directly applicable to two-component systems. To account for both neutrons and protons we have modified Fisher's model by introducing a chemical potential for each. In addition, we account for the entropy of mixing between neutrons and protons. Finally then, the fragment yield as a function of charge and mass is given by

$$Y(Z_f, A_f) = \frac{C}{A_f^\tau} \exp [(f(Z_f, A_f) + \mu_N N_f + \mu_Z Z_f)\beta + N_f \ln \frac{N_f}{A_f} + Z_f \ln \frac{Z_f}{A_f}] \quad (5)$$

where μ_N (μ_Z) is the neutron (proton) chemical potential and $\beta = 1/kT$.

We have fit our fragment data with the above expression. (See Ref. 2, 3 for parameters.) As the figures in Ref. 2, 3 show, the fit is quite impressive over three orders of magnitude with only 8 free parameters and about 50 degrees of freedom. It should be pointed out that we have not rigorously justified the modifications made to Fisher's theory. However, this model is simple and effective in parameterizing a large quantity of data.

As discussed in Reference 3, our model can also account for the fragment kinetic energy spectra. The low observed Coulomb energies follow in a natural way from the simultaneous multi-body nature of the breakup. The high

energy tails of the fragment kinetic energy spectra provide evidence that all of the observed fragments are created at the same time from a common system, and appear to be dominated by Fermi motion.

The droplet model isotopic yield distribution has been used to derive the form of the nuclear charge distribution (i.e., isobaric yield distribution). Nuclear charge distributions have been fit empirically with the Rudstam formula for the formation cross section of nuclide (Z,A):

$$\ln[\sigma(Z,A)] = Y(A) + C[Z_p(A) - Z] \quad (6)$$

where the nuclear charge dispersion, expressed in terms of fractional isobaric yields is

$$f_A(Z) = \frac{\exp C[Z_p(A) - Z]}{\exp Y(A)} \quad (7)$$

and Z_p is the most probable charge at mass A. On the basis of Equations 4 and 5, we have derived the following expression for $f_A(Z)$

$$\ln f_A(Z) = -\beta \left[1 + \frac{a_c A^{\alpha-1/3}}{4a_{\text{sym}}} \right] \frac{4a_{\text{sym}}}{A^\alpha} (Z_p - Z)^2 \quad (8)$$

where

$$Z_p = \frac{(1/2)A + \frac{[\mu_p - \mu_N] A^\alpha}{8a_{\text{sym}}}}{1 + 1/4 \frac{a_c}{a_{\text{sym}}} A^{\alpha-1/3}} \quad (9)$$

This expression gives a good fit to the nuclear charge distribution (Figure 2). The implications of the parameters of the fit will be examined.

In summary, the droplet model of fragmentation as a critical phenomenon can account for (1) the mass yield distribution of fragments, (2) the isotopic yield distribution, (3) the nuclear charge distribution, and (4) the kinetic energy spectra.

- a. Present address: Applied Mathematics, 1612 Route 12, Box 373, Gales Ferry, CT 06335
- b. Present address: Lawrence Livermore Laboratory, Livermore, CA 94550
1. J. E. Finn et al., Phys. Rev. Lett. 49, 1321 (1982).
2. R. W. Minich et al., Phys. Lett. 118B, 458 (1982).
3. A. S. Hirsch et al., Phys. Rev. C29, 508 (1984).
4. C. S. Kiang, Phys. Rev. Lett. 24, 47 (1970).
5. H. E. Stanley, Phase Transitions and Critical Phenomena, Oxford University Press (1971).
6. D. Stauffer, Phys. Rep. 54, 1 (1979).

7. M. E. Fisher, Physics 3, 255 (1967) and Rept. on Prog. Phys. 30, 615 (1967).
8. A. I. Warwick et al., Phys. Rev. C27, 1083 (1983).
9. G. Rustam, Z. Naturforsch. 21a, 1027 (1966).

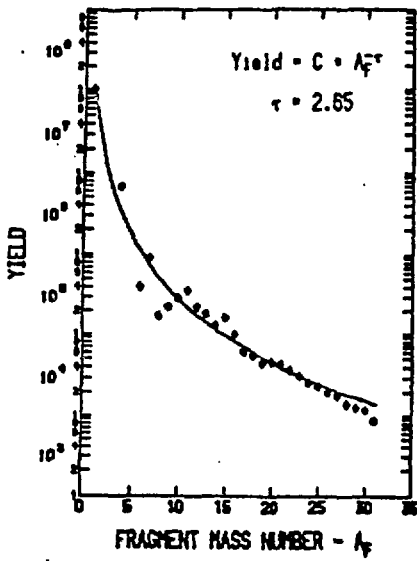


Figure 1

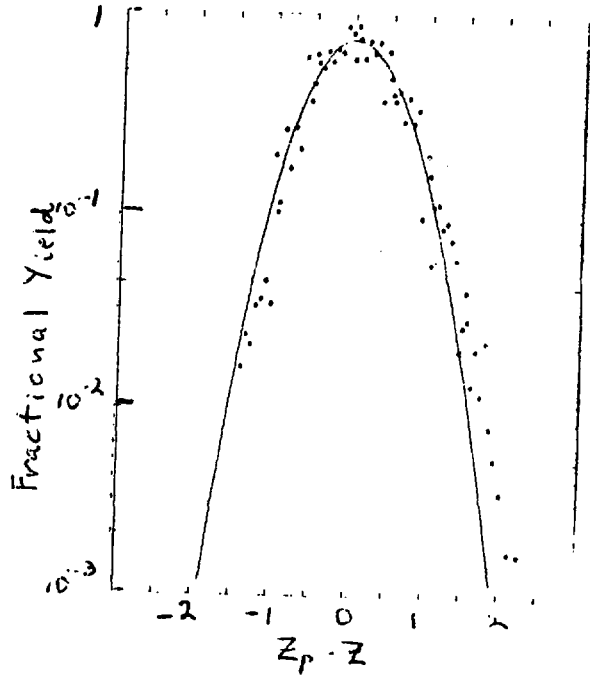


Figure 2

STOPPING POWER OF HEAVY NUCLEI

L. P. Csernai⁺ and J. I. Kapusta

School of Physics, University of Minnesota, Minneapolis MN 55455, USA

Inclusive cross sections for 100 GeV $p+A \rightarrow p+X$ are discussed in the framework of the evolution model proposed by Hwa¹. We will make 3 improvements on Hwa's analyses, obtaining an exact solution to his model. We infer a degradation length of 4.9fm rather than 17fm as inferred by Hwa.

According to the evolution model consider a proton penetrating through the nucleus A. depending on the impact parameter \vec{s} this proton collides on average with

$$\overline{N_A(s)} = \sigma_{NN} \int dz \rho_A(\vec{s}, z), \quad (1)$$

nucleons, where σ_{NN} is the nucleon-nucleon cross section (40mb), and $\rho_A(\vec{r})$ is the nuclear density distribution. The cross section for collision on N target nucleons in a line is then given by integrating the corresponding Poisson distribution over all impact parameters^{2,3}

$$\sigma_A(N) = \int ds^2 \frac{1}{N!} [\overline{N_A(s)}]^N \exp[-\overline{N_A(s)}]. \quad (2)$$

If we neglect the surface diffuseness of the nuclei and apply a uniform density distribution of $\rho_0=0.17\text{fm}^{-3}$ eq. (2) yields:

$$\sigma_A(N) = (N+1) \tilde{\pi} \left[1 - e^{-Q} \sum_{j=0}^{N+1} Q^j / j! \right] / (2 \sigma_{NN}^2 \rho_0^2); \quad Q = 2 \sigma_{NN} \rho_0 R_A. \quad (3)$$

We intend to describe the momentum degradation of the proton penetrating through the nucleus. Let us denote the invariant distribution function, i.e. the probability that the proton after traversing N nucleons has a momentum fraction x of its incident momentum by¹ $H(x, N)$, normalized to unity in the invariant phase space:

$$\int_0^1 H(x, N) \frac{dx}{x} = 1 \quad (4)$$

The distribution function H is integrated over the momentum components orthogonal to the beam.

In order to determine $H(x, N)$ it was assumed by Hwa¹ that H satisfies

⁺On leave of absence from the Central Research Institute for Physics, Budapest, Hungary

the following convolution equation:

$$H(x, N+1) = \int_x^1 \frac{dx'}{x'} H(x', N) Q(x/x'), \quad (5)$$

where $Q(x)$ is the probability in invariant phase space that a proton has momentum fraction x after a collision with one more target nucleon. We can assume that in high energy collisions the incoming nucleon (or its valence quarks) survive the collision with the target nucleons, so $Q(x)$ is normalized to unity. If we assume that the 1st and subsequent collisions in a tube show the same behaviour, $Q(x)$ can be approximated by¹:

$$Q(x) = \lambda x + \lambda^1 \delta(x-1), \quad (6)$$

inferred from the pp collision data⁴. Due to the normalization condition on $Q(x)$ the parameters λ and λ^1 satisfy the condition $\lambda + \lambda^1 = 1$.

In ref.¹ an approximate solution of eq. (5) is given for $N \rightarrow \infty$. Its applicability is, however, questionable since even for large nuclei the average collision number in a tube is $N \approx 3 - 4$. The complete solution of eqs. (5-6) can be given analytically for any N by the following simple formula:

$$H(x, N) = x \left[\sum_{n=1}^N \binom{N}{n} \lambda^n \lambda^{1(N-n)} \frac{(-\ln x)^{n-1}}{(n-1)!} \right] + \lambda^1 \delta(x-1). \quad (7)$$

This immediately gives the inclusive proton cross section integrated over the transverse momenta as:

$$\sum_N \sigma_A(N) H(x, N). \quad (8)$$

Assuming a factorization in p_L and p_T as⁵ $H(x, N) = \int d^2 p_T F_h(x, N) g_h(p_T)$ we can fit the experimental data of ref.⁴ at $p_T = 0.3$ GeV/c if we assume that $g_h(p_T=0.3 \text{ GeV/c}) = 0.99 (\text{GeV/c})^{-2}$. (Fig. 1)

A value of $\lambda = 0.52$ produces the best fit. It is about 20% bigger than the value obtained in ref.¹. Note that the x dependence of the of the cross sections at low x differs essentially from the result with the approximate solution of ref.¹. (Fig.1)

Using the solution (7) for $H(x, N)$ the momentum degradation of an incident nucleon in nuclear matter can be described. If its initial momentum is $p(0)$ the expected value of the longitudinal momentum after penetrating to a depth z into the matter is

$$\langle p(z) \rangle = p(0) \int_0^1 x H(x, \overline{N(z)}) \frac{dx}{x} = \left(1 - \frac{\lambda}{2}\right)^{\overline{N(z)}} \quad (9)$$

where $\overline{N(z)}$ is the average number of collisions up to this depth ,

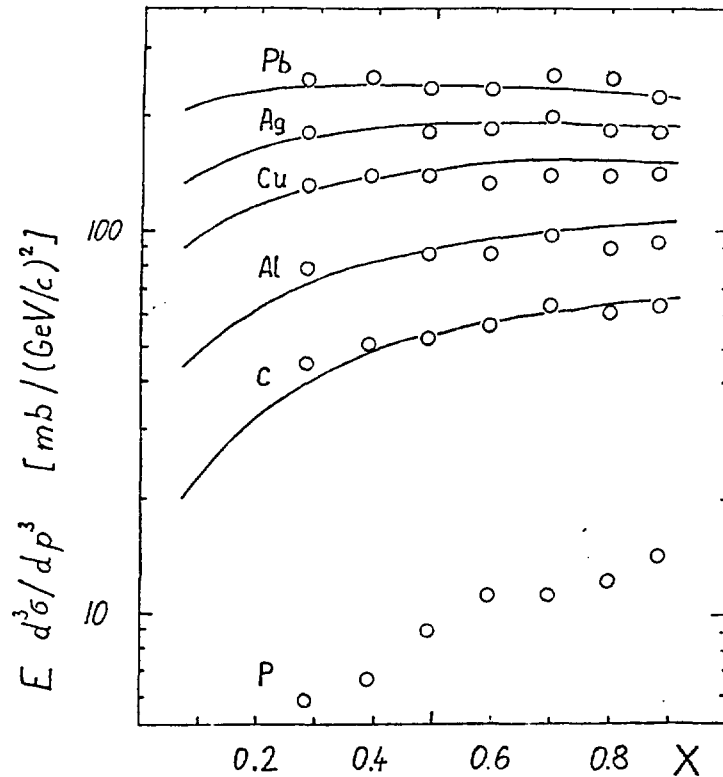


Fig. 1: Invariant differential cross section for 100 GeV/c $p+A \rightarrow p+X$ reaction at transverse momentum $p_T = 0.3$ GeV/c. Data points are from ref. 4, the full lines are predictions of the evolution model with $\lambda = 0.52$.

$\overline{N(z)} = \rho_0 \sigma_{NN} z = 0.68 \text{ fm}^{-1}$. The momentum degradation length in nuclear matter obtained this way is

$$\Lambda_p = - \left[\frac{1}{p_L} \frac{d p_L(z)}{dz} \right]^{-1} \cong 4.9 \text{ fm}. \quad (10)$$

This is substantially smaller than the $\Lambda_p = 17$ fm obtained in ref. 1, and only somewhat larger than 3 mean free path ($l = (\rho_0 \sigma_{NN})^{-1} = 1.5 \text{ fm}$ corresponding to the same parameters).

This work was supported by the U.S. Department of Energy under contract No. DE - AC02 - 79ER10364.

1. R.C. Hwa, OITS - 229 (1983) Oregon rep.
2. R.J. Glauber and C. Matthiae, Nucl. Phys. B21, 135 (1970)
3. J. Knoll and J. Randrup, Nucl. Phys. A324, 445 (1979)
4. D. Barton et al., Phys. Rev. D27, 2580 (1983)
5. R. Anishetty, P. Koehler, and L. McLerran, Phys. Rev. D22, 2793 (1980)

TRANSPORT PROPERTIES OF EXCITED NUCLEAR MATTER

P. Danielewicz[†]

Nuclear Science Division, Lawrence Berkeley Laboratory,
University of California, Berkeley, California 94720

Despite of the years of development of the hydrodynamic approach for the intermediate-energy heavy-ion collisions, one surprisingly finds that a major ingredient of the approach, the magnitude of the transport coefficient, has not been settled. The present study concerns with a microscopic evaluation of the shear viscosity and heat conduction coefficients from the Uhlenbeck-Uehling equation, and with an examination of the effect of the coefficients on the shock profile in the collisions. From a different perspective, on the basis of the Enskog equation, the coefficients are discussed by Malfliet [1].

The shear viscosity η and heat conduction κ coefficients are the coefficients of the expansion of the hydrodynamic momentum T^{ij} and energy T^{0i} fluxes in the particle rest-frame in terms of the macroscopic quantity gradients:

$$T^{(1)ij} = -\eta \left(\frac{\partial v^i}{\partial x^j} + \frac{\partial v^j}{\partial x^i} - \frac{2}{3} \delta^{ij} \frac{\partial v^l}{\partial x^l} \right) \equiv -\eta v'^{ij}, \quad (1)$$

$$T^{(1)0i} = -\kappa \frac{\partial T}{\partial x^i}, \quad (2)$$

with v the fluid velocity, T the temperature, and (2) being valid in the nonrelativistic limit. The most elementary mean-free-path arguments yield:

$\eta \sim \frac{1}{3} n m v \lambda$, and $\kappa \sim \frac{1}{3} n c v \lambda$, where n is the particle density, m mass, v average velocity, λ mean free path, and c the specific heat per particle.

With $\lambda \approx (n\sigma)^{-1}$, where σ the particle-particle cross-section, and the

Boltzmann statistics limit $c = \frac{3}{2}$, one finds density-independent

expressions: $\eta \sim \frac{1}{3} \frac{m v}{\sigma} = \frac{1}{\sigma} \left(\frac{m T}{3} \right)^{1/2}$, and $\kappa \sim \frac{1}{2\sigma} \left(\frac{3 T}{m} \right)^{1/2}$. Taking for

[†]On leave of absence from the Institute of Theoretical Physics, Warsaw University, Warsaw, Poland

the N-N cross-section $\sigma \approx 40$ mb, we get $\eta \sim 4.4 (T/\text{MeV})^{1/2} \cdot \text{MeV}/\text{fm}^2$ and $\kappa \sim 0.007 (T/\text{MeV})^{1/2} \text{ fm}^{-2}$. For the temperature $T = 60$ MeV, the mean-free-path estimate yields $\eta \sim 34 \text{ MeV}/\text{fm}^2$ and $\kappa \sim 0.055 \text{ fm}^{-2}$ which should be compared with the values used in the hydrodynamic calculations: $\eta = 6 \text{ MeV}/\text{fm}^2$ [2], and $\eta = (5-19) \text{ MeV}/\text{fm}^2$ and $\kappa = 0.015 \text{ fm}^{-2}$ [3]. At low temperatures the mean free path is known to diverge in the fermion system as $\lambda \sim T^{-2}$, and accordingly the transport coefficients diverge as $\eta \sim T^{-2}$ and $\kappa \sim T^{-1}$. We obtain the more fundamental results valid both at low and high temperatures by solving the Uhlenbeck-Uehling equation linearized in the gradients

$$D f_a^0 = \frac{g_b}{(2\pi)^3} \int d^3 p_b \int d\Omega' \frac{d\sigma}{d\Omega'} v_{ab} f_a^0 f_b^0 \tilde{f}_a^0 \tilde{f}_b^0 (\chi_{a'} + \chi_{b'} - \chi_a - \chi_b) \quad (3)$$

for the deviation δf of the distribution function $f(p, x, t)$ from equilibrium f^0 , $\delta f = \chi f^0 \tilde{f}^0$, with $\tilde{f} = 1 - f$, and here $D \equiv (\frac{\partial}{\partial t} + \frac{p}{m} \cdot \frac{\partial}{\partial x})$. Under $\text{div } \underline{V} = 0$ (which is a driving force for the bulk viscosity that may be considered negligible) $D f^0 = \frac{1}{2mT} f^0 \tilde{f}^0 [(p^i p^j - \frac{1}{3} \delta^{ij} p^2) v'^{ij} + \frac{1}{mT} (p^2 - \frac{5}{3} \langle p^2 \rangle) p^i \frac{\partial T}{\partial x^j}]$. We search for χ of the form $\chi = c_1 (p^i p^j - \frac{1}{3} \delta^{ij} p^2) v'^{ij} + c_2 (p^2 - \frac{5}{3} \langle p^2 \rangle) p^i \frac{\partial T}{\partial x^j}$, and we fix the constants in the expression by multiplying both sides of (3) by χ_a and integrating over the momenta. We find

$$\eta = \frac{5}{9} mT \left(\int_0^\infty dp p^4 f^0 \right)^2 / \int_0^\infty dp_a p_a^2 \int_0^\infty dp_b p_b^2 \int d\cos \theta_{ab} \int d\Omega' \frac{d\sigma}{d\Omega'} \sin^2 \theta' \times f_a^0 f_b^0 \tilde{f}_a^0 \tilde{f}_b^0 q_{ab}^5, \quad (4)$$

$$\kappa = \frac{1}{27m} \left(21 \int_0^\infty dp p^6 f^0 - 25 \left(\int_0^\infty dp p^4 f^0 \right)^2 / \int_0^\infty dp p^2 f^0 \right) / \int_0^\infty dp_a p_a^2 \int_0^\infty dp_b p_b^2 \int d\cos \theta_{ab} \int d\Omega' \frac{d\sigma}{d\Omega'} f_a^0 f_b^0 \tilde{f}_a^0 \tilde{f}_b^0 \times q_{ab}^3 [(p_b^2 - p_a^2)^2 + (p_b^2 - p_a^2)^2 - 2 (p_b^2 - p_a^2) (p_b^2 - p_a^2) \cos \theta'], \quad (5)$$

with $q_{ab} = \frac{1}{2} |p_a - p_b|$. The results using the experimental N-N cross sections are displayed in Fig. 1. By the variational principle for the transport coefficients [4] our results can be considered as the lower bounds for the transport coefficients associated with the kinetic equation. However in the Boltzmann statistics limit our results reduce to the first-order Chapman-Enskog result, and the higher-order corrections can raise η by only 1.5% and κ by 2.5%. In the degenerate Fermi gas limit the exact transport coefficients [5] occur to be: η greater by 2%, and κ by 12%, for the densities $n = (1-4) n_0$, and $T \gg 0$. The Chapman-Enskog result reads:

$$\eta = \frac{5\sqrt{\pi}}{16} \frac{\sqrt{mT}}{\sigma}, \quad \kappa = \frac{75\sqrt{\pi}}{64} \frac{1}{\sigma} \sqrt{\frac{T}{m}}, \quad (6)$$

with an effective cross-section

$$\tilde{\sigma} = \frac{1}{4} \int_0^{\infty} d \left(\frac{q^2}{mT} \right) \left(\frac{q^2}{mT} \right)^3 e^{-\frac{q^2}{mT}} \int d\cos\theta' \frac{d\sigma(E_{lab} = \frac{2q^2}{m})}{d\cos\theta'} \sin^2 \theta',$$

which exhibits the dependence on the scattering cross-section anisotropy.

For an isotropic energy-independent cross-section $\tilde{\sigma} \equiv \sigma$.

Using the obtained values of the transport coefficients we have solved the relativistic hydrodynamics equations, with the dissipative terms, for the shock profile in the nuclear matter corresponding to the projectile bombarding energy $E_{lab} = (100 - 800)$ MeV/nuc1. The shock-wave frame density profiles are displayed in Fig. 2. The 70% of the Rankine-Hugoniot density rise occurs at the distances in the shock frame: 5.5, 2.9, 2.2., and 1.8 fm, for $E_{lab} = 100, 200, 400,$ and 800 MeV/nuc1, respectively. These shock widths contain amounts of matter equivalent respectively to the distances in the normal nuclear matter of 8., 5.7, 4.8, and 4.5 fm. We may conclude that for $E_{lab} \lesssim 100$ MeV/nuc1 the possibility of creating a high density equilibrated nuclear matter state in the collisions is limited. For higher bombarding energies rather heavy nuclei with $A \gtrsim 100$ are required. It would be useful to learn what effect on the collision process has the proper magnitude of the transport coefficients in the full 3-dimensional calculations [3]. In general one may expect that the transport coefficients bring the hydrodynamics closer to the cascade (maybe fireball) type of the dynamics.

Acknowledgement:

The author substantially benefited from the discussions with M. Gyulassy.

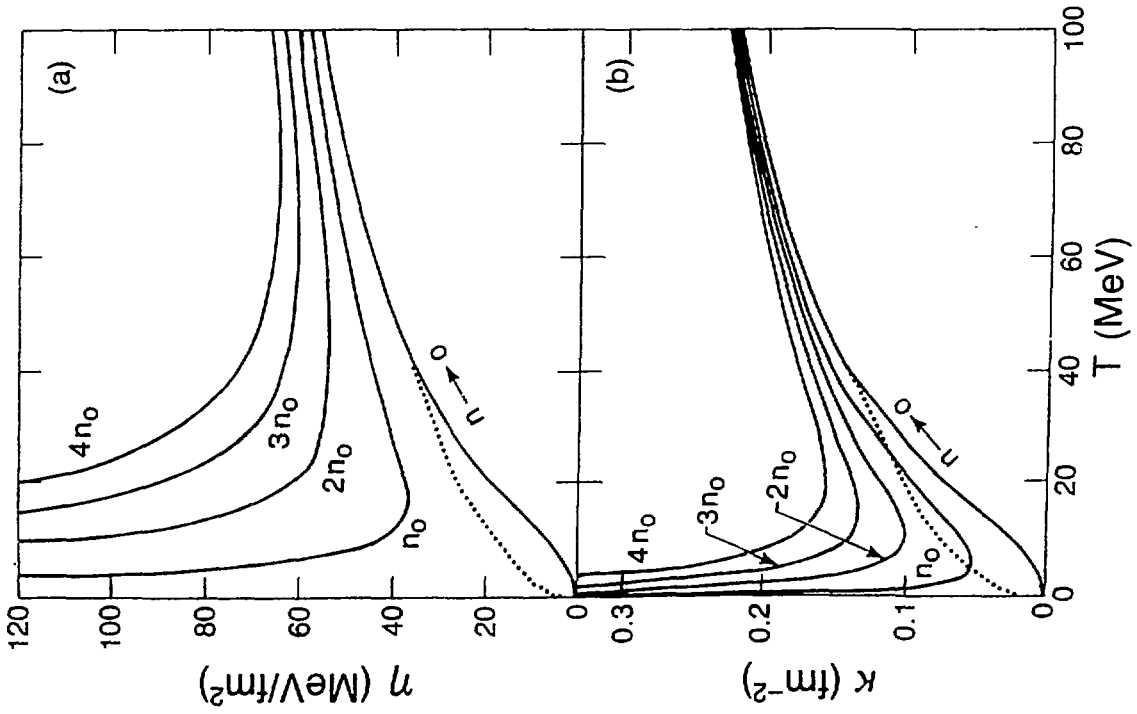
This work was supported by the Director, Office of Energy Research, Division of Nuclear Physics of the Office of High Energy and Nuclear Physics of the U.S. Department of Energy under Contract DE-AC03-76SF00098.

References:

- [1] R. Malfliet, Transport Properties of Nuclear Matter at High Densities and High Temperatures, Kernfysisch Versneller Instituut Report KIVI-458.
- [2] L.P. Csernai, Proc. Int. Workshop on Gross Properties of Nuclei and Nuclear Excitations VII, Hirschegg, Jan. 15-27, 1979, ed. H. Feldmeier (Technische Hochschule Darmstadt, 1979) p. 133.
- [3] G. Buchwald et al., Phys. Rev. C24 (1981) 135; C28 (1983) 1119.
- [4] E.J. Hellund and E.A. Uehling, Phys. Rev. 56 (1939) 818.
- [5] J. Sykes and G.A. Brooker, Ann. Phys. (N.Y.) 56 (1970) 1.

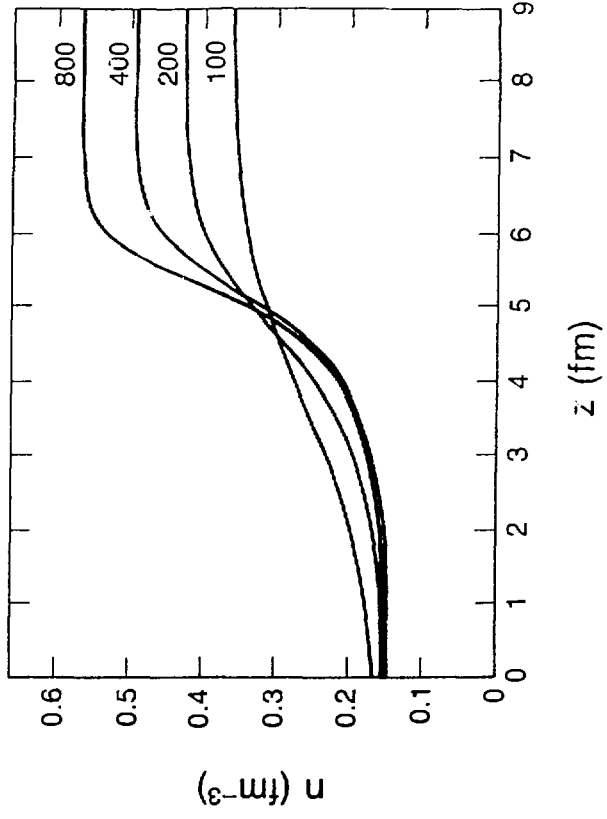
Figure Captions:

- Fig. 1 The temperature and density dependence of the nuclear-matter transport coefficients. The normal nuclear density has been taken $n_0 = 0.145 \text{ fm}^{-3}$. Dotted lines denote the Chapman-Enskog results (6), with the effective cross-section put equal to $\hat{\sigma} = 30 \text{ mb}$.
- Fig. 2 Rest-frame nuclear-matter densities as a function of the distance z in the shock-wave frame. The origin of the z axis is arbitrary. Numbers in the figure designate the projectile bombarding-energy in MeV/nucl to which the shock corresponds.



XBL 842 10062

Fig. 1



XBL 842 10073

Fig. 2

ROBUST OBSERVABLES IN NUCLEAR DYNAMICS

E.A. Remler

Department of Physics, College of William and Mary
Williamsburg Virginia, 23185

Nuclear dynamics describes in principle the time dependence of the density operator. Therefore, a well defined theory should contain some model of the density which can then lead to the unambiguous prediction of observables via basic scattering theory. Much theory being done in this field seems to needlessly ignore those exact results which are easily available from scattering theory and one purpose of this talk is to try to combat this state of affairs.

TDHF, intranuclear cascade and fluid dynamics are prominent dynamical theories in use today and explicit models of the density operator can be associated with each of them. None of them however explicitly describes the development of correlations during the disassembly of nuclear matter into fragments. No current dynamical theories do this. Therefore, an observable which is sensitive to disassembly dynamics is a correspondingly uncertain indicator of the system's state prior to disassembly. Observables which are insensitive to poorly understood details of theories can be called 'robust'. In heavy ion physics robust observables should therefore provide the most trustworthy tests of theories of nuclear matter prior to disassembly. This note will discuss a class of simple, robust observables and emphasize their close relation to observables introduced elsewhere(1)(2).

The summed charged nucleonic distribution, defined in terms of the observed inclusive fragment distribution by

$$d\sigma_{ch}(k) \cong \sum_T Z(T) d\sigma(T, A(T)k) \quad (1)$$

is usually assumed to be insensitive to disassembly. T is the fragment type - the set of all its quantum numbers except momentum k , and $Z(T)$ ($A(T)$) is the proton (nucleon) number of type T . The momentum of the fragment carrying the nucleonic charge is in this notation, $A(T)k$. Insensitivity can be assumed on the premise that disassembly dynamics affects some details of the relative probabilities for nucleons to distribute themselves amongst different T but cannot have much effect on the net number of protons coming off near a certain velocity.

σ_{ch} is closely related to the theoretical primordial proton distribution, which is defined (1) as the trace of the proton number density with the density operator in the asymptotic future

$$d\tilde{\sigma}(P, k) \cong \lim_{t \rightarrow \infty} \text{TR} [\hat{p}_e \hat{n}(P, k)] dk \quad (2)$$

$$\hat{n}(P, k) = \sum_i \delta(\hat{p}^{(i)} - k) \quad (3)$$

(carets denote operators). Eq.2 can be shown to be equivalent to

$$d\tilde{\sigma}(P, k) = \sum_T \left[\int \mathcal{N}(P, k; T, q) d\sigma(T, q) \right] dk \quad (4)$$

where \mathcal{N} is the number of protons to be found in a fragment T with momenta

k and p respectively. A formal expression for this in terms of the wave function for T is

$$\begin{aligned} \mathcal{N}(P, \underline{k}; T, q) &= \int \langle T, q | \hat{n}(P, \underline{k}) | T, q' \rangle dq' \\ &= \mathcal{N}(P, \underline{k} - q / A(T); T, q) \end{aligned} \quad (5)$$

Integration over q in Eq.5 yields $Z(T) * A(T) ** 3$. Comparing Eq.1 and Eq.4, one then sees that $d\sigma_{\text{th}}(\underline{k}) \approx d\bar{\sigma}(P, \underline{k})$ if fermi momenta of protons in all fragments are negligible. The expression on the r.h.s. of Eq.2 is evaluated by counting the number of protons in a bin about k in principle at infinite t , in practice just before disassembly. The equivalent expression in Eq.4 is what is needed to compare theory to experiment without approximation. It's usual approximation by Eq.1 is reasonable in portions of the spectra which are slowly changing on the scale of fermi momenta. Furthermore, it is consistent with neglect of disassembly dynamics during which momentum transfers of order of nuclear fermi momenta take place. The main ingredient in the derivation of Eq.4 is to use an exact expansion for the density operator at infinite times in terms of the outgoing channel eigenstates which has been described elsewhere(1).

The primordial proton distribution is the simplest example of a whole set of primordial multinucleon distributions. In particular a two proton distribution may be defined as

$$d\bar{\sigma}(P, \underline{k}, \underline{k}') \triangleq \lim_{t \rightarrow \infty} \text{TR} [\hat{\rho}_t \hat{n}(P, \underline{k}) \hat{n}(P, \underline{k}')] d\underline{k} d\underline{k}' \quad (6)$$

This observable should be as insensitive to disassembly as the primordial single proton distribution; it's theoretical value is obtained in as simple a way - by counting the number of pairs of protons found in bins about k and k' at the end of a calculation. The expression on the r.h.s of Eq.6 can be reformulated in terms of experimental observables just as Eq.2 was reformulated to yield Eq.4. This leads to the following equally intuitive formula

$$\begin{aligned} d\bar{\sigma}(P, \underline{k}, \underline{k}') &= \sum_T \left[\int \mathcal{N}(P, \underline{k}, \underline{k}'; T, q) d\sigma(T, q) \right] d\underline{k} d\underline{k}' \\ &+ \sum_{T, T'} \left[\int \mathcal{N}(P, \underline{k}; T, q) \mathcal{N}(P, \underline{k}'; T', q') d\sigma(T, q; T', q') \right] d\underline{k} d\underline{k}' \end{aligned} \quad (7)$$

The first term in Eq.7 gives the contribution from proton pairs bound in the same final state fragment. The number of such pairs per fragment is

$$\mathcal{N}(P, \underline{k}, \underline{k}'; T, q) = \int \langle T, q | \hat{n}(P, \underline{k}) \hat{n}(P, \underline{k}') | T, q' \rangle dq' \quad (8)$$

in complete analogy to Eq.5. In the second term which gives the contribution from protons bound in separate fragments, $d\bar{\sigma}$ is the observed two fragment inclusive cross-section.

Normalizations can be checked by integrating over all distinct pairs of momenta k and k' . Eq.6 shows that the l.h.s. of Eq.7 equals $Z(Z-1)/2$, the number of distinct proton pairs in the system. Similarly, Eqs.8 and 5 show that the r.h.s of Eq.7 integrates to

$$\sum_T \frac{1}{2} Z(T) (Z(T)-1) + \sum_{T, T'} Z(T) Z(T') \int \frac{1}{2} d\sigma(T, q; T', q') \quad (9)$$

The first term is the average number of distinct pairs emerging in the same T while the second is for those emerging in separate fragments. Since this covers all possibilities, the sum must equal the number all of distinct pairs.

As in the case of the primordial single proton distribution, we can approximate by neglecting fermi momentum in the integral over fragment momenta q and q' in Eq.7. This leads to

$$\begin{aligned} d\tilde{\sigma}(P, k, k') &= \sum_T z(T) (z(T)-1) f(P, k; T) d^3k d\sigma(T, A(T) \frac{1}{2}(k+k')) \\ &+ \sum_{T, T'} z(T) z(T') d\sigma(T, A(T) k; T', A(T') k') \end{aligned} \quad (10)$$

where f is the probability for finding any one pair of protons in T with relative momentum k. For large relative momentum, f vanishes so that only the contribution from protons in separate T remains. The expression for f in terms of the wave function of fragment T is

$$f(P, k; T) = \int \langle T, q | \delta(\frac{1}{2}(\hat{p}^{(1)} - \hat{p}^{(2)}) - k) | T, q \rangle d^3q \quad (11)$$

from which it can be seen to be unit normalized.

The primordial two proton distribution is very nearly as robust as that of the single proton. Only the probability distribution f needed to theoretically compute it contributes some uncertainty which is however, quite small as things go in heavy ion physics today. All cross-sections on the r.h.s of Eq.10 are directly observable. The lowest Z contribution to the term describing pairs in the same nucleus comes from T=He3. The first contribution to the second term comes from the inclusive two proton cross-section T=T'=P=H1.

There are obvious generalizations which are as insensitive to disassembly as the primordial two proton distribution but are nevertheless slightly less robust. Thus one could compute the two nucleon distribution which counts neutrons as well as protons. This is less robust because it requires free neutron cross-sections. Similarly, three and higher order primordial distributions will require knowledge of higher order nuclear correlation functions except if the momenta involved are far enough apart to cause the corresponding correlation functions $f(k_1, k_2, k_3, \dots)$ to be a priori negligible.

The primordial distributions discussed above are all defined by taking the trace of some observable with the system's density operator in the limit of infinite time. None of the observables discussed so far have contained spatial correlations and they therefor do not exhaust all usefull possibilities. The simplest example of an infinite class of distributions which do probe spatial correlations in the system is obtained using the primordial deuteron density as follows

$$d\tilde{\sigma}(D, k) \hat{=} \lim_{t \rightarrow \infty} \text{TR} [\hat{\rho}_t \hat{n}(D, k)] d^3k \quad (12)$$

$$\hat{n}(D, k) = \sum_{\langle i, j \rangle} |k, D(i, j)\rangle \langle D(i, j), k|$$

where $|q, D(i, j)\rangle$ denotes a state of nucleons i and j bound as a deuteron with momentum q. Using exactly the same asymptotic expansion of the density operator as led to Eqs.4 and 7, one obtains(1)

$$d\bar{\sigma}(D, \underline{k}) = \sum_T \left[\int N(D, \underline{k}; T, \underline{q}) d\sigma(T, \underline{q}) \right] d\underline{k} \quad (13)$$

where, in complete analogy to Eqs.5 and 8, the primordial deuteron content of fragment T is

$$N(D, \underline{k}; T, \underline{q}) = \int \langle T, \underline{q} | \hat{n}(D, \underline{k}) | \underline{q}', T \rangle d\underline{q}' \quad (14)$$

It is important to realize that Eqs.13 and 14 are exact even though in actual practice the evaluation of Eq.14 is somewhat limited by uncertainties regarding nuclear bound state wave functions and has only been done so far using the crudest possible model. Since these are unambiguous results of scattering theory there seems to be no excuse in promulgating recipes based on intuition in their stead.

Although calculation of primordial fragment numbers such as Eq.14 can and should be done more carefully, other experimental and theoretical uncertainties deserve equal attention. In particular it is possible that disassembly plays a greater role here than in the case of multi-nucleon primordial distributions. An indication of this is the fact that it is not even possible to compute Eq.12 in the same straightforward manner as its analogs, Eqs.2 and 6, since all current models lack disassembly dynamics and therefor, naively interpreted, would predict only unbound free-streaming nucleons in the final state. On the other hand, a more sophisticated approach described elsewhere, shows how to use such theories to predict primordial deuteron distributions and has had some success in the one case tested so far (1)(2).

In summary, the relation between the summed charged nucleonic distribution and the primordial proton distribution has been reviewed and these have been generalized to include an infinite class of almost equally robust observables. These probe momentum correlations in nuclear collisions prior to disassembly. They are closely related to previously introduced primordial fragment distributions which probe space-momentum correlations but are less robust to some as yet unknown degree.

(1) E.A.Remler, Annals of Physics 136 (1981) 293.

(2) M.Gyulassy, K.Frankel and E.A.Remler, Nuclear Physics A402 (1983) 596.

MEAN FIELD APPROACH TO PION PRODUCTION
IN INTERMEDIATE ENERGY HEAVY-ION COLLISIONS *

M. TOHYAMA, R. KAPS, D. MASAK and U. MOSEL

Institut für Theoretische Physik,
Universität Giessen, 6300 Giessen, West Germany

Pion production at incident energies below the NN threshold is one of the interesting phenomena in the field of intermediate-energy heavy ion physics. Since cooperative effects may play an essential role in heavy-ion subthreshold pion production, it is necessary to incorporate the dynamics of the collision into the theory. We do this here by using the time-dependent Hartree-Fock (TDHF) theory for the description of the dynamical evolution of the nucleus-nucleus collision. The Fermi motion, Pauli blocking, as well as dynamical distortions of the energy-momentum distributions are all inherent in this theory.

In the present paper we report results of calculations in the slab geometry that contains essential features of head-on collisions.

The inclusive number N of produced pions with momentum p and energy $\omega = \sqrt{p^2 + m_\pi^2}$ is given in terms of the pion source function $j(x)$ [1,2],

$$2\omega \frac{dN}{d^3p} = \frac{1}{(2\pi)^3} \int d^4x_1 d^4x_2 e^{ip(x_2-x_1)} \langle \psi_{in} | j^+(x_1) j(x_2) | \psi_{in} \rangle \quad (1)$$

Here $|\psi_{in}\rangle$ is the Heisenberg "in" state of the colliding system. We calculate the pion source function both in the one nucleon model (ONM) and in the two nucleon model (TNM) [3,4].

* Work supported by BMFT and GSI Darmstadt

The expectation value of the pion source function in eq.(1) is easily evaluated since the wave function $|\psi_{in}\rangle$ is a single Slater determinant in the TDHF theory. Then the number of produced pions is expressed in terms of matrix elements of the pion source function between occupied and unoccupied states.

We calculate the number of pions produced in symmetric slab collisions. The slab thickness is 4.6 fm. The obtained spectra of pions (in the ONM) produced in the forward direction per unit area are shown in fig.1 for various incident energies. The right hand scale denotes the cross section estimated by $\frac{d^3\sigma}{d^3p} = \frac{dN}{d^3p} \int S(b) 2\pi b db$. Here $S(b)$ is the area of the overlapping section of the two colliding nuclei at impact parameter b . The absolute value is by an order of magnitude smaller than experimental data [5]. The dependence of the number of produced pions on the incident energies is also too small.

The above estimates of the absolute cross section and its incident energy-dependence seem to indicate that the single nucleon process constitutes only a small part of the pion production cross section.

In the following we make a rough estimate of the two-nucleon processes. The pion production in the TNM is usually described by an effective two-body transition operator. As a guide, we use the simplified form given by Grossmann et al. (eq.(18) in ref.[4]) for (p, π) reactions.

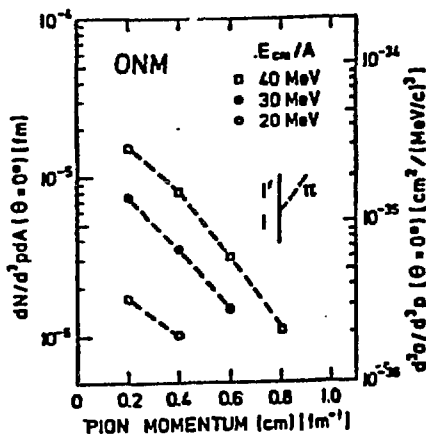
The pion spectra obtained from the pion source function in the TNM are shown in fig.2. To get an idea of the magnitude of the obtained pion yields, we show also the experimental data of the Ne + Na collision at $E_{lab}/A=164$ MeV. The data are averages of the π^+ and π^- cross sections. Compared to the spectra obtained in the ONM, the TNM spectra have by about an order of magnitude larger cross sections and different shapes in the low momentum region. The latter is due to the omission of the non-static term in the π -emission vertex, which would enhance the pion yields in the low momentum region. The overall larger values are in line with the results of calculation for the (p, π) reactions where the TNM was also found to dominate the cross section [4]. The larger cross section is due to the fact

that nucleons with lower momenta can contribute to the pion production in the TNM.

Again, as in the ONM calculations, the cross section does not increase fast enough with bombarding energy, possibly as a consequence of the one-dimensional geometry.

For a check of this point we have recently performed also calculations in a finite geometry TDHF code. The results obtained are very encouraging, the dependence of the π -production cross section on bombarding energy is now considerably steeper and the π -spectra fall off more rapidly towards higher energies. Both effects are clearly due to the possibility of transverse momentum transfer in the finite geometry calculation.

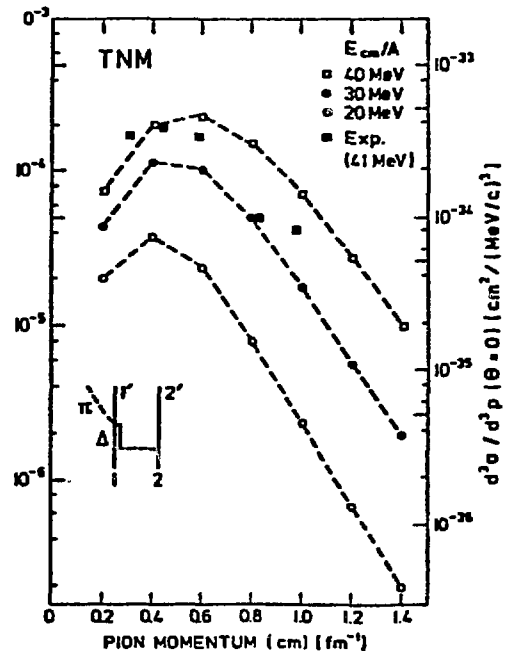
Fig. 1



Momentum spectra of pions produced in the forward direction per unit area as obtained in the ONM (fig. 1) and in the TNM (fig. 2). The right hand scale denotes the cross section calculated for the Ne+Ne collision.

The experimental data are from ref. 5.

Fig. 2



An important ingredient in all of these calculations is clearly the Pauli principle. This is most dramatically illustrated in fig.3 where the Wigner distribution function is shown for boosted Slater determinants first without (upper part) and with (lower part of fig.3) antisymmetrization between the single-particle states in the two different nuclei. One can

clearly see that the momentum distributions reach out to larger momenta thus enhancing π -production. Even more dramatic is the depletion of the distributions for $p \approx 0$ thus strongly increasing the available final state phase space. These effects that are energy dependent and diminish with increasing bombarding energy are all contained in the TDHF results reported above.

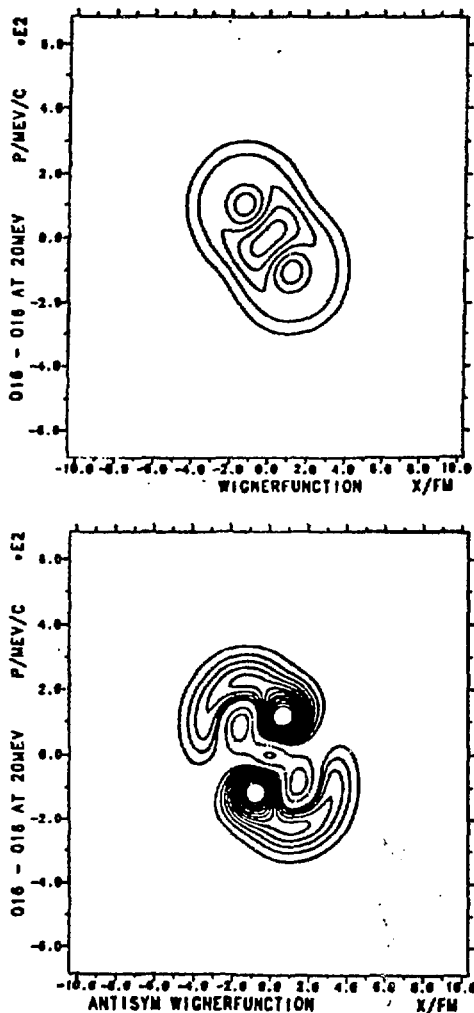


Fig. 3
Wigner function $f(p, x)$ for a central collision of $^{16}\text{O} + ^{16}\text{O}$ at $E/A = 20$ MeV (lab). The collision proceeds along the x -axis. The upper part of the figure gives the Wigner function without antisymmetrization between the nucleons in the two different nuclei; the lower part that with antisymmetrization.

- [1] P.Carruthers and F.Zachariasen, Rev.Mod.Phys. 55(1983)245.
- [2] M.Tohyama et al., to be published in Phys.Lett.B.
- [3] D.F.Measday and G.A.Miller, Ann.Rev.Nucl.Sci. 29(1979)121.
- [4] Z.Grossmann et al., Ann.Phys.(N.Y.) 84(1974)348.
- [5] W.Benenson et al., Phys.Rev.Lett. 43(1979) 683;
44(1980)55.

PION PRODUCTION IN HIGH ENERGY HEAVY ION COLLISIONS*

K.L.Wolf,¹ R.Bock,² R.Brockmann,² A.Daca,⁵ J.W.Harris,² M.Maier,⁴ M.E.Ortiz,⁵
 H.G.Pugh,³ R.E.Renfordt,⁴ A.Sandoval,² L.S.Schroeder,³ R.Stock,² and H.Stroebele²

¹Cyclotron Institute, Texas A&M University, College Station, TX 77843. ²Gesellschaft für Schwerionenforschung, D-6100 Darmstadt, West Germany. ³Lawrence Berkeley Laboratory, University of California, Berkeley, CA 94720. ⁴Universität Marburg, D-3550 Marburg, West Germany. ⁵Instituto de Física, UNAM, Mexico City, 21D.F. Mexico.

The emission patterns of pions produced in relativistic heavy ion collisions provided one of the early true heavy ion effects observed at the Bevalac. The mid-rapidity bumps seen in pion spectra remain unexplained, but undoubtedly reflect phenomena that occur late in the reaction,^{1,2} controlled by final state interactions. However this is not the case for the gross probability of pion production as shown by the intranuclear cascade calculations of Cugnon, et al.³ Figure 1 shows some results of this calculation in terms of the time dependence of the baryon density and the pion production as the reaction proceeds.

The number of pions that are emitted is determined rather early in the reaction, during the high density stage. This does not mean that the same pions or deltas are around at the end of the reaction, but the pion multiplicity is frozen in early. The reaction processes $NN \rightarrow \Delta N$ and $\Delta N \rightarrow \pi N$ subsequently change only such observables as the emission energies and the angular distributions. It follows that the pion multiplicity is dependent upon the value of the baryon density in the compressed state and thus the pion multiplicity becomes a probe of the early stages of the reaction. This cascade model scenario, however, has a serious flaw since the values predicted for the pion multiplicities from central collisions of the $^{40}\text{Ar}+\text{KCl}$ reaction are too large by factors ranging from 1.5-4, depending upon the bombarding energy. The situation is demonstrated by the data and calculations in Fig.2. Several accurate predictions of experimental results prevent one from simply discounting the cascade model: a) the proton participant number vs cross section data are reproduced exactly for the $^{40}\text{Ar}+\text{KCl}$ b) with modern values of the p+p cross sections as input, the experimental pion production cross sections in p+nucleus reactions are reproduced, as are pion + nucleus absorption cross sections, c) the pion cross sections that we have measured in peripheral $^{40}\text{Ar}+\text{KCl}$ collisions agree nicely with the predictions. Apparently pion production and absorption is treated adequately in the cascade for normal and low nuclear density situations, but something is lacking in the model for high densities or for some other "heavy ion effect." Stock, et al.⁴ proposed that the missing ingredient is the equation of state of nuclear matter. The cascade calculation agrees with the data if energy is removed from the pion producing degrees of freedom and stored as compressional energy. At each bombarding energy the energy per nucleon that must be subtracted from the cascade to

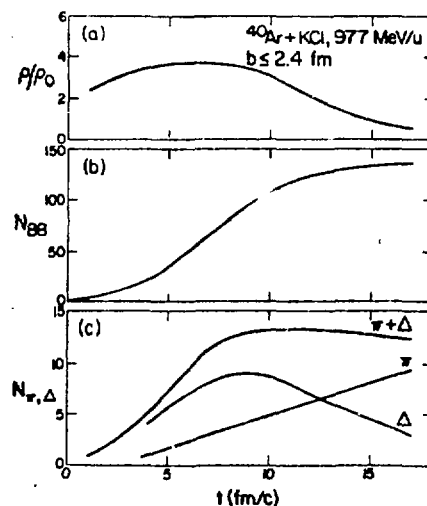


Fig.1. Results of a cascade calculation for central collisions of $^{40}\text{Ar}+\text{KCl}$. The time dependence of the reaction shows the baryon density, the integrated number of collisions, and the number of pions and deltas per unit time.

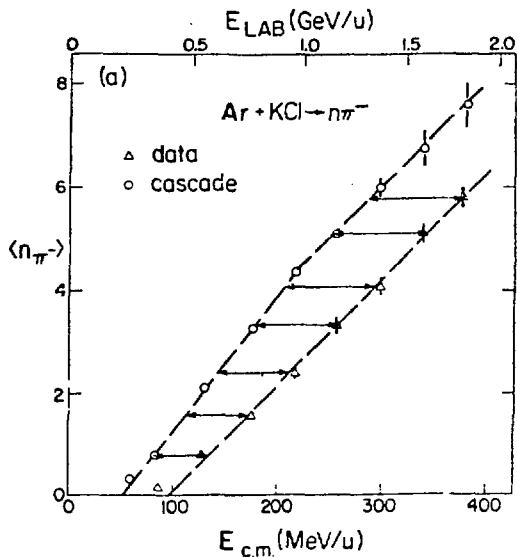


Fig.2. The mean negative pion multiplicity as a function of bombarding energy for near-central $^{40}\text{Ar} + \text{KCl}$ collisions. The triangles show the data and circles are the results of cascade calculations.

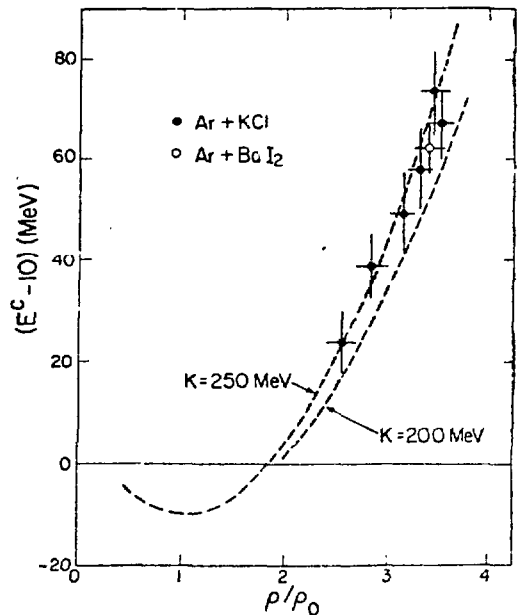


Fig.3. The values of the compressional energy from Fig.2 as a function of the calculated baryon density.

obtain agreement with the experimental data is represented by a horizontal arrow in fig.2. It is that energy difference which is plotted as a function of the baryon density in Fig.3 for the well known and somewhat controversial equation of state determination. It is clear that only one parameter of the equation of state could be determined from this procedure. Thus an assumed parabolic form yields an incompressibility constant of approximately 250 MeV. In this paper we will review further the evidence for the suppression of pion yields, and discuss some of the recently conceived explanations that may be alternatives to the compressional energy hypothesis.

The Cugnon cascade is not the only source of a baseline calculation. With the correct elementary cross sections as input, the Yariv and Fraenkel cascade predicts nearly the same inflated values of the pion multiplicities. Recent results presented at the Oaxtepec Meeting by Harris and Stock used a chemical model which combined the Berkeley Fireball Model (which also overestimates pion production) along with the Rankine-Hugoniot shock equation to relate temperature and density. A result that is completely consistent with, but independent of the cascade calculations for the compressional energy was obtained.

For comparisons with other experimental data, to my knowledge there are three examples which are relevant here. In the earlier generation of experiments² we showed that if one compares light-ion-induced with heavy-ion-induced reactions, there is an unexplained depression in the pion yields which becomes more important as the projectile becomes heavier. Figure 4 represents some accurate comparisons of the ratios of pion cross sections for p , ^4He , ^{20}Ne , ^{40}Ar projectiles on a uranium target. The scaling should be simple since the target is much heavier than the projectiles, as verified by the Yariv, Fraenkel cascade. But there is a 25% discrepancy, with the ^{40}Ar -induced production being low. The effect is much smaller than in the central trigger data in Fig.2, since we are dealing with single particle inclusive data in Fig.4. The peripheral collisions dilute the effect considerably,

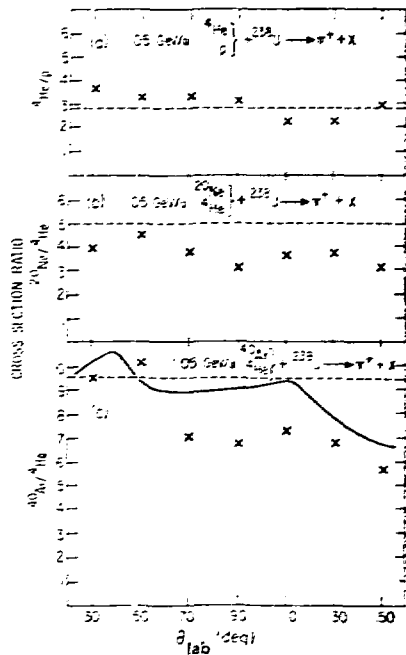


FIG. 4. Ratios of energy integrated cross sections (15–95 MeV) as a function of laboratory angle for π^- produced by p , ${}^4\text{He}$, ${}^{20}\text{Ne}$, and ${}^{40}\text{Ar}$ at 1.05 GeV/u on a ${}^{238}\text{U}$ target. Dashed lines represent predictions of scaling from an isobar model. The solid curve in the bottom figure for ${}^{40}\text{Ar}/{}^4\text{He}$ presents the results of an intranuclear cascade calculation.

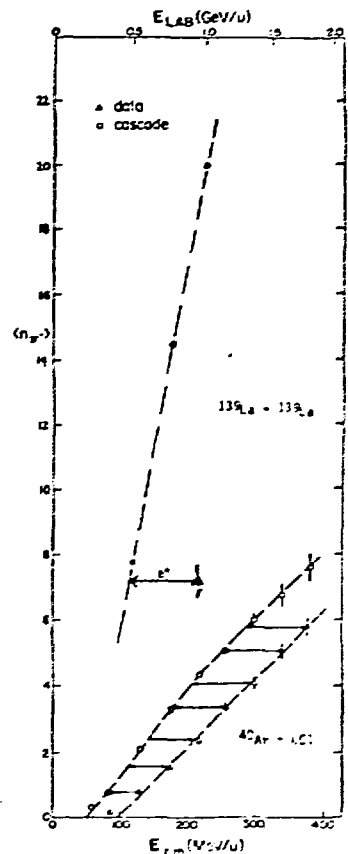


Fig. 5. Same as Fig. 2 except results for the ${}^{139}\text{La} + {}^{139}\text{La}$ reaction at 1.0 GeV/u are shown.

but the single particle inclusive data do eliminate the possibility of trigger bias and offer an independent test.

One of the most dramatic demonstrations of the pion suppression is in the recent results for the ${}^{139}\text{La} + {}^{139}\text{La}$ reaction at 1 GeV/nucleon from the streamer chamber. Instead of the predicted 20 negative pions, we observe only about 7 or 8 on the average, as shown in Fig. 5. The energy per nucleon that must be subtracted from the available energy in the cascade is quite consistent with the ${}^{40}\text{Ar} + \text{KCl}$ results. The implications toward the attainment of equilibrium are apparent. If we are dealing with a transient condition instead of a true equilibrium, the increase in the number of participants by a factor of three with associated increase in spatial dimensions and times, should alter the observables considerably. Thus in the compressed stage a thermal and a chemical equilibrium probably has set in.

Another test of pion suppression involves a different type of data from the streamer chamber, obtained by counting proton participants along with the pions. Figure 6 shows five sets of these data for bombarding energies from 1.0 to 1.8 GeV per nucleon. The data points have been omitted for all but the highest and lowest energies and only the linear fits are drawn. The linear increase of the pion multiplicity with participant number Q is striking, and is considerably different from the cascade results for 1.2 GeV, shown as the dashed line. The agreement for grazing collisions (small Q) is good, and the discrepancy between cascade and the data is largest for central collisions. We have carried out a calculation by assigning an impact parameter to a given Q , again using the cascade to make a correspondence. A simple participant-spectator model gives the same results. One can extract a compressional energy by using the value of the bombarding energy which matches the calculated pion multiplicity at each impact parameter and subtracting the actual beam energy.

Of course using the cascade results, an associated baryon density can be assigned to each impact parameter, the more central the collision the higher the compression. Values of $\rho/\rho_0 = 2-4$ are studied this way, and the corresponding compressional or "missing" energies are in good agreement with those obtained from the excitation function procedure. In fact the most recent analyses of the compressional energy use the data in Fig.6 to extrapolate to $b=0$ for the maximum compression.

We have seen several pieces of information that point to a much reduced pion yield in central heavy ion collisions. Throughout, an energy shift has been assumed, that is, the available ion energy was reduced early in the reaction and the extra pions and deltas were not produced in the first place. This is quite different from assuming a pion absorption mechanism, after the production of the many deltas predicted in the cascade. It should be pointed out that pion absorption is included in the cascade formalism through the $NN \rightleftharpoons N\Delta$, $\Delta \rightleftharpoons \pi N$ equilibria. More exotic (and unestablished) mechanisms for pion absorption on a pair (or more) of nucleons without going through the delta are somewhat inconsistent with the data. Exotic absorption should scale with some higher power of the density $(\rho/\rho_0)^n$ depending upon how many nucleons are taking part. The excitation function data however, show the maximum value of suppression relative to calculations at the lowest bombarding energies, where the density pileup is the lowest. Recently a paper by Cahay, Cugnon and Vandermeulen⁵ addressed this problem of direct absorption and found it to have a negligible affect on the pion yields.

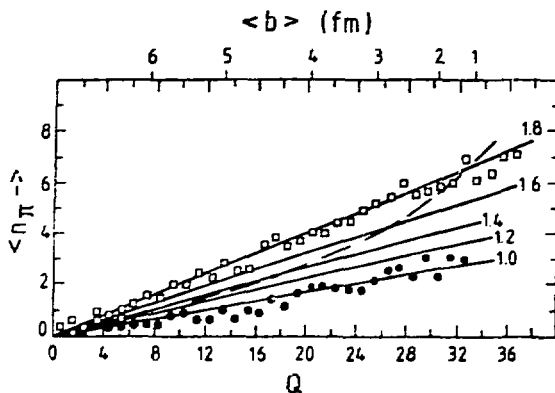


Fig. 6. The mean π^- -multiplicity observed in Ar + KCl reactions at 1.0, 1.2, 1.4, 1.6 and 1.8 GeV/u, plotted as a function of the observed number of proton participants, Q . Only interpolating straight lines are shown except for 1.0 and 1.8 GeV/u. The dashed curve gives the cascade multiplicity result for 1.2 GeV/u, plotted vs. Q as determined from the calculation. The mean values of the impact parameter $\langle b \rangle$ that correspond to sets of cascade events with given Q are shown on the upper scale.

Cahay, et al⁵ have also studied "off-shell effects" that is, the effect of having particles off of their mass shell in the nuclear potential. Naively, one might expect that the introduction of a 40 MeV attractive potential would

result in enhanced pion production cross sections, due to phase space factors. It is claimed that the important quantity is the transition matrix averaged over final states. If the calculation is performed in a straightforward manner within the cascade, only a 5-10 % reduction in the pion yield is obtained as shown in Fig.7. A further ansatz is necessary to obtain the lower solid curve in Fig.7, which we may call the "disappearing potential". It is assumed that the scattered nucleons and deltas no longer feel the nuclear potential since they are removed in phase space.

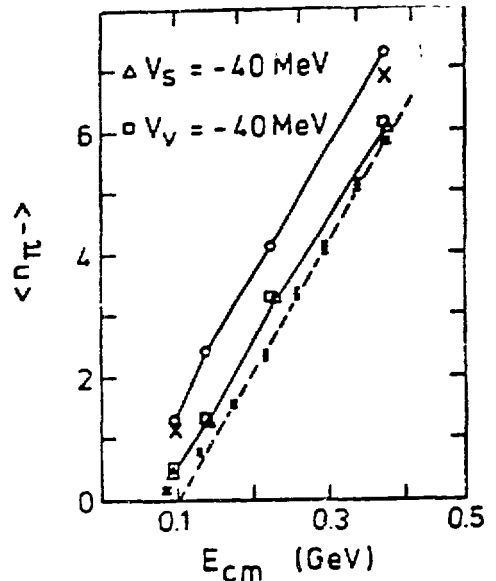


Fig.7. The experimental data from Fig.2 (dashed line) compared to an off-shell calculation of ref.5. The lower solid line also assumes destruction of the potential.

Operationally, after the first collision of a pair of nucleons the potential is turned off for that pair. The agreement with the excitation function data is good, since the energy is shifted by approximately $-2V_c$. This is another mechanism for removing energy from the pion producing degrees of freedom and producing an energy shift. Any calculation of this type must explain all of the data which we have reviewed here. The agreement of cascade with the p+nucleus cross sections may be retained in the disappearing potential model, since this is a rather dilute system of scattered nucleons i.e. the potential may continue to act. This point is not clear since the participants are separated from the rest of the nucleons in phase space. Another area where this calculation may have difficulties is in accounting for the impact parameter data in Fig.6. Over the range of $b=1-5 F$. the overlap density varies from about 2 to 4 ρ_0 . One would expect a saturated potential condition over this range and the energy shift of $-2V_c$ relative to the normal cascade would occur over the full b -range, thus overcorrecting the cascade for $b=3-5 F$. The calculation should be done and better data should be collected on the La+La system in an inelastic trigger mode.

Finally in reference 5 a pion source perturbation due to the surrounding matter was considered. This is, essentially a polarization of the nucleon (the pion source) by the surrounding matter. The result has the wrong energy dependence, failing to fit the pion data taken at low bombarding energies. Again, this is a general difficulty with mechanisms that simply reduce the pion yield instead of removing energy from the system.

*This work supported by the Director, Office of Energy Research, Division of Nuclear Physics of the Office of High Energy and Nuclear Physics of the U.S. Department of Energy under Contract DE-AC03-76SF00098; by the Bundesministerium für Forschung und Technologie, West Germany; and by the Robert A. Welch Foundation.

¹K.L.Wolf, et al., Phys. Rev. Lett. 42, 1448 (1979).

²K.L.Wolf, et al., Phys. Rev. C26, 2572 (1982).

³J. Cugnon, et al., Nucl. Phys. A332, 505 (1981) and A379, 533 (1982).

⁴R. Stock, et al., Phys. Rev. Lett. 49, 1236 (1982).

⁵M. Cahay, et al., Nucl. Phys. A411, 524 (1983).

NEW EVIDENCE FOR HOT SPOTS FROM SUBTHRESHOLD PIONS

J. AICHELIN

National Superconducting Cyclotron Laboratory
Michigan State University, East Lansing, Michigan 48824, U.S.A.

Recently pion production cross section was measured in heavy ion collisions at low and moderate bombarding energies [1,2]. The measurements show the systematic behavior of the excitation function, the energy and angular distribution, and the target mass dependence of the cross section. We make a statistical hypothesis about the reaction mechanism finding that the compound nucleus model describes the data on symmetric systems remarkably well [3]. We report here on this work and the extension to asymmetric systems.

The basic assumption in our analysis is that in a very short amount of time the nucleons in the combined system reach statistical equilibrium. Of course, from the point of view of the Boltzmann equation, the equilibration is far from instantaneous. Nevertheless, the assumption may not be so unreasonable because the strong nuclear force induces many of the correlations needed for the transition already in the initial state. Also, to produce an energetic particle by a low-energy collision requires consideration of high-order perturbations on the independent particle wave function. It is plausible that the mathematics of such higher-order perturbations yield results approaching the phase space limit. In this energy domain a pion cannot be created in a single nucleon nucleon collision [4] even if the Fermi momentum is properly taken into account. Thus the creation has to be a collective effect. Given a system in local equilibrium, the time required for a particle emission in a compound decay (5 fm/c) is small compared to the expansion time, or time for other disassembly mechanisms. However for large targets the time a nucleon needs to travel through the nucleus is larger than the compound decay time. Therefore it cannot be expected that in this case all nucleons participate in the equilibration. Rather we assume that only part of them form an equilibrated hot spot. We determine the number of nucleons in the hot spot by demanding that the velocity of the hot spot, as calculated from the momentum of the entrained nucleons, corresponds to the pion center of momentum distribution. This results in 34 ± 3 participants for Ni targets and 47 ± 4 for the U target.

The decay rate of a equilibrated system is given by [5]:

$$W_{if}(e) de = \frac{\rho(U)}{\rho(E)} \frac{(2S+1)m}{\pi^2} \sigma_{fi}(e) e de \quad (1)$$

where e is the kinetic energy of the evaporated particle, $\rho(U)$ is the level density of the evaporation residue, $\rho(E)$ is the same quantity for the compound nucleus, and σ_{fi} is the inverse cross section for the formation of the compound nucleus. The cross section is obtained from the decay rates by the formula:

$$d\sigma/d\epsilon = \sigma_0 W_{if}(\epsilon) / \sum_j \int W_{ij}(\epsilon_j) d\epsilon_j \quad (2)$$

where σ_0 is the cross section to form a compound nucleus in the entrance channel.

We determine the level densities by the Fermi gas model. For our applications, considering excitation energies between 9 and 21 MeV/N, i.e. temperatures between 12 and 23 MeV (at normal nuclear matter density), the standard low temperature level density formula is inaccurate and we use instead the general formulas to calculate the chemical potential and the temperature for a given density and excitation energy.

At the excitation energies considered the pion can be created not only in the first evaporation step but also after one or more nucleons are emitted. Therefore we apply a cascade program whose details can be found in [3]. Eq.(1) requires the inverse cross section, which we take to be geometric for the nucleon case. The pion cross section is far from being geometric. Optical model calculations show that for low energies the nucleus gets increasingly transparent for π_0 , whereas at higher energies there is an enhancement due to the delta resonance. We extract the π_0 absorption from the available π_+ and π_- measurements taking the geometric mean. Unfortunately both available data sets [6,7] disagree in the absolute magnitude as well as in the shape. Because of its agreement with optical model calculation for the low energy part we fix our parameterization at low energies at the data of Ref. [7] whereas at higher energies we follow the average of both data sets. A convenient parameterization for the pion absorption cross section in the range 20-200 MeV is:

$$\sigma_{\pi_0}(E) = \sigma_m - \alpha(E-E_0)**2.$$

with $\sigma_m = 390,550$ mb; $\alpha = 0.017, 0.026$ mb/MeV**2.; $E_0 = 145, 115$ MeV for Al and Ti respectively. For nuclei in between we interpolate these values.

Figure 1 shows the predicted excitation function compared with the available data [1,2]. (The data points at 35 MeV were obtained by applying our analysis to the reaction $35 \text{ MeV/N } ^{14}\text{N} + ^{27}\text{Al} \rightarrow \pi_0 + X$ and $^{14}\text{N} + ^{58}\text{Ni} \rightarrow \pi_0 + X$ and are transformed in the way described in [3]). The overall magnitude of the cross section is fit with a parameter σ_0 , corresponding to the equilibrated system formation cross section. The agreement in the shape of the excitation function is excellent. In the case of Uranium we calculated the cross section for two sets of parameters corresponding to two assumptions about the size of the hot spot.

Figure 2 shows the calculated π_0 energy distribution compared with the data of Ref [1]. The three lower curves show the energy distribution for 60, 74, 84 MeV/N C+C, the two upper curves 84 MeV/N C+Ni and C+U, respectively.

The energy distribution is well described in the C+C system but fails at higher energies in the asymmetric systems. An inspection of the rapidity plot shows that the high energy π_0 's of the Ni and U target originate from a system of higher rapidity. It is an open question whether this is a consequence of different impact parameters resulting in different numbers of participants or whether it originates from the early stage of the hot spot where less nucleons participate and therefore the temperature is higher. Furthermore it may reflect the lack of information about the inverse cross section.

The total compound formation cross section σ_0 shows a simple systematic behavior. If we express the cross section in the form $\sigma_0 = \pi b_{\max}^2$, then the maximum impact parameter is roughly given by $b_{\max} = R_T - R_P + 1.5$, showing that target and projectile must overlap nearly completely. Larger impact parameter results in fragmentation of the projectile as observed by [8]. The data also shows a small angular anisotropy which cannot be explained in this simple model because of the neglect of the spin of the compound nucleus.

References:

- [1] H. Noll et al., preprint
- [2] P. Braun-Munzinger, P. Paul, L. Ricken, J. Stachel, P.H.Zhang, G.R. Young, F.E. Obenshain and E. Grosse, Phys. Rev. Lett 52 (1984) 255
- [3] J. Aichelin and G. Bertsch, Phys. Lett. B in press
- [4] V. Weisskopf, Phys. Rev. 52 (1937) 295
- [5] R. Shyam and J. Knoll, preprint GSI-83-22
- [6] D. Ashery, Phys. Rev. C23 (1980) 2173
I. Navon et al., Phys. Rev. C28 (1983) 2548
- [7] K. Nakai et al., Phys. Rev. Lett 44 (1980) 1446
- [8] J. Mougey, Nucl. Phys A387 (1982) 109c

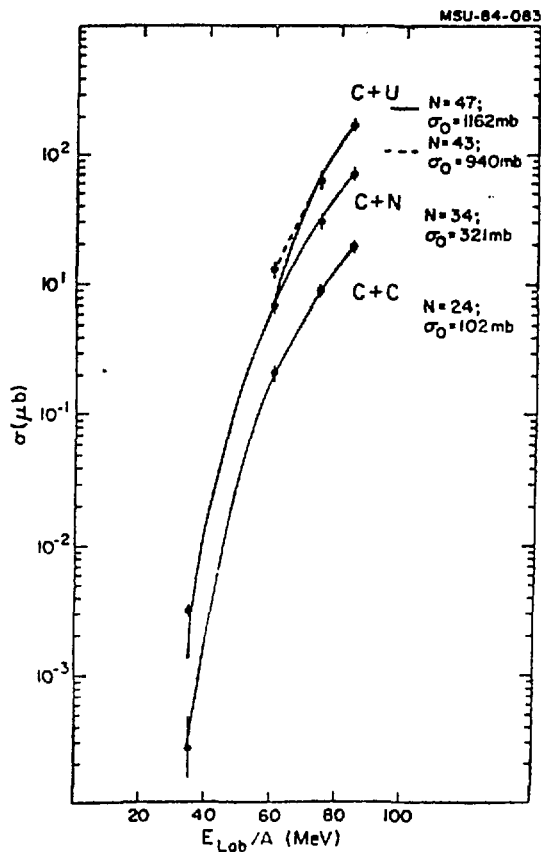


Figure 1

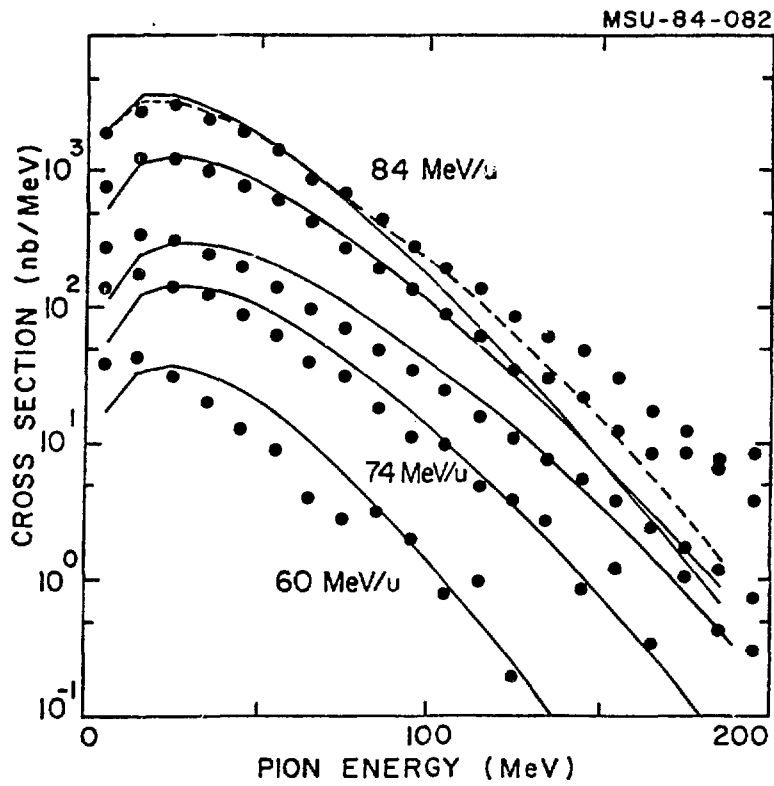


Figure 2

THE ANISOTROPY RATIO FOR PARTICLE-INCLUSIVE PRODUCTION IN HIGH
ENERGY NUCLEUS-NUCLEUS COLLISIONS: A SENSITIVE PROBE FOR PION
PRODUCTION MECHANISMS

Rudi Malfliet

Kernfysisch Versneller Instituut, Zernikelaan 25, 9747
AA Groningen, The Netherlands

Bernd Schürmann

Physik-Department, Technische Universität München,
8046 Garching, Federal Republic of Germany

We have developed a near-analytic multiple collision (transport) model which describes nucleon and meson as well as light fragment emission in the energy range of 400 to 2100 MeV per nucleon. Our approach is based on the relativistic Boltzmann equation for nucleon production [1]. Through an expansion of the one-particle distribution function in terms of the number n of independent nucleon-nucleon (NN) collisions the Boltzmann equation can be recast in an infinite set of coupled integro-differential equations. Linearizing these equations by letting the test nucleon scatter with a partner nucleon whose distribution is stationary (a Fermi distribution for the first collision $n=1$, a thermal distribution for $n \geq 2$) they can be solved in the eikonal approximation. Each solution represents a multiple collision term with collision number n and factorizes in a coordinate dependent (geometrical) and a momentum dependent (dynamical) part. The geometrical part is given by the well-known Glauber-Matthiae factors, and the dynamical part is to a good approximation given by the solution of a Fokker-Planck type equation with known "drift" and "diffusion" coefficients [2]. As described in [3] we assume light fragment formation to occur in the expansion phase of the collision. To obtain the final light fragment cross sections we use Hagedorn's thermodynamics of strong interactions [4] in the local rest frame of the non-equilibrated participant zone. Good agreement with the measured light fragment inclusive spectra at 400 and

800 MeV per nucleon is obtained.

The pion inclusive data are more difficult to reproduce. The fact that cascade models overestimate the measured pion production rate has been utilized to gain information on the nuclear equation of state through the compressional energy as a function of the nuclear density [5].

In this contribution, we present another observable sensitive to the mechanism of pion production in high energy nucleus-nucleus collisions. This is the anisotropy ratio

$$R_{\pi}(E_k^*) = \frac{d\sigma_{\pi}(30^{\circ}, E_k^*)}{d\sigma_{\pi}(90^{\circ}, E_k^*)} \quad (1)$$

constructed from the differential pion inclusive production cross section for identical colliding nuclei at c.m. angles of thirty and ninety degrees as a function of the outgoing pion c.m. kinetic energy. In the framework of our transport model we have studied the following three scenarios for pion production:

- (i) Δ -resonances are created in the first collision ($n=1$) and are allowed to undergo final state interactions, i.e. to decay and recombine again until a thermal and chemical equilibrium among all the species considered is reached; at the end of the collision the remaining Δ 's decay into nucleons and pions. For the higher order collisions ($n \geq 2$) pions are produced purely thermal.
- (ii) Δ 's are created for $n=1$ but no $\bar{\pi}$'s are allowed to be formed through final state interactions; i.e. the Δ 's decay only at the end of the collision. Same as (i) for $n \geq 2$.
- (iii) Same as (i) for $n=1$. For $n \geq 2$, only one third of the produced pions is allowed to escape (absorption scenario [6]).

The anisotropy ratio (1) for the cases (i) to (iii) is displayed in fig. 1 for the reaction $Ar + KCl$ at 800 MeV per nucleon, with data from [7]. The pions from the first collision are seen to play a prominent role, in particular at moderate energies ($E_k^* \approx 200$ MeV). The maximum indicated by the data points is absent for possibility (i) where the contribution of $\bar{\pi}$'s from the first collision is relatively low at moderate

energies as compared to the thermally produced $\bar{\pi}$'s for $n \geq 2$. In scenario (ii) the fact that all $\bar{\pi}$'s in $n=1$ come from Δ -decay results in a maximum around 200 MeV. In case (iii) the Δ 's are allowed to rescatter but since there are so few pions from $n \geq 2$ the contribution of those $\bar{\pi}$'s coming from the decay of remaining Δ 's at the end of the collision still shows up. The data points appear to be more consistent with the cases (ii) and (iii) than with (i).

To discriminate between the cases (ii) and (iii) we show in fig. 2 the corresponding anisotropy ratios for proton inclusive production. The data are again from [7]. Only case (iii), the absorption scenario, leads to a satisfactory description of the experimental points. A Boltzmann-type equation which includes the average nuclear potential field has to be solved to see what kind of result the inclusion of the compressional energy gives. A first step in this direction has been taken [8].

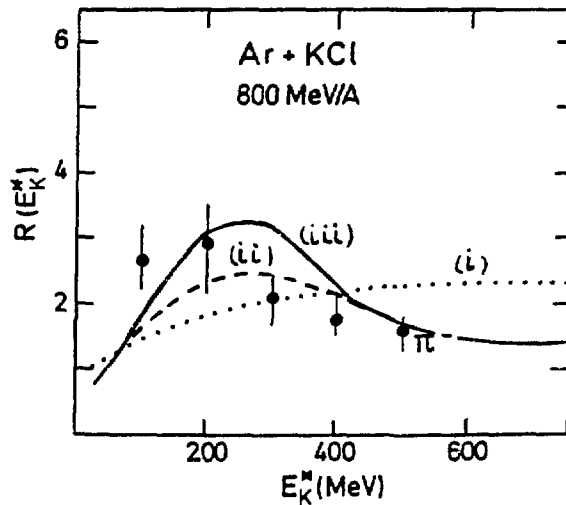


Fig. 1

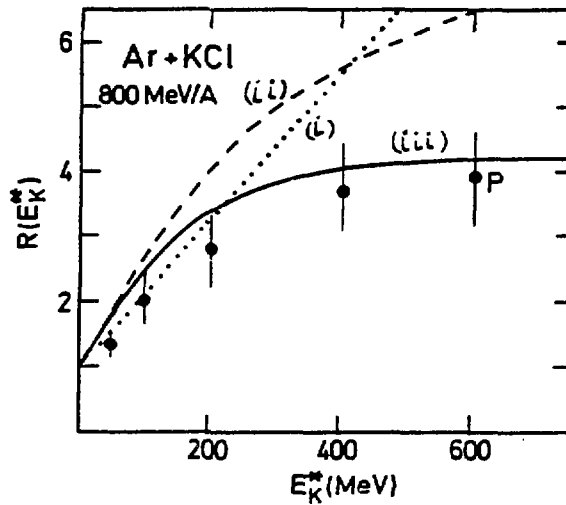


Fig. 2

1. R. Malfliet, Phys.Rev.Lett. 44(1980) 864; Nucl.Phys. A 363 (1981) 429.
2. B. Schürmann and D.P. Min, Nucl.Phys. A 370(1981) 496.
3. R. Malfliet et al., Phys.Lett. B 124(1983) 152.
4. R. Hagedorn and J. Ranft, Nuovo Cimento Supp. 6(1968) 169.
5. R. Stock et al., Phys.Rev.Lett. 49(1982) 1236.
6. R. Malfliet and B. Schürmann, Phys.Rev. C 28(1983) 1136.
7. S. Nagamiya et al., Phys.Rev. C 24(1981) 917.
8. G.F. Bertsch et al., Michigan State University preprint (1983).

ASPECTS OF PARTICLE-INCLUSIVE PRODUCTION IN NUCLEUS-NUCLEUS
COLLISIONS AT 2.1 GeV PER NUCLEON

Winfried Zwermann and Bernd Schürmann

Physik-Department, Technische Universität München,
8046 Garching, Federal Republic of Germany

In this contribution, we discuss some typical aspects of nuclear collisions at the incident energy of 2.1 GeV per nucleon. In particular, we will focus on proton and kaon inclusive production in the collision Ne on NaF at 2.1 GeV per nucleon where good quality experimental data exist [1,2]. We perform our study within the framework of a multiple collision approach based on sequences of independent baryon-baryon collisions. The momentum distributions of the baryons (needed later for the calculation of the K^+ inclusive spectra) are determined by use of the almost analytical, parameter-free model of transport theory [3].

Transport theory for baryons

We use a simplified version of the transport model [3], i.e. we restrict ourselves to the determination of the first two moments of the actual baryon momentum distributions. In other words, we assume (relativistically generalized) Gaussian distributions of the baryons after each collision number n , with different average momenta and energies. To determine the latter, we make use of [3] where the considered baryon ("test baryon") is assumed to interact, after the first collision, with a heat bath of temperature T . Then the moments $\langle \vec{p} \rangle_n$ and $\langle p^2 \rangle_n$ after each collision number n can be expressed in terms of those after the first collision. Because of lack of space, we give the explicit expressions only in the nonrelativistic limit, and neglect all baryon resonances:

$$\begin{aligned} \langle \vec{p} \rangle_n &= \langle \vec{p} \rangle_1 e^{-\beta(n-1)}, \\ \langle p^2 \rangle_n &= \langle p^2 \rangle_1 e^{-2\beta(n-1)} + 3mT(1 - e^{-2\beta(n-1)}). \end{aligned} \quad (1)$$

The moments after the first collision $\langle \vec{p} \rangle_1$ and $\langle p^2 \rangle_1$ are determined non-statistically. The dimensionless number β has the

meaning of a friction constant in an equation of Fokker-Planck type. It is essentially determined [3] by the ratio of the inverse slope Γ^2 of the elementary elastic NN scattering cross section and the temperature T of the heat bath:

$$\beta = \Gamma^2 / 6 m T. \quad (2)$$

Taking the experimental value for Γ^2 and calculating T by requiring energy conservation, we obtain a numerical value of $\beta \approx 0.2$. From the first eq.(1) which actually remains true in the relativistic case, it can be seen that the number of collisions necessary for reaching equilibrium is given by

$$n_{\text{req}} \approx 1/\beta - 1; \quad (3)$$

this means that the system thermalizes only after the quite large number of roughly 6 collisions! This is illustrated in fig. 1, where the average momenta and widths of the baryon distributions as functions of the collision number n are displayed. (We have included in our actual calculations the existence of delta resonances and used relativistic generalisations of eqs.(1).) Since the average number of collisions is only

$$\langle n \rangle \approx \frac{4}{3} R \rho_0 \sigma_{\text{NN}} \approx 3, \quad (4)$$

the large transparency of the system, caused by the small friction constant β , does not allow the baryons to reach equilibrium in the reaction considered here. This results in a pronounced anisotropy of the inclusive proton spectrum in the c.m. system of the colliding nuclei. In fig. 2, we compare the results of our calculations (full lines) with the experimental data of ref. [1] (dashed lines). Reasonable agreement is obtained, concerning the slope as well as the absolute magnitude of the differential inclusive cross section for various c.m. angles. Especially our prediction concerning the large transparency of the system, leading to a high degree of anisotropy of the spectrum, is well supported by the data, as can be seen by comparing the lines representing the cross section at 30 and 90 degrees.

Transport theory for kaons

Once knowing the baryon distributions after each collision, the kaon distributions J_{mn} are obtained by folding the elementary kaon production cross section [4] with the projectile baryon distribution after the m -th, and the target baryon distribution after the n -th collision. The functions J_{mn} can in general not be obtained in closed form; however, if we again restrict ourselves to the determination of the integrated cross sections and the first two moments of the distributions J_{mn} , we succeed in doing the calculations analytically up to a remaining one-dimensional numerical quadrature. Albeit straightforward, the procedure is rather cumbersome; details can be found elsewhere [5].

Although the functions J_{mn} lead to the primary K^+ distribution (i.e. the possibility of interaction of the produced kaons with the surrounding baryons is not yet taken into account), the total kaon yield is now completely determined, since rescattering does not alter the number of produced baryons. (We can neglect the absorption of K^+ 's because of strangeness conservation.) In fig. 3 we display the total inclusive K^+ production cross section (full line) in the reaction Ne on Ne as a function of the incident beam energy per nucleon. The measured value at 2.1 GeV is from ref. [2]. First we remark that our calculations give a K^+ yield which remains sizeable far below the threshold for elementary kaon production. For comparison the contribution from the first collision only (dashed-dotted line) as well as the result of a hadrochemical model [6] (dotted line) are also shown. Although positive kaons have a mean free path in baryonic matter long compared to that of nucleons and pions, their probability to scatter on a baryon is not completely negligible. (In fact, the average collision number of a kaon in a neon nucleus is about $\langle n \rangle \approx 0.65$, cf. ref. [7].) Instead of displaying the results explicitly, we just want to mention that the inclusion of rescattering leads to a considerable improvement of the results for the differential K^+ production cross section, compared to those without rescattering. For more details of our calculations, we refer to [5].

References

1. S. Nagamiya et al., Phys.Rev. C24(1981) 971

2. S. Schnetzer et al., Phys.Rev.Lett. 49(1982) 989
3. H.J. Pirner and B. Schürmann, Nucl.Phys. A316(1979) 461;
B. Schürmann and D.P. Min, Nucl.Phys. A370(1981) 496
4. J. Randrup and C.M. Ko, Nucl.Phys. A343(1980) 519; A411(1983) 537
5. W. Zwermann et al., Phys.Lett. 134B(1984) 397;
W. Zwermann and B. Schürmann, to be published in Nucl.Phys. A
6. H.W. Barz et al., Z.Phys. A311(1983) 311
7. J. Randrup, Phys.Lett. 99B(1981) 9

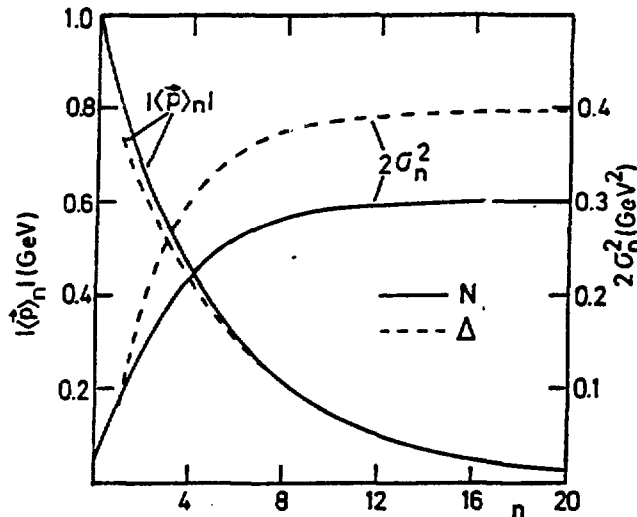


Fig. 1

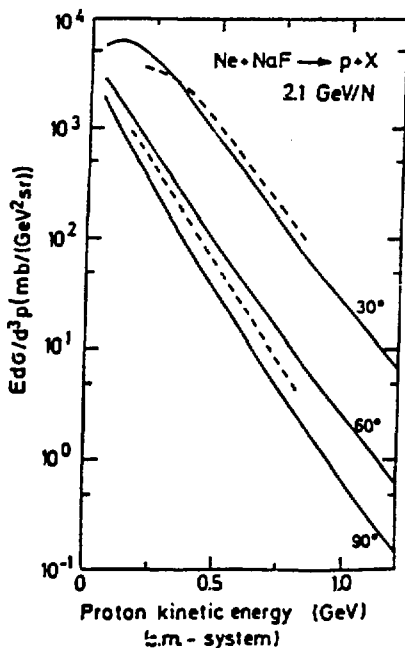


Fig. 2

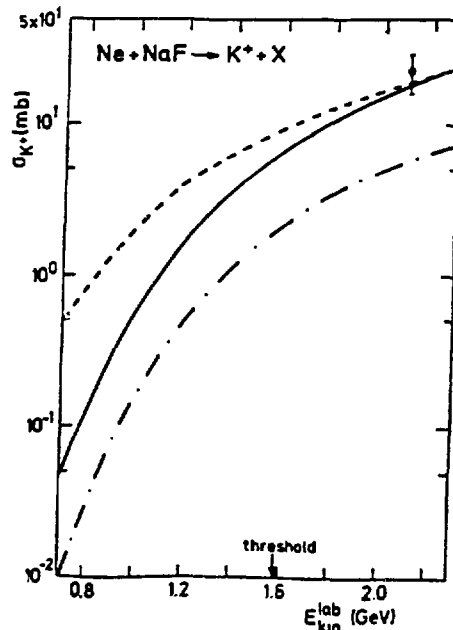


Fig. 3

COLLECTIVE FLOW EFFECTS OBSERVED WITH THE PLASTIC BALL

H. A. Gustafsson, H. H. Gutbrod, B. Kolb, H. Lohner, B. Ludewigt,
 A. M. Poskanzer, T. Renner, H. Riedesel, H. G. Ritter, A. Warwick,
 F. Weik, H. Wieman

Gesellschaft für Schwerionenforschung, Darmstadt, West Germany
 and
 Nuclear Science Division, Lawrence Berkeley Laboratory,
 University of California, Berkeley, CA 94720

The study of relativistic heavy ion collisions is the only way to explore the properties of nuclear matter at high temperatures and densities in the laboratory and to extract the equation of state of nuclear matter away from the ground state region. The Bevalac provides the unique opportunity to study collisions of heavy nuclei in the incident energy region from about 100 MeV/nucleon to 2 GeV/nucleon. First attempts to relate the measured pion multiplicity to the equation of state have been made recently [1]. A direct experimental signature for the compression would be collective flow of the nuclear matter upon reexpansion as predicted and linked to the equation of state by hydrodynamical models [2,3]. With 4π detectors like the Plastic Ball, which are ideally suited to study emission patterns and event shapes, one might be able to observe this effect and distinguish between predictions of cascade and hydrodynamical models [4].

At the Bevalac, collisions of Ca + Ca and Nb + Nb at 400 MeV/nucleon have been studied with the Plastic Ball/Plastic Wall detector [5]. The Plastic Ball covers the angular region between 10° and 160° . It consists of 815 detectors where each module is a ΔE -E telescope capable of identifying the hydrogen and helium isotopes and positive pions. The ΔE measurement is performed with a 4-mm thick CaF crystal and the E counter is a 36-cm long plastic scintillator. Both signals are read out by a single photomultiplier tube. Due to the different decay times of the two scintillators, ΔE and E information can be separated by gating two different ADC's at different times. The positive pions are additionally identified by measuring the delayed decay. The Plastic Wall, placed 6 m downstream from the target, covers the angular range from 0° to 10° and measures time of flight, energy loss and position of the reaction products. In addition, the information from the inner counters (0° to 2°) is used to produce a trigger signal [6].

Since the momentum distribution of almost all charged particles in each event were measured with a 4π detector the ratio $R = \frac{2}{\pi} \frac{\sum_{i=1}^N |p_{\perp}^i|}{\sum_{i=1}^N |p_{\parallel}^i|}$ [7] of the perpendicular and longitudinal momentum components of all measured particles in an event could be determined. By this ratio the degree of isotropy and thermalization reached in the collision (isotropy corresponds to $R=1$) can be judged. A comparison for systems of different sizes and energies is shown in fig. 1. Here the mean ratio R is plotted as a function of the detected fraction of all charges in the system N_z/Z . Assuming that the multiplicity decreases with increasing impact parameter the increase of R with the charged particle multiplicity can be understood as spectator fragments or leading particles produced in non central collisions strongly enhance the parallel momentum component, thus reducing the ratio R . On the other hand, only very few spectators are left and R can reach rather high values in high multiplicity events. R reaches almost 1 for the heavier system Nb+Nb but is significantly lower for the lighter system Ca+Ca at the same incident energy of $E/A=400$ MeV. A possible explanation for the observed difference is the

different surface to volume ratio since the surface zones show some transparency and a few spectators may be left even at the highest multiplicities. With increasing bombarding energy the mean ratios decrease indicating an increase in transparency, but there are still events with $R=1$.

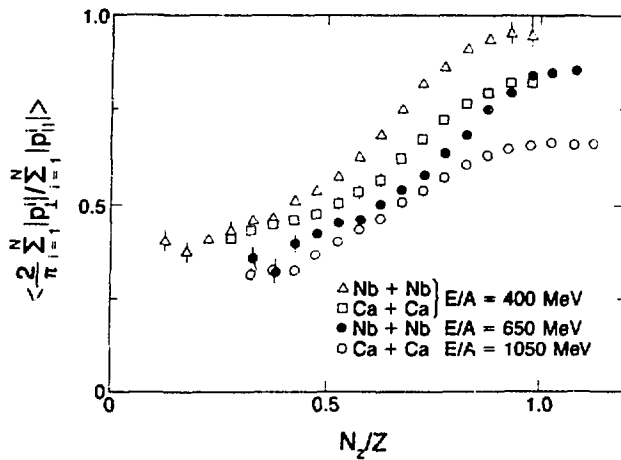


Fig. 1: Ratio of the average perpendicular to parallel momentum as a function of the detected fraction of all charges in the system N_z/A . The error bars indicate the statistical error only.

For kinematical reasons proton spectra at $\theta_{cm} = 90$ degree are free of spectator particle contributions. Spectra from Ca+Ca and Nb+Nb collisions at $E/A = 400$ MeV were fitted with a relativistic Boltzmann distribution and temperature parameters T_0 were extracted. With increasing multiplicity T_0 rises from 42 to 65 MeV. This may either reflect an approach towards equilibrium or the experimentally observed increase in composite particle production [6] which reduces the number of degrees of freedom and therefore enhances the temperature in thermal models.

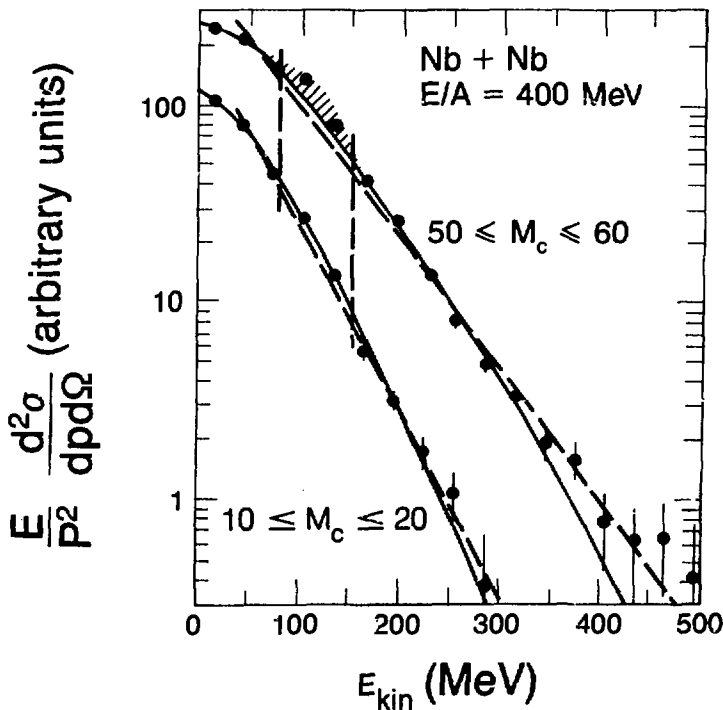


Fig. 2: Proton spectra at $\theta_{cm}=90$ from Nb + Nb collisions at $E/A=400$ MeV. Dots: experimental data points; Dashed lines: fitted Boltzmann distributions; Explosion model: full lines. The vertical dashed lines mark the region which is excluded from the fits because of possible deuteron contaminations indicated in the high multiplicity spectrum by the shaded area.

However, a clear deviation from a Boltzmann distribution becoming more pronounced with increasing multiplicity can be seen at the very low energy part of the proton spectra (fig. 2). Siemens and Rasmussen [8] offered an explanation by assuming a spherically symmetric fireball expanding with a radial velocity v and a temperature T . As seen in fig. 2 the shape of the proton spectra at low and high multiplicities can well be fitted. The fit results correspond to the case that approximately an equal amount of energy goes into radial expansion and into thermal motion, respectively. On the other hand the deviation may as well be caused by the depletion of the primordial proton yield at low energies by the formation of composite particles which increases with multiplicity [6].

In the ratio of the longitudinal to perpendicular momentum components as well as in the inclusive spectra only very dramatic collective flow effects would ever show up. Therefore it is necessary to do a more sophisticated flow analysis [2,4,7]. In particular, flow angle distributions were studied since they are much less severely distorted by finite particle number effects than the aspect ratios [9].

The energy flow tensor [4] in the center of mass system has been determined and diagonalized for each individual event. The distribution of the flow angles (angle between the major axis of the flow ellipsoid and the beam axis) is shown in fig. 3 for different multiplicity selections. A striking difference between the Ca and Nb data can be observed. For all but the highest multiplicity bins the distribution of the flow angles for the Ca data is peaked at 0 degrees. For Nb, however, there is a finite deflection angle increasing with increasing multiplicity. The same analysis has been performed with events from an cascade code calculation [10] individually filtered with the known experimental acceptance and detector efficiencies (fig. 3). For both systems studied the distributions are always peaked at zero degrees. It is not so evident that the Ca + Ca collision differs from its simulation with the cascade model, whereas a new collective phenomenon definitely appears in the larger mass system which is not accounted for by the present cascade models.

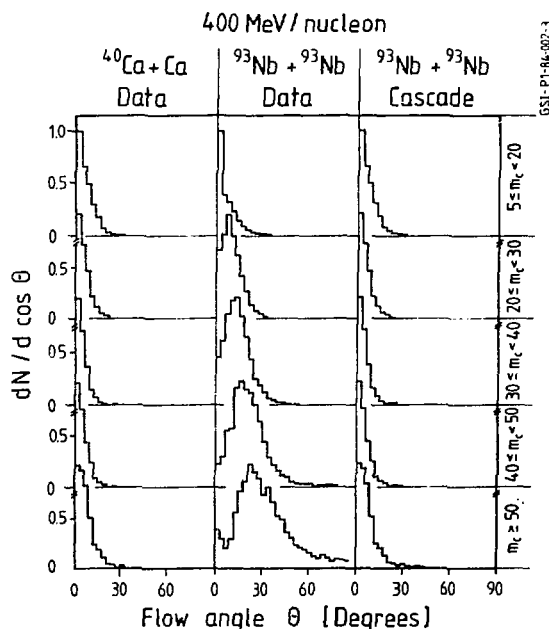


Fig. 3:
Frequency distributions of the flow angle θ for two sets of data and a cascade calculation for different multiplicity bins. For the case of Ca the multiplicities are half the indicated values.

The fact that finite flow angles are seen in the data indicates that in those events a reaction plane exists that is defined by the flow axis and the beam axis. All events can be rotated by the azimuthal angle ϕ determined by the flow analysis so that their individual reaction planes all fall into the x-z plane, with the z-axis being the beam axis. For those rotated events the invariant cross section in the reaction plane ($d^2\sigma/dy d(p_x/m)$) [2] can be plotted, where p_x is the projection of the perpendicular momentum into the reaction plane and y is the center of mass rapidity. Fig. 4 shows this plot for a selected multiplicity bin for 400 MeV/nucleon Ca + Ca and Nb + Nb data, together with cascade calculations. The depletion near target rapidities is due to limited experimental acceptance for low energy particles in the lab system. This depletion enhances the flow angles artificially but does not change the reaction plane. The cascade plot is symmetric around the beam axis, whereas the Ca and Nb in-plane data plots are clearly asymmetric. The highest level contour results largely from the projectile remnants and indicates a definite bounce-off effect. The multiplicity dependence of the outer contour lines seems to follow the trend indicated by the flow angle distributions (fig. 3). However, the position of the peak from the projectile remnants changes only slightly with multiplicity. Thus one can conclude that the strong sideward peaking seen in fig. 3 is mainly due to the mid-rapidity particles. It should be noted that the bounce-off and side-splash effects appear to be in the same plane. There is also the possibility that the increased prominence of projectile fragments at low multiplicity could contribute to the decreasing splash angle. The peak in the projectile rapidity region is located below the beam rapidity whereas the p_x distribution indicates a perpendicular momentum component of about 50 MeV/c per nucleon. The bounce-off process is therefore a slowing down of the projectile fragments and a sideways deflection in the reaction plane.

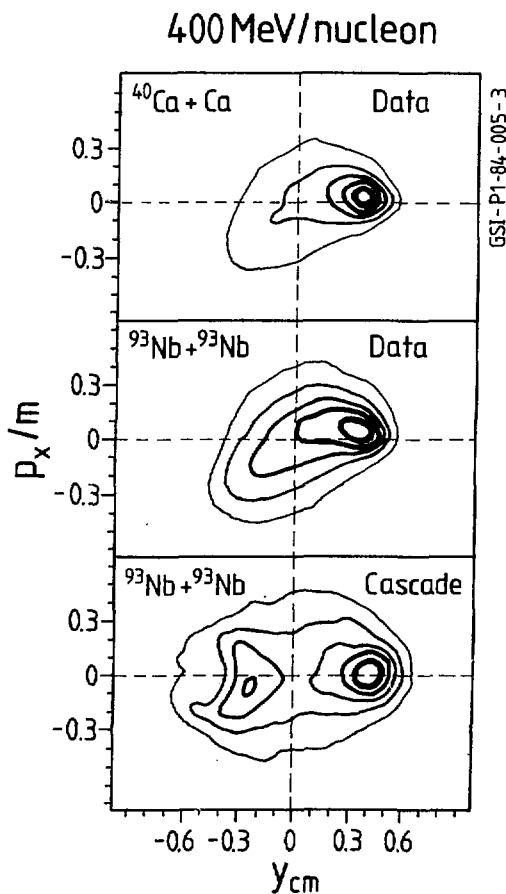


Fig. 4:
Contour plots (linear contours) of p_x as a function of cm rapidity for multiplicities selected between 40 and 49 charged particles for Nb and 20 and 24 for Ca.

The hydrodynamical prediction for the flow angle seems to be qualitatively in agreement with the measurement, but the very small variation of the deflection of the projectile fragments as a function of multiplicity does not show the behaviour predicted by one fluid hydrodynamical model calculations [2].

The Plastic Ball data show for the first time two different collective effects: the bounce-off in the fragmentation region and the side-splash of the participants. It is now a challenge to models that include collective phenomena, like the hydrodynamical model, to explain those effects and to relate them to compression and density [16], and thus to the equation of state of nuclear matter.

References:

- 1 R. Stock et al, Phys. Rev. Lett. 49 (1982)
- 2 H. Stocker, J. Hofmann, J. A. Maruhn and W. Greiner, Progr. in Part. and Nucl. Phys. Vol. 4, 133 (1980)
H. Stocker, L. P. Csernai, G. Graebner, G. Buchwald, H. Kruse, R. Y. Cusson, J. A. Maruhn, and W. Greiner, Phys. Rev. C25, 1873 (1982)
- 3 J. Kapusta and D. Strottman, Phys. Lett. 106B, 33 (1981)
- 4 M. Gyulassy, K. A. Frankel, and H. Stocker, Phys. Lett. 110B, 185 (1982)
- 5 A. Baden, H. H. Gutbrod, H. Loehner, M. R. Maier, A. M. Poskanzer, T. Renner, H. Riedesel, H. G. Ritter, H. Spieler, A. Warwick, F. Weik and H. Wieman, Nucl. Instr. Meth. 203, 189 (1982)
- 6 H. H. Gutbrod, H. Lohner, A. M. Poskanzer, T. Renner, H. Riedesel, H. G. Ritter, A. Warwick, F. Weik and H. Wieman, Phys. Lett. 127B, 317 (1983);
H. H. Gutbrod, H. A. Gustafsson, B. Kolb, H. Lohner, B. Ludewigt, A. M. Poskanzer, T. Renner, H. Riedesel, H. G. Ritter, A. Warwick, F. Weik and H. Wieman, in: Proceedings of the Int. Conf. on High Energy Nucl. Phys. in Balatonfured, Hungary, 269 (1983)
- 7 H. Stroebele, R. Brockmann, J. W. Harris, F. Riess, A. Sandoval, R. Stock, K. L. Wolf, H. G. Pugh, L. S. Schroeder, R. E. Renfordt, K. Tittel and M. Maier, Phys. Rev. C27, 1349 (1983)
- 8 P. J. Siemens and J. O. Rasmussen, Phys. Rev. Lett. 42, 880 (1979)
- 9 P. Danielewicz and M. Gyulassy, Phys. Lett. 129B, 283 (1983)
- 10 Y. Yariv and Z. Fraenkel, Phys. Rev. C20, 2227 (1979)
- 11 The acceptance of the Plastic Ball is complicated. There is a Fortran routine available that describes the acceptance rather well but not perfectly.
- 12 G. Buchwald, G. Graebner, J. Theis, J. Maruhn, W. Greiner and H. Stocker, MSU Preprint MSUCL 438, to be published

EFFECT OF FINAL STATE INTERACTIONS ON SUBTHRESHOLD K^-
PRODUCTION IN HEAVY-ION COLLISIONS

Che Ming Ko

Cyclotron Institute and Physics Department, Texas A&M University
College Station, TX 77843

Recently, experiments were carried out at Bevalac to detect K^- in heavy-ion collisions at an incident energy of 2.1 GeV/nucleon.¹ The threshold for K^- production in the nucleon-nucleon collision is ~ 2.5 GeV. The observation of K^- at subthreshold energies in heavy-ion collisions implies that more than one projectile nucleon must be involved in converting their kinetic energies into the mass of K^- . This experiment provides therefore the possibility of studying nuclear collective effects, such as Fermi motions, coherent productions, and multiple collisions. Shor et al.¹ showed that the simple nucleon-nucleon collision model with Fermi motions underestimated the number of K^- by more than an order of magnitude. Muller² suggested that the decay of the coherently produced ϕ -meson into K^+K^- might be responsible for the enhanced production of K^- . But his predicted K^- energy spectra disagree with that from the experiments. On the other hand, it was recently shown that the observed K^- production cross section could be explained by the strangeness-exchange reactions $\pi Y \rightarrow K^- N$ between the hyperons and pions initially produced in the collision.³

For the reaction ^{28}Si on ^{28}Si at 2.1 GeV/nucleon, the total K^- production cross section was estimated in Ref. 3 to be

$$\sigma_{K^-} \sim 0.02 \sigma_Y \sim 1.2 \text{ mb} \quad (1)$$

This was obtained by using the cascade model to determine the cross section σ_Y for the hyperon production. The fraction of hyperons being converted into K^- was determined by using the experimental cross section for the strangeness-exchange reaction⁴ and the fireball model for the pion distribution. In this model, it is therefore assumed that both hyperons and pions are produced during the collision and participate subsequently in the strangeness exchange reactions. Delayed productions of these particles after the collision would diminish the probability of the strangeness exchange reactions. Although pions come mainly from the decay of baryon resonances, their productions are not expected to be delayed significantly because of the large widths of these resonances, which are certainly further increased substantially through collisions with the surrounding hot dense matter. This effect of the collisional broadening was not properly taken into account in all the cascade calculations. Similarly, one expects that the part of hyperon production through resonance would not be delayed appreciably either.

On its way out of the interaction region, K^- is rescattered by the surrounding nuclear matter. The nonresonant K^-N interaction cross section is ~ 40 mb, which leads to a mean free path $\lambda = 1/\sigma_{KN}\rho_N$ in the participant region or fireball, where ρ_N is the density of the fireball. The size R of the fireball is given by $R = [3N/(4\pi\rho_N)]^{1/3}$, with N the number of participants. For the reaction $^{28}\text{Si} + ^{28}\text{Si}$, the mean number of participants can be estimated from the Glauber theory and is ~ 14 . The ratio of the size of the fireball to the K^- mean

free path is thus $R/\lambda \approx 6.0 \rho_N^{2/3}$. Since the hyperons are produced in the initial stage of the collision before the energies of the projectile nucleons have degraded appreciably, the density of the nuclear matter is high when K^- is produced via the strangeness-exchange reactions. Taking the density to be twice the normal nuclear matter density $\rho_0 = 0.17 \text{ fm}^{-3}$, one obtains $R/\lambda \approx 3$. Therefore K^- is rescattered, on the average, three times by the nucleons. Because K^- is mainly produced with low kinetic energy in the fireball, its interaction with nucleons is dominated by low partial waves. One therefore expects that the momentum distribution of K^- is thermalized after a few collisions. Hufner and Knoll⁵ showed via the rows on rows model that for intermediate energy heavy ion collisions the nucleon momentum distribution approached the Maxwellian distribution after ~ 4 collisions. From the cascade calculation of Cugnon,⁶ the maximum density achieved in heavy-ion collisions can be as large as four times the normal nuclear matter density. So K^- suffers much more than three collisions on its way out of the fireball. Although the fireball expands and this reduces the number of rescattering that K^- has to encounter, one still anticipates that K^- approximately has a thermalized momentum distribution. Also, K^- interacts strongly with pions through the resonance K^{*-} (890 MeV). The cross section can be estimated by assuming the dominance of a single partial wave and is found to be $\sim 60 \text{ mb}$.⁷ This would further enhance the possibility that the momentum distribution of K^- is thermalized in the fireball produced during the collision. One thus writes

$$\left(\frac{d^3\sigma}{dP_K^3}\right)_{\text{rescat}} = \sigma_{K^-} \frac{1}{(2\pi m_K T)} e^{-E_K/T} \quad (2)$$

where E_K is the kinetic energy of the K^- in the fireball frame, and T is the temperature of the fireball when K^- freezes out, i.e. the fireball has expanded to the critical density such that the mean free path of K^- is comparable to the size of the fireball. Since the K^-N cross section has similar magnitude as the NN cross section, K^- and N freeze out at same temperature if one neglects the difference of their interactions with pions. From experimental data of nucleon inclusive spectra in heavy-ion collisions at 2.1 GeV/nucleon, a temperature $T \approx 120 \text{ MeV}$ has been extracted by Nagamiya et al.⁸ Using this temperature the K^- energy spectrum at 0° has been calculated with Eq. (2) and is shown by the short-dashed curve in Fig. 1 in which the preliminary data from Berkeley¹ are also given. The calculated cross sections agree with the data of low energy K^- but are unable to explain those of high energy K^- .

The K^-N interaction is dominated by resonances; the lowest resonance Λ has a mass $\sim 1520 \text{ MeV}$ and a width of only $\sim 15 \text{ MeV}$. The cross section at the resonance can be estimated to be $\sim 250 \text{ mb}$ assuming again the dominance by a single partial wave. Because of its narrow width, this resonance has a relatively long lifetime $\sim 4.5 \times 10^{-23} \text{ s}$ and decays, therefore, mostly outside the interaction region. Assuming that the observed K^- results from the decay of $\Lambda(1520)$, then the momentum distribution of K^- is given by

$$\left(\frac{d^3\sigma}{dP_{-K}^3}\right)_{\text{res.}} = \frac{1}{4} \sigma_K N \int d^3P_{\Lambda} f(P_{\Lambda}) \int \frac{d^3P_N}{(2E_N)(2E_K)} \quad (3)$$

$$* \delta(E_{\Lambda} - E_N - E_K) \delta^3(P_{\Lambda} - P_N - P_K)$$

where P's and E's are respectively, the momenta and energies of the particles in the fireball frame. The quantity N is a normalization constant. The factor 1/4 in Eq. (3) accounts for the fact that the $\Lambda(1520)$ decays into K^- with a branching ratio ~25%. Since both K^- and \bar{K}^0 can interact with nucleons to form the Λ resonance, the production cross section in Eq. (3) is determined by σ_K which is twice of σ_{K^-} in Eq. (1). The momentum distribution of Λ is denoted by $f(P_{\Lambda})$ with normalization one. Although one does not know exactly the interaction cross sections of $\Lambda(1520)$ with other hadrons, one expects that they have magnitudes of typical strong interaction cross section, i.e. a few tens mb. Hence one assumes that it also acquires a thermal distribution in momentum with a temperature equal to that of the fireball i.e.

$$f(P_{\Lambda}) = \frac{1}{(2\pi m_{\Lambda} T)^{3/2}} e^{-E_{\Lambda}/T} \quad (4)$$

Then Eq. (3) becomes simply

$$\left(\frac{d^3\sigma}{dP_{-K}^3}\right)_{\text{res.}} = \frac{\sigma_{K^-}}{2XE_K P_K} \frac{m_{\Lambda}^2}{(2\pi)^{3/2} (Tm_{\Lambda})^{1/2}} (e^{-Z^-} - e^{-Z^+}) \quad (5)$$

with

$$Z_{\pm} = \frac{1}{2Tm_{\Lambda}} \left[\frac{1}{2m_K^2} (E_K X \pm P_K Y) \right]^2 \quad (6)$$

$$\text{where } X = \{m_{\Lambda}^2 - (m_N + m_K)^2\} [m_{\Lambda}^2 - (m_N - m_K)^2]^{1/2} \quad (7)$$

$$\text{and } Y = m_{\Lambda}^2 + m_K^2 - m_N^2 \quad (8)$$

In the above, m_K , m_N and m_{Λ} are, respectively, the masses of kaon, nucleon and Λ resonance. The resulting energy distribution is shown by the long-dashed curve in Fig. 1. Aside from the datum point of 200 MeV K^- , the calculated cross section does not agree with the data.

The actual cross section for the K^- should be determined both by the nonresonant scattering from the surrounding nuclear matter and from the decay of the Λ resonance. The relative importance of the two contributions should be in general energy dependent. For simplicity, this energy dependence is neglected and the ratio of the two contributions can be determined by their relative cross sections, i.e. $250/(40+60) \sim 3$, then the final cross section is approximately given by

$$\frac{d^3\sigma}{dP_{-K}^3} \approx \frac{1}{4} \left(\frac{d^3\sigma}{dP_{-K}^3}\right)_{\text{rescat}} + \frac{3}{4} \left(\frac{d^3\sigma}{dP_{-K}^3}\right)_{\text{res.}} \quad (9)$$

This is shown as the solid curve in Fig. 1 and it follows the general trend of the experimental data. The low energy data can be better fitted if one reduces the contribution from the resonance decay. To improve the fit to higher energy data may require the inclusion of other resonances.

It is therefore fair to say that the preliminary data on K^- production at subthreshold energies can largely be explained by the conventional theory of multiple scatterings. To substantiate the physical picture described in this report it is necessary to extend the cascade calculations to include the production of strange particles, to take into account the strangeness-exchange reactions, and to allow the final state interactions for the kaons. Certainly, more data are needed so that by comparing with detailed theoretical calculations one is able to understand better the reaction mechanism. Only after this has been achieved, then it is possible to learn about nuclear Fermi motions and coherent productions from subthreshold K^- production.

This work is supported in part by NSF grant under Contract No. PHY8109019.

- [1] A. Shor et al., Phys. Rev. Lett. 48 (1982) 159, Contributed papers in Proceedings of Sixth High Energy Heavy Ion Study, Berkeley (1983) p. 109.
- [2] K. H. Muller, Nucl. Phys. A395 (1983) 509.
- [3] C. M. Ko, Phys. Lett. 120B (1983) 294.
- [4] A. D. Martin and G. G. Ross, Nucl. Phys. B16 (1970) 479.
- [5] J. Hufner and J. Knoll, Nucl. Phys. 290 (1977) 460.
- [6] J. Cugnon et al., Nucl. Phys. A379 (1982) 553.
- [7] C. M. Ko, Phys. Rev. C 23 (1981) 2760.
- [8] S. Nagamiya et al., Phys. Rev. C 24 (1981) 971.

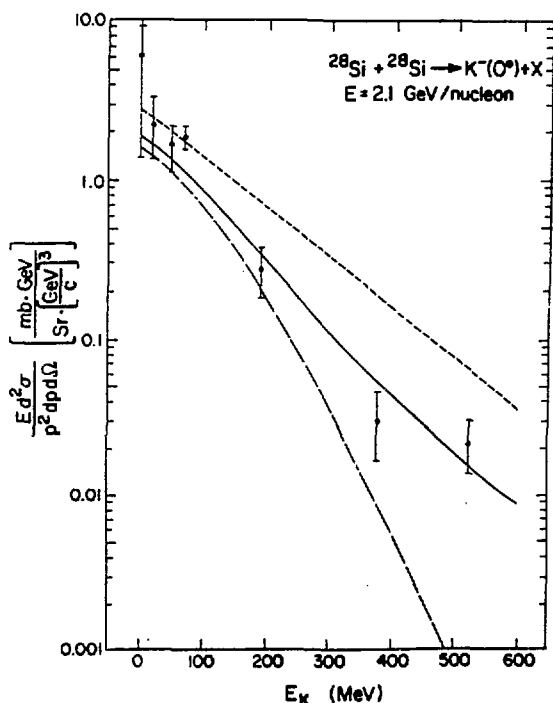


Fig. 1. 0° kinetic energy spectrum of K^- in the center-of-mass frame from the reaction ^{28}Si on ^{28}Si at 2.1 GeV/nucleon. The data are from Ref. 1. The short-dashed curves is due to non-resonant rescattering; the long-dashed curve is from the decay of the resonance $\Lambda(1520)$; the solid curve is the actual theoretical cross section resulting from the combination of both.

MICROSCOPIC CALCULATIONS OF NUCLEAR MATTER
COLLECTIVE FLOW IN Nb(400 MeV/N) + Nb

J.B. Hoffer*, H. Kruse**, J.J. Molitoris, and H. Stöcker
National Superconducting Cyclotron Laboratory
Michigan State University, East Lansing, Michigan 48824

The recent experimental observation¹ of sideways peaks in the emission pattern of fragments emitted in collisions of heavy nuclear systems has stimulated a dispute among theorists about how to interpret these data. It has been shown² that the observations are in agreement with the results of macroscopic nuclear fluid dynamical calculations, but several microscopic calculations done to simulate the sideways emission (via the intranuclear cascade (INC) approach^{3,4}) failed - the angular distributions obtained were always forward peaked.^{1,2}

We have recently developed a many body equations of motion (EOM) approach to study heavy ion collisions. Our approach is analogous to the early work of Bodmer et al.,⁵ and Willets et al.⁶ Hamilton's equations of motion are solved for an ensemble of nucleons with simultaneous mutual two-body interactions between all particles:

$$\begin{aligned}\dot{\vec{p}}_i &= - \frac{\partial H}{\partial \vec{r}} \\ \dot{\vec{r}}_i &= \frac{\partial H}{\partial \vec{p}}.\end{aligned}$$

This approach is nonrelativistic and neglects even the basic quantum mechanics, such as the Pauli exclusion principle and Heisenberg uncertainty principle. On the other hand, this approach allows for a study of the simultaneous (classical) interactions between many particles in sharp

* Permanent address: Laboratory for Atmospheric and Space Physics,
University of Colorado, Boulder, Co 80309

** Permanent address: TELCO Research Corporation, Nashville, TN.

contrast to the independent particle models such as the intranuclear cascade, which treat nuclear collisions as a simple superposition of successive free space nucleon - nucleon collisions. Also, the EOM approach allows for a systematic study of the repulsive core of the nucleon nucleon interaction (due to its deterministic nature, the EOM calculation produces an excluded volume effect) which is of interest in connection with the possible study of nuclear matter properties at high baryon densities.

In the EOM approach, nuclei are described as an ensemble of protons and neutrons initially distributed randomly throughout a sphere with the nuclear radius $R = 1.2 A^{1/3}$ fm. However, the obtained nuclei are not stable: they tend to collapse and evaporate many nucleons when the classical equations of motion are integrated over not too long a time interval ($t = 10-30$ fm/c). In the present approach, a metastable ground state has been obtained by allowing the nucleons to drift toward the configuration of minimum energy of the chosen nucleon-nucleon potential (Fig. 1). The state of minimum energy is found to be a crystalline structure (Fig. 2).

The nucleon-nucleon potential consists of two terms, an attractive long range Yukawa interaction, and a repulsive short range core.

$$V = (V_R e^{-K_R \cdot r} - V_A e^{-K_A \cdot r})/r,$$

where

$$\begin{aligned} V_R &= 2970 \text{ MeV-fm} & V_A &= 765 \text{ MeV-fm} \\ K_R &= 2.66 \text{ fm}^{-1} & K_A &= 1.75 \text{ fm}^{-1} . \end{aligned}$$

The parameters in the potential were chosen in a compromise between reproducing in the EOM calculation the n-p differential scattering cross section at large angles $\theta_{cm} = 90^\circ$ (which influences the transverse momentum

transfer the most) and at the same time giving reasonable nuclear radii and binding energies. This leads to nuclei sufficiently stable for a collision calculation to be meaningful rather than resulting in a disruption of the nuclei before a collision can actually take place. This potential has a minimum of -4.67 MeV at $R = 1.85$ fm. The resulting crystalline ground state configuration has an average binding energy of -31 MeV/N. The nucleons then are given random Fermi momenta with an average Fermi energy of 23 MeV/N which results in an average binding energy of 7 MeV/N. These nuclei are stable for $t > 20$ fm/c, i.e. typical collision times.

To numerically simulate a collision process, these nuclei are Galilei-boosted with the respective center of mass momenta at given impact parameters. The equations of motion are integrated using a technique described elsewhere.⁷ The second-order differential equations are solved by a fourth order Adams-Moulton predictor-corrector method which is started by a fourth order Runge-Kutta integration procedure. Energy conservation to better than 1% has been demanded. A total of 535 collisions of Nb (400 MeV/N) + Nb have been performed. This provides reliable statistics for the global event-by-event analysis subsequently performed on the numerical 'data'. The computations are stopped after $t = 30-50$ fm/c, since the results are insensitive to the exact 'break-up time'. The typical late stage of a collision at $b = 4$ fm impact parameter is shown in Fig 3. The resulting sideways flow can clearly be seen. We also display the evolution of the center-of-mass trajectory for four collisions at the same impact parameter in Fig. 4. Note that the deflection angle (25°) has approximately the same value as the flow angle (23°).

The individual collisions are analyzed by diagonalizing the kinetic energy flow tensor,⁸

$$F_{ij} = \sum_{\mathbf{v}} p_i(\mathbf{v}) p_j(\mathbf{v}) / 2m(\mathbf{v}) ,$$

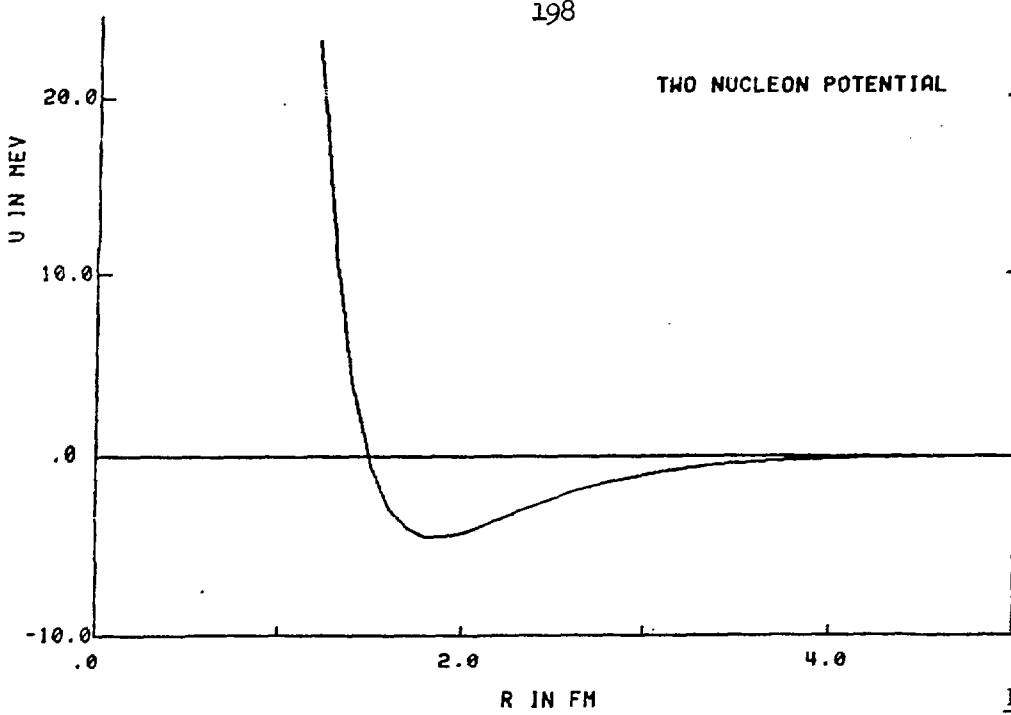


Figure 1

INTERPARTICLE SEPARATION HISTOGRAM

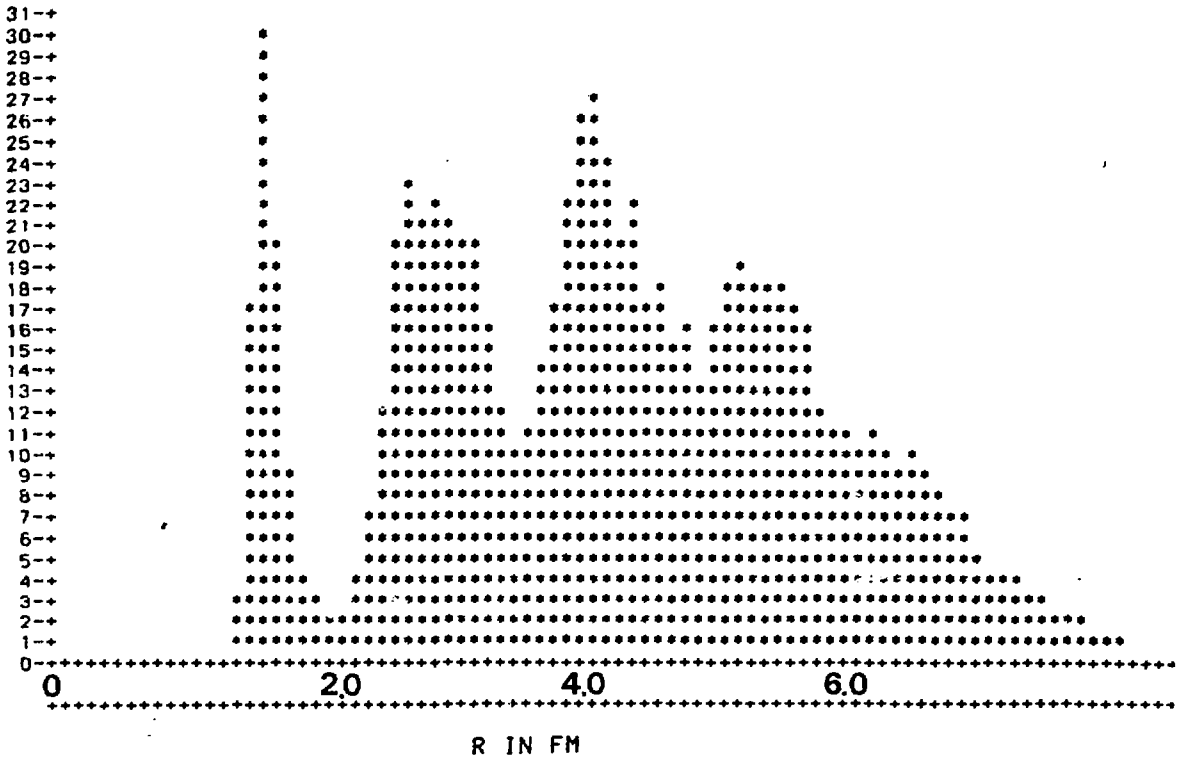


Figure 2

where the sum is over all particles in a given event. By diagonalizing this tensor, the flow angle θ_F and kinetic flow aspect ratio $R_{1,3}$ is obtained for each event. The distribution of flow angles is presented in Fig. 5 for various impact parameter intervals. The qualitative behavior of the flow pattern in the EOM model is as follows: the flow angle θ_F rises smoothly from 0° at large impact parameters to 90° at $b=0$. However, the contribution of zero impact parameter collisions to the observable cross sections is negligible. Thus a finite range of impact parameters is sampled to compute the angular distributions of the flow angles, $dN/d\cos\theta_F$, which is to be compared to the experimental data of the GSI/LBL collaboration. Fig. 5 also shows the experimental data for the Nb(400 MeV/N)+Nb case discussed above, together with the predictions of the intranuclear cascade^{1,2} and fluid dynamical² calculations. The data exhibit nonzero average flow angles once high multiplicity, i.e. small impact parameter collisions, are selected. This is in contrast to the intranuclear cascade calculation, which yields zero flow angles even at the highest multiplicities.

The present microscopic EOM model, on the other hand, predicts peaks in the angular distributions of the flow angles. The peak shifts to larger angles with increasing multiplicity which is in qualitative agreement with the experimental data. The difference in the physics of the INC model and the EOM approach leading to the distinct differences in the predictions is twofold. The INC applies a stochastic 4π scattering at the point of closest approach of straight line trajectories which allows for substantial transparency. In contrast, the short range repulsion in the EOM approach, results in an excluded volume effect. The nuclei are not as transparent and easily compressible in the EOM as in the INC. This causes the incident nucleons to be deflected towards sideways angles. The apparent success of

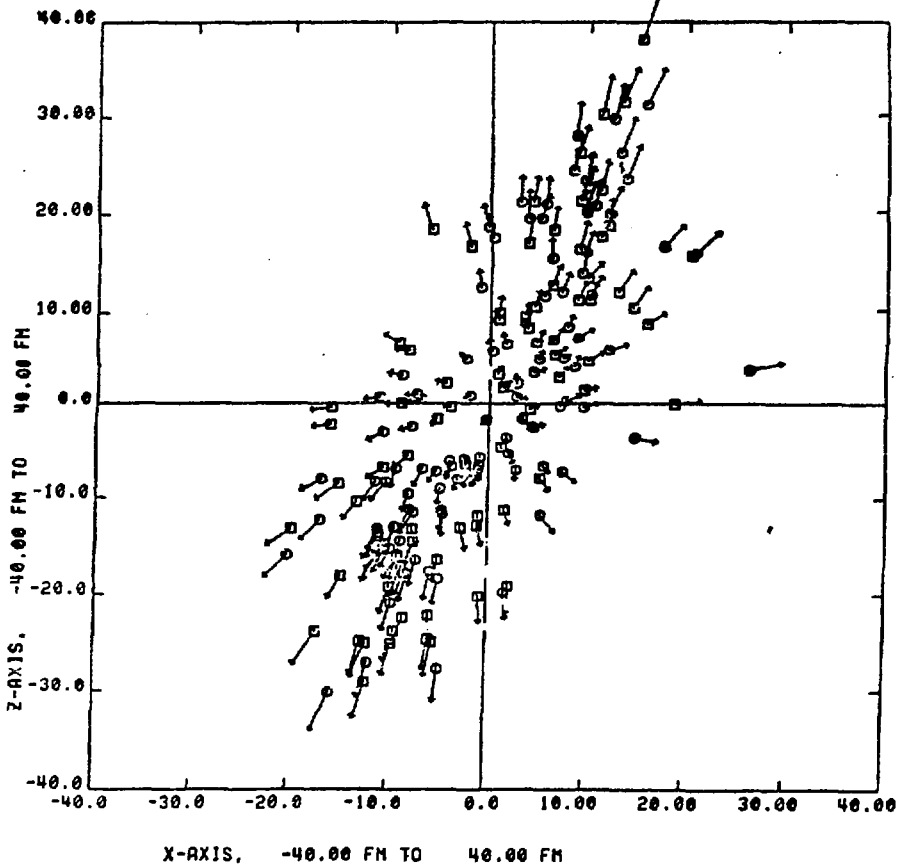


Figure 3

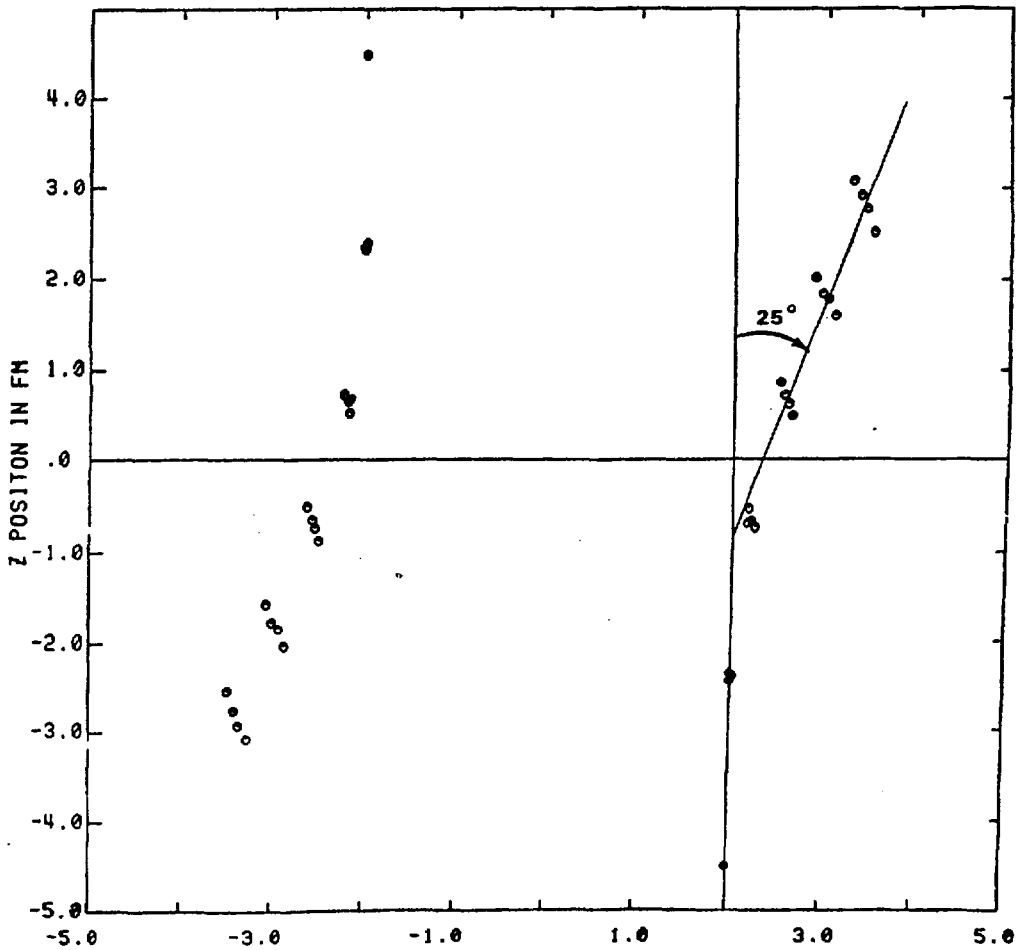


Figure 4

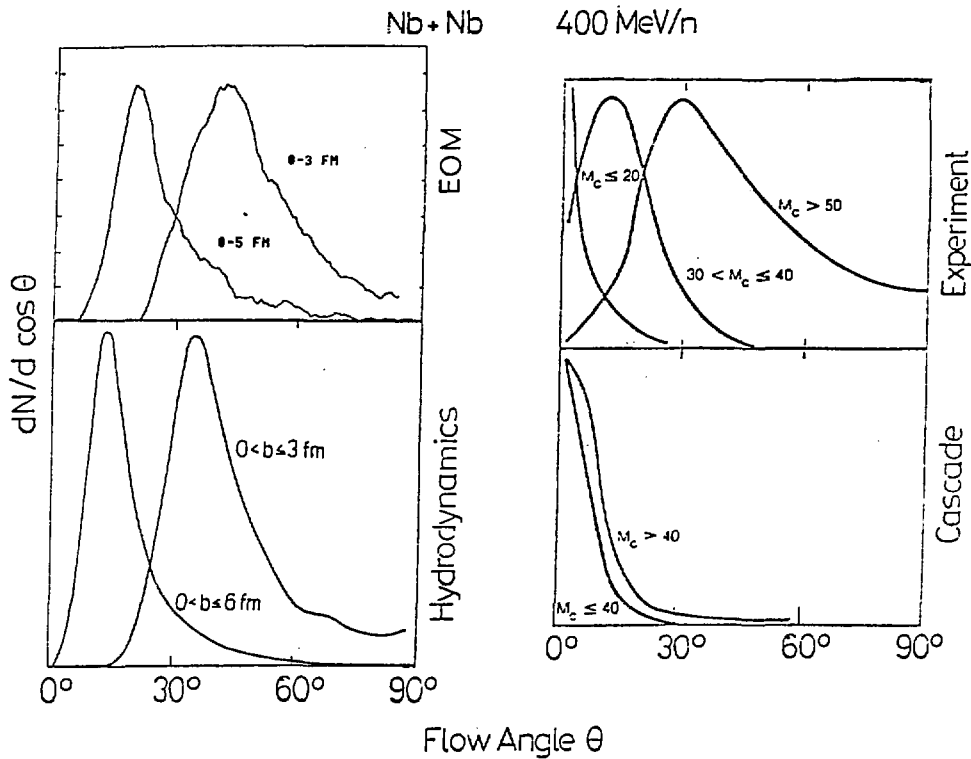


Figure 5

the EOM simulations in providing a microscopic basis for the study of the sideways flow makes us confident that the implementation⁹ of Pauli and Uncertainty Principles, as well as relativistic corrections will be worth the effort. This may well result in a tractable model useful for a quantitative understanding of the dynamics of nuclear collisions at medium and high energy. A study of the influence of the nucleon nucleon potential on the dynamics is presently underway.

References

1. H.G. Ritter et al., Global Analysis of Relativistic Nuclear Collisions Detected by the Plastic Ball, Proc. 6th Balatron Conf. on Nuclear Physics, 1983 J. Erö (ed.), p. 25.
H.A. Gustafsson, H.H. Gutbrod, B. Kolb, H. Löhner, B. Ludewigt, A.M. Poskanzer, T. Renner, H. Riedesel, H.G. Ritter, A. Warwick, F. Weik, and H. Wieman, submitted to Phys. Rev. Lett.
2. G. Buchwald, G. Graebner, J. Theis, J. Maruhn, W. Greiner, and H. Stöcker, preprint MSUCL-438 (1983), submitted to Phys. Rev. Lett.
3. Y. Yariv, Z. Frankel, Phys. Rev. C20 (1979) 2227.
4. J. Cugnon, D. Kinet, J. Van der Meulen, Nucl. Phys. A379 (1982) 553.
5. A.R. Bodmer, C.N. Panos, Phys. Rev. C15 (1977) 1342.
6. L. Wilets, E.M. Henley, M. Kraft, A.D. MacKellar, Nucl. Phys. A282 (1977) 341.
7. J.B. Hoffer, Ph.D. thesis, MSU, 1983, Computer Simulations of Gravitational Encounters between Pairs of Binary Star Systems, Astronomical Journal 88 (1983) 1420.
8. M. Gyulassy, K. Frankel, and H. Stöcker, Phys. Lett. 110B (1982) 185.
9. J. Molitoris, Ph.D. Thesis, MSU (1984).

BARYON DISTRIBUTION IN RELATIVISTIC HEAVY-ION COLLISIONS*

Cheuk-Yin Wong

Oak Ridge National Laboratory, Oak Ridge, TN 37831

Recently there is considerable interest in highly relativistic heavy-ion collisions¹ which was suggested as a way to produce a phase transition from the ordinary confined matter to the unconfined quark-gluon plasma. As the fraction of baryons in the early universe was small,² it seems desirable to design a heavy-ion collider such that when the energy density in the central rapidity is high enough for a phase transition, there is no net baryon density there.

Recent investigations reveal that the average downward shift of the projectile baryon rapidity is quite large.³ The formation of a pure quark-gluon plasma depends on the shape of the baryon momentum distributions. It is of interest to estimate the baryon momentum distribution.

We shall study the baryon distribution using the Glauber-type multiple collision model.⁴ In this model, a nucleon in one nucleus makes many inelastic collisions with nucleons in the other nucleus, the probability being given by the thickness function and the total nucleon-nucleon inelastic cross section. Each baryon-baryon collision results in a degradation of their energies and momenta in accordance with experimental nucleon-nucleon inelastic differential cross section data. This model is an extension of the model of Blankenbecler et al.⁵ to include the effect of energy degradation. We shall focus our attention on the longitudinal momentum distribution in terms of the Feynman scaling variable x .

We examine first the case of nucleon-nucleus collisions. The momentum distribution of the incident nucleon after n inelastic collisions $D^{(n)}(x_n)$ is related to that after $(n-1)$ inelastic collisions $D^{(n-1)}(x_{n-1})$ by

$$D^{(n)}(x_n) = \int dx_{n-1} D^{(n-1)}(x_{n-1}) w(x_{n-1}, x_n), \quad (1)$$

where the function $w(x_{n-1}, x_n)$ is the probability for finding a "leading" baryon with x_n after a baryon-baryon inelastic collision if the initial Feynman scaling variable is x_{n-1} . Experimental $pp+pX$ data at high energies show a nearly flat⁶ and energy-independent⁷ differential cross section $d\sigma/dx$ as a function of x . Thus, the normalized probability distribution $w(x_{n-1}, x_n)$ can be approximated by

$$w(x_{n-1}, x_n) = \theta(x_{n-1} - x_n) \theta(x_n - x_L) / (x_{n-1} - x_L), \quad (2)$$

where x_L is the lower limit of x in accordance with energy-momentum conservation. It is approximately the value of x corresponding to the projectile baryon being stopped in the target frame or the rapidity variable y being equal to the target rapidity. Initially, the momentum distribution is $D^{(0)}(x) = \delta(x-1)$. The momentum distribution of the baryon after n inelastic collisions is therefore

$$D^{(n)}(x) = \frac{1}{1-x_L} \frac{1}{(n-1)!} \left[-\ln \left(\frac{x-x_L}{1-x_L} \right) \right]^{n-1} \theta(1-x) \theta(x-x_L), \quad (3)$$

which is normalized according to $\int D^{(n)}(x) dx = 1$.

In the reaction $pA \rightarrow p+X$ where A is the target nucleus with mass number A and b is a baryon, the inelastic cross section $d\sigma^{pA}/dx$ is

$$\frac{d\sigma^{pA}}{dx} = \int d\vec{b} \sum_{n=1}^A \binom{A}{n} D^{(n)}(x) [T_A(b)\sigma_{in}]^n [1-T_A(b)\sigma_{in}]^{A-n}, \quad (4)$$

where

$$T_A(b_A) = \int dz_A \rho_A(b_A, z_A)$$

and

$$\int \rho_A(\vec{r}) d\vec{r} = 1.$$

To calculate $d\sigma^{pA}/dx$ for the reaction $pA \rightarrow p+X$, we take a Fermi-type nuclear density distribution with a radius parameter $r_0 = 1.25$ fm and a diffuseness $a = 0.523$ fm. To compare with the experimental cross sections, we shall assume that in the range of interest, $0.3 < x < 1$, the longitudinal and transverse degrees of freedom are factorizable. The theoretical results thus obtained give good agreement with experimental data⁸ (Fig. 1).

We generalize the above results to the collision of a target nucleus A with and a projectile nucleus with a mass number B . We neglect the collisions between projectile nucleons and the shift of the rapidities of the target nucleons. Within this approximation, all the projectile nucleons are alike and degrade in energy in the same manner. The projectile baryon distribution after the collision is therefore

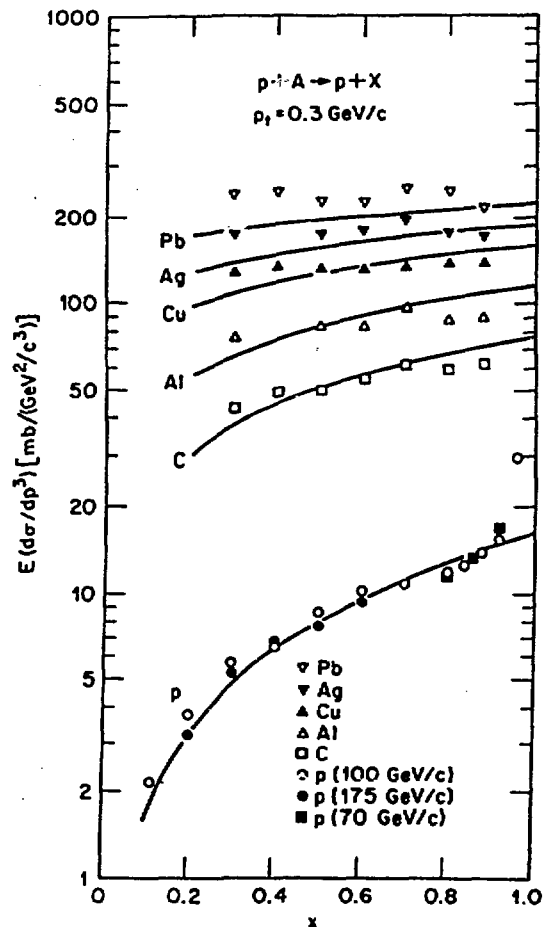


Figure 1

$$\frac{dN}{dx}(x) = B \int db_B^{\vec{}} T_B(b_B^{\vec{}}) \sum_{n=0}^A \binom{A}{n} D^{(n)}(x) [T_A(b_B^{\vec{}}) \sigma_{in}]^n [1 - T_A(b_B^{\vec{}}) \sigma_{in}]^{A-n}. \quad (5)$$

We calculate the part of projectile baryons which suffer at least one inelastic collision, dN_{IN}^B/dy , for the collisions of equal nuclei at two different bombarding energies. After taking into account the Fermi motion, the results are shown in Fig. 2 where we plot the quantity $(dN_{IN}^B/dy)/\pi R_A^2$ as a function of $y-y_B$ with R_A the radius of the target nucleus and y_B the beam rapidity. Figure 2(a) is for a bombarding energy of $\sqrt{s}/A = 30$ GeV per nucleon and Fig. 2(b) is for $\sqrt{s}/A = 100$ GeV per nucleon. This quantity gives the proper baryon density in the central rapidity region at the proper time t_0 of 1 fm/c when the produced mesons and other particles begin to emerge.¹ As the mass of the colliding nuclei increases, the peak of the projectile baryon distribution becomes wider and moves to a lower rapidity. The distribution is not symmetrical about the peak. It extends well into the target rapidity region.

Of particular interest is the baryon spatial density in the central rapidity region. It has contributions from both the projectile nucleus and the target nucleus. For $\sqrt{s}/A = 30$ GeV per nucleon, the mid-rapidity point is at $y-y_B = -4.16$. The total baryon density there at $t_0 = 1$ fm/c is 0.04 baryon/fm³ for O+O, 0.14 baryon/fm³ for Cu+Cu, and 0.28 baryon/fm³ for Pb+Pb. For the higher energy $\sqrt{s}/A = 100$ GeV per nucleon, the mid-rapidity point is at $y-y_B = -5.36$. The total baryon density there at $t_0 = 1$ fm/c is 0.02 baryon/fm³ for O+O, 0.08 baryon/fm³ for Cu+Cu, and 0.21 baryon/fm³ for Pb+Pb. One can compare these densities with the energy densities of the produced mesons in this mid-rapidity region.⁹ One finds that the baryon energy density is about 6% of the total energy density for $\sqrt{s}/A = 30$ GeV per nucleon, and is about 2 to 3% for $\sqrt{s}/A = 100$ GeV per nucleon.

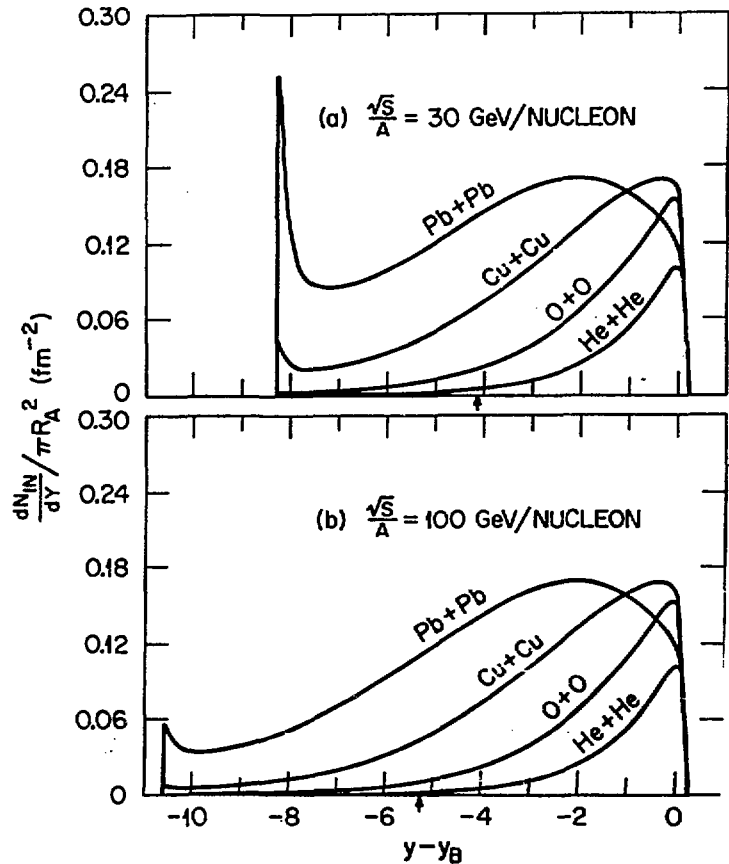



Figure 2

Our result indicates that in the energy range of $\sqrt{s}/A \sim 10\text{-}100$ GeV, it is difficult to form a pure quark-gluon plasma in the mid-rapidity region without a baryon impurity of a few percent (in energy density). Increasing the collider energy brings some improvement to the degree of baryon impurity. However, by nature of the skew distributions due to multiple inelastic collisions, some baryon impurity remains.

REFERENCES

- *Research sponsored by the Division of High Energy and Nuclear Physics, U.S. Department of Energy, under contract W-7405-eng-26 with the Union Carbide Corporation.
1. J. D. Bjorken, *Phys. Rev. D* **27**, 140 (1983) and references cited therein.
 2. D. Schramm, Proceedings of the Third International Conference on Ultra-Relativistic Nucleus-Nucleus Collisions, Brookhaven National Laboratory, September 1983 (Fermilab Report Conf-83/92-AST).
 3. W. Busza and A. S. Goldhaber, Proceedings of the Third International Conference on Ultra-Relativistic Nucleus-Nucleus Collisions, Brookhaven National Laboratory, September 1983 (SUNY Institute of Theoretical Physics preprint ITP-SB-82, 1983).
 4. R. J. Glauber, *Lectures in Theoretical Physics*, ed. by W. E. Brittin and L. G. Dunham, Vol. 1, p. 315, Interscience, New York (1959).
 5. R. Blankenbecler, A. Capella, J. Tran Thanh Van, C. Pajares, and A. V. Ramallo, *Phys. Lett.* **107B**, 106 (1981).
 6. A. E. Brenner et al., *Phys. Rev. D* **26**, 1497 (1982).
 7. F. E. Taylor et al., *Phys. Rev. D* **14**, 1217 (1976).
 8. D. S. Barton et al., *Phys. Rev. D* **27**, 2580 (1983).
 9. C. Y. Wong, ORNL preprint, submitted to *Physical Review D*.



INITIAL ENERGY DENSITY OF QUARK-GLUON PLASMA
IN RELATIVISTIC HEAVY-ION COLLISIONS*

Cheuk-Yin Wong
Oak Ridge National Laboratory, Oak Ridge, TN 37831

Recently, there is considerable interest in the central rapidity region of highly relativistic heavy-ion collisions.¹⁻⁵ Such an interest stems from the possibility of creating hadron matter of high energy density which may exceed the critical energy density for a phase transition between ordinary confined matter and the unconfined quark-gluon plasma.⁶ The experimental searches and identification of the quark-gluon plasma may provide a new insight into the question of quark confinement. Furthermore, the creation of a domain of high-energy density may allow one to study matter under unusual conditions such as those which exist in the history of the early universe.

The estimate of the initial energy density is quite uncertain. The initial energy density is nonetheless an important physical quantity. It is one of the factors which determines whether the produced matter can undergo phase transition or not. In Ref. 1 it was assumed that in a central collision a nucleon in one nucleus only makes a single collision with nucleons in the other nucleus. The number of collisions a nucleon suffers in traversing the other nucleus has not been properly treated. The energy density has also been estimated previously by using the color neutralization model of Brodsky et al.⁷ However, the color neutralization model gives a central rapidity multiplicity in heavy-ion collision too low by a factor of two.⁴ For this reason, we wish to obtain a better estimate of the energy density (in the central rapidity region).

As is well known, a simple Glauber-type multiple collision model can reproduce the total multiplicity and multiplicity plateau near the central rapidity region to within 30%.⁸ The simple multiple collision model has an approximate validity as a gross description of the reaction process. We shall adopt a semi-empirical approach. Using the multiple collision model and the thickness function of Glauber,⁹ we obtain analytical functional form for all the quantities in question. A single parameter, r_{rms} , is adjusted to fit the experimental central rapidity multiplicity data. The semi-empirical results provide a useful tool to extrapolate to the unknown central rapidity region of heavy-ion collisions.

In the multiple collision model, a nucleon in one nucleus makes many inelastic collisions with nucleons in the other nucleus, the probability of collision being given by the thickness function and the total nucleon-nucleon inelastic cross section. A nucleon may change its identity during its passage through the other nucleus, but its baryon number remains unchanged. Each nucleon-nucleon or baryon-baryon collision degrades the energies and momenta of the colliding baryons and produces particles outside the nucleus¹⁰ in accordance with the experimental nucleon-nucleon particle production data. Thus, the initial multiplicity distribution shortly after the two nuclei interpenetrate each other comes from nucleon-nucleon collisions in an additive manner. For a given configuration, the degree of this additivity is related to the number of nucleon-nucleon collisions $n(b)$ when the two nuclei pass through each other.

We discuss first the crudest approximation in which one takes the multiplicity distribution to be the same for each nucleon-nucleon or baryon-baryon collision. Then, the initial multiplicity distribution for the collision of nuclei A and B at an impact parameter b is related to the multiplicity distribution for nucleon-nucleon collision dN/dy for the same nucleon-nucleon center-of-mass energy by

$$\frac{dN^{AB}}{dy}(b) = \frac{dN}{dy} n(b). \quad (1)$$

When we average over the impact parameters, the average multiplicity distribution is given by

$$\left\langle \frac{dN^{AB}}{dy} \right\rangle = \frac{dN}{dy} \frac{AB\sigma_{in}}{\sigma_{in}^{AB}}, \quad (2)$$

where σ_{in} is the nucleon-nucleon inelastic cross section and σ_{in}^{AB} is the nucleus-nucleus inelastic cross section.

With a Gaussian form of the thickness function, we obtain the following functional form for the multiplicity distribution

$$\frac{dN^{AB}}{dy}(b) = \frac{dN}{dy} \frac{ABfe}{[1-(1-fe)^{AB}]}, \quad (3)$$

where

$$f = \sigma_{in}/2\pi\beta^2,$$

$$e = \exp[-b^2/2\beta^2],$$

$$\text{and } \beta^2 = r_{rms}^2 (A^{2/3} + B^{2/3})/3 + \beta_p^2.$$

Here, r_{rms} is the root-mean-square radius parameter and $\beta_p = 0.68$ fm is the standard deviation of the nucleon-nucleon thickness function. The functional form of the ratio of the average multiplicity distributions is then

$$R\left(\frac{AB}{pp}, y\right) = \frac{\left\langle \frac{dN^{AB}}{dy} \right\rangle}{\frac{dN}{dy}} = \frac{ABf}{\sum_{i=1}^{AB} [1 - (1-f)^i] / i}. \quad (4)$$

If we mindlessly apply Eqs. (3) and (4) by using the root-mean-squared radius parameter as determined by electron scattering, the theoretical results consistently exceed the experimental values. In order to correct for this

systematic discrepancy, we shall adopt a semi-empirical approach. This consists of assuming the functional form of Eqs. (3) and (4) with its only parameter r_{rms} so chosen as to fit the available central rapidity multiplicity data. We found that $r_{rms} = 1.15$ fm gives good fits to the experimental central multiplicity data¹¹⁻¹³ of p α , dd, $\alpha\alpha$, Si+Ag, and Ca+C (Table I). The results of Eqs. (3) and (4) can be used to discuss the collisions of other nuclei.

Using the relationship between dN^{AB}/dy and the energy density ϵ as given by Ref. 1, we can calculate the energy density in the central rapidity region. The energy density $\epsilon(b)$ in the collision of nuclei A and B with an impact parameter b is given by

$$\frac{\epsilon(b)}{\epsilon_0} = \frac{AB T(b) \sigma_{in}}{\{1 - [1 - T(b) \sigma_{in}]^{AB}\} \mathcal{A}(b)} \quad (5)$$

where $T(b)$ is the normalized thickness function and can be approximated by

$$T(b) = \exp[-b^2/2\beta^2]/2\pi\beta^2,$$

$\mathcal{A}(b)$ is the transverse overlap area of the two nuclei, and ϵ_0 is a bombarding-energy-dependent unit of energy density. At the time of 1 fm/c after the nuclei collide with each other, particles are produced. The energy density unit ϵ_0 at that time is 0.84 GeV/fm³ for $\sqrt{s}/A = 11.8$ GeV, 1.14 GeV/fm³ for $\sqrt{s}/A = 31.4$ GeV, and 1.80 GeV/fm³ for $\sqrt{s}/A = 270$ GeV. We calculate the initial energy density for head-on collisions of two equal nuclei. In Fig. 1 we show this quantity as a function of A. The numerical result can be parameterized as

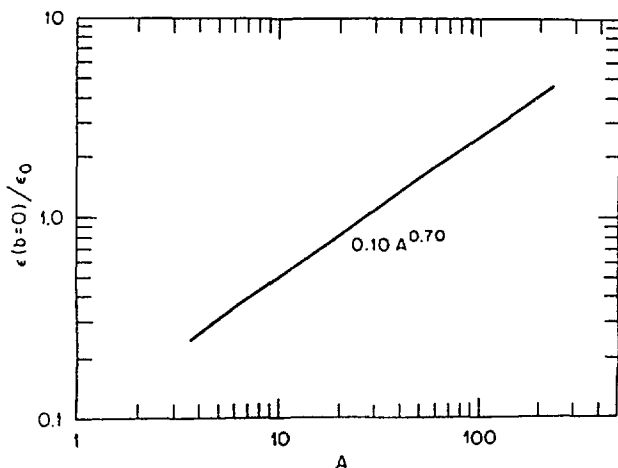


Figure 1

Nuclei		$(dN^{AB}/dy)/(dN/dy)$	
A	B	exp	Theory
p	p	1	1
p	α	1.18 ± 0.07	1.19
d	d	1.24 ± 0.10	1.21
α	α	1.74 ± 0.09	1.71
Si	Ag	~ 95	96.0
Ca	C	~ 25	27.1

$$\frac{\epsilon(b=0)}{\epsilon_0} = 0.10 A^{0.709}$$

which goes approximately as $A^{2/3}$, as expected from Eq. (5). We also calculate the energy density in units of ϵ_0 as a function of the impact parameter for the collision of ^{238}U on ^{238}U . The results are shown in Fig. 2. The energy density is about 5 units of ϵ_0 . It oscillates as a function of the impact parameter with an amplitude of about $0.5 \epsilon_0$. Our energy density estimates are greater than those of the previous estimates^{1,4} as the detailed treatments are different. At an incident energy of $\sqrt{s}/A = 30$ GeV per nucleon,

this corresponds to an energy density of about $5 \text{ GeV}/\text{fm}^3$ which exceeds the energy density of $2 \text{ GeV}/\text{fm}^3$ estimated to be the critical energy density for a phase transition.⁴

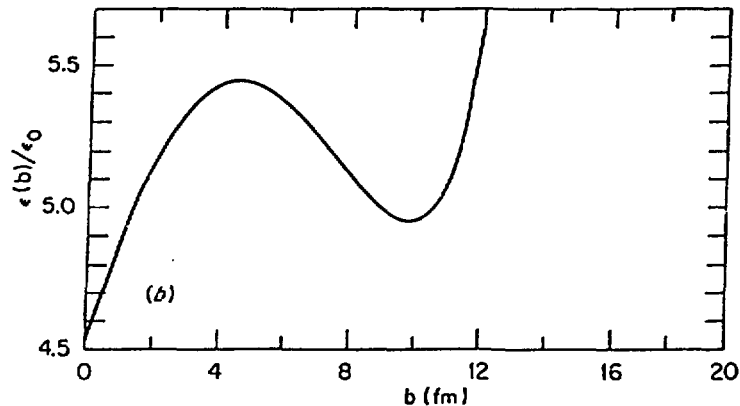


Figure 2

REFERENCES

- *Research sponsored by the Division of High Energy and Nuclear Physics, U.S. Department of Energy, under contract W-7405-eng-26 with the Union Carbide Corporation.
1. J. D. Bjorken, *Phys. Rev. D* **27**, 140 (1983).
 2. K. Kajantie and L. McLerran, *Phys. Lett.* **119B**, 203 (1982).
 3. T. D. Lee, Columbia University Report No. CU-TP-226, 1981.
 4. M. Gyulassy, Lawrence Berkeley Report No. LBL-15175, 1982.
 5. J. Rafelski and M. Danos, N.B.S. Report No. NBSIR 83-2725, 1983.
 6. For example, L. McLerran and B. Svetitsky, *Phys. Lett.* **96B**, 195 (1981); *Phys. Rev. D* **24**, 450 (1981); L. Montvay and H. Pietarinen, *Phys. Lett.* **115B**, 151 (1982); J. Kogut et al., *Phys. Rev. Lett.* **48**, 1140 (1982).
 7. S. J. Brodsky, J. F. Gunion, and J. H. Kuhn, *Phys. Rev. Lett.* **39**, 1120 (1977).
 8. J. E. Elias, W. Busza, C. Halliwell, D. Luckey, L. Votta, and C. Young, *Phys. Rev. Lett.* **41**, 285 (1978); J. E. Elias, W. Busza, C. Halliwell, D. Luckey, L. Votta, and C. Young, *Phys. Rev. D* **22**, 13 (1980).
 9. R. J. Glauber, *Lectures in Theoretical Physics*, ed. by W. E. Brittin and L. G. Dunham, Vol. 1, p. 315, Interscience, New York (1959).
 10. W. Busza, Proceedings of 4th High Energy Heavy Ion Summer Study, June 1978, LBL-7766, p. 253 (unpublished).
 11. W. Bell et al., Proceedings of 5th High Energy Heavy Ion Study, Berkeley, May 1981, p. 540.
 12. M. Jacobs, Proceedings of 5th High Energy Heavy Ion Study, May 1981, LBL-12652, p. 581 (unpublished).
 13. T. H. Burnett et al., *Phys. Rev. Lett.* **50**, 2062 (1983).

STATISTICALLY GENERATED EVENTS AND THE FLUID-DYNAMICAL
EXPECTATION IN HIGH ENERGY NUCLEON COLLISIONS

Laszlo P. Csernai[†] and Jørgen Randrup
LBL, University of California, Berkeley, CA 94720

and

George Fai
Kent State University, Kent, OH 44242

Experimental developments point in the direction of measuring exclusive quantities in high-energy nuclear collisions. On the theory side a computer simulation model has been put forward recently to generate complete (exclusive) events statistically.¹ In the present work we use this model together with fluid-dynamical results to see how the formation of composite fragments, the finiteness of the multiplicity, and the statistical fluctuations in the final states affect the event analysis. From a series of detailed three-dimensional fluid-dynamical calculations² we extract certain gross features that are used to give an approximate characterization of the final state of the fluid dynamical stage of the collision in terms of a few subsystems (sources), a participant source and up to two spectator sources.

More specifically, the flow angle can be reasonably well approximated (at the intermediate and large impact parameters) by the following function of the impact parameter s :

$$\theta_{CM}(s) \approx z_0 \left(1 - \frac{s}{s_{max}}\right) \frac{\pi}{2} . \quad (1)$$

Here z_0 is the parameter governing the transverse momentum transfer. In fluid dynamical models it is of the order of unity and we shall adopt the value $z_0 = 1$ in our present studies.

The inelasticity can be described by the CM momentum per nucleon, p'_{CM} , of the projectile-like part of the system after the collision. For this quantity we find:

$$p'_{CM} \approx p_{CM} \left(1 - \left(1 - \frac{s}{s_{max}}\right)^2 y_0\right) , \quad (2)$$

where $p_{CM} = P_0/A_0$ is the initial CM momentum per nucleon of the projectile. The detailed three-dimensional calculations² show that $y_0 \approx 0.5-0.7$, and we shall adopt the value $y_0 = 0.6$ in our studies.

The above characteristic features of the fluid-dynamical results permit us to approximate the final state of the fluid-dynamical stage by three sources A, B, C. We assume the source momenta p^A , p^B , p^C to be given (in the CM frame) in terms of the parameters y and z as:

$$\begin{aligned}
 \begin{matrix} p^A \\ \parallel \end{matrix} &= (1 - y) \frac{A}{A_0} P_0, & \begin{matrix} p^A \\ \perp \end{matrix} &= z \frac{A}{A_0} P_0 \\
 \begin{matrix} p^B \\ \parallel \end{matrix} &= -(1 - y) \frac{B}{B_0} P_0, & \begin{matrix} p^B \\ \perp \end{matrix} &= -z \frac{B}{B_0} P_0 \\
 \begin{matrix} p^C \\ \parallel \end{matrix} &= -\begin{matrix} p^A \\ \parallel \end{matrix} - \begin{matrix} p^B \\ \parallel \end{matrix}, & \begin{matrix} p^C \\ \perp \end{matrix} &= -\begin{matrix} p^A \\ \perp \end{matrix} - \begin{matrix} p^B \\ \perp \end{matrix}
 \end{aligned} \quad (3)$$

where, as in (2), P_0 is the absolute value of the initial CM momentum of either nucleus A_0 or B_0 . Furthermore, we adopt the parameter $x \in [0,1]$ to govern the leakage of excitation energy from the participant source C into the two spectator sources A and B.

The three parameters x, y, z , which determine the source characteristics, are taken as:

$$\begin{aligned}
 x &= x_0 \left(1 - \left(\frac{s}{s_{\max}}\right)^2\right) \\
 y &= 1 - \left[1 - \left(1 - \frac{s}{s_{\max}}\right)^2 y_0\right] \cos \left[z_0 \left(1 - \frac{s}{s_{\max}}\right) \frac{\pi}{2}\right] \\
 z &= \left[1 - \left(1 - \frac{s}{s_{\max}}\right)^2 y_0\right] \sin \left[z_0 \left(1 - \frac{s}{s_{\max}}\right) \frac{\pi}{2}\right]
 \end{aligned} \quad (4)$$

with $x_0 = 0.3$, so that the fluid-dynamical results be reproduced as well as possible.

The expectation value of the flow tensor can be calculated analytically in the fluid-dynamical model.³ We evaluate the flow tensor as follows,²

$$\begin{aligned}
 \overleftrightarrow{F} &= \sum_k \frac{\vec{p}(k)\vec{p}(k)}{2M_k} \\
 &= \sum_S \sum_{\alpha} \frac{1}{2M_{\alpha}} \sum_{k \in S, \alpha} \vec{p}(k)\vec{p}(k) \\
 &= \sum_S \sum_{\alpha} \frac{1}{2M_{\alpha}} \int d\vec{p} f_{\alpha} \left(\frac{\vec{p}}{M_{\alpha}} - \vec{v}(S), \tau_S, \rho_S^{(\alpha)} \right) \vec{p} \vec{p}
 \end{aligned} \quad (5)$$

The first line gives the definition of the flow tensor \overleftrightarrow{F} as a sum over all fragments k in a given event; a fragment has the momentum $\vec{p}(k)$ and the mass M_k . The system is divided into a number of fluid elements, or sources, which are denoted by S (later to take on the values A, B, C). The sum over fragments located within a given source can be carried out separately for each particular fragment species α . This is indicated in the second line of (5). In the third line we have introduced the fact that the fragments are assumed to have a certain characteristic distribution f within a given source. This distribution is taken as a thermal Maxwell-Boltzmann distribution depending on the source temperature $\tau_S^{(\alpha)}$ and source $\rho_S^{(\alpha)}$ of the particular species α ; it is isotropic in the source frame, which moves with the velocity $\vec{v}(S)$ relative to the chosen reference frame.

The fragment momentum has a global and a local (or a collective and a thermal) part, $\vec{P} = M_\alpha \vec{V}(S) + (\vec{p} - M_\alpha \vec{V}(S))$. The momentum integral in (5) can then be carried out and we obtain:

$$\begin{aligned} \overleftrightarrow{F} &= \sum_S \sum_\alpha \bar{v}_S^{(\alpha)} \left(\frac{1}{2} M_\alpha \overleftrightarrow{V}(S) \overleftrightarrow{V}(S) + \frac{1}{2} \tau_S \overleftrightarrow{I} \right), \quad (6) \\ &= \sum_\alpha \sum_S \bar{v}_S^{(\alpha)} \left[\frac{M_\alpha}{2} \overleftrightarrow{V}(S) \overleftrightarrow{V}(S) + \frac{\tau_S}{2} \overleftrightarrow{I} \right] \end{aligned}$$

where \overleftrightarrow{I} is the identity tensor and $\bar{v}_S^{(\alpha)}$ is the mean multiplicity of the species α arising from the source S . (The total mean multiplicity from the source S is denoted by \bar{v}_S .) The first term in (6) is associated with the global collective motion of the system, while the second term arises from the local thermal motion of the fragments. This latter term is isotropic and, therefore, has no effect on the orientation of the principal direction of \overleftrightarrow{F} , hence also no effect on the extracted flow angle.

It is of interest theoretically, and often also necessitated by experimental conditions, to study the flow tensor $\overleftrightarrow{F}^{(\alpha)}$ associated with a particular fragment species. We have

$$\begin{aligned} \overleftrightarrow{F} &= \sum_\alpha \overleftrightarrow{F}^{(\alpha)} \\ &= \sum_\alpha \left[\sum_S \bar{v}_S^{(\alpha)} \left(\frac{M_\alpha}{2} \overleftrightarrow{V}(S) \overleftrightarrow{V}(S) + \frac{\tau_S}{2} \overleftrightarrow{I} \right) \right] \quad (7) \end{aligned}$$

It is clear that the thermal contribution is most important for the flow tensors for light species since the collective term is proportional to the fragment mass M_α .

The particular advantage of approximating the final fluid-dynamical stage of the collision by a few sources is the ease with which the subsequent disassembly into a finite number of physical fragments can be calculated. Indeed, all that is required is to use the appropriate parameters x, y, z (4) as input into the event generation model developed in ref. 1). In that model, each source explodes statistically into a number of excited nucleides, which subsequently decay by light-particle evaporation if sufficiently excited. The final evaporation stage is very important since the evaporated light fragments constitute a substantial fraction of the total yield and change the emission pattern considerably. In particular, spectator sources with low excitation give a significant contribution to the light particle yield in the microcanonical event generation via their evaporation. In the micro-canonical model, a sample of final states is generated, each of which satisfy conservation of four-momentum, baryon number, and charge. The formation of composite fragments plays an important role in the event analysis, and the present study pays particular attention to the composite fragments.

For each specified impact parameter, the model of ref. 1) is employed to generate a sample of complete events. The microcanonical event generation is implemented as a Monte Carlo computer code and it yields exclusive events that incorporate the full complexity associated with fragment formation, finite multiplicity and statistical fluctuations. This advantage necessitates the handling of large sets of data much in the same way as in the experimental case. The calculation of the flow tensor, on the other hand, simply amounts to a straightforward application of the definition.

The resulting fluid-dynamical and statistically generated flow diagrams have been compared for the collision $93\text{Nb} + 93\text{Nb}$ at 400 MeV/nucleon.⁴ We also investigated the effect of different species selections: calculations were carried out with three selections: 1) protons only, 2) all hydrogen and helium fragments (i.e.: p, d, t, ^3He , α), and 3) all fragments, including neutrons. The parameter values have been fixed to $x_0 = 0.3$, $y_0 = 0.6$ and $z_0 = 1.0$ for simplicity.

In the fluid-dynamical description a given impact parameter yields a well-defined point in the flow diagram, while the statistically generated points are strongly fluctuating. Nevertheless, they loosely follow the fluid-dynamical expectation.

When comparing different selections one should remember that the flow tensor, although ideally coalescence invariant, depends on the specific species selection which must always be made in a real experiment. Thus, in contrast to naive expectations, the observed flow tensor is not coalescence invariant. Due to the final evaporation there is an observable shift for light fragments (selections 1 and 2) towards more elongated emission patterns compared to fluid-dynamical expectations. The fluctuations associated with these selections are also considerably larger than those of selection 3. Especially the fluctuation of the flow angle θ is very large for small impact parameters, because the events are rather close to spherical.

In conclusion we have shown that the total flow tensor \overleftrightarrow{F} (selection 3) is fairly close to the fluid-dynamical expectation. However, in the experimental situation, where only light fragments are considered, the measured flow tensor depends strongly on the cut off on the fragment mass considered. It is very important to take account of this fact when comparing experimental and theoretical results.

† On leave from CRIP, Budapest, Hungary

1. G. Fai and J. Randrup, *Nucl. Phys.* **A404**, 551 (1983).
2. L.P. Csernai, H. Stocker, P.R. Subramanian, G. Graebner, A. Rosenhauer, G. Buchwald, J.A. Maruhn and W. Greiner, *Phys. Rev.* **C28**, 2001 (1983).
3. H. Stocker, G. Buchwald, G. Graebner, J.A. Maruh, W. Greiner, K. Frankel and M. Gyulassy, *MSU Rep. No. MSUCL-409* (1983).
4. L.P. Csernai, G. Fai and J. Randrup, submitted to *Phys. Lett.*

THERMAL PROPERTIES OF LIGHT NUCLEI WITH REALISTIC EFFECTIVE HAMILTONIANS*

G.Bozzolo and J.P.Vary

Physics Department

Iowa State university

Ames Ia 50011

INTRODUCTION

A realistic microscopically derived nuclear equation of state for finite nuclei would be of great utility for interpreting current experiments in heavy ion scattering and high energy particle-nucleus experiments.

A necessary and major step towards obtaining this equation of state involves solving for the thermal properties of nuclei without external constraints. A theoretical framework to explore the thermal properties of finite nuclei in the mean field approximation has been introduced by Bloch and di Domenico¹⁾. This framework and extensions to include the effects of superconductivity²⁾ have been applied to nuclei with phenomenological Hamiltonians³⁾. In this paper we present a sample of an initial set of results for two representative nuclei, ^{16}O and ^{40}Ca in the finite temperature Hartree-Fock approximation (FIHF).

THEORETICAL METHOD

Given an effective Hamiltonian H_{eff} for a chosen model space, we minimize the free energy

$$F = H_{\text{eff}} - TS \quad (1)$$

assuming a mean field approximation at fixed temperature T and obtain the FIHF equations^{1,2)}. The fully self-consistent solutions of these equations provides the binding energy, free energy, density distribution, entropy, neutron and proton chemical potentials and single particle energies, occupation probabilities and other properties all as a function of temperature.

In principle, H_{eff} is also T dependent⁴⁾ but we have ignored this complication in our initial applications. Our approach is based on the philosophy that we will first develop the H_{eff} that would be appropriate to the full diagonalization of the no-core many nucleon problem in the chosen finite model space. We have previously applied moment methods⁵⁾ to obtain spectral properties from these same effective no-core Hamiltonians. In brief, we write H_{eff} as

$$H_{\text{eff}} = T_{\text{rel}} + V_{\text{eff}} + V_c \quad (2)$$

where T_{rel} is the relative kinetic energy operator between pairs of nucleons, V_c is the Coulomb interaction between protons and V_{eff} is the sum of the Brueckner G -matrix and the lowest order folded diagram (second order in G) acting between pairs of nucleons in the model space⁵⁾. The underlying nucleon-nucleon interaction is the Reid soft core potential⁶⁾. For evaluating matrix elements of H_{eff} we choose the harmonic oscillator basis with $\hbar\omega = 14$ Mev and we select a sequence of model spaces abbreviated as the 2-space (0s-0p and 1s-0d shells), the 3-space (0s,0p,1s-0d,1p-0f shells), the 4-space(0s,0p,1s-0d,1p-0f,2s-1d-0g shells) and the 5-space (2p-1f-0h shells). This sequence of model spaces permits us to estimate convergence properties of physical quantities evaluated for many-nucleon systems.

In a recent application⁷⁾ of these same Hamiltonians we have introduced scaling rules that account for the major role of changing the harmonic oscillator constant for the basis space in order to accommodate a change in nucleon number. With these scaling procedures we need only calculate H_{eff} for one representative value of the oscillator constant. It is then a simple matter to apply this same Hamiltonian to both ^{16}O and ^{40}Ca as we have done for these initial applications.

At $T=0$ we expect our results to be similar to those of the Brueckner Hartree-Fock (BHF) approximation. Small differences may be ascribed to different choices for the Pauli operator and single particle spectra in the two-particle propagators of the G -matrix. Therefore, we expected and found the standard deficiencies in the $T=0$ ground state solution for ^{16}O and ^{40}Ca

in the spherical Hartree-Fock (SHF) approximation. Our philosophy is to adjust the H_{eff} in order to achieve agreement with measured ground state properties in the SHF approximation before proceeding with the FIHF calculations. To do this we simply introduce overall factors t_1 and t_2 for the kinetic energy and effective interaction terms respectively in Eq. (2). We then adjust t_1, t_2 and the harmonic oscillator constant simultaneously to achieve the correct rms radius and binding energy for a given nucleus within SHF for a fixed model space. The best fit values are found to vary smoothly with increasing model space and increasing number of nucleons. For example, in the 5-space results for ^{16}O we obtain parameter values (0.98, 1.30, 9.71 MeV) respectively for $(t_1, t_2, \hbar\omega)$. For ^{40}Ca in the 5-space the results are (0.98, 1.28, 7.97 MeV).

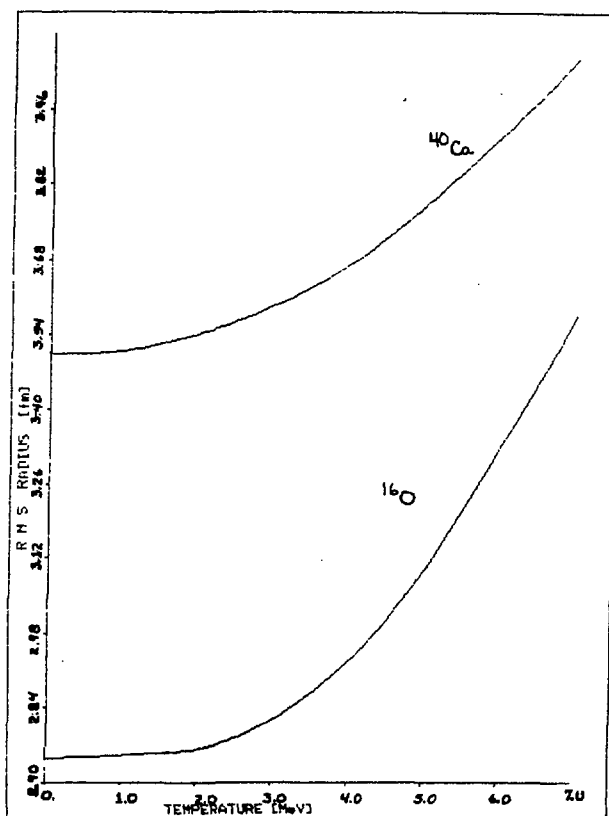


Fig. 1

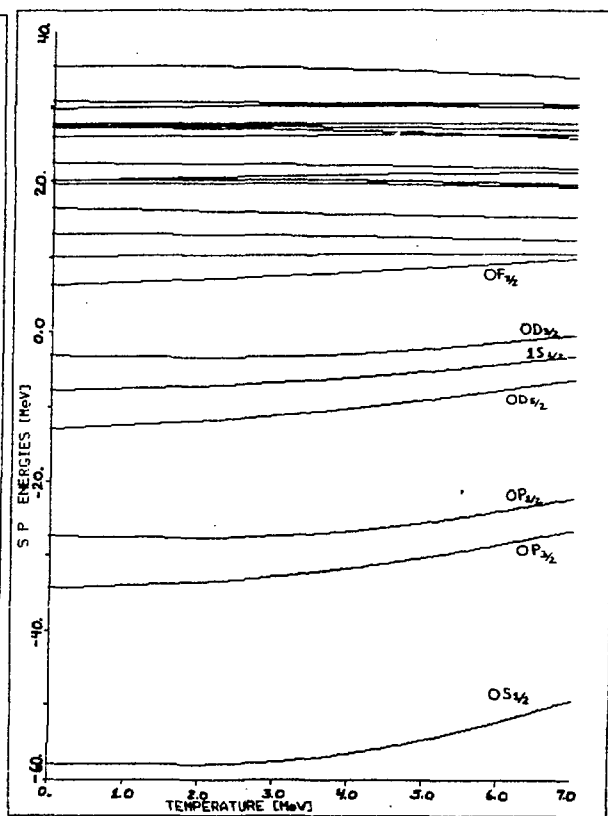


Fig. 2

RESULTS

We display the FTHF results for the rms radii of ^{16}O and ^{40}Ca as a function of temperature in Fig.1. These results and those of Fig.2 are obtained in the 5-space with adjustments to H_{eff} as described above. For low temperatures, $T \leq 2$ MeV in ^{16}O and $T \leq 1$ MeV in ^{40}Ca the radius exhibits almost no thermal response due to the shell closure effects. Then with increasing T , both nuclei undergo a radial expansion proportional to T^2 . With a more complete presentation of these results⁸⁾ we elaborate on the apparent larger coefficient of thermal expansion for ^{16}O than for ^{40}Ca .

In Fig.2 we present the neutron single particle energies for ^{40}Ca as a function of T . Although all the levels are not labeled they are in the order of the standard nuclear shell model. Note especially that with increasing T the spin-orbit splitting decreases fast enough to actually preserve the shell gaps to higher temperatures that might have otherwise been expected.

*This work was supported by the Director, Office of Energy Research, Division of Nuclear Physics of the Office of High Energy and Nuclear Physics of the U.S. Department of Energy under contract DE-AC02-82-ER40068.

REFERENCES

- 1) C. Bloch and C. de Dominicis, Nucl. Phys. 7, 459 (1958)
- 2) A. L. Goodman, Nucl. Phys. A352, 30 (1981)
- 3) U. Mosel, P. -G. Zint and K. H. Passler, Nucl. Phys. A236, 252 (1974) and references therein; G. Sauer, H. Chandra and U. Mosel, Nucl. Phys. A264, 221 (1976) and references therein.
- 4) C. Bloch in "Studies in Statistical Mechanics", Vol. 3, edited by de Boer and G. Uhlenbeck, North Holland, 1965; J. R. Buchler and S. A. Coon, Ap. J. 212, 807 (1977); M. Barranco and J. R. Buchler, Phys. Rev. C24, 1191 (1981).
- 5) J. P. Vary in "Applications of Moment Methods in Many Fermion Systems" edited by B. J. Dalton, S. M. Grimes, J. P. Vary and S. A. Williams, Plenum, New York, 1980; F. J. Margetan and J. P. Vary, Phys. Rev. C28, 907 (1983).
- 6) R. V. Reid, Ann. Phys. (N.Y.) 50, 411 (1968)
- 7) G. Bozzolo, A. Klar and J. P. Vary, Phys. Rev. C29, 1069 (1984)
- 8) G. Bozzolo and J. P. Vary, to be published.

HIGH ENERGY NUCLEAR STRUCTURES

J. Boguta
Accelerator and Fusion Research Division
Lawrence Berkeley Laboratory, Berkeley, CA 94720

and

J. Kunz
Theoretical Division, Los Alamos National Laboratory
Los Alamos, NM 87545

In conventional nuclear physics the nucleus is described as a non-relativistic many-body system, which is governed by the Schrödinger equation. Nucleons interact in this framework via static two-body potentials, mesonic degrees of freedom are neglected. However, although this conventional approach has usually been very successful, the validity of its basic assumptions is questionable[1,2].

An alternative description of nuclear physics in terms of a relativistic field theory has been developed by Walecka [1]. The model Lagrangian containing baryons, σ -mesons and ω -mesons was subsequently extended to include also π -mesons and ρ -mesons [3,4]. An essential feature of such a nuclear Lagrangian is its renormalizability.

Nuclear field theory has been applied to study nuclear matter as well as finite nuclei. Within the mean field approximation the known bulk properties of nuclei such as binding energy, density, and compressibility are well reproduced. Charge and matter distributions of closed shell nuclei are in good agreement with experimental results, so are rms radii and single-particle energy levels [4].

In addition to the description of known nuclear structure the field theoretical approach may reveal entirely new nuclear phenomena, based on the explicit treatment of mesonic degrees of freedom. The existence of such abnormal nuclear states was proposed by Lee and Wick employing the σ -model Lagrangian [5]. There the non-linearity of the meson field equations allows for soliton solutions in the presence of nucleons, in particular the σ -field may exhibit a kink.

Different types of soliton solutions occur in gauge theories with hidden symmetries. In the phenomenological Lagrangian [3] the ρ -meson is described by a non-abelian gauge field, that acquires its mass spontaneously due to the

non-vanishing vacuum expectation value of a Higgs field. A general ansatz for soliton solutions of such a gauge theory was given by Dashen et al. [6]. A specific solution and its possible implications for nuclear physics like anomalous nuclear states were discussed by Boguta [7].

In the following we address the question whether anomalous nuclear structures do occur in the full phenomenological Lagrangian [8]

$$\begin{aligned}
 \mathcal{L} = & -\frac{1}{4} \hat{F}_{\mu\nu} \cdot \hat{F}_{\mu\nu} - \bar{\psi} \gamma_{\mu} \left(\frac{\partial}{\partial x_{\mu}} - ig_{\rho} \frac{\hat{t}}{2} \cdot \hat{\rho}_{\mu} \right) \psi - g_s \bar{\psi} (\sigma + i \gamma_5 \hat{t} \cdot \hat{\pi}) \psi \\
 & - \frac{1}{2} \left(\frac{\partial \sigma}{\partial x_{\mu}} \right)^2 - \frac{1}{2} \left(\frac{\partial \hat{\pi}}{\partial x_{\mu}} + g_{\rho} \hat{\rho}_{\mu} \times \hat{\pi} \right)^2 - \frac{1}{2} \left| \left(\frac{\partial}{\partial x_{\mu}} - ig_{\rho} \frac{\hat{t}}{2} \cdot \hat{\rho}_{\mu} \right) H \right|^2 \\
 & - \lambda_H / 4 (H^{\dagger} H - V^2)^2 - \lambda_c / 4 (\sigma^2 + \hat{\pi}^2 - \sigma_0^2)^2 .
 \end{aligned} \tag{1}$$

Here ψ represents the nucleon field, that couples to the ρ -field through the covariant derivative and to the σ - and π -field. Note that no explicit mass term for the nucleon occurs, its mass is given by the non-vanishing expectation value of the σ -field

$$m_N = g_s \langle \sigma \rangle = g_s \sigma_0 .$$

The field strength of the ρ -meson is denoted by $\hat{F}_{\mu\nu}$. The hat symbolizes an isovector. \hat{t} represents the usual Pauli matrices acting in isospin space. The ρ -field mass is given by

$$m_{\rho} = \frac{1}{2} g_{\rho} V ,$$

where V is the non-vanishing component of the expectation value of the Higgs field H .

The Lagrangian (1) joins the linear σ -model with a gauge field theory with hidden symmetry. Finite energy soliton solutions to both parts separately have been studied [6,7,9]. We therefore combine the ansatz for the gauge field

$$\rho_c^a \propto \epsilon_{abc} x^b$$

and the Higgs field [6]

$$H \propto \hat{t} \cdot \underline{r} \begin{pmatrix} 0 \\ 1 \end{pmatrix}$$

with the hedgehog ansatz for the pion field [9]

$$\hat{\pi} \propto \underline{r} .$$

The Euler-Lagrange equations derived from Lagrangian (1) then reduce to a set of non-linear coupled differential equations, depending only on the radial variable. The nucleon wavefunction possesses the conserved quantum number k ($k = \underline{l} + \underline{s} + \hat{t}/2$).

A remarkable feature of the above Lagrangian is that it leads to a conserved topological quantum number of the Skyrme type. It can be constructed from the quaternion

$$U = \sigma + i \hat{t} \cdot \hat{\pi} ,$$

when the σ - and π -fields are normalized to satisfy $U^\dagger U = 1$ [8].

Let us now turn to the physical properties of soliton solutions obtained with the above ansatz. First we have to address the question of stability of such solitons. The existence of a conserved topological quantum number alone does not assure stability of the solution. The topological structure of the σ - and π -field may remain unaffected by a change in the structure of the ρ - and Higgs fields [6], that is consistent with the hedgehog ansatz. We suppose, however, that the presence of nucleons renders the solution stable.

We estimate the excitation energy of such states to be of the order of several hundred MeV. The rho soliton contributes about 1.5 GeV. Considerable energy is regained, however, due to the strong binding of nucleons by the σ - and π -field. An exact numerical computation of the excitation energy is in progress.

The possible anomalous nuclei are limited to states with small electric charge and baryon number. This is due to the fact that we obtain self-consistent solutions to the equations only for nucleons in $k = 0$ states, corresponding to the $s_{\frac{1}{2}}$ and $p_{\frac{1}{2}}$ states of the Dirac equation. Thus to increase the number of nucleons present, states with $k = 0$ higher in energy have to be occupied. Clearly only a limited number of such states will be bound.

Finally, we note that the usual short-range hadronic interaction undergoes a metamorphosis in the soliton solution and becomes long-ranged [7,8]. Consequently, such an anomalous nuclear state will exhibit a huge reaction cross section. Anomalous nuclei with large lifetimes and cross sections have been observed experimentally [10].

REFERENCES

- (1) J. D. Walecka, Ann. Phys. 83 (1974) 491.
- (2) J. D. Walecka, Proc. 5th High Energy Heavy Ion Study (1981) 91.
- (3) B. D. Serot, Phys. Lett. 86B (1979) 146.
- (4) J. Boguta, Proc. 6th High Energy Heavy Ion Study and 2nd Workshop on Anomalons (1983) 111.
- (5) T. D. Lee, and G. C. Wick, Phys. Rev. D9 (1974) 2291.
- (6) R. F. Dashen, B. Hasslacher, and A. Neveu, Phys. Rev. D12 (1974) 4138.
- (7) J. Boguta, Phys. Rev. Lett. 50 (1983) 148.
- (8) J. Boguta, and J. Kunz, Los Alamos Preprint LA-UR-83-3562 (1983).
- (9) S. Kahana, G. Ripka, and V. Soni, Brookhaven Preprint BNL-33577 (1983).
- (10) Proc. 6th High Energy Heavy Ion Study and 2nd Workshop on Anomalons (1983) 3-94.

LIST OF PARTICIPANTS

- Jorg Aichelin
Cyclotron Laboratory
Michigan State University
East Lansing, MI 48824
- Terry Awes
Oak Ridge National Laboratory
Oak Ridge, TN 37830
- Sakir Ayik
Department of Physics & Astronomy
University of Maryland
College Park, MD 20742
- Dana Beavis
Department of Physics
University of California
Riverside, CA 92521
- Frederick H. Beck
Institut für Kernphysik
T. H. Darmstadt
Schlossgartenstrasse 9
D-6100 Darmstadt
WEST GERMANY
- Yehuda Boneh
Nuclear Research Center-Negev
P. O. Box 9001
Beer-Sheva (84190) ISRAEL
- Guillermo H. Bozzolo
Physics Department
Iowa State University
Ames, Iowa 50011
- Herbert Breuer
Department of Physics
University of Maryland
College Park, MD 20742
- Yuen-dat Chan
Building 88
Lawrence Berkeley Laboratory
Berkeley, CA 94720
- Douglas Cline
Nuclear Structure Research Laboratory
University of Rochester
Rochester, NY 14627
- Laszlo P. Csernai
Central Research Institute for Physics
H-1525 Budapest
P. O. Box 49, HUNGARY
- Pawel D. Danielewicz
70A - 3307
Lawrence Berkeley Laboratory
University of California
Berkeley, CA 94709
- Thomas Dössing
Nuclear Science Division
Lawrence Berkeley Laboratory
University of California
Berkeley, CA 94720
- Maria Dworzecka
Department of Physics
George Mason University
Fairfax, VA 22030
- George Fai
Smith Laboratory of Physics
Kent State University
Kent, OH 44240
- Hans Feldmeier
Max-Planck-Institut für Kernphysik
Saupfercheckweg 1
D-6900 Heidelberg, WEST GERMANY
- Hartwig Freiesleben
Ruhr-Universität Bochum
Institut für Experimentalphysik
Postfach 10 21 48, D-4630 Bochum
WEST GERMANY
- James J. Griffin
Department of Physics
University of Maryland
College Park, MD 20742

Hans-Ake Gustafsson
 Building # 70A
 Lawrence Berkeley Laboratory
 Berkeley, CA 94720

John R. Huizenga
 Nuclear Structure Laboratory
 University of Rochester
 Rochester, NY 14627

Barbara Jacak
 Cyclotron Laboratory
 Michigan State University
 East Lansing, MI 48824

Che Ming Ko
 Cyclotron Institute
 Texas A & M University
 College Station, TX 77843

Jutta Kunz
 Nuclear Theory, T-9, MS B279
 Los Alamos National Laboratory
 Los Alamos, NM 87544

Kris Kwiatkowski
 Chemistry Department
 Indiana University
 Bloomington, IN 47405

Kevin Lesko
 Building 203
 Argonne National Laboratory
 9700 South Cass
 Argonne, IL 60439

F. Lefebvres
 Laboratoire De Physique Corpusculaire
 Université De Caen
 Esplanade De La Paix
 14032 Caen, Cedex, FRANCE

Michael J. LeVine
 Building 901A
 Brookhaven National Laboratory
 Upton, NY 11973

Bernhard Ludewigt
 Lawrence Berkeley Laboratory
 1 Cyclotron Road, 70A-3307
 Berkeley, CA 94720

William G. Lynch
 Cyclotron Laboratory
 Michigan State University
 East Lansing, MI 48824

John F. Mateja
 Physics Department
 Tennessee Technological University
 Cookeville, TN 38505

Kirk W. McVoy
 Physics Department
 University of Wisconsin
 Madison, Wisconsin 53706

Alice C. Mignerey
 Department of Chemistry
 University of Maryland
 College Park, MD 20742

Klaus Mähring
 Nuclear Science Division, Building 70A
 Lawrence Berkeley Laboratory
 Berkeley, CA 94720

Peter Möller
 Nuclear Science Division
 Building 70A, Room 3307
 Lawrence Berkeley Laboratory
 Berkeley, CA 94720

Ulrich Mosel
 Institute für Theoretical Physik I
 Giessen-Heinrich-Buff-Ring 16
 D-6300 Giessen
 WEST GERMANY

W. D. Myers
 Nuclear Science Division
 Lawrence Berkeley Laboratory
 Building 70A, Room 3307
 Berkeley, CA 94720

J. Rayford Nix
 Nuclear Theory, T-9, MS B279
 Los Alamos National Laboratory
 Los Alamos, New Mexico 87545

Helmut Oeschler
 Institut für Kernphysik
 T. H. Darmstadt
 D-6100 Darmstadt
 WEST GERMANY

Franz Plasil
Oak Ridge National Laboratory
P. O. Box X
Oak Ridge, TN 37830

Norbert T. Porile
Department of Chemistry
Purdue University
West Lafayette, IN 47907

Jørgen Randrup
Nuclear Science Division
Lawrence Berkeley Laboratory
Berkeley, CA 94720

E. A. Remler
Physics Department
College of William & Mary
Williamsburg, VA 23185

Mark Rhoades-Brown
State University of New York
Stony Brook, NY 11794

Russell L. Robinson
Holifield Heavy Ion Research Facility
Oak Ridge National Laboratory
Oak Ridge, TN 37830

Horst Stoecker
Department of Physics & Astronomy
Michigan State University
East Lansing, MI 48823

Stephen T. Thornton
Department of Physics
University of Virginia
Charlottesville, VA 22901

Wolfgang Trautmann
Brookhaven National Laboratory
Physics 901A
Upton, NY 11973

Jacques Treiner
Nuclear Science Division
Lawrence Berkeley Laboratory
Building 70A, Room 3307
Berkeley, CA 94720

Man-Yee Betty Tsang
Cyclotron Laboratory
Michigan State University
East Lansing, MI 48824

Robert Vandenbosch
Nuclear Physics Laboratory GL10
University of Washington
Seattle, WA 98195

V. E. Viola
Chemistry Department
Indiana University
Bloomington, IN 47405

H. A. Weidenmüller
Max-Planck-Institut für Kernphysik
P. O. Box 103980
(69) Heidelberg, WEST GERMANY

Gary D. Westfall
National Superconducting Cyclotron Laboratory
Michigan State University
East Lansing, MI 48824

Ulrich Winkler
Physikalisches Institut
Philosophenweg 12
6900 Heidelberg, WEST GERMANY

Kevin L. Wolf
Cyclotron Institute
Texas A&M University
College Station, TX 77843

Gordon Wozniak
Lawrence Berkeley Laboratory
1 Cyclotron Road
Berkeley, CA 94720

Cheuk-Yin Wong
Oak Ridge National Laboratory
Oak Ridge, Tennessee 37830

Margaret Zielinska-Pfabé
Department of Physics
Smith College
Northampton, MA 01063